Ollscoil na hÉireann, Corcaigh

NATIONAL UNIVERSITY OF IRELAND, CORK

Atomic Layer Deposition of Photovoltaics

A thesis presented to

The National University of Ireland

For the degree of Doctor of Philosophy

by

Melissa M. McCarthy B.Sc.

Department of Chemistry,

Tyndall National Institute,

University College Cork.

January 2019

Principle supervisor: Dr Ian M. Povey

Co-supervisors: Dr Shane O'Brien & Professor Martyn E. Pemble

Head of School of Chemistry: Dr Humphrey Moynihan

TABLE OF CONTENTS:

CHAPTER 3:

OVERVIEW OF ATOMIC LAYER DEPOSITION 60

DECLARATION:

This is to certify that the work I am submitting is my own and has not been submitted for another degree, either at University College Cork or elsewhere. All external references and sources are clearly acknowledged and identified within the contents. I have read and understood the regulations of University College Cork concerning plagiarism.

03-01-2019

Melissa M. McCarthy Date

ACKNOWLEDGEMENTS:

I would like to sincerely thank my supervisor Dr Ian Povey for providing me with the opportunity to pursue this research. His advice, direction and sheer positivity throughout all aspects of this PhD have been invaluable. I'd like to especially thank my co-supervisors Dr Shane O'Brien and Professor Martyn Pemble for their knowledge, support and guidance throughout the course of my studies. I want to extend my gratitude to all past and present members of the Advanced Materials and Surfaces Group, in particular Louise Ryan, Dr Adrian Walsh, Jennifer Halpin, Shona Doyle, Dr. Jan Kegal and Dr Barry Hutchinson who have all contributed to an enjoyable experience at Tyndall National Institute.

I would like to express my sincere gratitude to Dr Sylvain Nicolay and Arnaud Walter for providing me with the opportunity to spend time at CSEM to learn essential deposition and characterisation methods. Similarly, I would like to offer a special thanks to Professor Henry Snaith and Dr Bernard Wenger for allowing me to intern at the University of Oxford and broaden my knowledge on perovskite devices. Thanks to CHEOPS for providing an interesting project as well as financial support through my PhD.

A special thanks to the colleagues at Tyndall National Institute who I have had the pleasure of working with – Dr Brendan Sheehan, Dr James Connolly, Dan O'Connell, Vince Lodge and Dr Mircea Modreanu. To Dr Fathima Laffir from the University of Limerick for the XPS measurements performed. Thanks to the friends outside AMSG who I have had the pleasure to get to know at Tyndall, namely Marco Dalla Santa, Dr Stefano Moroni, Andrea Pacheco, Natalia Canasestrada, Aziz Takrouni and Meysam Khanghah.

Love and thanks to my parents for their support and encouragement over the years as well as to my sister, Niamh, and brother, John. Thank you to my friends especially Claire, Eileen and the Wongs for providing much needed distractions. Most importantly, I would like to thank my partner Barry for the support, encouragement and long hours spent proofreading. Thank you for always being there.

LIST OF ABBREVIATIONS

ACN/MA	Acetonitrile/methylamine
AFM	Atomic Force Microscopy
Ag(fod)(PEt_3)	2,2,6,6-tetramethyl-3,5-heptanedionate silver
ALD	Atomic Layer Deposition
ALE	Atomic Layer Epitaxy
AM	Air Mass
APCVD	Atmospheric Pressure Chemical Vapour Deposition
APT	Atom Probe Tomography
AZO	Aluminium doped zinc oxide
BL	Blocking Layer
CBD	Chemical Bath Deposition
c-TiO_2	Compact TiO_2
c-Si	Crystalline silicon
CIGS	Copper Indium Gallium Selenide solar cell
CVD	Chemical Vapour Deposition
DEZ	Diethylzinc
DMF	N,N-Dimethylformamide
DMSO	Dimethyl sulfoxide

DSSC	Dye Sensitised Solar Cell
ETA	Extremely Thin Absorber
ETL	Electron Transport Layer
EQE	External Quantum Efficiency
FA	$HC(NH_2)_2^+$
FET	Field Effect Transistor
FF	Fill Factor
FTO	Fluorine doped tin oxide
GBL	γ-Butyrolactone
GPC	Growth Per Cycle
HTL	Hole Transport Layer
HTM	Hole Transport Material
IEP	Intramolecular Exchange Process
IPA	Isopropanol
ITO	Indium doped tin oxide
J_{sc}	Short-circuit current
KPFM	Kelvin Probe Force Microscopy
LED	Light Emitting Diode
LiTFSI	Lithium bis(trifluoromethanesulfonyl)imid
LiF	Lithium Fluoride
m-TiO_2	Mesoporous TiO_2

MA	$CH_3NH_3^+$
MBE	Molecular-Beam Epitaxy
MBTC	Monobutyl tin trichloride
MFC	Mass Flow Controller
MOVPE	Metalorganic Vapour-Phase Epitaxy
MPP	Max power point
MSE	Mean square error
PCBM	Phenyl-C_{61}-butyric acid methyl ester
PCE	Power Conversion Efficiency
PEALD	Plasma Enhanced Atomic Layer Deposition
PDS	Photothermal Deflection Spectroscopy
PEDOT:PSS	Poly(3,4-ethylenedioxythiophene)-poly(styrenesulfonate)
PL	Photoluminescence
PSC	Perovskite Solar Cell
PTAA	Poly-triarylamine
QCM	Quartz Crystal Microbalance
QE	Quantum Efficiency
RF	Radio Frequency
RMS	Root Mean Square
R_{oc}	Series resistance
R_s	Series resistance

R_{sc}	Shunt resistance
R_{sh}	Shunt resistance
RTA	Rapid Thermal Annealing
S-ALD	Spatial Atomic Layer Deposition
Sccm	Standard cubic centimetre per minute
SE	Spectroscopic Ellipsometry
SEM	Scanning Electron Microscopy
Spiro-OMeTAD	2,2',7,7'-Tetrakis[N,N-di(4-methoxyphenyl)amino] -9,9'-spirobifluorene
TA	Transient Absorption
tBP	4-tert-butylpyridine
TCO	Transparent Conductive Oxide
TDEAT	Tetrakis(diethylamido)titanium
TDMASn	Tetrakis(dimethylamido)tin
TDMAT	Tetrakis(dimethylamido)titanium
TDMAV	Tetrakis(dimethylamido)vanadium
tDOS	Trap Density of States
TEM	Transmission Electron Microscopy
TEMAH	Tetrakis(ethylmethylamino)hafnium
TFAA	Trifluoroacetic acid
TFEL	Thin Film Electroluminescence
TFT	Thin Film Transistor

TMA	Trimethyl Aluminum
TTIP	Titanium Isopropoxide
UPS	Ultraviolet Photoelectron Spectroscopy
V_{oc}	Open-circuit voltage
XPS	X-Ray Photoelectron Spectroscopy
XRD	X-Ray Diffraction
XTEM	Cross-Sectional Transmission Electron Microscopy
ZTO	Zinc tin oxide
p	Resistivity
μ	Mobility
N	Carrier concentration
Hν	Energy of photon
λ	Wavelength
ν	Frequency

ABSTRACT:

In recent years organic-inorganic halide perovskites have gained significant interest due to their high power conversion efficiencies (PCEs). These high efficiencies can be attributed to the perovskites' tuneable optical bandgap and long carrier diffusion length, with their low fabrication cost facilitating accelerated research. The first reported PCE using an organic-inorganic halide perovskite was 3.8 %, achieved in 2009 in conjunction with a liquid electrolyte. Since then, the perovskite field has been extensively studied and efficiencies now reach over 24.2 %. Despite these advances, long term stability and scalability have remained major challenges. Atomic layer deposition (ALD) is a low processing temperature technique capable of providing unrivalled thin-film conformality with uniform sub-nanometre thickness on large scale areas. Its use in depositing thin charge selective contacts as well as passivation layers in upscaled perovskite devices could further the field toward viable commercialisation.

The work carried out in this thesis is primarily concerned with the control and modification of electron transport layers (ETLs) deposited by ALD for use in mesoporous and planar perovskite solar cells (PSCs). ALD TiO_2 was compared to TiO_2 deposited by the alternative methods of spin-coating and RF sputtering and incorporated into mesoporous devices using both commercial and atmospheric pressure chemical vapour deposited (APCVD) FTO coated glass. The ability of ALD to produce conformal and pinhole free layers with high thickness uniformity at < 200˚C was demonstrated and the optimisation of ALD TiO_2 led to the fabrication of 1 cm^2 mesoporous PSCs with efficiencies of 16.45 %, matching the performance of cells incorporating RF sputtered TiO_2 and exceeding that of cells containing spin coated TiO_2. Following on from this, alternative growth chemistries and laminate doping of ALD TiO_2 were explored for use in mesoporous PSCs. For planar perovskite devices, ALD TiO_2 was problematic. Impurities and non-stoichiometry, previously improved by an anneal step for mesoporous devices, hampered performance. To counter this, rapid thermal annealing and in-situ interface engineering were investigated. Improvements were observed but the performance of TiO_2 in the mesoporous structure was not matched in the planar configuration. Attention was then turned to SnO_2, a material with a superior conduction band alignment with perovskites. In the planar n-i-p configuration 18.3 % PCE was achieved on 0.09 cm^2 and 15.9 % PCE was obtained on 0.7 cm^2 demonstrating considerable promise for commercial processes. Finally, the p-i-n configuration of planar

cell architecture was considered, where the ETL is grown directly on to the perovskite by ALD. Initial studies indicate that ALD chemistry can be tuned to prevent damage to either the bulk perovskite or its interface. The work presented in this thesis has demonstrated ALD to be an ETL deposition technique of great potential for efficient upscaled perovskite devices particularly in the reverse p-i-n architecture.

CHAPTER 1:

Outline of Thesis

The motivation of this thesis was to investigate metal oxide layers deposited by ALD for use as electron transport layers in mesoporous and planar perovskite solar devices. ALD was investigated due to its ability to produce high quality thin films at low deposition temperatures. The precise control of film thickness at the angstrom level in conjunction with the resulting conformal and uniform films allow the process to be scalable over large areas. The ALD process also has the potential to aid tuning of interfaces within the perovskite solar devices. Improving the charge carrier selective contacts is crucial to increasing PCE on upscaled perovskite devices. Selective contacts require a balance of thin layers to minimise resistive losses, and dense, uniform films to prohibit shunt pathways. Surfaces, bulk defects and interfaces all contribute to the admittance of recombination centres when scaling up in device area, which in turn leads to non-radiative and interface losses lowering the performance of cells. Another objective was to establish a full fabrication process for the synthesis and assembly of perovskite solar devices at Tyndall National Institute.

All ALD layers were deposited by commercial ALD systems, a Picosun R200 or a Cambridge Nanotech Fiji at Tyndall National Institute. An internship was arranged at the Swiss Centre for Electronics and Microtechnology (CSEM) to study established deposition and characterisation methods for PSCs. The results from Chapter 5 and part of Chapter 6 were obtained by the author on this placement.

Following the author's work depositing and characterising ALD SnO_2 ETLs at Tyndall National Institute, samples were sent to CSEM and the University of Oxford to be fabricated into planar PSCs. The power conversion efficiencies of these devices are discussed as part of Chapter 7. An internship was then arranged at the University of Oxford to study established methods of depositing mixed cation perovskite materials. Here, the author carried out a study comparing passivation layers on ALD SnO_2 to the same layers on spin-coated SnO_2 as detailed in Chapter 7.

Chapter 2 – This chapter provides an introduction to perovskite solar devices by first giving a synopsis of their historic development. This is followed by a brief overview of basic solar cell operation. The advantages and challenges of perovskite solar devices are examined along with a review of their progression to high power conversion efficiencies. Within this section various hybrid perovskite materials are described, as are different perovskite device architectures and processing methods.

Chapter 3 – Chapter 3 addresses the technique of ALD. This chapter consists of an overview of the development of ALD from its origin along with the key principles and characteristics of the deposition technique. Thermal and plasma enhanced ALD processes are described as well as the ALD growth of titanium dioxide and tin oxide. The application of these two metal oxides for use in perovskite cells is detailed.

Chapter 4 – This chapter focuses on the fabrication of mesoporous perovskite devices as part of a collaboration. The transparent conducting oxide, FTO, deposited by APCVD is compared to commercial FTO coated glass. TiO_2 blocking layers deposited by ALD, spin coating and RF sputtering are also compared. ALD layers are thermally deposited at 200°C in a range of thicknesses. The resulting mesoporous perovskite devices are characterised electrically.

Chapter 5 – The aim of Chapter 5 is to optimise ALD TiO_2 in an attempt to enhance the power conversion efficiency in mesoporous perovskite devices. The deposition temperature of films is reduced from 200°C to 185°C. This reduction is made in consideration of later integrating ALD layers into perovskite/silicon heterojunction tandem cells, one of the promising applications for PSCs. An ALD growth study is performed comparing different titanium precursors and reactants, as well as a range of metal dopants in a 19:1 and 99:1 TiO_2:dopant pulse ratio. As well as this, the effects of O_2 plasma in situ in the ALD chamber prior to deposition is examined. These depositions were carried out on two commercial reactors to determine if a difference in film quality could be observed or, alternatively, if the growths would be reproducible across both reactors. The ALD TiO_2 films are characterised structurally and electrically. The ALD thin films deposited at Tyndall National Institute are transported to CSEM and fabricated into mesoporous cells by the author. These resulting devices are then characterised electrically and compared to devices incorporating RF sputtered TiO_2.

Chapter 6 – The aim of this chapter is the optimisation of undoped ALD TiO_2 layers in terms of thickness for use in planar perovskite solar devices. The removal of the mesoporous TiO_2 layer permits the thickness of the ALD TiO_2 to be reduced as thin ALD films are unlikely to withstand the high temperature anneal employed in the mesoporous perovskite device fabrication method without cracking. In this section a thickness series of between 5 nm and 25 nm ALD TiO_2 is investigated along with the use of ALD interface control layers between the ALD TiO_2 and perovskite material. The final planar perovskite devices are characterised and discussed. The behaviour of low temperature ALD TiO_2 when deposited on top of the sensitive perovskite material is also explored.

Chapter 7 – In Chapter 7 the growth and characterisation of ALD SnO_2 is reviewed. The aim of this work is to investigate ALD SnO_2 as an alternative to ALD TiO_2 for use in planar perovskite solar devices. The metal oxides are compared in terms of morphology as well as optical and electrical properties. Surface passivation using C_{60}, PCBM as well as SnO_2 deposited by chemical bath deposition on various thicknesses of ALD SnO_2 is detailed for planar *n-i-p* device architectures. Low temperature ALD SnO_2 deposited on top of the perovskite material is also investigated with and without C_{60} passivation. The resulting planar perovskite devices are characterised electrically.

Chapter 8 – Finally, Chapter 8 presents conclusions arising from the research work outlined in this thesis. Suggestions for future experimental work are detailed.

CHAPTER 2:

Introduction to Perovskite Solar Cells

2.1 Origin of the Perovskite Semiconductor

The first identified perovskite material was $CaTiO_3$ discovered in 1839 by Gustav Rose and named after the Russian mineralogist, Perovski.[1] This class of compounds all produce the same crystal structure as $CaTiO_3$ with the general formula ABO_x in the cubic structure. A is an alkaline earth or rare-earth element which forms the ions on the corners of the lattice. B-site ions are found in the centre of the lattice and are either 3d, 4d, or 5d transition metal elements.[2] The crystal structure was first described by Victor Goldschmidt in 1926 during his work on tolerance factors.[3] In traditional perovskite oxides a large number of metallic elements are stable in the structure if the tolerance factor (t) is in the range of 0.75 to 1.0. Goldschmidt's work gained a considerable amount of attention due to the substantial size of the chemical class as well as the unique and benign properties they have produced.[4] The crystal structure of $BaTiO_3$ was described by Forrester and Hinde in 1945 and demonstrated an exceptional ferroelectric response as well as an extremely high dielectric constant in energy storage applications.[5] In 1988 high-temperature superconductivity was identified in other materials of the perovskite class such as $La_{2-x}Ba_xCuO_4$ and $YBa_2Cu_3O_{7-\delta}$.[6]

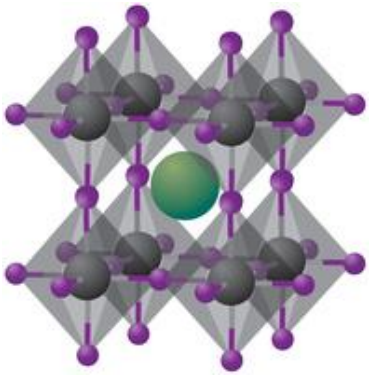

Figure 2. 1: *Crystal structure of cubic metal halide perovskite with the chemical formula ABX_3. The organic/inorganic cations occupy position A (green), the cation occupies B (grey) and the halide occupies position X (purple).*[7]

In addition to perovskite oxides, the perovskite structure also exists in perovskite halides. These types of perovskite bear the general formula ABX_x where B usually represents Pb^{2+} or Sn^{2+}, the anion X is a halogen (usually I^-, Br^- or Cl^-), and the A cation includes $CH_3NH_3^+$, $HC(NH_2)_2^+$, Cs^+, or Ru^+. Ideally, these perovskite halides have a cubic crystal structure consisting of a corner sharing BX_6 octahedral network with a large cation in the interstices. Müller first reported on semiconducting perovskite halides in 1958 as he described the structure and photoconductivity in all organic $CsPbI_3$ and $CsPbBr_3$ systems.[8] Weber went on to discover that the incorporation of organic cations had the ability to obtain the same crystal structure in the organic-inorganic hybrid perovskite halide, $CH_3NH_3PbX_3$.[9]

Present day interest in perovskite solar cells (PSCs) has been greatly assisted by the work of Mitzi and colleagues[10] in the early 1990s which reported on the synthesis of a conducting organic based layered halide perovskite, $(C_4H_9NH_3)_2(CH_3NH_3)_{n-1}\ Sn_nI_{3n-1}$ (n = 1 to 5). This material demonstrated a transition from semiconducting to metallic behaviour with increased dimensionality (*n*). The addition of an organic layer between sheets of tin iodide allowed for the tuning of electrical properties without introducing significant disorder. Mitzi et al.[11] explored the structural properties of these organic-inorganic perovskite materials and showed that the perovskite orientation could be modified by the choice of organic cation used. In this case butylammonium which formed <100> terminated perovskite sheets, was replaced with iodoformamidinium to form perovskites which terminated on a <110> crystallographic plane. These perovskites exhibited a similar trend toward metallic behaviour with increasing *n*. The

optoelectronic properties of these organic-inorganic perovskite materials worked well in transistors and light emitting diodes (LEDs), even exhibiting photovoltaic properties. The use of organic-inorganic perovskite materials in solar cells was predicted later by Mitzi[12] but was not investigated at the time, presumably due to the toxicity of Pb. This work conducted by Mitzi successfully incorporated organic-inorganic perovskites into field-effect transistors (FETs) and demonstrated the promising property of perovskites in electronic devices.

2.2 Operating principle of solar cells

Light is made up of pockets of energy known as photons. The energy and momentum of a photon is dependent on its frequency (ν) or wavelength (λ), where the photon moves at c, the speed of light, in an empty space.

$$E = h\nu = \frac{hc}{\lambda} \qquad \textbf{2.1}$$

Electrons can be optically excited by absorbing photons with an energy greater than the bandgap of their material. In this way electrons which are bound to a solid are freed from the valence band and injected into the conduction band where they can move freely and are able to conduct electricity. This phenomenon is known as the photoelectric effect.

The photovoltaic effect is the generation of voltage or electric current in a material when exposed to light energy. This was first reported by Alexandre-Edmund Becquerel in 1839 when he observed an electric current produced when a silver coated platinum electrode immersed in electrolyte was subjected to light. Similar effects for solid state devices were observed using selenium and two heated platinum contacts in 1876 by William Adams and Richard Day. It was not until the 1950's when the first solid state silicon solar cell was developed achieving an efficiency of 6 %.[13, 14]

A solar cell is composed of a light absorbing material connected to an external circuit in an asymmetric manner. Photoexcited charge carriers are generated within the material and separated allowing photovoltage and photocurrent to be produced.[14]

Photovoltaic devices depend on the generation of current and voltage under illumination. The short-circuit current (J_{sc}) is the maximum current obtained from a

solar cell. This is produced when the voltage between the two connected terminals of a device is zero. Current is dependent on the light intensity and the area of the cell therefore J_{sc} is expressed as current density. The voltage produced when the terminals are isolated (no flow of current) is called the open circuit voltage (V_{oc}). This is the maximum voltage obtained from a solar cell. While the J_{sc} is observed to decrease with increasing band gap, the V_{oc} increases with increasing band gap. For an intermediate load resistance of R, the solar cell produces a voltage (V) between 0 and V_{oc} and a current (I) between 0 and J_{sc} such that V = IR. IV is established by the current-voltage characteristics of the device under illumination.

The quantum efficiency (QE) of a solar cell expresses the probability of an incident photon of energy (E) delivering one electron to the external circuit. The photocurrent generated by a device at short-circuit is dependent on incident light, and so the total J_{sc} can be derived from the following formula in equation 2.2:

$$J_{sc} = q \int b_s(E) QE(E)\, dE \qquad \textbf{2.2}$$

Here, q represents the electronic charge and $b_s(E)$ represents the incident spectral photon flux density. E to $E+dE$ is the energy range of the number of photons which are incident on a unit area in a unit time.[14]

When a solar cell is under a load, as well as photogenerated current, a voltage is generated. The potential difference developed between the two terminals produces a current which flows in the opposite direction to the photocurrent. For V_{oc} this current would equal that of the photocurrent flowing in the opposite direction producing a net current of zero. This reverse current flows across the device under an applied voltage without illumination and so is termed dark current. The dark current follows an ideal diode formula as solar cells behave similarly to a diode in the dark due to the asymmetry required to achieve charge separation. From equation 2.3, J_0 represents a constant, k_B is Boltzmann's constant and T is temperature in degrees Kelvin:

$$J_{dark} = J_0 \left(e^{\frac{qV}{k_B T}} - 1 \right) \qquad \textbf{2.3}$$

For an ideal diode, the overall current in a solar cell under illumination can then be calculated by adding the photocurrent (forward direction) and the dark current (reverse direction) as displayed in equation 2.4:

$$J = J_{sc} - J_0 \left(e^{\frac{qV}{k_B T}} - 1 \right) \quad \textbf{2.4}$$

With regard V_{oc}, the maximum voltage is produced when the terminals are isolated and the photocurrent and the dark current cancel out. Equation 2.5 describes an ideal diode:

$$V_{oc} = \frac{kT}{q} \ln \left(\frac{J_{sc}}{J_0} + 1 \right) \quad \textbf{2.5}$$

In real cells, parasitic resistances effect the current-voltage characteristics. Series resistance (R_s) results from the resistance of the cell material to current flow as well as from the resistive contacts. This type of resistance is most prevalent at higher levels of illumination and higher current densities. Shunt resistance (R_{sh}) is a parasitic resistance in parallel with the solar cell. This results from the leakage of current in and around the edges of the cell, as well as between contacts. This can be caused by pinholes within the layers of a device and recombination in poorly rectifying cells. For efficient photovoltaic devices, the R_s is required to be as small as possible and the R_{sh} as large as possible. The overall current under illumination can then realistically be calculated using an ideality factor, *m*, and area of the device, A, with equation 2.6:

$$J = J_{SC} - J_0 \left(e^{\frac{q(V+JAR_S)}{mk_B T}} - 1 \right) - \frac{V+JAR_S}{R_{sh}} \quad \textbf{2.6}$$

The short circuit current and open circuit voltage describe the respective current and voltage of the solar cell. The cells power density is given in equation 2.7:

$$P = JV \quad \textbf{2.7}$$

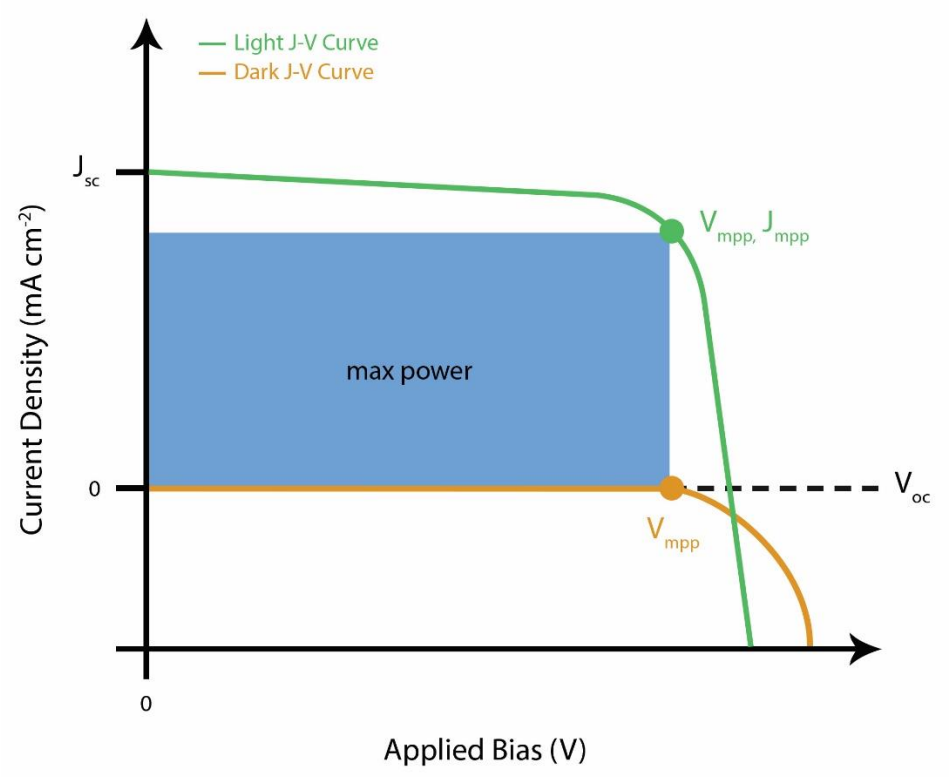

Figure 2. 2: *Current-voltage curve for photovoltaic device under illumination and in the dark*

At the respective points of V_{oc} and J_{sc} the power from the cell is zero. This is described in Figure 2.2 where the short-circuit current can be observed where the light curve intersects at V=0, and the open circuit voltage at an intersect where J=0. The power density reaches a limit at a maximum power point (P_{mpp}) which occurs at a certain voltage (V_{mpp}) and a corresponding current density (J_{mpp}). The fill factor (FF) is a parameter which in conjunction with the J_{sc} and V_{oc} determines the maximum power of the device. It is defined as the ratio of the maximum power from the cell to the ideal power of (J_{sc} x V_{oc}). The FF describes the "squareness" of the J-V curve displaying losses as given by equation 2.8.

$$FF = \frac{J_{mpp}V_{mpp}}{J_{sc}\,V_{oc}} \qquad \textbf{2.8}$$

The power conversion efficiency (PCE) of a device can be represented by η and is defined as the power density produced to the power density of the incident light (P_1) as shown in equation 2.9:

$$\mathrm{PCE} = \frac{P_{mpp}}{P_{in}} = \frac{J_{mpp}V_{mpp}}{P_{in}} = \frac{V_{oc}J_{sc}FF}{P_{in}} \quad \textbf{2.9}$$

The key performance characteristics of a solar cell are V_{oc}, J_{sc}, FF and η. To allow comparison to other photovoltaic devices they are usually measured under standard test conditions of an incident power density of 100 mW cm^{-2}, an Air Mass (AM) 1.5 illumination spectrum at 25°C. [14]

2.2.1 Types of solar devices

As noted previously, a solar cell is composed of a light absorbing material connected to an external circuit in an asymmetric manner. The light absorbing material employed is usually a semiconductor while the asymmetry built into the system allows electrons in the conduction band to be extracted from the cell in one preferential direction and holes to be extracted in a different direction. Band gap, work function, spatial variation in the electronic properties, and density of states can all be used to introduce asymmetry. There are several types of solar cells which all depend upon creating asymmetry to direct the flow of electrons and holes.

The p-n junction is the most commonly used photovoltaic device type for producing the majority of silicon solar cells today. This junction is formed when a p-type semiconductor and an n-type semiconductor are brought together. Excess electrons from the n-type material diffuse across the junction to the p-type material and recombine with holes. Likewise excess holes from the p-type material diffuse to the n-type material and recombine with electrons. This recombination process leaves behind positive ions from the dopant material on the n-type interface and negative ions from the dopant material on the p-type interface. This is known as the depletion zone as it is exhausted of free carriers. The recombination continues until a sufficient electric field is built up at the interface preventing further diffusion across the junction. The potential taken up in the semiconductor is represented by band bending. Upon illumination electrons are attracted down in energy towards the n-type material, and holes toward the p-type material as illustrated in Figure 2.3.

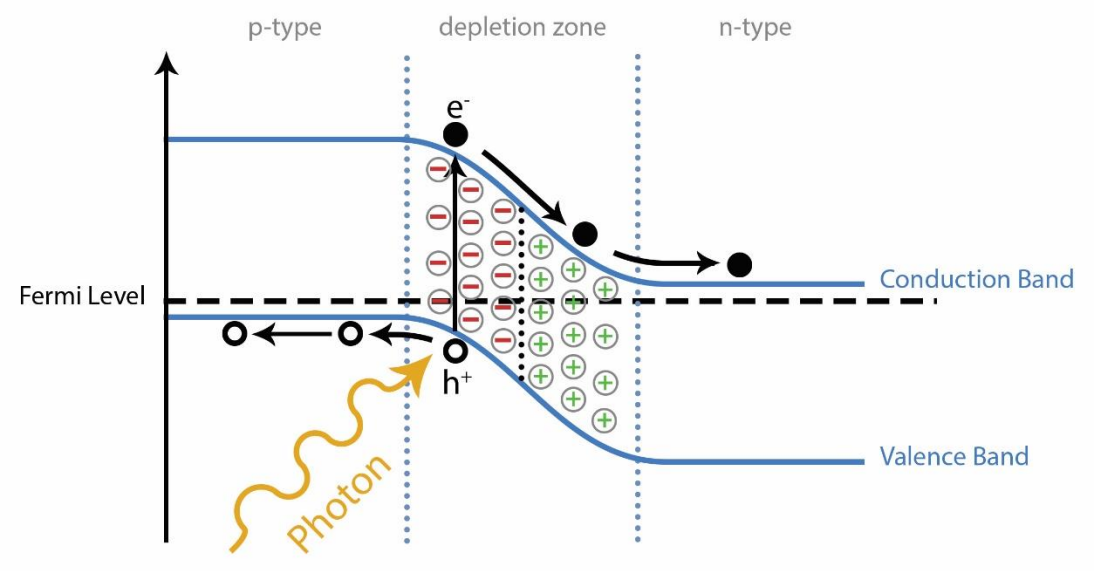

Figure 2. 3: *Schematic of a p-n junction solar cell under open circuit*

A p-i-n junction consists of three alternatively doped regions. This is similar to a p-n junction with an undoped or intrinsic layer sandwiched between the p-type and n-type materials. As with a p-n junction a built in bias is established, however the electric field extends over a wider region due to the intrinsic layer. This type of solar cell is favoured when the photogenerated charge carriers in the n-type or p-type material are unlikely to contribute to photocurrent or when the minority carrier diffusion lengths are short. Photogenerated charge carriers in the intrinsic region are accelerated toward their respective contacts by the large electric field and persist over a longer distance than charges in the doped materials.[14]

By employing materials of different band gaps heterojunctions can be formed from p-n junctions and p-i-n junctions. The change in band gap causes a potential step at the interface due to the break in the conduction and valence band edges. Heterojunctions may be required due to the doping of materials employed or may be selected to improve carrier collection.

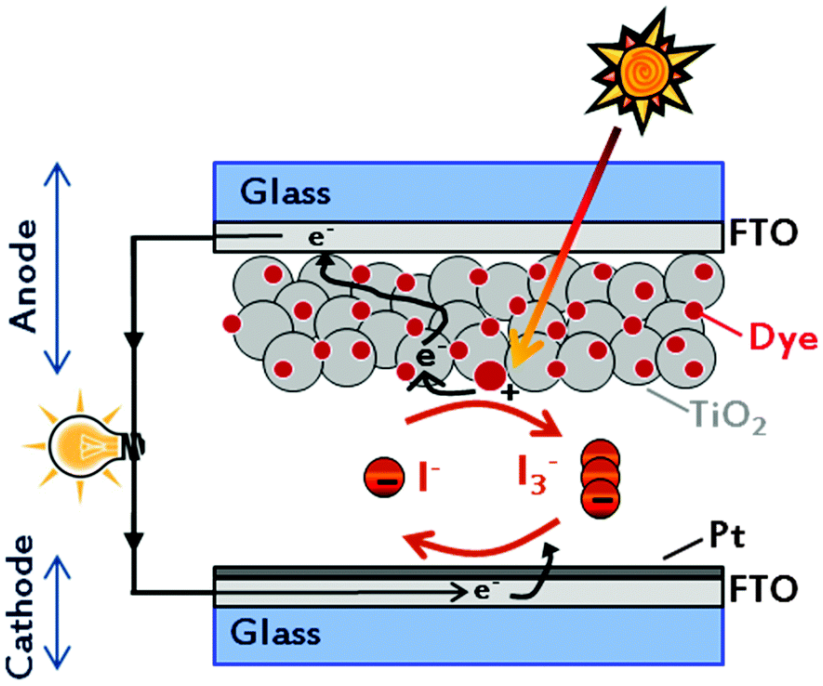

Figure 2. 4: *Schematic representation of the components and of the basic operating principle of a DSSC*[15]

Dye-sensitised devices allow charge generation and transportation to occur in separate materials. A dye absorbs photons from sunlight forming electron hole pairs. The excited electron is then injected into the conduction band of an n-type semiconductor, usually TiO_2, and diffuses to the anode. Following this, the electron passes through a load and comes to the cathode where a redox reaction occurs. I_3^- is reduced to I^- in the electrolyte solution which then donates an electron to the hole remaining in the electrolyte. This completes the circuit and regenerates an I_3^- as illustrated in Figure 2.4. Electrons are unable to transfer into the electrolyte and holes are restricted from passing into the semiconductor. The energetic difference between the semiconductor and the electrolyte forms the built in field.

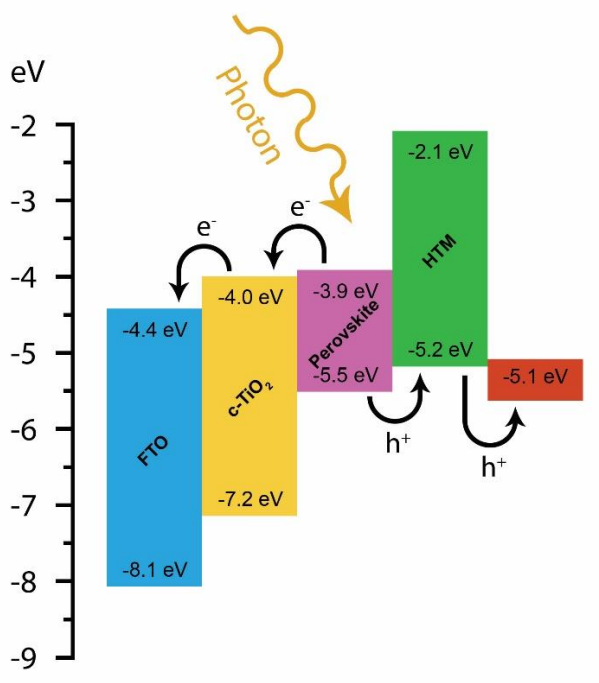

Figure 2. 5: *Energy level diagram of materials used in perovskite solar cells*

In perovskite devices, the light absorbed by the cell produces electron-hole pairs in the perovskite material. The electron-hole pairs subsequently separate and are transported through the material to their respective charge selective contacts (Figure 2.5). This charge separation can occur through two possible reactions. 1. Photogenerated electrons are injected into the ETL first, followed by the injection of holes into the hole transport layer (HTL), or 2. Photogenerated holes are injected into the HTL first, followed by the injection of electrons into the ETL (Figure 2.6).

1a. $(e^- - h^+)\ [\text{perovskite}] \rightarrow e_{cb}^-\ [TiO_2] + h^+\ [\text{perovskite}]$ **2.10**

1b. $h^+\ [\text{perovskite}] \rightarrow h^+\ [\text{HTL}]$ **2.11**

2a. $(e^- - h^+)\ [\text{perovskite}] \rightarrow h^+\ [\text{HTL}] + e^-\ [\text{perovskite}]$ **2.12**

2b. $e^-\ [\text{perovskite}] \rightarrow e_{cb}^-\ [TiO_2]$ **2.13**

Exciton annihilation can also occur causing disadvantageous reactions like photoluminescence and non-radiative recombination (3 and 4).

3. $(e^- - h^+)\ [\text{perovskite}] \rightarrow h\nu'$ **2.14**

4. $(e^- - h^+)$ [perovskite] $\rightarrow \nabla$ **2.15**

Recombination of the charge carriers can occur at the ETL/perovskite interface, the HTL/perovskite interface, or the ETL/HTL interface (5, 6 and 7).

5. e_{cb}^- [TiO_2] + h^+ [perovskite] $\rightarrow \nabla$ **2.16**

6. h^+ [HTL] + e^- [perovskite] $\rightarrow \nabla$ **2.17**

7. e_{cb}^- [TiO_2] + h^+ [HTL] $\rightarrow \nabla$ **2.18**

The overall efficiency of the device depends on the kinetics of these reactions.[16]

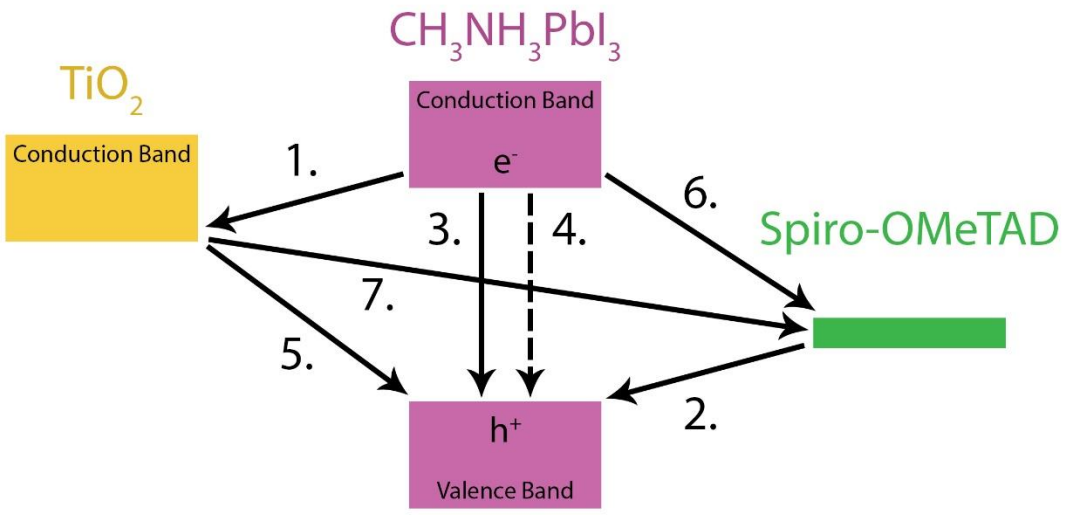

Figure 2. 6: *Schematic diagram of the electron transfer process in a perovskite cell*

2.3 Noteworthy properties

2.3.1 Long Carrier Diffusion Length

Unlike organic semiconductors, perovskite materials have an exceptionally large electron and hole diffusion length allowing them to reach high PCEs in solar cell devices. In 2013 Xing et al. reported both electron and hole transport diffusion lengths to be at least 100 nm in solution processed $CH_3NH_3PbI_3$.[17] In the same year Stranks

and colleagues also affirmed $CH_3NH_3PbI_3$ diffusion lengths of 100 nm, only an order shorter than its absorption depth. The mixed halide perovskite, $CH_3NH_3PbI_{3-x}Cl_x$, greatly surpassed these measurements with carrier diffusion lengths measuring > 1μm, a factor of 5-10 times greater than its absorption depth. The dramatic increase in electron-hole diffusion length by the addition of Cl^- is thought to have arisen from the inhibition of non-radiative recombination.[18] In 2015 carrier diffusion lengths of > 175 μm in a single-crystal $CH_3NH_3PbI_3$ were reported, by altering the deposition method. SCLC and hall effect measurements acquired hole mobilities > 100 $cm^2\ V^{-1}\ s^{-1}$ and an electron mobility of ~24.0 $cm^2\ V^{-1}\ s^{-1}$ as displayed in Figure 2.7.[19] These long carrier diffusion lengths along with the excellent light absorbing capabilities of perovskite materials allow them to be adapted into planar structures for use in solar cells. Planar heterojunction devices consist of the perovskite material sandwiched between an n-type and p-type interface forming either an *n-i-p* or *p-i-n* structure. Planar perovskite solar devices are comparable to the efficiency achieved with mesoporous cells. The omission of a mesoporous scaffold allows low-temperature processing of the entire cell, increasing the prospect of a commercially viable device.

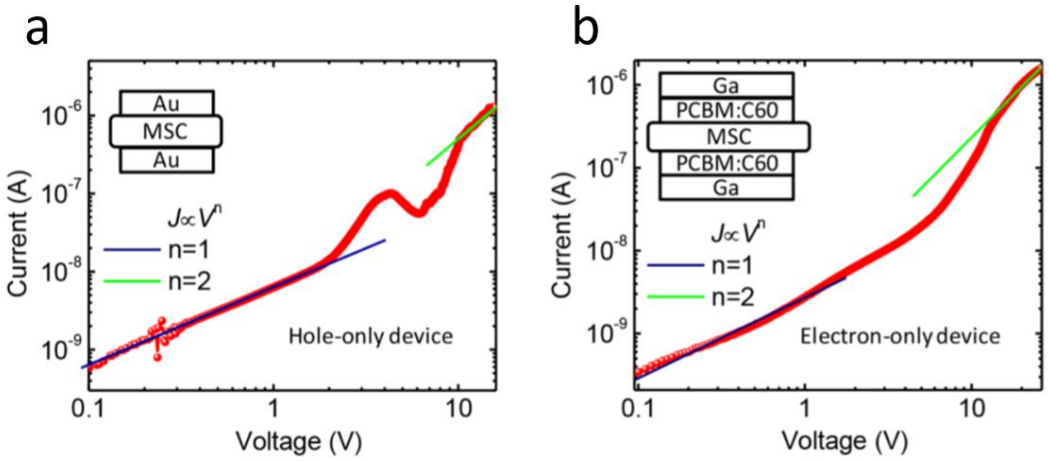

Figure 2. 7: *Carrier mobility characterization of $CH_3NH_3PbI_3$ single crystals.* ***(a)*** *current-voltage curve for a hole-only $CH_3NH_3PbI_3$ single crystal device, while* ***(b)*** *is for an electron-only $CH_3NH_3PbI_3$ single crystal device.*[19]

2.3.2 High absorption and tuneable bandgap

Perovskite semiconductors possess large absorption coefficients in the solar spectrum. An absorption coefficient exceeding 10^4 cm^{-1} near the band edge has been determined for $CH_3NH_3PbI_3$.[20] This measurement is on par with absorption measurements obtained from GaAs thin films and exceeds that of c-Si as displayed in Figure 2.8.[21]

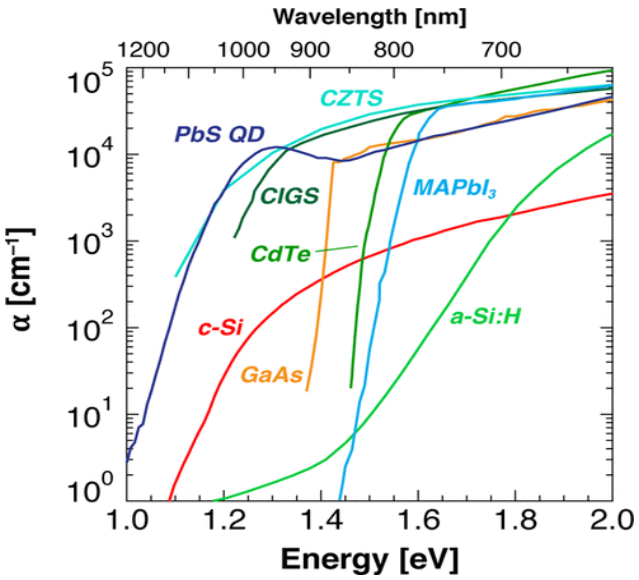

Figure 2. 8: *Absorption spectra of commercial and emerging PV technologies.*[21]

The direct bandgap of an organic-inorganic perovskite semiconductor can be spectrally tuned through the substitution of cations ($CH_3NH_3^+$, $HC(NH_2)_2^+$, Cs^+, or Ru^+) and compositional control of halides (I^-, Br^- or Cl^-).[22] The most studied perovskite material, $CH_3NH_3PbI_3$, has a red shifted electronic absorption of 800 nm. By exchanging Pb for Sn an absorption of up to 1060 nm can be achieved.[23] The flexibility in composition allows organic-inorganic perovskites to encompass an extensive range of band gap energies as seen below in Table II.I.

Table II. I: *Organic-inorganic perovskites comprise of a range of band gap energies*

Perovskite composition	Band gap
$CH_3NH_3SnI_3$	1.3 eV
$CH_3NH_3SnI_2Br$	1.56 eV
$CH_3NH_3SnIBr_2$	1.75 eV
$CH_3NH_3SnBr_3$	2.15 eV
$HC(NH_2)_2PbI_3$	1.50 eV
$CH_3NH_3PbI_3$	1.55 eV
$CH_3NH_3PbBr_3$	2.3 eV
$CH_3NH_3PbCl_3$	3.1 eV

2.3.3 Low cost

Organic-inorganic perovskites can achieve a high quality crystalline structure by precipitating out of solution before being annealed at a low-temperature (~100°C). This low energetic barrier for crystal formation allows for cheap deposition processes without compromising the performance of the device. Without the need for expensive growth chambers or annealing equipment, the low cost fabrication process is also beneficial for large scale commercialisation. Incorporating perovskite devices onto flexible substrates is also achievable through the scale up method of roll-to-roll.[24-26] Other photovoltaic devices in the field such as c-Si, CdTe and GaAs have not been as fortunate as perovskite devices with regard to processing cost.

2.4 Challenges

2.4.1 Stability

Perovskite solar devices have become one of the most promising emerging photovoltaic technologies due to their exceptional power conversion efficiencies. Despite this, their practical applications are limited due to issues with stability. Crystalline silicon solar cells, which are the market reference, have an average

degradation of 0.5 % per year. It is necessary for PSCs to reach similar levels of stability in order to compete in the market.

During fabrication and testing of perovskite solar cell devices the exposure to humidity, oxygen, UV radiation, and high temperatures can affect stability. A proposed mechanism for the degradation of $CH_3NH_3PbI_3$ in the presence of moisture is provided below: [27]

1. $CH_3NH_3PbI_3$ (s) ↔ PbI_2 (s) + CH_3NH_3I (aq) **2.19**

2. CH_3NH_3I (aq) ↔ CH_3NH_2 (aq) + HI (aq) **2.20**

3. 4HI (aq) + O_2 (g) ↔ $2I_2$ (s) + $2H_2O$ (l) **2.21**

4. 2HI (aq) ↔ H_2 (g) + I_2 (s) **2.22**

$CH_3NH_3PbI_3$ is first observed to hydrolyse in water before degrading. Step 3 demonstrates a redox reaction where hydrogen iodide degrades in the presence of oxygen. Step 4 displays a photochemical reaction where hydrogen iodide decomposes under UV radiation.[28-30] Encapsulation of the perovskite can help address the moisture sensitivity of these devices.[31-33] CIGS solar cells have already shown that the incorporation of encapsulation techniques are successful in preserving their efficiency, and it is thought that the same techniques can be adapted to PSCs.[27]

Organic-inorganic perovskites are also sensitive to humidity. $CH_3NH_3PbI_3$ has been reported to start decomposing at a humidity of 55 %.[34] This is clearly observed as the perovskite film bleaches, changing colour from dark brown to yellow. The incorporation or exchange of halide may offer a solution to this stability issue. The perovskite, $CH_3NH_3PbBr_3$, does not exhibit the same decomposition under the same humidity conditions.

Temperature is another factor that decomposes perovskite devices. While annealing is necessary to improve crystallinity and orientation of the perovskite film, increased temperature can degrade the cell. Pistor et al.[35] investigated a mixed halide perovskite film which was deposited by co-evaporation in a vacuum. Afterwards the film was annealed in the same vacuum environment where no reactive water or air was present. In situ XRD showed that the perovskite film decomposed to PbI_2 at temperatures of

200°C and above. The same mixed halide perovskite, $CH_3NH_3PbI_{3-x}Cl_x$, decomposes after 50 minutes of annealing at 100°C in a nitrogen atmosphere, and after 10 minutes at 100°C in air.[36] According to these results it is necessary to fabricate and deposit the perovskite in a glove-box, and not in ambient air. Thermal stability could also be a degrading factor when the solar cell is illuminated by sunlight. The thermal conductivity of $CH_3NH_3PbI_3$ has also been studied by Pisoni et al.[37] Much of the solar radiation in a perovskite device is converted into heat which the device is unable to be disperse evenly. This can cause mechanical stress limiting the lifetime of the perovskite device.

Perovskite solar devices are sensitive to UV degradation at the ETL/perovskite interface when TiO_2 is incorporated as the ETL. TiO_2 is the most commonly used ETL to date in PSCs, however it possesses photocatalytic properties which oxidise water and organic matter under UV illumination.[38]

$$2I^- \leftrightarrow I_2 + 2e^- \text{ (at the interface between } TiO_2 \text{ and } CH_3NH_3PbI_3) \quad \textbf{2.23}$$

$$3CH_3NH_3^+ \leftrightarrow 3CH_3NH_3 \uparrow + 3H^+ \quad \textbf{2.24}$$

$$I^- + I_2 + 3H^+ + 2e^- \leftrightarrow 3HI \uparrow \quad \textbf{2.25}$$

TiO_2 first extracts electrons from the I^- ions in the perovskite layer, deconstructing the perovskite crystal. Ito and co-workers[38] have demonstrated that the incorporation of Sb_2S_3 layers between TiO_2 and $CH_3NH_3PbI_3$ improves stability under UV illumination. The introduction of ETLs with wide band gaps, such as lanthanum doped $BaSnO_3$, can also offer photostability under UV radiation.[39] Alternately, it has been proposed that fluoropolymeric layers can be inserted as a coating into a perovskite cell. These have the ability to prevent the UV portion of the incident solar spectrum from degrading the perovskite solar cell. Instead the UV light is converted into visible light by the fluorophores, enhancing the overall photocurrent of the cell.[40]

The organic based HTL, Spiro-OMeTAD, has received attention in recent years due to its role in the instability of PSCs. Under thermal stress the compound can crystallise, causing metal electrode diffusion into the perovskite material.[41] It has also been observed that the dopant, lithium bis(trifluoromethanesulfonyl)imide (LiTFSI),

migrates from the HTL through to the perovskite material and ETL affecting overall efficiency of the cell.[42]

2.4.2 Hysteresis

The presence of hysteresis in the J-V curve of PSCs presents a challenge when determining the actual PCE of the cell. Hysteresis refers to a time dependant loss of output in a given system. In PSCs this is identified by a higher PCE observed in the reverse scan from V_{oc} condition to short-circuit condition, and a lower PCE exhibited from the forward scan from short-circuit condition to V_{oc}. From where this hysteresis originates is still under debate. However it is thought to depend on many parameters such as scan direction, scan rate, the architecture of the solar cell, voltage range, and preconditioning.[43-45] Immense research efforts over the last number of years have determined multiple possible causes for this hysteresis behaviour. These include slow transient capacitive current, the dynamic trapping and detrapping process of charge carriers, band bending due to ion migration, and band bending due to ferroelectric polarisation as illustrated in Figure 2.9.[46]

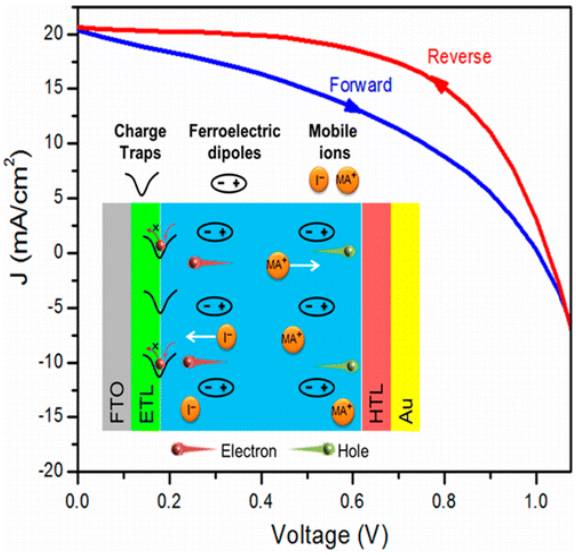

Figure 2. 9: *J-V curve showing hysteresis and difference in PCE along with cell schematic illustrating the causes of hysteresis.*[46]

Hysteresis due to the capacitance of the solar cell can be reduced and even eliminated when the scan rate is slowed sufficiently.[47] However for planar heterojunction perovskite solar devices, this hysteresis can persist at slow scan rates. Snaith and colleagues[48] found electron transfer to be weak when examining the interface between c-TiO_2 and a perovskite material in planar configurations. Modifying the c-TiO_2 with a self-assembled fullerene monolayer of C_{60}-SAM, demonstrated increased electron transfer, yielding a higher PCE with reduced hysteresis. Photothermal deflection spectroscopy (PDS) measurements showed that the incorporation of C_{60}-SAM discouraged the formation of trap states at the ETL/perovskite interface, reducing non-radiative recombination.

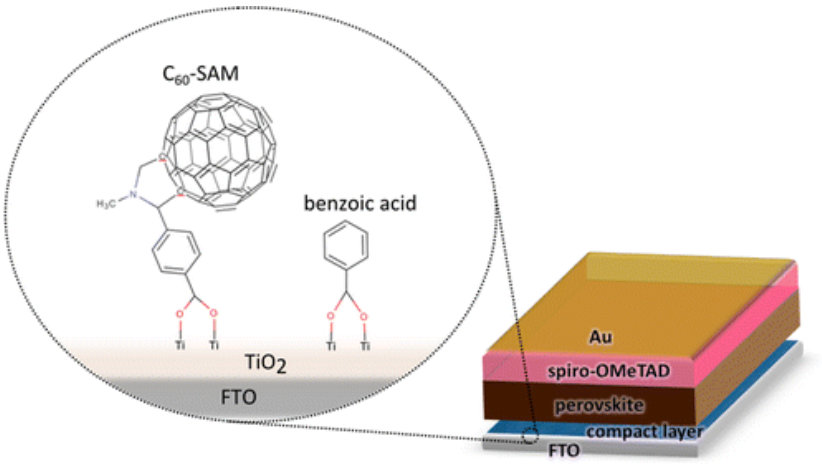

Figure 2. 10: *Schematic of planar perovskite device incorporating C_{60}-SAM on the TiO_2 surface.*[48]

Grätzel and co-workers found evidence that the slow process of ion migration resulted in hysteresis in the J-V curve.[44] A mesoporous scaffold perovskite device was pretreated under illumination for 30 s at an open circuit. The device was then measured with a reverse scan and directly afterward a forward scan at different voltage sweep rates. J-V curve hysteresis was observed to be rate dependant (Figure 2.11 a). A device was then kept under illumination at varying starting voltages ($V_{present}$) for 30 s before a J-V curve was measured. After pre-treatment with $V_{present}$, it was observed that the photocurrent was smaller at $V > V_{present}$ and was larger at $V < V_{present}$ (Figure 2.11 b). It was determined that devices which were pre-treated with illumination at an applied

voltage could compensate for the net built-in potential (Figure 2.11 c). Dark J-V curves were measured for a device without a TiO_2 hole blocking layer once the device had equilibrated at $V_{present}$ (Figure 2.11 d). The results demonstrated that the applied bias which modified the net built-in electric field was independent of illumination. The authors suggested that the electric field generated by the built-in potential and applied bias caused mobile charge carriers to move toward their respective electrodes. If the electric field is offset by a voltage larger than $V_{present}$ applied in a fast scan then charge extraction is weaker, causing the slow process of ion migration resulting in hysteresis.

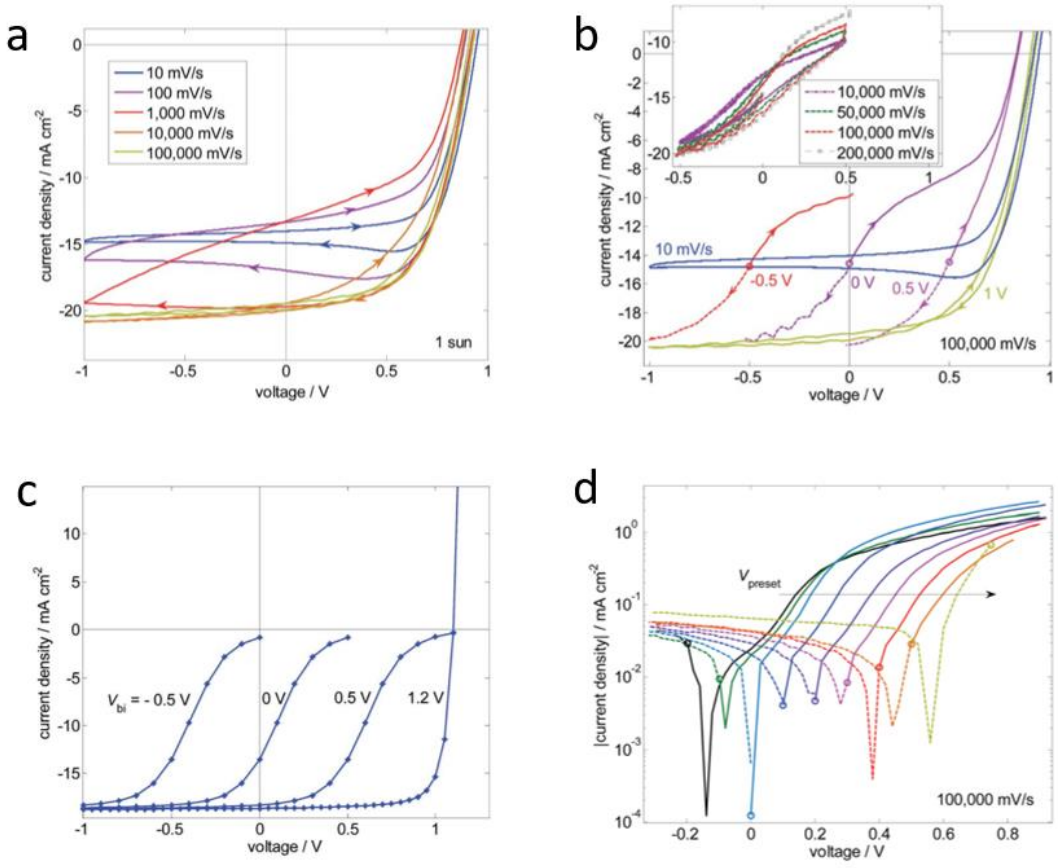

Figure 2. 11: (a) *J-V curves with different scan rates from 1V to -1V and back to 1 V. Arrows denote sweep direction.* ***(b)*** *J-V curves of a cell once it was kept for 30 s at different starting voltages ($V_{present}$ = -0.5, 0, 0.5, 1V). Inset shows the shape of the J-V curve for $V_{present}$ = 0 V between -0.5 and 0.5 V.* ***(c)*** *Device simulations with built-in potential V_{bi}* ***(d)*** *Electronic J–V curves for device without TiO_2 in the dark after the device equilibrated at $V_{present}$, which is marked with a circle. Solid lines are forward scans, and dashed lines denote backward scans.*[44]

The most widely used perovskite material for solar cells, $CH_3NH_3PbI_3$, has an intrinsic ferroelectric property. This ferroelectric behaviour can be enhanced when the material is deposited as a thin film and sandwiched between a metal oxide ETL and an insulating HTL. Wei et al. showed that the mixed halide perovskite, $CH_3NH_3PbI_{3-x}Cl_x$, produced hysteresis in the J-V curve. This hysteresis was dependant on scan range and velocity which were attributed to the ferroelectric effect of the perovskite material.[47] The interface band structure of a perovskite material can be engineered to manifest a different polarisation character if the perovskite thin film contains ferroelectric domains. This change can exhibit different PCEs for the device under forward and reverse sweeping scans. Negative poling produces a polarisation within the perovskite film which prevents charge separation and reduces the performance of the cell. The perovskite material is especially sensitive to an external bias when incorporated into a planar structure (Figure 2.12). This may account for the pronounced hysteresis observed in planar heterojunction structures compared to mesoporous structures.[49]

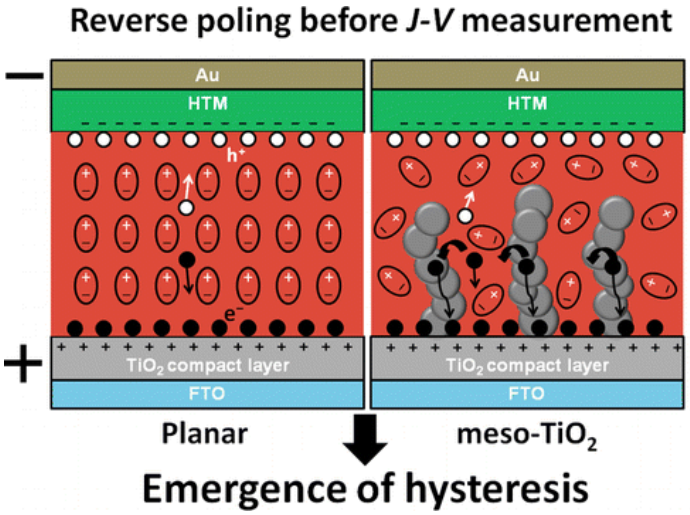

Figure 2. 12: *Schematic illustration of perovskite cells in the planar structure and with a mesoporous TiO_2 scaffold under applied electric field, and physical mechanism of polarisation in the ferroelectric perovskite material.*[49]

The use of C_{60}/fullerene molecules such as polystyrene sulfonate (PEDOT:PSS), phenyl-C61-butyric acid methyl ester (PCBM) and lithium fluoride (LiF) have been reported to eliminate hysteresis when used as interlayers in planar PSCs using a $CH_3NH_3PbI_3$ perovskite. It has been proposed that these fullerene molecules passivate

trap states by interacting with halide rich defective regions at grain boundaries of the perovskite.[50-52] Low-temperature studies on these hysteresis free perovskite devices employing fullerene passivation have exhibited substantial hysteresis at sub-zero conditions of 175 K. This indicates that the issue with J-V hysteresis is related to the relaxation process of the $CH_3NH_3PbI_3$ induced by applied voltages. The half-time for the relaxation process underlying this hysteresis slowed from 0.6 seconds at 298 K to 15.5 seconds at 175 K. This study provides insight into device stability over time yielding an activation energy of 0.12 eV.[53]

2.5 Ascension of Power Conversion Efficiency in PSCs

2.5.1 Introduction of mixed-halide perovskites in photovoltaics

The first photovoltaic results using organic-inorganic perovskites was reported in a 2006 poster abstract by Kojima et al.[54] The perovskite compound, $CH_3NH_3PbBr_3$, appealed to the research group due to its self-organised semiconductor crystal structure. The perovskite compound was spin-coated onto a nanoporous TiO_2 electrode which had been deposited on fluorine doped tin oxide (FTO) coated glass. Pt coated glass acted as a counter electrode while the electrolyte solution was synthesised from LiI and I_2 in a mixed acetonitrile/isobutyronitrile solvent. The resulting liquid electrolyte based dye sensitised solar cell (DSSC) reached a maximum power conversion efficiency (PCE) of 2.19 % under an irradiated condition of 100 $mWcm^{-1}$. This result was improved by to 3.8 % PCE in 2009 by replacing bromine with iodide in the perovskite compound.[55] The stability of all of these devices was extremely poor due to the immediate dissolution of the perovskite compound in the liquid electrolyte and so did not gather much interest. Miyasaka and colleagues later attempted to replace the liquid type electrolyte with a solid state hole transport material (HTM).[56] PPCB was used as a conductive polymer but proved unsuccessful at 0.37 % PCE for $CH_3NH_3PbI_3$ and 0.21 % PCE for $CH_3NH_3PbBr_3$.

Park et al. achieved 6.5 % PCE by changing the electrolyte formation and the way in which the perovskite was deposited.[57] The perovskite material, $CH_3NH_3PbI_3$, was

deposited as quantum dot semi-spheres with an average diameter of 2.5 nm on the surface of TiO_2. The TiO_2 surface itself was nanocrystalline and was deposited on cleaned FTO coated glass which had been pre-treated with titanium (IV) bis(ethyl acetoacetato)diisopropoxide. A Pt counter electrode was employed on FTO coated glass. The report showed that $CH_3NH_3PbI_3$ acted as an improved light harvester compared to the conventional ruthenium-based organometallic N719 dye used at the time, allowing a thin absorbing layer of perovskite nanoparticles to sufficiently absorb and convert light. The dissolving of the perovskite in the electrolyte remained an issue causing the performance of the cell to degrade almost instantly.

2.5.2 Replacement of liquid electrolyte

2.5.2.1 $CsSnI_3$ perovskite as a p-type semiconductor

The significant obstacle posed by the electrolyte containing an iodide/tri iodide redox couple required a fundamental advancement in the field. Chung et al. attempted replacing the liquid electrolyte with the p-type semiconductor, $CsSnI_3$, resulting in a solid-state DSSC.[58] This type of solar cell consisted of the commonly used molecular N719 ruthenium sensitizer rather than an organic-inorganic perovskite material. Doping of $CsSnI_3$ with F and SnF_2 was found to dramatically increase both short-circuit voltage (J_{sc}) and final power conversion efficiency, achieving 10.2 % PCE. $CsSnI_3$ adopts a distorted three dimensional perovskite structure at room temperature with a notably high hole mobility of 585 $cm^2\ V^{-1}\ s^{-1}$. This study demonstrated that the doped perovskite did not just act as a p-type semiconductor but also effectively separated photogenerated holes and electrons. A solid state cell without ruthenium based dye was fabricated and worked as a photovoltaic device producing very low efficiencies of 0.2 % PCE. Charge separation was accelerated by the addition of the ruthenium dye leading to the high 10.2 % efficiency.

2.5.3 Incorporation of Spiro-OMeTAD

The most influential alternative to the liquid electrolyte in perovskite devices came as an amorphous organic compound called 2,2′7,7′-tetrakis-(N,N-di-p-methoxyphenyl-amine)-9,9′-spirobifluorene (Spiro-OMeTAD). This was first introduced by Bach et al. in 1998 for use in a DSSCs which exhibited a poor PCE of 0.04 %.[59] This value

increased to 0.74 % efficiency with the addition of a Li^+ salt as a dopant. In 2006 work by Snaith and Grätzel showed that the charge carrier mobility of Spiro-OMeTAD could be enhanced by an order of magnitude with the addition of lithium bis(trifluoromethanesulfonyl)imide (LiTFSI) and chemical p dopants (antimony salt).[60] A 100 fold increase in conductivity could also be observed when this HTM was incorporated within a TiO_2 mesoporous network.

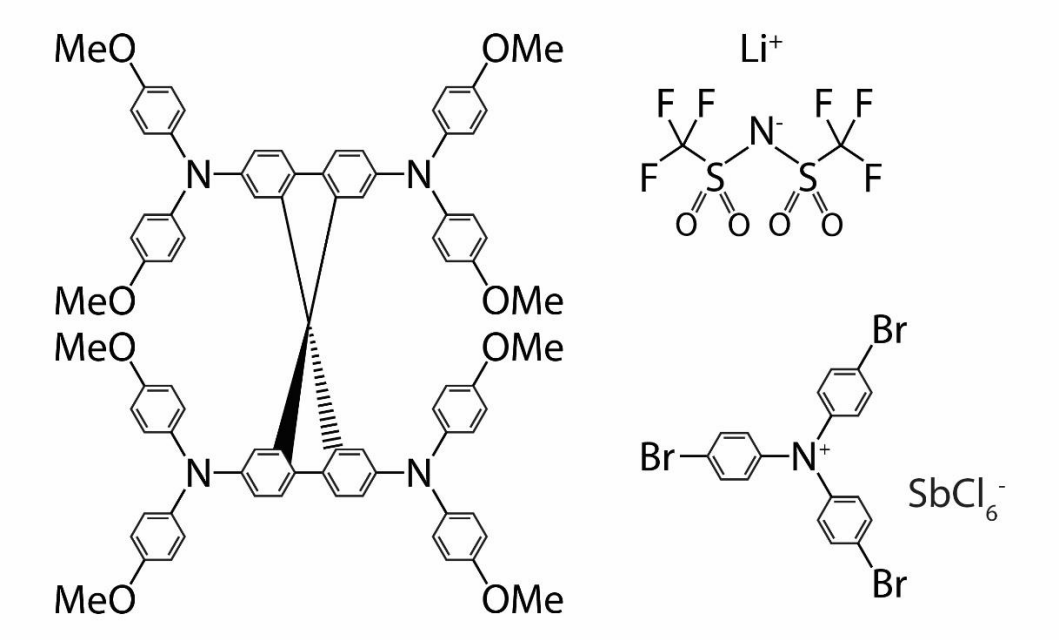

Figure 2. 13: *Chemical structure of Spiro-OMeTAD, LiTFSI and antimony salt*

Spiro-OMeTAD was not introduced into PSCs until 2012.[61] The device comprised an FTO coated glass substrate, a compact TiO_2 blocking layer, a nanocrystalline mesoporous sub-micron thick anatase layer, $CH_3NH_3PbI_3$ nanoparticles as the perovskite material, a Spiro-OMeTAD hole conductor, and a gold top contact. This structure made PSCs almost identical to that of solid-state DSSCs. The device exhibited a record PCE of 9.7% under simulated AM1.5G sun illumination. The thickness of the mesoporous TiO_2 (m-TiO_2) layer was shown to influence the photovoltaic performance of the device greatly. V_{oc} and FF decreased by increasing thickness from 0.6 – 1.4 μm. The adoption of Spiro-OMeTAD as a solid HTM notably improved the stability and efficiency of the device compared to its liquid electrolyte

counterpart. The cell was stored without encapsulation in air at room temperature for over 500 hours. Ex-situ results showed that the V_{oc} stayed stable, the FF improved and then stabilised, and the J_{sc} exhibited a slight decrease and eventual plateau after 200 hours. Photovoltaic activity was present throughout this test.

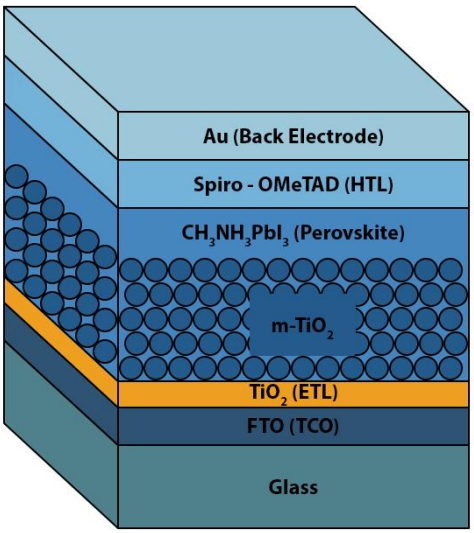

Figure 2. 14: *Schematic illustration of a mesoporous scaffold perovskite solar cell*

Concurrently, Snaith and colleagues were also independently incorporating Spiro-OMeTAD into perovskite solar devices.[62] Contrary to Park however, the Spiro-OMeTAD HTM was integrated into a device consisting of a mixed halide perovskite material, $CH_3NH_3PbI_{3-x}Cl_x$. This organic-inorganic perovskite material exhibited improved stability when processed in air as well as improved stability in extended light exposure (1000 hours of continual illumination under simulated sunlight), when compared to the more common $CH_3NH_3PbI_3$. The perovskite layer was spin-coated and annealed forming a markedly thin layer infiltrating the nanoporous m-TiO_2. This approach differed from work at the time involving nanoparticle perovskite structures, instead forming an extremely thin absorber (ETA) device. This type of perovskite solar cell exhibited a PCE of 7.6 %. The m-TiO_2 layer was then replaced with an insulating Al_2O_3 mesoporous scaffold, coining the term "meso-super-structured solar cell". This produced an enhanced PCE of 10.9% under simulated AM1.5G sun illumination. Al_2O_3 has a wide bandgap (7 – 9 eV) compared to TiO_2 and so is not

able to aid in electron extraction. The report suggested that the perovskite material itself was transporting electrons to the compact TiO_2 (c-TiO_2) layer. The improvement in efficiency by replacing m-TiO_2 with mesoporous Al_2O_3 demonstrated that the mixed halide perovskite, $CH_3NH_3PbI_{3-x}Cl_x$, was faster at transporting electronic charge than m-TiO_2. These cells produced a V_{oc} that was more than 200 mV greater than those with an m-TiO_2 layer, boosting the final performance. This report also suggested toward a new simpler planar structure for PSCs in which no scaffolding was needed.

2.5.4 HTM-free device

During the same year, 2012, Etgar et al.[63] demonstrated that the organic-inorganic perovskite material, $CH_3NH_3PbI_3$, could also play the part of a hole conductor allowing for HTM-free perovskite solar devices. This cell did employ a m-TiO_2 layer which was composed of anatase nanosheets with dominant (001) facets as the electron collector and transporter. The nanosheets showed an enhanced photovoltaic performance compared to the commonly used TiO_2 nanoparticulate films. The authors suggested that this was due to the higher ionic charge concentration found in exposed (001) facets compared to (101) facets. A gold contact was evaporated on top of the $CH_3NH_3PbI_3$ perovskite layer and the entire cell reached a PCE of 5.5 %.

2.5.4.1 Ambipolar nature of perovskite

In 2013, Seok, Grätzel and colleagues further proved that $CH_3NH_3PbI_3$ could be used to transport both holes and electrons.[64] In this study various polymeric mesoporous scaffolds and HTMs, as well as the absence of a HTM or mesoporous layer, were investigated alongside m-TiO_2 and Spiro-OMeTAD. The polymeric hole conductor poly-triarylamine (PTAA) worked the best and produced a record efficiency of 12 % PCE when incorporated into a perovskite solar cell. The Spiro-OMeTAD counterpart cell achieved a poorer 8 %. From EDS mapping and XPS depth profiling a clear difference could be seen in the interaction of each of these HTMs with the perovskite material. The Spiro-OMeTAD was observed to permeate the m-TiO_2 pores easier than the polymer PTAA due to its lower molecular weight. PTAA was mostly found at the surface of the m-TiO_2/ $CH_3NH_3PbI_3$ composite layer. Perovskite solar cells with an absent HTM, as well as cells without a mesoporous scaffold were both shown to

exhibit power conversion efficiencies but were greatly improved by their presence. This was further supported by constructing a thin film transistor (TFT) device which showed $CH_3NH_3PbI_3$ behaving as an ambipolar semiconductor able to transport both electrons and holes. This confirmed results observed by Lee and Etgar previously.[62, 63] The PTAA perovskite solar cell was improved from 12 % to 12.3 % PCE by replacing $CH_3NH_3PbI_3$ with a mixed halide perovskite, $CH_3NH_3PbI_{3-x}Br_x$.[34] The band gap of $CH_3NH_3PbI_3$ is reported at 1.53 eV[61] while that of $CH_3NH_3PbBr_3$ is much higher at 2.3 eV.[55] By altering the amount of Br content, the light harvester perovskite could easily be tuned. The most efficient device had a low Br content (<10 %) incorporated in the mixed halide perovskite, however higher content also proved useful by remaining stable at high humidity. The authors suggested that this may be due to the smaller ionic radius of Br allowing for a more condensed and stable perovskite structure. The lattice constant was reduced with the incorporation of a higher Br content and the perovskite phase transitioned from tetragonal to pseudo-cubic.

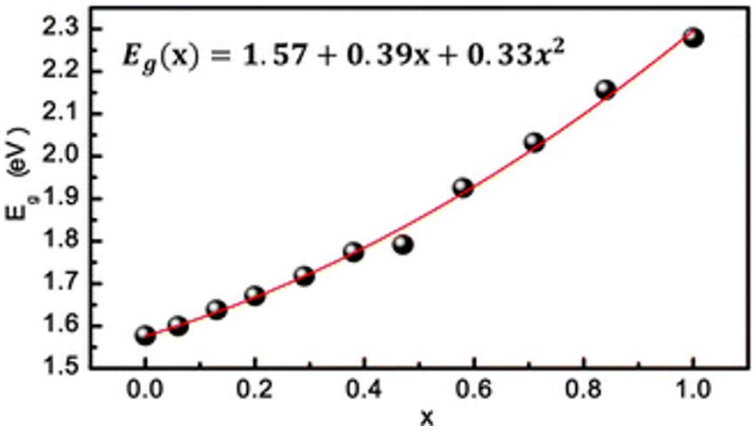

Figure 2. 15: *Graph showing the quadratic relationship of the band gaps of $CH_3NH_3Pb(I_{1-x}Br_x)_3$ as a function of Br composition (x).*[34]

2.5.5 Alterations in deposition process

2.5.5.1 Sequential deposition

Up until this point in time the perovskite precursors PbX_2 and CH_3NH_3X (X = I, Cl or Br) had been mixed in a common solvent and deposited in a single step. In 2013 a sequential deposition procedure was established which allowed for improved reproducibility and better control over perovskite morphology.[65] Grätzel's group first dissolved PbI_2 in N, N-Dimethylformamide (DMF) and spin-coated the solution, which was kept at 70°C, onto a m-TiO_2 layer. The m- TiO_2/PbI_2 composite layer was then dipped in a solution of CH_3NH_3I in 2-propanol for 20 s. After drying, a standard Spiro-OMeTAD HTL was spin-coated on top followed by an evaporated Au contact. These solar cells yielded a reproducible efficiency with the highest achieving 12.9 % PCE. Characterisation of the m-TiO_2/PbI_2 composite layer by Scanning Electron Microscopy (SEM) showed no PbI_2 crystals extruding from the m-TiO_2 surface. This indicated that the PbI_2 layer was contained completely within the pores of the anatase m-TiO_2. During X-Ray Diffraction (XRD), additional peaks which did not arise from the TiO_2 layer could be observed from PbI_2/m-TiO_2/glass when compared to PbI_2/glass (Figure 2.16). This implied that the m-TiO_2 scaffold caused PbI_2 crystal growth to differ in orientation. Without the TiO_2 scaffold present, the perovskite precursors converted at a much slower rate. The authors noted that when PbI_2 was deposited on the scaffold, its crystal size was limited to ~22 nm due to the scaffold pores. When exposed to a solution of CH_3NH_3I the rate of conversion to perovskite was dramatically increased. This two-step deposition technique caused the perovskite, $CH_3NH_3PbI_3$, to assume a restricted nanomorphology. This method was improved further by slightly altering the deposition methods to yield a PCE of 15.0 %. The modifications involved spin-coating the PbI_2 solution at a shorter time of 5 s and an additional pre-wetting step of the m- TiO_2/PbI_2 composite layer in 2-propanol before being dipped in the CH_3NH_3I solution. The boosted efficiency obtained from these small changes was generated by increased light-scattering from the pre-wetting step and an added filling of the m-TiO_2 pores with perovskite pigment. This was also the first report of independent measurements for certification. The independent accredited test centre confirmed a PCE of 14.1 % measured under AM1.5G standard reporting conditions. The use of independent measurements for photovoltaic technology went

on to become imperative as it controlled the quality of cells, preventing inflated results from reaching the literature.[66]

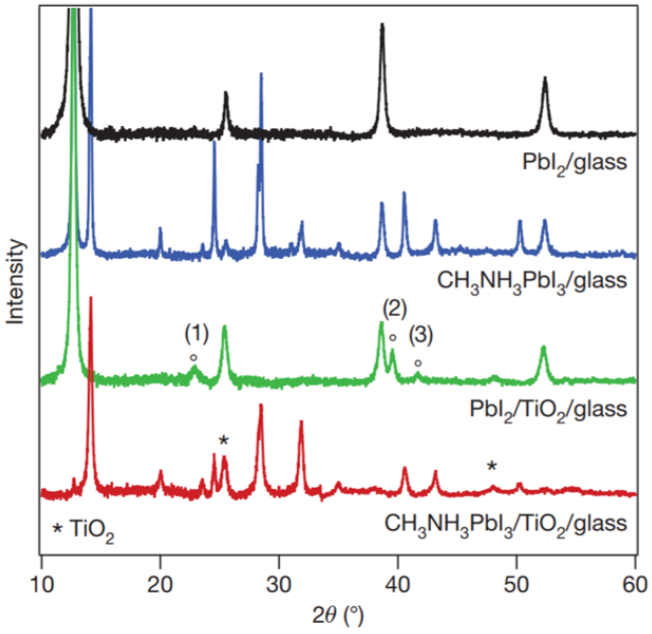

Figure 2. 16: *XRD spectra of PbI_2 on glass and porous TiO_2/glass before and after the sequential deposition transformation.*[65]

2.5.5.2 Vapour deposition

Snaith et al. achieved similar high efficiencies of 15.4 % PCE in 2013 with a simple planar structure heterojunction cell.[67] The mixed halide organic-inorganic perovskite, $CH_3NH_3PbI_{3-x}Cl_x$, was deposited by dual source vapour deposition on a dense c-TiO_2 layer. The standard Spiro-OMeTAD HTM was then spin-coated on top, followed by an Ag evaporated contact. The vapour deposition allowed precursors $PbCl_2$ and CH_3NH_3I to simultaneously be evaporated on the c-TiO_2/FTO substrate under high vacuum. This vapour method allowed for extremely uniform perovskite films to be deposited with an average thickness of 300 nm. Planar solar cells fabricated using a solution-processed mixed halide were made up alongside these to compare in the study. XRD characterisation exhibited the same diffraction peaks at identical positions for both solution-processed and vapour-deposited perovskite films, indicating that the same orthorhombic crystal structure was produced in the mixed halide perovskite with

a strong degree of phase purity. SEM showed a vast contrast between solution-processed and vapour-deposited films in terms of morphology. The solution-processed films did not have full coverage on the substrate with film thickness varying from 0 - 465 nm. Crystalline platelets could be observed on a scale of tens of micrometers lengthways. In contrast, the vapour-deposited films were exceptionally uniform with crystalline features measuring hundreds of nanometres on the length scale (Figure 2.17). This uniformity appeared to be what achieved such a high efficiency as the best solution-processed cell only yielded 8.6 % PCE. The authors noted that it was fundamental to optimise film thickness in the perovskite layer to reach highly efficient solar cells. The device would be unable to absorb an adequate amount of sunlight if the perovskite film was too thin. Adversely, it would be impossible to collect electrons and holes at their respective heterojunctions if the perovskite film was too thick due to exciton diffusion length being shorter than the film thickness. Results from this study proposed an ideal film thickness of 330 nm, however it was acknowledged that further investigation was required. The vapour deposition technique posed the benefit of being effective on large area substrates for the manufacturing industry.

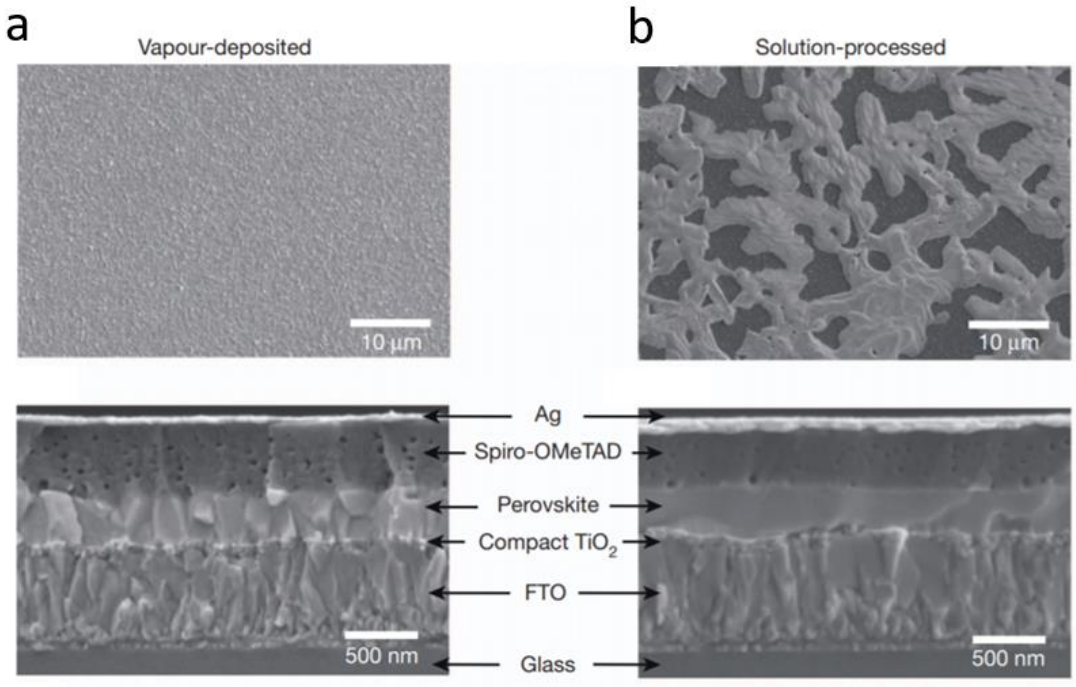

Figure 2. 17: *SEM plan view images of perovskite and cross sectional images of full sell from (a) vapour deposited perovskite film and (b) solution processed perovskite film*[67]

2.5.5.3 Solvent engineering

In 2014, Seok et al.[68] obtained an independently confirmed 16.2 % PCE using a mixed halide perovskite, $CH_3NH_3Pb(I_{1-x}Br_x)_3$ (x = 0.1 - 0.15), and a careful selection of solvent mixtures. The polymer, PTAA, was again used as a HTM and evaporated Au as contact. The use of γ-butyrolactone (GBL) and dimethylsulphoxide (DMSO) together in suitable ratios as a mixed solvent for the perovskite precursors produced extremely uniform and dense films when followed by a toluene drip during spin-coating. This solvent engineering method also detected an intermediate phase in the perovskite formation which could be isolated. Figure 2.18 outlines the procedure involved in this solvent engineering method.

1. The perovskite precursors CH_3NH_3I, CH_3NH_3Br, PbI_2 and $PbBr_2$ are mixed with GBL and DMSO in suitable ratios before being deposited by dropper, fully coating the surface of the m-TiO_2/c-TiO_2/FTO coated glass substrate.
2. The spin-coater is turned on and solvent is evaporated.
3. Toluene, a solvent which can be mixed with GBL and DMSO but does not dissolve the perovskite precursors, is dripped by dropper on the substrate during spinning.
4. An immensely crystalline and self-organised intermediate phase (CH_3NH_3X – PbX_2 - DMSO) is formed.
5. Upon annealing, the intermediate phase transforms into an extremely uniform and crystalline perovskite film.

This solvent engineering method significantly improved the morphology of the perovskite layer. Without the addition of DMSO in the solvent mixture, coverage was poor and uneven islands formed on the substrate surface. DMSO slowed the fast reaction between CH_3NH_3X and PbX_2 in the intermediate phase allowing the addition of toluene to even out the perovskite, producing a dense and uniform film. In-situ high-temperature XRD of the intermediate phase as it transitioned into the perovskite phase showed that complete conversion did not occur until 130°C. Both CH_3NH_3X - PbX_2 - DMSO and the perovskite existed in the film together at the standard perovskite annealing temperature of 100°C. The authors also attempted to execute this solvent engineering method in planar perovskite cells. A PCE of 14.4 % was achieved but

significant hysteresis and distortion could be observed in the J-V curves when measured under AM1.5G illumination. The resultant overestimation in the reverse scan and underestimation in the forward scan could cause error when measuring cell efficiency. When a 200 nm m-TiO_2 layer was employed, a symmetrical efficiency was observed in each scan direction. It was proposed that generated electrons may remain for longer in the thick perovskite material without an m-TiO_2 layer for fast charge collection. This solvent engineering method of quenching the perovskite precursors in a polar solvent with a non-polar solvent such as toluene (or chlorobenzene or diethyl ether later on) during spin coating became the preferred method of deposition among researchers and has achieved all subsequent efficiency records since then.

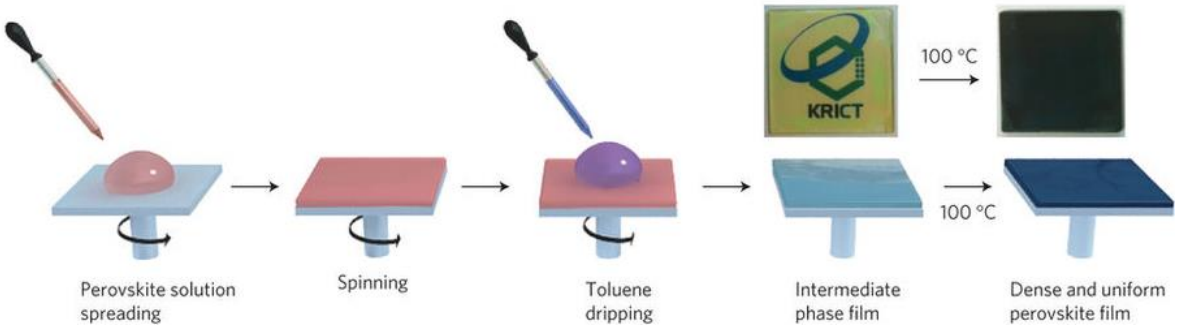

Figure 2. 18: *Solvent engineering procedure for preparing uniform and dense perovskite films* [68]

2.5.6 Alterations in compositional engineering

2.5.6.1 Incorporation of the formamidinium cation

In early 2015 Seok's group[69] went on to report a record 17.9 % PCE mixed-halide perovskite cell using the same solvent engineering process described earlier (Figure 2.19). The mixed halide perovskite material used was $(HC(NH_2)_2PbI_3)_{1-x}(CH_3NH_3PbBr_3)x$ (x = 0.15). The $HC(NH_2)_2^+$ ion (FA) is larger than the $CH_3NH_3^+$ ion (MA) and develops a cubic structure with a marginally larger lattice. Formamidinium lead iodide ($FAPbI_3$) exhibits a p-type character, is unstable on its own and has a narrow bandgap of 1.4 eV.[70] In contrast, methylammonium lead iodide ($MAPbI_3$)

exhibits an n-type character and has a bandgap of 1.5 - 1.6 eV. At this time there were several reports on $FaPbI_3$ based perovskite solar devices, many of which produced lower efficiencies than $MAPbI_3$ when incorporated into photovoltaic devices.[70, 71] The black $FAPbI_3$ perovskite was only stable at temperatures above 160°C and became inactive and yellow as it cooled down, transitioning from α-phase to δ-phase. Gradually replacing MA^+ with FA^+ cations was reported to increase the stability of the $FAPbI_3$ perovskite phase and increase PCE. This was due to increased current density as the absorption range shifted toward red.[72] Alternatively, replacing $MAPbI_3$ with $FAPbI_3$ results in a larger lead iodide based crystal lattice which allows favourable narrowing of the band gap.[70, 72] When fabricated into semi-transparent perovskite solar device $FaPbI_3$ was found to outperform $MaPbI_3$.[73] In this report, Seok et al. found that a stabilised perovskite phase of $(FAPbI_3)_{0.85}(MAPbBr_3)_{0.15}$ could be formed by adding 15 % mol MA^+ and Br^- concurrently to $FAPbI_3$. Its decreased bandgap allowed the absorption of photons over a wider spectrum. Negligible hysteresis was observed in the J-V curve for both forward and reverse scan sweeps. The solvent engineering process allowed the perovskite layer to be highly crystalline with a uniform and dense morphology on the m-TiO_2/c-TiO_2/FTO coated glass substrate. This was topped with a PTAA HTM and an Au counter electrode forming the highly efficient perovskite device.

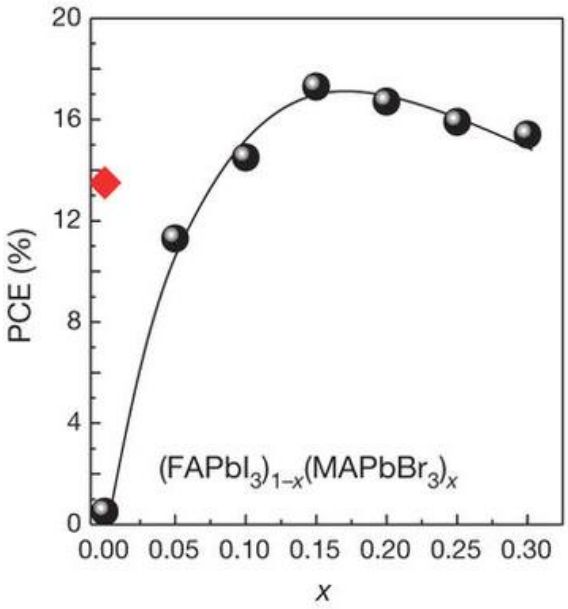

Figure 2. 19: *PCE values for cells using $(FAPbI_3)_{1-x}(MAPbBr_3)_x$ materials. x = 0.15 exhibited the best performance in terms of PCE. The red diamond indicates the PCE value for the cell fabricated using pure $FAPbI_3$ (x = 0)* [69]

That same year Seok and colleagues improved the efficiency even further to 20.1 % certified PCE through use of an intramolecular exchange process (IEP).[74] This involved a two-step spin coating procedure before obtaining the final $(FAPbI_3)_{0.95}(MAPbBr_3)_{0.05}$ (x = 5) perovskite film. The first solution to be spin coated was prepared by dissolving PbI_2 in DMSO at 60°C. The addition of toluene caused a $PbI_2(DMSO)_2$ complex to precipitate out and $PbI_2(DMSO)$ was eventually obtained by annealing in a vacuum for 24 hours. This complex was dissolved in DMF and was spin coated on the m-TiO_2/c-TiO_2/FTO coated glass substrate forming a transparent $PbI_2(DMSO)$ film. FAI and MABr were added in suitable ratios to 2-propanol and spin coated on top as the second step. A direct intramolecular exchange occurred between DMSO and FAI before DMSO was evaporated by spinning.

$$PbI_2\text{-}DMSO + FAI \rightarrow PbI_2 - FAI + DMSO \uparrow \qquad \textbf{2.26}$$

The volume of the perovskite layer was not expanded, unlike that in sequential deposition, as the molecular size of DMSO and FAI are approximately equal. This IEP method produced high quality, uniform $FAPbI_3$ based films at low temperatures during spin coating. The $(FAPbI_3)_{0.95}(MAPbBr_3)_{0.05}$ films produced had a preferred

orientation of (111) unlike films that were solution-processed and annealed afterward. The authors identified that the perovskite film thickness needed to be larger than that of previous $MAPbI_3$ films to ensure light absorption around the 800 nm wavelength region. A 500 nm thick perovskite layer was used in record 20.1% certified PCE solar cells with a high degree of reproducibility. It should be noted that the solvent engineering method was not employed for this procedure as it had resulted in pinholes and an uneven surface when used with $FAPbI_3$.

The most studied perovskite composition for achieving photovoltaic efficiency to date has been $MAPbI_3$. Due to the large success of mixed perovskites by Seok et al. above, Jacobsson et al.[75] decided to further explore the alluring $(FAPbI_3)_{1-x}(MAPbBr_3)_x$ composition. A total of 49 different compositions were investigated by varying the ratio of MA/FA and I/Br in the mixed perovskites. The deposition method was kept the same for each mesoporous device with perovskite precursors dissolved in a mixed solvent of DMF and DMSO in the ratio of 4:1 and a one-step antisolvent method carried out for perovskite deposition using chlorobenzene. The band gap of each independent cell composition was extracted. It was observed that an increased amount of bromide increased the band gap, while an increased amount of FA decreased the band gap, but to a much lesser extent. The authors noted that this ability to tune the band gap would be beneficial for application in tandem cells matching two photoabsorbers with a perovskite device as a top cell. Perovskite devices which contained a high bromide content appeared to produce intense photoemission from the sub band gap states causing detrimental results in the efficiency of the cell. A proposed explanation for this was a phase separation occurring with the development of a majority phase and a minority phase. This minority phase would be an iodide rich perovskite phase at a lower band gap. Photo-excited charge carriers could then become trapped in the minority phase as demonstrated in Figure 2.20. From this study it was observed that a small change in composition could have a large impact on the performance of the cell. Efficiencies varied from 2.3% PCE, for a mixed perovskite that contained a high bromide content, to 20.7% PCE, for a composition of $FA_{4/6}MA_{2/6}PbBr_{1/2}I_{5/2}$.

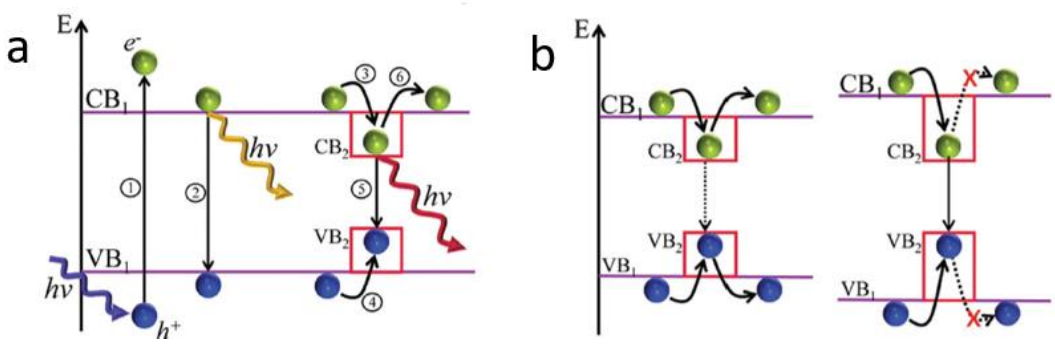

Figure 2. 20 (a): *Illustration of trap assisted recombination by an iodide rich minority phase. The different processes are: (1) absorption, (2) band edge recombination, (3) trapping of electrons by minority phase, (4) trapping of hole by minority phase, (5) radiative recombination by the minority phase, de-trapping of the electron.* ***(b):*** *Illustration of the increased importance of trapping as the band gap difference between the minority and the majority phase increases.*[75]

2.5.6.2 Incorporation of the caesium cation

Purely inorgainc perovskite devices have been investigated using caesium lead trihalide perovskites. These exhibit a superior thermal stability when compared to organic-inorganic perovskite materials. Kulbak et al.[76] showed $CsPbBr_3$ to exhibit a photovoltaic performance of 5.95 % efficiency in the forward scan and 5.72 % efficiency in the reverse scan in the J-V curve when incorporated into a mesoporous cell with PTAA as the HTM used. Unfortunately with the band gap of $CsPbBr_3$ being 2.97 eV it is unsuitable for use in perovskite cells. $CsPbI_3$ has a more suitable band gap of 1.73 eV and has also been investigated. It forms a photoactive perovskite with an appropriate Goldschmidt tolerance factor. However, the black photoactive perovskite α-phase of $CsPbI_3$ is only stable at temperatures above 300°C and becomes inactive and yellow as it cools down to its δ-phase.[8]

Jeon et al.[69] had previously shown that by incorporating a limited amount of the smaller cation MA, the black photoactive phase of FA could be stabilised. Complete conversion of the FA from its yellow to black phase still proved difficult as even small traces of the yellow phase could limit the performance of the device by inhibiting charge collection. Cs has a much smaller ionic radius of 1.81 Å when compared to that of MA (2.70 Å). Saliba et al. [77] incorporated the small inorganic Cs ion forming a triple cation mixture of Cs/MA/FA. The resultant perovskite material, $Cs_x(MA_{0.17}FA_{0.83})_{(100-}$

$_{x)}Pb(I_{0.83}Br_{0.17})_3$ (x = 5 %), was incorporated into a mesoporous cell with the standard Spiro-OMeTAD as HTM. XRD characterisation showed the yellow FA δ-phase to completely disappear with the incorporation of Cs while absorption and photoluminescence (PL) spectra exhibited a blue shift. This suggests that the Cs ion was successfully incorporated into the perovskite lattice with a shift toward the cubic structure. Improved stability could be observed when compared to the same perovskite without Cs incorporation when the devices were kept at 130°C for 3 hours in dry air. The cell without Cs had a decreased absorption spectrum and bleached rapidly. In contrast the cell which included Cs retained its active black colour with slight degradation. Cross-sectional SEM showed that the triple cation perovskite developed highly uniform perovskite grains. The authors proposed that the Cs ions provided seed layers for the nucleation of further uniform perovskite growth. These cells exhibited a reproducible stabilised power output of 21.1 % PCE. Long-term stability was then explored by keeping the device in a nitrogen atmosphere at room temperature under constant illumination. Max power point (MPP) tracking showed the efficiency to decrease after a few hours and then stabilise at 18 % PCE for over 250 hours (Figure 2.21). J_{sc} and V_{oc} did not change significantly within this time with FF showing the most significant drop. The authors suggested that replacement of the HTM could be a suitable solution to this decrease in FF for future work.

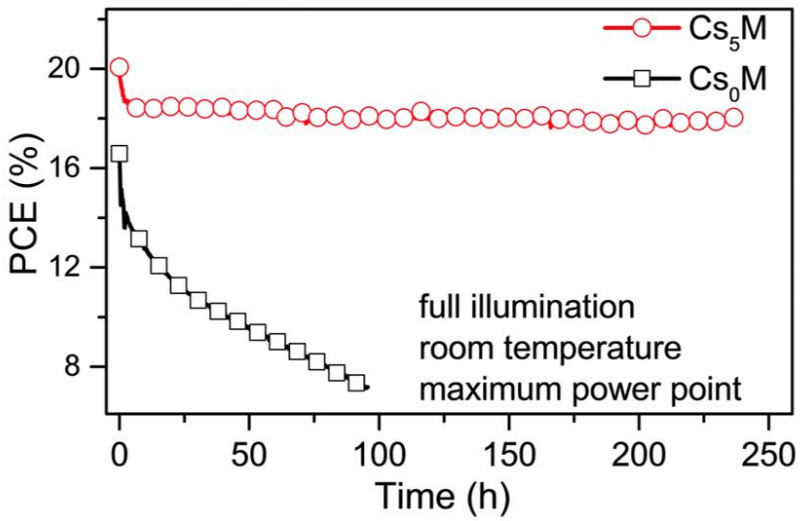

Figure 2. 21: *250 hour aging of $Cs_x(MA_{0.17}FA_{0.83})_{(100-x)}Pb(I_{0.83}Br_{0.17})_3$ where x = 5 for Cs_5M and x = 0* [77]

2.5.6.3 Incorporation of the rubidium cation

$MAPbI_3$, $FAPbI_3$, and $CsPbI_3$ all have a Goldschmidt tolerance factor between 0.8 and 1.0 allowing them to be established perovskite materials with a black α-phase. The ionic radius (*r*) of Rb is very slightly smaller than that of Cs. Despite the small ionic radius as well as its beneficial oxidation stability, $RbPbI_3$ falls just under the 0.8 tolerance factor limit making it a photoinactive non-perovskite. This material remains in the inactive yellow δ-phase even when heated until eventually melting at 460°C.[41]

$$Goldschmidt\ tolerence\ factor\ (T) = \frac{r_A + r_1}{\sqrt{2}(r_B + r_1)} \qquad \textbf{2.27}$$

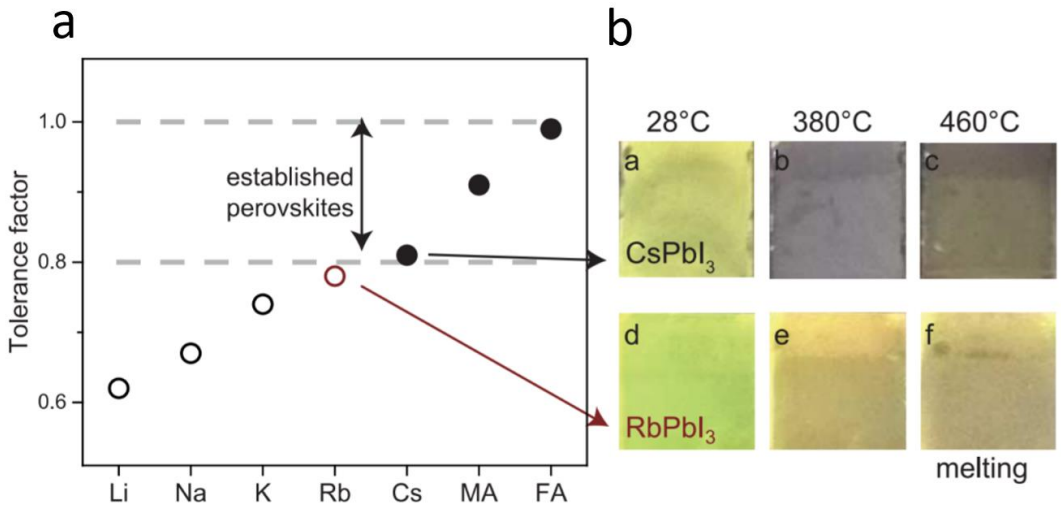

Figure 2. 22 (a): *Tolerance factor of the perovskites $APbI_3$ where A = Li, Na, K, Rb, Cs, MA and FA.* ***(b):*** *$CsPbI_3$ [a to c] and $RbPbI_3$ [d to f] at 28°, 380°, or 460°C. Irreversible melting for both compounds occured at 460°C. $RbPbI_3$ never shows a black phase* [41]

Due to Rb existing so close to the tolerance factor margin, Saliba et al. incorporated it into a quadruple cation perovskite to aid, in conjunction with MA, in stabilising the black α-phase of FA.[41] The perovskite material, $Rb_xCsMAFA$, was fabricated into a mesoporous cell with Spiro-OMeTAD used as the HTM. The PL spectra from the perovskite film showed a sharp peak at 770 nm in contrast to MAFA films which displayed several peaks ranging from 670 to 790 nm. This narrow peak suggests homogeneous crystallisation for the $Rb_xCsMAFA$ film with an absence of the inactive

yellow phase. XRD characterisation confirmed this absent yellow phase and exhibited a higher intensity perovskite peak for $Rb_xCsMAFA$ when compared to the MAFA perovskite. A stabilised PCE of 21.6 % was yielded using this "cation cascade" perovskite material. These devices displayed an exceptionally high V_{oc} of up to 1240 mV. The difference between V_{oc} and band gap (or loss in potential) was measured to be ~0.39 V. In contrast, the most efficient photovoltaic commercial silicon devices exhibit a loss in potential of ~0.4 V due to their indirect band gap and Auger recombination.[66] In theory, the loss in potential for defect-free materials that only feature radiative combination are in the range of 0.23 V (for 1 eV band gap) to 0.3 V (for 2 eV band gap). The high V_{oc} displayed in these $Rb_xCsMAFA$ cells is of significant interest as achieving this is one of the major challenges preventing PSCs from extending to their thermodynamic limit. The $Rb_xCsMAFA$ perovskite was then developed into a solar cell with PTAA as a buffer layer between the perovskite and HTM for a stress test. This thin film of PTAA was used to prevent the Spiro-OMeTAD HTM from becoming permeable, causing metal electrode diffusion into the perovskite material at high temperatures. The device was kept in a nitrogen atmosphere under constant illumination at 85°C for 500 hours. MPP tracking demonstrated that the device retained 95 % of its initial performance confirming its stability and robustness.

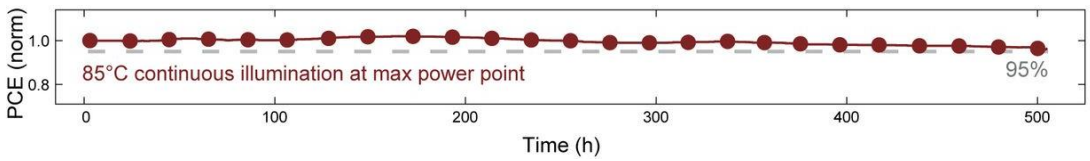

Figure 2. 23: *Thermal stability test for solar cell containing $Rb_xCsMAFA$* [41]

2.5.6.4 Excess of iodide ions

In mid-2017 Seok and colleagues reported a record certified PCE of 22.1 % with the ability to preserve >93 % of its original PCE after 13 months in ambient conditions.[78] A modified intramolecular exchange process (IEP) from their earlier work in 2015 [74] was adapted to deposit the perovskite material. PbI_2 and $PbBr_2$ were first dissolved in a 4:1 ratio of DMF and DMSO. This precursor solution was spin coated on the m-TiO_2 scaffold forming a transparent $PbI_2(PbBr_2)$-DMSO intermediate film. An iodide (I_3^-) solution was prepared by stirring iodine (I_2) in IPA at 80°C for seven days. The

oxidation of IPA formed iodide ions (I^-) and eventually triiodide ions (I_3^-) from the equation below.

$$(CH_3)_2CHOH + I_2 \xrightarrow{\Delta} (CH_3)_2C{=}O + HI + I^- \quad \textbf{2.28}$$

$$I_2 + I^- \leftrightarrow I_3^-$$

FAI and MABr were then dissolved in IPA containing the I_3^- and subsequently spin coated on the $PbI_2(PbBr_2)$-DMSO intermediate film. This solution was kept on the surface to promote an IEP between DMSO and the FAI(+MABr) before being annealed at 150°C. As with Seok's previous work, PTAA was used as the HTM in the cell. Power conversion efficiency was observed to increase with the introduction of these additional iodide ions in the cation solution and the black active α-phase of FA present was seen to increase. Grain boundaries in the perovskite layer are one of the many causes of recombination centres. Chen et al. had previously shown the treatment of $MAPbI_3$ with surplus PbI_2 to improve efficiency of the overall device. Excess PbI_2 reduced charge separation from defect states by passivating under-coordinated Pb and I ions.[79] Seok et al. demonstrated that this also worked for mixed cation and halide perovskites. The enhancement in V_{oc} and FF demonstrated a reduced number of trapping sites which cause non-radiative charge recombination of the perovskite. This enhancement also achieved improved crystallinity. Cells were then produced on ~ 1 cm active areas and yielded a certified PCE of 19.7 %. The slight decrease from the world record 22.1 % on smaller cells appeared to be due to sheet resistance of the FTO coated glass substrate and not the perovskite itself. With this world record efficiency, it is recognised that a careful control of deficient halide anions is required to achieve high PCEs for perovskite solar devices.

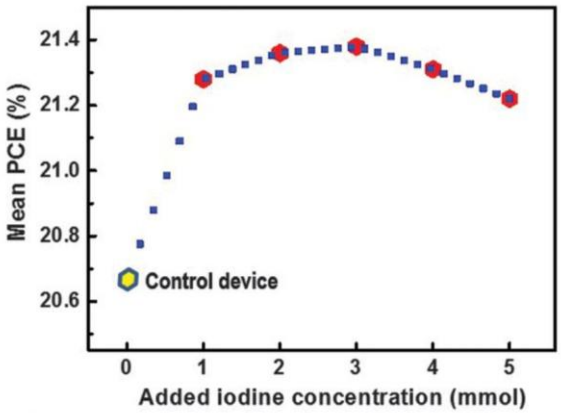

Figure 2. 24: *Relation between the relative power conversion efficiency and the concentration of iodide ions added into the dripping solution.*[78]

2.5.6.5 Surface passivation

One of the primary causes of low performing perovskite solar devices is non-radiative recombination of charge carriers in the perovskite layer. This is caused by trap states at grain boundaries and surfaces as well as point defects such as interstitial defects or vacancies in the perovskite lattice.[19, 50 80-82] Surface passivation of the perovskite layer has emerged as one of the most advantageous methods to combat interfacial recombination in recent years. A diverse number of methods and materials have been explored as passivation layers which successfully tune the V_{oc} of a solar cell without compromising J_{sc} and FF.[83-87] The majority of this research has focused on improving the interface between the ETL and the perovskite layer in planar cells once the mesoporous TiO_2 layer was removed.[88-91]

Recent work by Cho et al.[92] has demonstrated surface passivation at the rear of the perovskite material producing devices with negligible hysteresis reaching a maximum PCE of 21.31 %. A second thin perovskite layer was introduced on top of the original perovskite layer allowing a gradient in the conduction band. This was carried out by spin coating a FABr solution which was dissolved in isopropanol (IPA) on top of an $(FAPbI_3)_{0.85}(MAPbBr_3)_{0.15}$ thin film with the presence of excess PbI_2. Upon annealing at 100°C a second perovskite layer, $FAPbBr_{3-x}I_x$, was formed. The final device architecture was FTO/ c-TiO_2/ m-TiO_2/ perovskite: $[(FAPbI_3)_{0.85}(MAPbBr_3)_{0.15}]$ – $[FAPbBr_{3-x}I_x]$/ Spiro-OMeTAD/ Au. The wider bandgap of the second thin perovskite acted as a passivation layer preventing charge carrier recombination and improving

charge collection. XRD analysis suggested that the FABr had successfully reacted with the excess PbI_2 present on the surface of the first perovskite layer without inhibiting the original $(FAPbI_3)_{0.85}(MAPbBr_3)_{0.15}$. SEM imaging of the passivated perovskite film exhibited a denser and more homogenous surface morphology compared to the original perovskite film. From this work it was suggested that the improvement in PCE and V_{oc} of the final cell was due to upward band gap bending from the passivation layer. This prevented the backflow of electrons from the conduction band of the perovskite to the hole transport layer.

The field of perovskite photovoltaics has experienced a significant improvement from 3.8 % PCE in 2009 to 24.2 % PCE today.[93] These research efforts have not only improved efficiencies but also provided a deeper understanding on PSCs. Their excellent electrical and optical properties such as largely-tunable band gaps, high absorption coefficients, large carrier diffusion lengths and great carrier mobility have been well established while various fabrication methods have also been demonstrated. Many of the properties that are conducive to the high solar efficiency of perovskite solar cells are also attractive to realise optoelectronic devices beyond solar devices such as light-emitting devices (LEDs),[94-100] lasers,[101-107] and photodetectors.[108-111] Despite these advancements, barriers such as the natural instability of the perovskite material, lead toxicity and hysteresis of solar cells remain.

2.6 Bibliography

[1] G. Rose, Description of some New Minerals from the Urals, Ann. Phys., 124, 551−573, 1939 (in German)

[2] L. Singh, U. S. Rai, K. D. Mandal, N. B. Singh, Progress in the growth of $CaCu_3Ti_4O_{12}$ and related functional dielectric perovskites, Progress in Crystal Growth and Characterization of Materials, 60, 2, 15-62, 2014

[3] V. M. Goldschmidt, Die Gesetze der Kristallochemie, Naturwissenschaften, 14, 477–85, 1926

[4] Z. Li, M. Yang, J.-S. Park, S.-H. Wei, J. J. Berry, K. Zhu, Stabilizing Perovskite Structures by Tuning Tolerance Factor: Formation of Formamidinium and Cesium Lead Iodide Solid-State Alloys, Chem. Mater., 28, 1, 284-292, 2016

[5] W. F. Forrester, R. M. Hinde, Crystal Structure of Barium Titanate, Nature, 156, 177, 1945

[6] M. K. Wu, J. R. Ashburn, C. J. Torng, P. H. Hor, R. L. Meng, L. Goa, Z. J. Huang, Y. Q. Wang, C. W. Chu, Superconductivity at 93 K in a new mixed-phase Y-Ba-Cu-O compound system at ambient pressure, Phys. Rev. Lett. 58, 908, 1987

[7] M. Grätzel, The light and shade of perovskite solar cells, Nature Materials, 13, 838–842, 2014

[8] C. K. Møller, Crystal structure and photoconductivity of cæsium plumbohalides, Nature, 182, 1436, 1958

[9] D. Weber, $CH_3NH_3PbX_3$, ein Pb(II)-System mit kubischer Perowskitstruktur / $CH_3NH_3PbX_3$, a Pb(II)-System with Cubic Perovskite Structure, Z. Naturforsch, 33b, 1443, 1978

[10] D. B. Mitzi, C. A. Field, W. T. A. Harrison, A. M. Guloy, Conducting tin halides with a layered organic-based perovskite structure, Nature, 369, 467-469, 1994

[11] D. B. Mitzi, S. Wang, C. A. Field, C. A. Chess, A. M. Guloy, Conducting Layered Organic-inorganic Halides Containing <1 1 0> Oriented Perovskite Sheets, Science, 267, 1473-1476, 1995

[12] D. B. Mitzi, C. Chondroudis, C. Kagan, Organic-inorganic electronics, IBM Journal of Research and Development, 45, 29-45, 2001

[13] D. M. Chapin, C. S. Fuller, G. L. Pearson, A new p–n junction photocell for converting solar radiation into electrical power, J. Appl. Phys., 25, 676–7, 1954

[14] J. Nelson, The Physics of Solar Cells, Imperial College Press, 2004

[15] F. Bella, C. Gerbaldi, C. Barolo, M. Grätzel, Aqueous dye-sensitized solar cells, Chem. Soc. Rev.,44, 3431-3473, 2015

[16] A. Marchioro, J. Teuscher, D. Friedrich, M. Kunst, R. van de Krol, T. Moehl, M. Grätzel, J. E. Moser, Unravelling the mechanism of photoinduced charge transfer processes in lead iodide perovskite solar cells, Nature Photonics, 8, 250–255, 2014

[17] G. Xing, N. Mathews, S. Sun, S. S. Lim, Y. M. Lam, M. Grätzel, S. Mhaisalkar, T. C. Sum, Long-Range Balanced Electron- and Hole-Transport Lengths in Organic-Inorganic $CH_3NH_3PbI_3$, Science, 342, 344-347, 2013

[18] S. D. Stranks, G. E. Eperon, G. Grancini, C. Menelaou, M. J. P. Alcocer, T. Leijtens, L. M. Herz, A. Petrozza, H. J. Snaith, Electron-Hole diffusion lengths exceeding 1 micrometre in an organometal trihalide perovskite absorber, Science, 342, 341-344, 2013

[19] Q. Dong, Y. Fang, Y. Shao, P. Mulligan, J. Qiu, L. Cao, J. Huang, Electron-hole diffusion lengths >175 μm in solution-grown $CH_3NH_3PbI_3$ single crystals, Science, 347, 967-970, 2015

[20] B. R. Sutherland, S. Hoogland, M. M. Adachi, P. Kanjanaboos, C. T. O. Wong, J. J. McDowell, J. Xu, O. Voznyy, Z. Ning, A. J. Houtepen, E. H. Sargent, Perovskite Thin Films via Atomic Layer Deposition, Adv. Mater., 27, 53–58, 2015

[21] C. Das, S. Choudhury, T. Begum, J. Begum, Effect of thickness on the optical properties of GaAs thin films, Journal of Bangladesh Academy of Sciences, 37, 83-91, 2013

[22] J. Berry, T. Buonassisi, D. A. Egger, G. Hodes, L. Kronik, Y.-L. Loo, I. Lubomirsky, S. R. Marder, Y. Mastai, J. S. Miller, D. B. Mitzi, Y. Paz, A. M. Rappe, I. Riess, B. Rybtchinski, O. Stafsudd, V. Stevanovic, M. F. Toney, D. Zitoun, A. Kahn, D. Ginley, D. Cahen, Hybrid Organic–Inorganic Perovskites (HOIPs): Opportunities and Challenges, Adv. Mater., 27, 5102–5112, 2015

[23] Y. Ogomi, A. Morita, S. Tsukamoto, T. Saitho, N. Fujikawa, Q. Shen, T. Toyoda, K. Yoshino, S. S. Pandey, T. Ma, S. Hayase, $CH_3NH_3Sn_xPb_{(1-x)}I_3$ Perovskite Solar Cells Covering up to 1060 nm, J. of Phys. Chem. Lett., 5, 6, 1004-1011, 2014

[24] J. Troughton, D. Bryant, K. Wojciechowski, M. J. Carnie, H. J. Snaith, D. A. Worsleya, T. M. Watson, Highly efficient, flexible, indium-free perovskite solar cells employing metallic substrates, J. Mater. Chem. A, 3, 9141-9145, 2015

[25] A. Uddin, M. A. Mahmud, N. K. Elumalai, D. Wang, M. B. Upama, M. Wright, K. H. Chan, F. Haque, C. Xu, Perovskite solar cells for roll-to-roll fabrication, Renew. Energy Environ. Sustain., 2, 7, 2017

[26] D. Burkitt, J. Searle, T. Watson, Perovskite solar cells in n-i-p structure with four slot-die-coated layers, R. Soc. Open sci., 5, 172158, 2018

[27] M. D. Kempe, A. A. Dameron, M. O. Reese, Evaluation of moisture ingress from the perimeter of photovoltaic modules, Prog. Photovolt: Res. Appl., 22, 1159–1171, 2013

[28] J. Y. Jeng, K. C. Chen, T. Y. Chiang, P. Y. Lin, T. D. Tsai, Y. C. Chang, T. F. Guo, P. Chen, T. C. Wen, Y. J. Hsu, Nickel oxide electrode interlayer in $CH_3NH_3PbI_3$ perovskite/PCBM planar-heterojunction hybrid solar cells, Adv. Mater., 26, 4107-4113, 2014

[29] D. Bi, A. M. El-Zohry, A. Hagfedlt, G. Boscloo, Unraveling the effect of PbI_2 concentration on charge recombination kinetics in perovskite solar cells, ACS Photonics, 2, 5, 589-594, 2015

[30] T. Dewinggih, Shobih, L. Muliani, Herman, R. Hidayat, The Temperature Effect on the Working Characteristics of Solar Cells Based on Organometal Halide Perovskite Crystals, J. Phys.: Conf. Ser. 877, 012043, 2017

[31] F. Matteocci, L. Cinà, E. Lamanna, S. Cacovich, G. Divitini, P. A. Midgley, C. Ducati, A. Di Carlo, Encapsulation for long-term stability enhancement of perovskite solar cells, Nano Energy, 30, 162-172, 2016

[32] B. McKenna, J. R. Troughton, T. M. Watson, R. C. Evans, Enhancing the stability of organolead halide perovskite films through polymer encapsulation, RSC Adv., 7, 32942-32951, 2017

[33] G. Niu, X. Guoa, L. Wang, Review of recent progress in chemical stability of perovskite solar cells, J. Mater. Chem. A, 3, 8970-8980, 2015

[34] J. H. Noh, S. H. Im, H. J. Heo, T. N. Mandal, S. I. Seok, Chemical Management for Colorful, Efficient, and Stable Inorganic−Organic Hybrid Nanostructured Solar Cells, Nano Letters, 13, 4, 1764-1769, 2013

[35] P. Pistor, J. Borchert, W. Fränzel, R. Csuk, R. Scheer, Monitoring the Phase Formation of Coevaporated Lead Halide Perovskite Thin Films by in Situ X-ray Diffraction, J. of Phys. Chem. Lett., 5, 19, 3308-3312, 2014

[36] K. W. Tan, D. T. Moore, M. Saliba, H. Sai, L. A. Estroff, T. Hanrath, H. J. Snaith, U. Wiesner, Thermally Induced Structural Evolution and Performance of Mesoporous Block Copolymer Directed Alumina Perovskite Solar Cells, ACS Nano, 8, 5, 4730-4739, 2014

[37] A. Pisoni, J. Jaćimović, O. S. Barišić, M. Spina, R. Gaál, L. Forró, E. Horváth, Ultra-Low Thermal Conductivity in Organic-Inorganic Hybrid Perovskite $CH_3NH_3PbI_3$, J. of Phys. Chem. Lett., 5, 14, 2488-2492, 2014

[38] S. Ito, S. Tanaka, K. Manabe, H. Nishino, Effects of Surface Blocking Layer of Sb_2S_3 on Nanocrystalline TiO_2 for $CH_3NH_3PbI_3$ Perovskite Solar Cells, J. of Phys. Chem. C, 118, 30, 16995-17000, 2014

[39]S. S. Shin, E. J. Yeom, W. S. Yang, S. Hur, M. G. Kim, J. Im, J. Seo, J. H. Noh, S. I. Seok, Colloidally prepared La-doped $BaSnO_3$ electrodes for efficient, photostable perovskite solar cells, Science, 356, 167–171, 2017

[40] F. Bella, G. Griffini, J. P. Correa-Baena, G. Saracco, M. Grätzel, A. Hagfeldt, S. Turri, C. Gerbaldi, Improving efficiency and stability of perovskite solar cells with photocurable fluoropolymers, Science, 354, 203–206, 2016

[41] M. Saliba, T. Matsui, K. Domanski, Y.-J. Seo, A. Ummadisingu, S. M. Zakeeruddin, J. P. Correa-Baena, W. R. Tress, A. Abate, A. Hagfeldt, M. Grätzel, Incorporation of rubidium cations into perovskite solar cells improves photovoltaic performance, Science, 354, 206–209, 2016

[42] Z. Li, C. Xiao, Y. Yang, S. P. Harvey, D. H. Kim, J. A. Christians, M. Yang, P. Schulz, S. U. Nanayakkara, C.-S. Jiang, J. M. Luther, J. J. Berry, M. C. Beard, M. M. Al-Jassima, K. Zhu, Extrinsic ion migration in perovskite solar cells, Energy Environ. Sci., 10, 1234, 2017

[43] H. J. Snaith, A. Abate, J. M. Ball, G. E. Eperon, T. Leijtens, N. K. Noel, S. D. Stranks, J. T.-W. Wang, K. Wojciechowski, W. Zhang, Anomalous Hysteresis in Perovskite Solar Cells, J. of Phys. Chem. Lett., 5, 9, 1511-1515, 2014

[44] W. Tress, N. Marinova, T. Moehl, S. M. Zakeeruddin, M. K. Nazeeruddina, M. Grätzel, Understanding the rate-dependent J–V hysteresis, slow time component, and aging in $CH_3NH_3PbI_3$ perovskite solar cells: the role of a compensated electric field, Energy Environ. Sci., 8, 995-1004, 2015

[45] R. S. Sánchez, V. Gonzalez-Pedro, J.-W. Lee, N.-G. Park, Y. S. Kang, I. Mora-Sero, J. Bisquert, Slow Dynamic Processes in Lead Halide Perovskite Solar Cells. Characteristic Times and Hysteresis, J. Phys. Chem. Lett., 5, 2357– 2363, 2014

[46] B. Chen, M. Yang, S. Priya, K. Zhu, Origin of J-V hysteresis in perovskite solar cells, J. of Phys. Chem. Lett., 7, 5, 905-917, 2016

[47] J. Wei, Y. Zhao, H. Li, G. Li, J. Pan, D. Xu, Q. Zhao, D. Yu, Hysteresis Analysis Based on the Ferroelectric Effect in Hybrid Perovskite Solar Cells, J. of Phys. Chem. Lett., 5, 21, 3937-3945, 2014

[48] K. Wojciechowski, S. D. Stranks, A. Abate, G. Sadoughi, A. Sadhanala, N. Kopidakis, G. Rumbles, C.-Z. Li, R. H. Friend, A. K.-Y. Jen, H. J. Snaith, Heterojunction Modification for Highly Efficient Organic–Inorganic Perovskite Solar Cells, ACS Nano, 8, 12, 12701-12709, 2014

[49] H.-W. Chen, N. Sakai, M. Ikegami, T. Miyasaka, Emergence of Hysteresis and Transient Ferroelectric Response in Organo-Lead Halide Perovskite Solar Cells, J. of Phys. Chem. Lett., 6, 1, 164-169, 2015

[50] Y. Shao, Z. Xiao, C. Bi, Y. Yuan, J Huang, Origin and Elimination of Photocurrent Hysteresis by Fullerene Passivation in $CH_3NH_3PbI_3$ Planar Heterojunction Solar Cells, Nat. Commun., 5, 5784, 2014

[51] Q. Lin, A. Armin, R. C. R. Nagiri, P. L. Burn, P. Meredith, Electro-Optics of Perovskite Solar Cells. Nat. Photon., 9, 106– 112, 2014

[52] J. W. Seo, S. Park, Y. C. Kim, N. J. Jeon, J. H. Noh, S. C. Yoon, S. I. Seok, Benefits of Very Thin PCBM and LiF Layer For Solution-Processed P-I-N Perovskite Solar Cells., Ener Environ. Sci., 7, 2642– 2646, 2014

[53] D. Bryant, S. Wheeler, B.C. O'Regan, T. Watson, P.R.F. Barnes, D. Worsley, J. Durrant, Observable hysteresis at low temperature in “hysteresis free” organic–inorganic lead halide perovskite solar cells, J. Phys. Chem. Lett., 6, 3190–3194, 2015

[54] A. Kojima, K. Teshima, T. Miyasaka, Y. Shirai, Novel photoelectrochemical cell with mesoscopic electrodes sensitized by lead-halide compounds (2). 210th ECS Meeting; The electrochemical society, abstract 397, 2006

[55] A. Kojima, K. Teshima, Y. Shirai, T. Miyasaka, Organometal Halide Perovskites as Visible-Light Sensitizers for Photovoltaic Cells, J. Am. Chem. Soc., 131, 6050−6051, 2009

[56] A. Kojima, K. Teshima, Y. Shirai, T. Miyasaka, Novel photoelectrochemical cell with mesoscopic electrodes sensitized by lead-halide compounds (11). 214th ECS Meeting; The Electrochemical Society, abstract 27, 2008

[57] J.-H. Im, C.-R. Lee, J.-W. Lee, S.-W. Park, N.-G. Park, 6.5% efficient perovskite quantum-dot-sensitized solar cell, Nanoscale, 3, 4088–4093, 2011

[58] I. Chung, B. Lee, J. He, R. P. H. Chang, M. G. Kanatzidis, All-solid-state dye-sensitized solar cells with high efficiency, Nature, 485, 486–489, 2012

[59] U. Bach, D. Lupo, P. Comte, J. E. Moser, F. Weissörtel, J. Salbeck, H. Spreitzer, M. Grätzel, Solid-state dye-sensitized mesoporous TiO_2 solar cells with high photon-to-electron conversion efficiencies, Nature, 395, 583–585, 1998

[60] H. J. Snaith, M. Grätzel, Enhanced charge mobility in a molecular hole transporter via addition of redox inactive ionic dopant: Implication to dye-sensitized solar cells, Appl. Phys. Lett., 89, 262114, 2006

[61] H.-S. Kim, C.-R. Lee, J.-H. Im, K.-B. Lee, T. Moehl, A. Marchioro, S.-J. Moon, R. Humphry-Baker, J.-H. Yum, J. E. Moser, M. Grätzel, N.-G. Park, Lead iodide perovskite sensitized all-solid-state submicron thin film mesoscopic solar cell with efficiency exceeding 9%, Sci. Rep., 2, 591, 2012

[62] M. M. Lee, J. Teuscher, T. Miyasaka, T. N. Murakami, H. J. Snaith, Efficient hybrid solar cells based on meso-superstructured organometal halide perovskites, Science, 338, 643–647, 2012

[63] L. Etgar, P. Gao, Z. Xue, Q. Peng, A. K. Chandiran, B. Liu, M. K. Nazeeruddin, M. Grätzel, Mesoscopic $CH_3NH_3PbI_3/TiO_2$ Heterojunction Solar Cells, J. Am. Chem. Society, 134, 42, 17396-17399, 2012

[64] J. H. Heo, S. H. Im, J. H. Noh, T. N. Mandal, C.-S. Lim, J.-A. Chang, Y.-H. Lee, H.-J. Kim, A. Sarkar, M. K. Nazeeruddin, M. Grätzel, S. I. Seok, Efficient inorganic–organic hybrid heterojunction solar cells containing perovskite compound and polymeric hole conductors, Nature Photonics, 7, 486–491, 2013

[65] J. Burschka, N. Pellet, S.-J. Moon, R. Humphry-Baker, P. Gao, M. K. Nazeeruddin, M. Grätzel, Sequential deposition as a route to high-performance perovskite-sensitized solar cells, Nature, 499, 316–319, 2013

[66] M. A. Green, Y. Hishikawa, E. D. Dunlop, D. H. Levi, J. Hohl-Ebinger, A. W.Y. Ho-Baillie, Solar cell efficiency tables (version 52), Prog Photovolt Res Appl, 26, 7, 427-436, 2018

[67] M. Liu, M. B. Johnston, H. J. Snaith, Efficient planar heterojunction perovskite solar cells by vapour deposition, Nature, 501, 395–398, 2103

[68] N. J. Jeon, J. H. Noh, Y. C. Kim, W. S. Yang, S. Ryu, S. I. Seok, Solvent engineering for high-performance inorganic–organic hybrid perovskite solar cells, Nature Materials, 13, 897–903, 2014

[69] N. J. Jeon, J. H. Noh, W. S. Yang, Y. C. Kim, S. Ryu, J. Seo, S. I. Seok, Compositional engineering of perovskite materials for high-performance solar cells, Nature, 517, 476–480, 2015

[70] G. E. Eperon, S. D. Stranks, C. Menelaou, M. B. Johnston, L. M. Herza, H. J. Snaith, Formamidinium lead trihalide: a broadly tunable perovskite for efficient planar heterojunction solar cells, Energy Environ. Sci., 7, 982-988, 2014

[71] T. M. Koh, K. Fu, Y. Fang, S. Chen, T. C. Sum, N. Mathews, S. G. Mhaisalkar, P. P. Boix, T. Baikie, Formamidinium-Containing Metal-Halide: An Alternative Material for Near-IR Absorption Perovskite Solar Cells, J. Phys. Chem. C, 118, 30, 16458-16462, 2014

[72] N. Pellet, P. Gao, G. Gregori, T.-Y. Yang, M. K. Nazeeruddin, J. Maier, M. Grätzel, Mixed-Organic-Cation Perovskite Photovoltaics for Enhanced Solar-Light Harvesting, Angew. Chem. Int. Ed., 53, 3151–3157, 2014

[73] G. E. Eperon, D. Bryant, J. Troughton, S. D. Stranks, M. B. Johnston, T. Watson, D. A. Worsley, H. J. Snaith, Efficient, semitransparent neutral-colored solar cells based on microstructured formamidinium lead trihalide perovskite, J. Phys. Chem. Lett. 6, 129–138, 2015

[74] W. S. Yang, J. H. Noh, N. J. Jeon, Y. C. Kim, S. Ryu, J. Seo, S. I. Seok, High-performance photovoltaic perovskite layers fabricated through intramolecular exchange, Science, 348, 6240, 1234-1237, 2015

[75] T. J. Jacobsson, J. P. Correa-Baena, M. Pazoki, M. Saliba, K. Schenk, M. Grätzel, A. Hagfeldt, Exploration of the compositional space for mixed lead halogen perovskites for high efficiency solar cells, Energy Environ. Sci., 9, 1706-1724, 2016

[76] M. Kulbak, D. Cahen, G. Hodes, How Important Is the Organic Part of Lead Halide Perovskite Photovoltaic Cells? Efficient $CsPbBr_3$ Cells, J. Phys. Chem. Lett., 6, 13, 2452-2456, 2015

[77] M. Saliba, T. Matsui, J.-Y. Seo, K. Domanski, J. P. Correa-Baena, M. K. Nazeeruddin, S. M. Zakeeruddin, W. Tress, A. Abate, A. Hagfeldtd, M. Grätzel, Cesium-containing triple cation perovskite solar cells: improved stability, reproducibility and high efficiency, Energy Environ. Sci., 9, 1989-1997, 2016

[78] W. S. Yang, B.-W. Park, E.-H. Jung, N. J. Jeon, Y. C. Kim, D. U. Lee, S. S. Shin, J. Seo, K. Kim, J. H. Noh, S. I. Seok, Iodide management in formamidinium-lead-halide–based perovskite layers for efficient solar cells, Science, 356, 1376–1379, 2017

[79] Q. Chen, H. Zhou, T.-B. Song, S. Luo, Z. Hong, H.-S. Duan, L. Dou, Y. Liu, Y. Yang, Controllable self-induced passivation of hybrid lead iodide perovskites toward high performance solar cells, Nano Letters, 14, 7, 4158-4163, 2014

[80] W. Nie, H. Tsai, R. Asadpour, J. Blancon, A. Neukirch, G. Gupta, J. Crochet, M. Chhowalla, S. Tretiak, M. Alam, H Wang, A. Mohite, High-Efficiency Solution-Processed Perovskite Solar Cells with Millimeter-Scale Grains, Science, 347, 522−525, 2015

[81] D. Zhao, M. Sexton, H. Park, G. Baure, J. Nino, F. So, High-Efficiency Solution-Processed Planar Perovskite Solar Cells with a Polymer Hole Transport Layer, Adv. Energy Mater., 5, 1401855, 2015

[82] B. Li, Y. Zhang, L. Fu, T. Yu, S. Zhou, L. Zhang, L. Yin, Surface passivation engineering strategy to fully-inorganic cubic $CsPbI_3$ perovskites for high-performance solar cells, Nature Communications, 9, 1076, 2018

[83] Q. Wang, Q. Dong, T. Li, A. Gruverman and J. Huang, Thin Insulating Tunneling Contacts for Efficient and Water-Resistant Perovskite Solar Cells, Adv. Mater., 28, 6734–6739, 2016

[84] F. Wang, W. Geng, Y. Zhou, H. Fang, C.-J. Tong, M. A. Loi, L. Liu, N. Zhao, Phenylalkylamine Passivation of Organolead Halide Perovskites Enabling High-Efficiency and Air-Stable Photovoltaic Cells, Adv. Mater., 28, 9986–9992, 2016

[85] X. Wen, J. Wu, D. Gao, C. Lin, Interfacial engineering with amino-functionalized graphene for efficient perovskite solar cells, J. Mater. Chem. A, 4, 13482–13487, 2016

[86] X. Zheng, B. Chen, J. Dai, Y. Fang, Y. Bai, Y. Lin, H. Wei, X. Zeng, J. Huang, Defect passivation in hybrid perovskite solar cells using quaternary ammonium halide anions and cations, Nat. Energy, 2, 17102, 2017

[87] Y. Yue, N. T. Salim, Y. Wu, X. Yang, A. Islam, W. Chen, J. Liu, E. Bi, F. Xie, M. Cai, L. Han, Enhanced Stability of Perovskite Solar Cells through Corrosion-Free Pyridine Derivatives in Hole-Transporting Materials, Adv. Mater., 28, 10738–10743, 2016

[88] Y. H. Lee, J. Luo, M.-K. Son, P. Gao, K. T. Cho, J. Seo, S. M. Zakeeruddin, M. Grätzel, M. K. Nazeeruddin, Enhanced Charge Collection with Passivation Layers in Perovskite Solar Cells, Adv. Mat., 28, 3966-3972, 2016

[89] F. Giordano, A. Abate, J. P. Correa Baena, M. Saliba, T. Matsui, S. H. Im, S. M. Zakeeruddin, M. K. Nazeeruddin, A. Hagfeldt, M. Graetzel, Enhanced electronic properties in mesoporous TiO_2 via lithium doping for high-efficiency perovskite solar cells, Nat. Commun., 7, 2016

[90] E. Edri, S. Kirmayer, S. Mukhopadhyay, K. Gartsman, G. Hodes, D. Cahen, Elucidating the charge carrier separation and working mechanism of $CH_3NH_3PbI_{(3-x)}Cl_{(x)}$ perovskite solar cells, Nat. Commun., 5, 2014

[91] Y. Lee, S. Lee, G. Seo, S. Paek, K. T. Cho, A. J. Huckaba, M. Calizzi, D.-W. Choi, J.-S. Park, D. Lee, H. J. Lee, A. M. Asiri, M. K. Nazeeruddin, Efficient Planar Perovskite Solar Cells Using Passivated Tin Oxide as an Electron Transport Layer, Adv. Sci., 5, 1800130, 2018

[92] K. T. Cho, S. Paek, G. Grancini, C. Roldán-Carmona, P. Gao, Y. Lee, M. K. Nazeeruddin, Highly efficient perovskite solar cells with a compositional engineered

perovskite/hole transporting material interface, Energy Environ. Sci., 10, 621-627, 2017

[93] National Renewable Energy Laboratory: Efficiency Chart (2018). Available at: https://www.nrel.gov/pv/cell-efficiency.html (accessed 17 April 2019)

[94] O. D. Miller, E. Yablonovitch, S. R. Kurtz, Strong Internal and External Luminescence as Solar Cells Approach the Shockley–Queisser Limit, IEEE Journal of Photovoltaics, 2, 3, 303-311, 2012

[95] D. Shi, V. Adinolfi, R. Comin, M. Yuan, E. Alarousu, A. Buin, Y. Chen, S. Hoogland, A. Rothenberger, K. Katsiev, Y. Losovyj, X. Zhang, P. A. Dowben, O. F. Mohammed, E. H. Sargent, O. M. Bakr, Low trap-state density and long carrier diffusion in organolead trihalide perovskite single crystals, Science, 347, 6221, 519-522, 2015

[96] B. R. Sutherland, E. H. Sargent, Perovskite photonic sources, Nature Photonics, 10, 295–302, 2016

[97] M. Era, S. Morimoto, T. Tsutsui, S. Saito, Organic- inorganic heterostructure electroluminescent device using a layered perovskite semiconductor $(C_6H_5C_2H_4NH_3)_2PbI_4$, Appl. Phys. Lett. 65, 676, 1994

[98] Z.-K. Tan, R. S. Moghaddam, M. L. Lai, P. Docampo, R. Higler, F. Deschler, M. Price, A. Sadhanala, L. M. Pazos, D. Credgington, F. Hanusch, T. Bein, H. J. Snaith, R. H. Friend, Bright light-emitting diodes based on organometal halide perovskite, Nature Nanotechnology, 9, 687–692, 2014

[99] A. Mei, X. Li, L. Liu, Z. Ku, T. Liu, Y. Rong, M. Xu, M. Hu, J. Chen, Y. Yang, M. Grätzel, H. Han, A hole-conductor–free, fully printable mesoscopic perovskite solar cell with high stability, Science, 345, 6194, 295-298, 2014

[100] D. P. McMeekin, G. Sadoughil, W. Rehman, G. E. Eperon, M. Saliba, M. T. Hörantner, A. Haghighirad, N. Sakai, L. Korte, B. Rech, M. B. Johnston, L. M. Herz, H. J. Snaith, A mixed-cation lead mixed-halide perovskite absorber for tandem solar cells, Science, 351, 6269, 151-155, 2016

[101] F. Deschler, M. Price, S. Pathak, L. Klintberg, D. D. Jarausch, R. Higler, S. Huettner, T. Leijtens, S. D. Stranks, H. J. Snaith, M. Atature, R. T. Phillips, R. H. Friend, High photoluminescence efficiency and optically pumped lasing in solution-processed mixed halide perovskite semiconductors, J. Phys. Chem. Lett., 5, 1421–1426, 2014

[102] H. Zhu, Y. Fu, F. Meng, X. Wu, Z. Gong, Q. Ding, M. V. Gustafsson, M. T. Trinh, S. Jin, X.-Y. Zhu, Lead halide perovskite nanowire lasers with low lasing thresholds and high quality factors, Nature Materials, 14, 636–642, 2015

[103] R. Dhanker, A. N. Brigeman, A. V. Larsen, R. J. Stewart, J. B. Asbury, N. C. Giebink, Random lasing in organo-lead halide perovskite microcrystal networks, Appl. Phys. Lett. 105, 151112, 2014

[104] B. R. Sutherland, S. Hoogland, M. M. Adachi, C. T. O. Wong, E. H. Sargent, Conformal organohalide perovskites enable lasing on spherical resonators, ACS Nano, 8, 10, 0947–10952, 2014

[105] B. R. Sutherland, E. H. Sargent, Perovskite photonic sources, Nature Photonics, 10, 295–302, 2016

[106] J. R. Harwell, G. L. Whitworth, G. A. Turnbull, I. D. W. Samuel, Green Perovskite Distributed Feedback Lasers, Scientific Reports, 7, 11727, 2017

[107] J. Sun, J. Wu, X. Tong, F. Lin, Y. Wang, Z. M. Wang, Organic/Inorganic Metal Halide Perovskite Optoelectronic Devices beyond Solar Cells, Adv. Sci., 5, 1700780, 2018

[108] F. Li, C. Ma, H. Wang, W. Hu, W. Yu, A. D. Sheikh, T. Wu, Ambipolar solution-processed hybrid perovskite phototransistors, Nat. Commun., 6, 8238, 2015

[109] W. Niu, A. Eiden, G. V. Prakash, J. J. Baumberg, Exfoliation of self-assembled 2D organic-inorganic perovskite semiconductors, Appl. Phys. Lett., 17, 171111, 2014

[110] J. Liu, Y. Xue, Z. Wang, Z.-Q. Xu, C. Zheng, B. Weber, J. Song, Y. Wang, Y. Lu, Y. Zhang, Q. Bao, Two-Dimensional $CH_3NH_3PbI_3$ Perovskite: Synthesis and Optoelectronic Application, ACS Nano, 10, 3536, 2016

[111] W. Wei, Y. Zhang, Q. Xu, H. Wei, Y. Fang, Q. Wang, Y. Deng, T. Li, A. Gruverman, L. Cao, J. Huang, Monolithic integration of hybrid perovskite single crystals with heterogenous substrate for highly sensitive X-ray imaging, Nat. Photonics, 11, 315, 2017

CHAPTER 3:

Overview of Atomic Layer Deposition

3.1 Origin of Atomic Layer Deposition

Atomic layer deposition (ALD), originally referred to as atomic layer epitaxy (ALE), is an adaption of the chemical vapour deposition (CVD) process. ALD allows the deposition of highly conformal, ultra-thin layers of precise uniformity and thickness. This deposition process consists of sequential self-limiting surface reactions which allow monolayer control of film growth. Control at the atomic level makes ALD a favourable technique for scaling down microelectronic devices, advancing Moore's Law. The uniformity of ALD has also made it an ideal method for the deposition of uniform films on high aspect ratio structures.

ALD originated in the 1960s from the work of Professor Aleskovskii's group in the Soviet Union. In the proceedings of a conference in 1965, which was later published in 1967, the growth of TiO_2 and GeO_2 were described on high surface area SiO_2 substrates.[1] These "molecular layer reactions" were soon deposited on single crystal substrates and a plethora of papers on the subject were published around the time by S. I. Kol'tsov and co-workers.[2-8] ALD was separately developed, depositing ZnS for thin-film electroluminescent (TFEL) flat panel displays, and patented by T. Suntola and J. Antson in Finland in 1977.[9] It was here that the term ALE was coined to explain the process. A second patent presented in 1983 contained modifications to the flow-type ALE equipment which provided enhanced precursor delivery.[10] From 1985 the use of ALE for the deposition of II-VI and III-V compounds gained some interest.[11-14] The deposition of III-V compounds was replaced by metal organic vapour phase epitaxy (MOVPE) and molecular beam epitaxy (MBE) due to the unfavourable chemistry between group III alkyl compounds and group V hydrides using ALE.[15] In the late 1990s interest in the technique, now referred to as ALD, gained a strong momentum

as it was applied to silicon based microelectronics. ALD was able to deposit conformal and uniform layers on ever smaller device dimensions with increasing aspect ratios in integrated circuits.[16] ALD has become essential to deposit materials such as metal oxides for high-k dielectrics. It is also useful in the production of precise nanostructures such as nanowires and nanotubes.

There are some subtle but substantial differences which separate CVD and ALD. A CVD process introduces all precursors into a reaction simultaneously. In contrast, for ALD the reaction chamber is exposed to precursors separately allowing for the growth of a thin film in a stepwise and digital manner. The self-limiting nature of ALD allows for precise control of deposition down to an atomic scale which provides higher conformality compared to CVD. A CVD process generally occurs at significantly higher temperatures than ALD which allows for faster reaction rates and hence higher deposition rates. A significant limitation of the ALD process is its low growth rate as less than one monolayer is usually deposited in one cycle.

3.2 Principles and characterisation of ALD

3.2.1 ALD Principles

Film growth via ALD operates in a cyclic manner through a sequence of alternating half cycles. Gas phase precursors are alternately pulsed into the reactor, separated by an inert gas purge. This purge removes any surplus precursor and by-products from the reaction chamber and flow lines which could cause superfluous reactions in the gas phase. The ALD process itself is self-limiting so that under ideal conditions one cycle achieves one monolayer of deposition. The thickness of the thin film created can be precisely controlled due to the fixed growth rate per cycle. Chemical reactions that cause film deposition occur solely on the substrate surface. This happens at temperatures below the gas phase thermal decomposition temperature of the precursor used. The step-coverage greatly exceeds that of traditional CVD and provides improved conformity and uniformity. This self-limiting nature generally prohibits the films from becoming rough, instead causing them to be smooth and uniform due to the reactions from each cycle being driven to completion. No surface sites are left

unreacted during the film growth of each layer, allowing them to be uninterrupted and 'pinhole-free'.

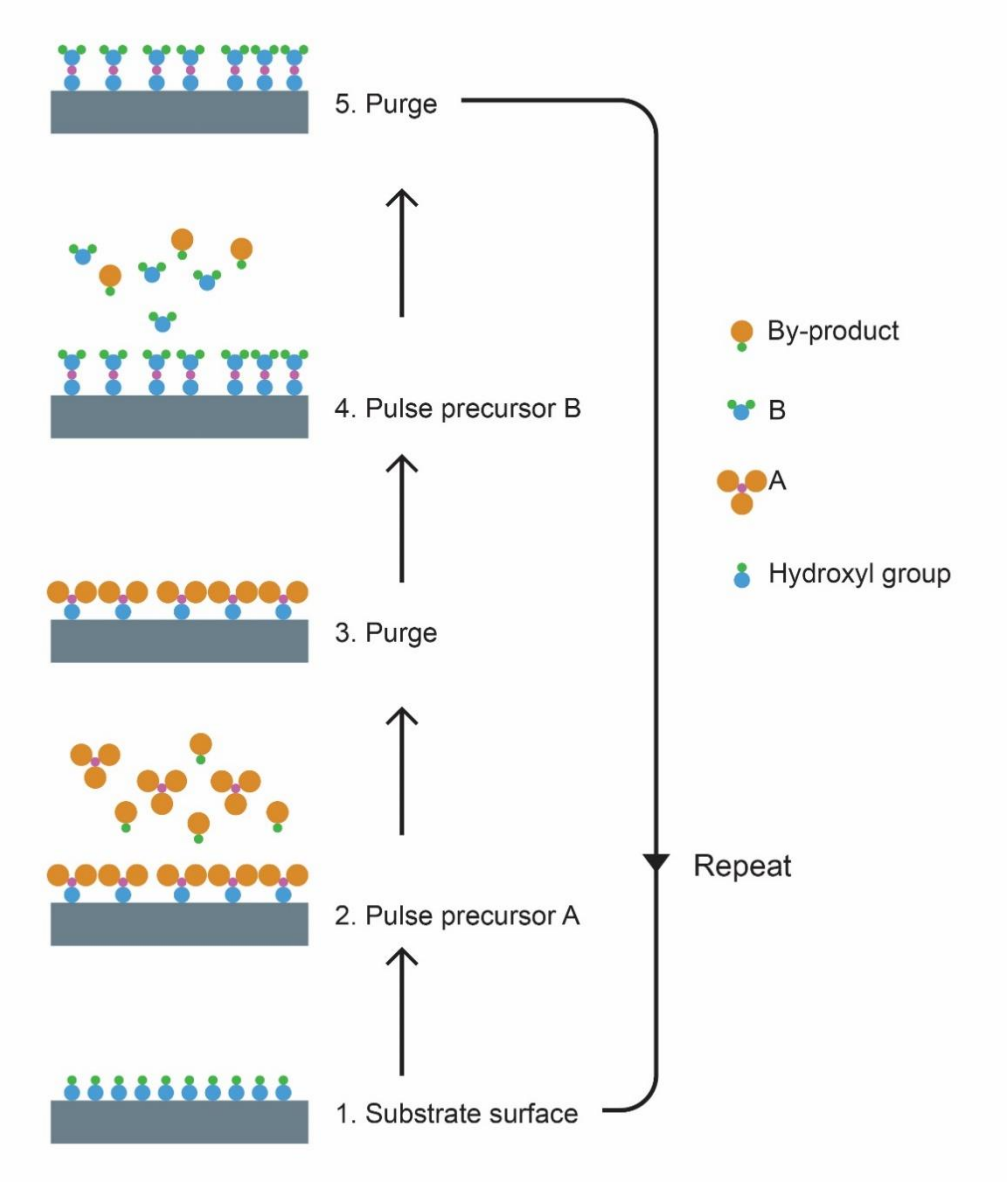

Figure 3. 1: *Schematic representation of ALD cycle, composed of two alternating half cycles of precursors A and B.*

Figure 3.1 illustrates an ALD cycle where precursor A reacts with hydroxyls or oxygen groups. A substrate terminated with hydroxyl groups is first placed within the ALD reactor. A single pulse of precursor A is introduced into the reaction chamber. This precursor interacts with the heated surface of the substrate but not with itself,

generating a chemisorbed surface species. The purge sequence of an inert gas removes any unreacted precursor, physisorbed precursor as well as any gas phase by-product species created. This purge prevents reactions from taking place in the gas phase of the reaction chamber as well as the flow lines. The self-limiting behaviour of ALD is maintained as the precursor only reacts with the available reactive surface sites on the substrate. A pulse of the second precursor, B, is introduced as a reactant in Figure 3.1 which reacts with A forming a monolayer of oxygen containing reactive groups on the surface. A second purge again removes any unreacted precursor or by-products, completing the ALD cycle. This cycle is repeated until the desired thickness of film growth is achieved.

3.2.2 Growth Per Cycle

The incremental increase in thickness of the film per deposition cycle is defined as a growth per cycle (GPC) and can be measured in Angstrom per cycle or nanometre per cycle. GPC is calculated by dividing the thickness of the deposited film by the total number of cycles as shown in equation 3.1:

$$\mathrm{GPC} = \frac{\text{thickness of film (Å or nm)}}{\text{Total number of ALD cycles}} \qquad \textbf{3.1}$$

GPC is determined by the partial pressure of the precursors used, the number of reactive sites available, the exposure time of the precursors, the purge length, the ALD processing temperature, and sometimes the substrate material itself.[17]

Steric hindrance caused by bulky precursor ligands can also limit growth. As a precursor molecule bonds with an active site, large ligands can prevent adjacent sites from reacting. The resultant number of chemisorbed species is often too low for the formation of a complete monolayer of growth within one cycle.[18] Steric hindrance has been demonstrated with the ALD growth of TiO_2 using various titanium precursors with the chemical formula $Ti(R)_4$ where R represents different chain length ligands. TiO_2 deposited using the titanium precursor $TiCl_4$ has been reported to provide a growth rate of 0.56 Å/cycle.[19] Halide atoms such as Cl have low steric hindrance, can be used in a wide temperature range and are extremely reactive. On the other hand, halides tend to generate reactive by-products, such as HCl, which may cause back-etching. The halide atoms can also unintentionally be incorporated into the deposited

material producing doped films.[20] TiO_2 deposited using the sterically crowded titanium precursor $Ti^{i}OPr$ has been reported to provide a reduced growth rate of 0.30 Å/cycle in the same study.[19] It is preferable if precursors are small in size to avoid reduced surface coverage due to steric hindrance. While ideally the mechanism for ALD growth occurs monolayer by monolayer, growth experiments have shown that a chemisorbed monolayer is rarely achieved in one ALD cycle after ligands are removed.

The ALD process requires adequate chemical species on the substrate surface for precursors to effectively react with. If the initial substrate is inert then the ALD film may not nucleate or only nucleate at defect sites. The agglomeration of adsorbed molecules can form island growth. With multiple ALD cycles these islands may connect forming a continuous film. For uniform ALD film growth the ALD precursors are required to react with the substrate surface species on the first ALD cycle.[21]

3.2.3 Self-limiting nature

The cyclic manner and self-limiting feature of ALD enables the monolayer by monolayer growth of a material. As previously mentioned, the incoming precursor only reacts with the available reactive surface sites on the outermost layer of molecules forming a chemisorbed surface species. Excess precursor may physisorb on top of this chemisorbed species. With a sufficient purge the weak bonds of the physisorbed species are detached and extracted along with unreacted precursor and any by-products formed. Monolayer coverage in a single pulse is defined as the number of atoms that remain on the substrate divided by the number of atoms needed for one monolayer of coverage as provided in equation 3.2. Here θ_i represents the atomic density for one monolayer of coverage ($\theta = 1$). I_i is the number of atoms per second impinging on the substrate of unit area. I_e is the number of atoms per second re-evaporated from the substrate during deposition, and t_i is the duration of the pulse.[22]

$$\theta = (I_i - I_e)\, t_i/\theta_i \qquad \textbf{3.2}$$

According to this equation, under ideal conditions only a monolayer of chemisorbed precursor A will remain while the physisorbed species of A is re-evaporated. Likewise once the surface is subjected to a pulse of precursor B, all possible A-B chemisorbed

bonds form before the physisorbed species of B re-evaporate. As the number of molecules of precursor equals the number of molecules being re-evaporated off the substrate surface, no more deposition of material will take place. Two main types of chemisorption can occur as part of the ALD mechanism: (1) Ligand exchange reaction and (2) Dissociation or association. [17]

3.2.3.1 Ligand exchange reaction

A precursor molecule, (ML_n), is split and one of its ligands (L) is adsorbed onto a surface group (-a) forming a volatile gas phase by-product in ligand exchange. The symbol || represents the surface in the following equation:

$$||-\mathrm{a} \;+\; ML_n(g) \;\leftrightarrow\; ||-ML_{n-1} \;+\; aL\,(g) \qquad \textbf{3.3}$$

Ligand exchange can also occur between an adsorbed reactant complex (ML_{n-y}) and a surface group. [17]

$$||-ML_{n-y-1} \;+\; ||-\mathrm{a} \;\leftrightarrow\; ||-ML_{n-y-1} \;-\; ||+aL\,(g) \qquad \textbf{3.4}$$

3.2.3.2 Dissociation and association

(a) Dissociative mechanism

The dissociation method involves the incoming precursor molecule (ML_n) being split into reactive *M'-Z* sites on the surface. Two species are coordinated to the substrate surface in this step and no gaseous by-products are produced. [17]

$$||\mathrm{M}'-\mathrm{Z}|| \;+\; ML_n(g) \;\leftrightarrow\; ||\mathrm{M}'-\mathrm{L} \;+\; ||Z-ML_{n-1} \qquad \textbf{3.5}$$

(b) Associative mechanism

The association method involves the incoming precursor molecule (ML_n) bonding to an active site on the substrate surface. The precursor molecule is chemisorbed without the release of a ligand. [17]

$$||+ML_n \;\leftrightarrow\; ||\ldots ML_n \qquad \textbf{3.6}$$

Of these mechanisms, ligand exchange is preferred as the gaseous reaction products can be removed by the ALD purge with the product chemisorbed to the substrate surface.

3.2.4 ALD Temperature Window

ALD processes generally operate at temperatures below 350°C. These temperatures are considerably lower than those required for corresponding film growth using CVD.[23, 24] The temperature range in which growth is saturated and deposition is self-limiting is referred to as the ALD temperature window. This is essential for ALD GPC as deposition temperatures outside of this window generally result in poor growth rates. Non-ALD type deposition also effects the quality of the material (Figure 3.2). At temperatures lower than the defined ideal ALD window slow reaction kinetics may occur. Incomplete reaction of ALD precursors result in a lower GPC. Alternatively, at low ALD deposition temperatures the precursors may also condense leading to an increase in the GPC with a greater level of impurities in the thin film. At increased temperatures above the ideal ALD window, precursors may decompose leading to a higher GPC with a greater level of impurities. In contrast, desorption may occur where the precursors re-evaporate from the substrate surface reducing the GPC. These processes are outlined in Figure 3.2.

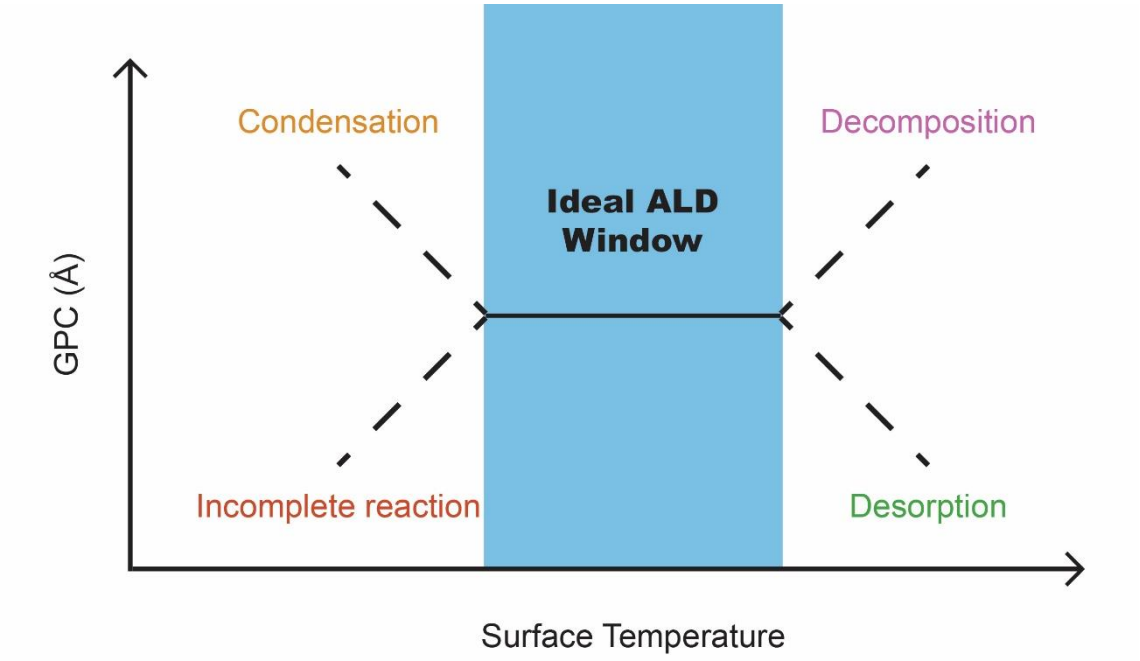

Figure 3. 2: *Schematic of ideal ALD window illustrating areas below and above the ALD temperature range*

Non-ALD type deposition which takes place outside the ALD window may not produce uniform and conformal films. To determine the ALD window of a particular process, the thin film should be deposited across a range of temperatures as well as a variation of precursor pulse lengths and purge lengths. Once the precursor pulse saturates the surface there should be no increase in GPC with increased pulse length. The self-limiting nature of ALD should be satisfied once the purge sequence is increased to remove all physisorbed and unreacted precursors along with any by-products produced. Form this, a temperature range in which the thin film deposits at the same GPC while exhibiting the self-limiting nature of ALD should be displayed. The thickness of the deposited material should also increase linearly with the number of ALD cycles. This implies that there is no nucleation period and GPC is constant from the first cycle.

3.3 ALD Processes

3.3.1 Thermal ALD

A thermal ALD process is the most established and commonly employed ALD method. Heating of the reaction chamber, and subsequently the substrate, provides the energy required for surface reactions to take place. Thus, the surface chemistry is driven solely by thermal energy.[25] Thermal ALD processes usually rely on H_2O as a reactant for metal oxides or on NH_3 as a reactant for metal nitrides. The use of the strong oxidant O_3 as a reactant has also become increasingly popular as it provides additional reactivity compared to H_2O. Many thermal ALD processes are based on binary processes. The ALD growth of TiO_2 and ZnO are based on binary CVD reactions and their corresponding reaction enthalpies.[26]

$$TiCl_4 + 2\,H_2O \rightarrow TiO_2 + 4HCl \qquad \Delta H = \textit{-16 kcal} \qquad \textbf{3.7}$$

$$Zn(CH_2CH_3)_2 + H_2O \rightarrow ZnO + 2C_2H_6 \qquad \Delta H = \textit{-70 kcal} \qquad \textbf{3.8}$$

Thermal ALD process can be carried out in both hot-wall and cold-wall reactors depending on the material to be deposited. In cold-wall reactors only the substrate and lines to prevent condensation are heated without any external heating of the reaction chamber walls. In hot-wall reactors the walls, flow lines and substrate can all be heated by external heating sources.[26]

3.3.2 Plasma Enhanced ALD

In some cases an ALD process can be used in combination with a RF plasma source. This method is known as plasma enhanced atomic layer deposition (PEALD). At a particular point during an ALD reaction cycle plasma energy is applied to the process. This acts as a reactant precursor as it is able to dissociate gas and produce the required radicals, electrons and ions. The use of these reactive species can eliminate the incomplete reaction of precursors as faster chemical reactions can take place. The use of plasma can also allow the ALD window to be broadened and materials deposited at lower temperatures.[27] This increased reaction rate by use of radicals allows for greater precursor fragmentation, improved process efficiency, and improves the removal of product molecules.[28] By adopting plasma in the ALD process the range of materials

that can be grown and precursors used is broadened.[27] Another advantage of PEALD is that the use of a H_2O reactant can be avoided. This is beneficial to the growth as water and hydrogen atoms can be difficult to completely purge from the system [26] and can be useful for ALD deposition on substrates which are water sensitive.

3.4 ALD of Titanium Dioxide

TiO_2 is a thermodynamically stable compound and is most commonly found in nature as the minerals rutile, brookite and anatase. It is the most investigated of all transition metal oxides due to its high use in industry for the production of white paint and other substances which contain a high refractive index. It is also commonly used in physical sunscreens due to its high refractive index and ability to absorb harmful UV rays. TiO_2 has emerged as a key area of interest in DSSCs due to its stable form and high electronic mobility for photogenerated electron collection. The suitable band gap of TiO_2 also allows for electron injection from most successful commercial dyes. TiO_2 is also the most commonly used ETL in PCSs to date following on from its success with DSSCs.

3.4.1 Titanium precursor $TiCl_4$

The first reported ALD growth of TiO_2 was Al_2O_3-TiO_2 to form dielectric layers in 1985.[29] No work was published on the growth mechanism of TiO_2 until 1992 by Lakomaa et al.[30] and 1993 by Ritala et al.[31] using $TiCl_4$ and H_2O as respective precursor and reactant. In the later report 2000 cycles of TiO_2 were deposited between 150°C and 600°C on soda lime glass and Corning 1773 glass substrates. Film growth was found to take place over the wide temperature range with GPC varying from 0.35 Å/cycle at a deposition temperature of 200°C to 0.56 Å/cycle at a deposition temperature of 400°C. The GPC was also found to be influenced by the substrate used as observed in Figure 3.3.

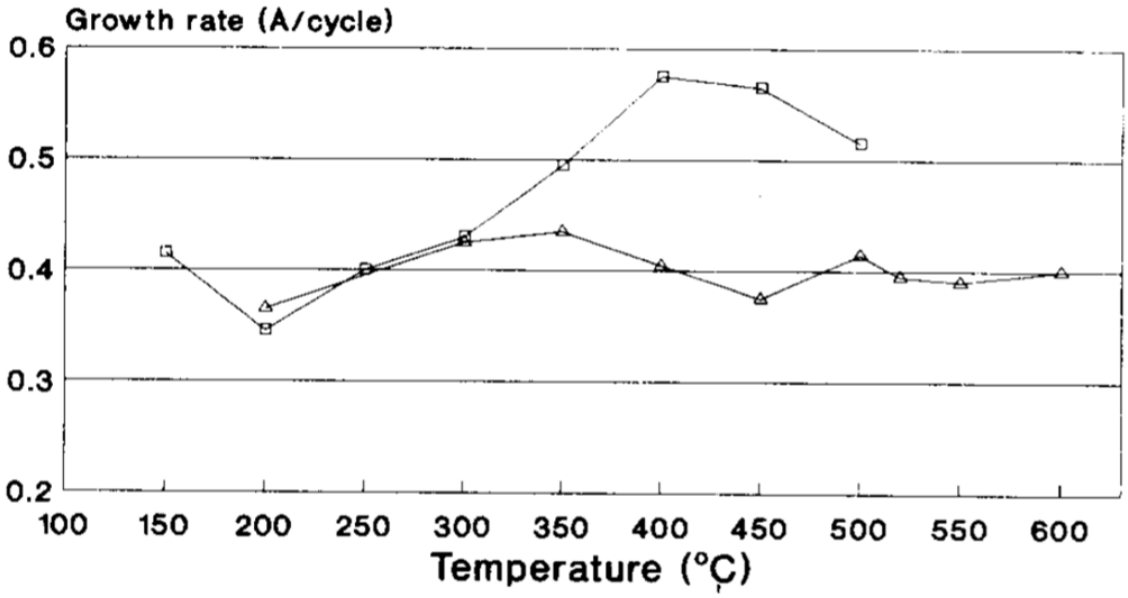

Figure 3. 3: *The growth rates on soda lime (□) and Coming 1733 (△) glass substrates as a function of temperature* [31]

The titanium precursor, $TiCl_4$, is highly reactive toward water and hydroxyl groups allowing for deposition over a wide temperature range. Due to such high reactivity the growth mechanism of TiO_2 was suggested to follow that of Al_2O_3 using the aluminium precursor $AlCl_3$. This idealised mechanism given in equations 3.9 and 3.10 requires the precursor and reactant to be chemisorbed onto the surface through irreversible exchange reactions with n = 1-3.[31]

$$\mathrm{n(OH)} + \mathrm{TiCl_4}(g) \rightarrow (-\mathrm{O}-)_\mathrm{n}\mathrm{TiCl_{4-n}} + \mathrm{n\ HCl}(g) \qquad \textbf{3.9}$$

$$(-\mathrm{O}-)_\mathrm{n}\mathrm{TiCl_{4-n}} + (4-\mathrm{n})H_2O(g) \rightarrow \qquad \textbf{3.10}$$

$$(-\mathrm{O}-)_\mathrm{n}\mathrm{Ti(OH)_{4-n}} + (4-\mathrm{n})\ \mathrm{HCl}(g)$$

Equation 3.9 shows the $TiCl_4$ precursor interacting with a hydroxyl terminated surface. This bonds with an O on the surface releasing an HCl gaseous by-product. During a reactant pulse in equation 3.10 the titanium intermediate reacts with water again releasing HCl as a gaseous by-product resulting in a hydroxyl terminated surface.

Realistically, the growth mechanism is more complicated as the species involved may exist in different configurations and undergo alternative mechanisms during reaction. Hydroxyl groups on the deposition surface are not always terminated and may be bridged between two cations. The terminated hydroxyl groups themselves can be either adjacent with hydrogen bond interaction or isolated.[31, 32] The amphoteric nature of TiO_2 is caused by both terminal and bridging hydroxyl groups as their chemical behaviour differs. Bridging hydroxyl groups are acidic due to the polarisation of cations while terminated hydroxyl groups are more basic in nature.[33] As well as reacting with $TiCl_4$, hydroxyl groups on the surface of the deposition material can condensate with each other as outlined in reaction 3.11 and 3.12:[31]

$$\mathrm{Ti(OH) - O - Ti(OH) \rightarrow Ti(-O-)_2Ti + H_2O}(g) \qquad \textbf{3.11}$$

$$\mathrm{2 - Ti(OH) \rightarrow -Ti - O + -Ti + H_2O}(g) \qquad \textbf{3.12}$$

Equation 3.11 takes place at low temperatures when terminal hydroxyl groups are adjacent with hydrogen bond interaction. This allows the oxygen to coordinate with two cations. Separately when terminal hydroxyl groups are isolated, as in equation 3.12, the oxygen is coordinated to one cation allowing the other to be coordinately unsaturated.[32] As mentioned above, reaction 3.11 generally takes place at lower temperatures than reaction 3.12. This is because hydrogen-bonded hydroxyls are more favourable for dehydroxylation compared to isolated hydroxyls. For reaction 3.12 to occur proton or hydroxyl migration is required, therefore dihydroxylation tends to take place over a wide range of deposition temperatures. For that reason the reactivity of the surface deposition material toward $TiCl_4$ is temperature dependant as the density and relative amounts of surface hydroxyls in the varying configurations differ with temperature.

In the ideal reaction mechanism from equation 3.9 it was assumed that $TiCl_4$ only reacted with terminated hydroxyl groups. Equation 3.13 below shows that it can also react with bridging oxygen species:

$$\mathrm{Ti(-O-)_2Ti + TiCl_4}(g) \leftrightarrow \mathrm{Ti(Cl) - O - Ti(OTiCl_3)} \qquad \textbf{3.13}$$

As observed above, this reaction does not produce a gaseous product and so is entropically less favourable to occur compared to equation 3.9. Moreover, the reaction is reversible due to the close proximity of the products formed.[34]

The complexity of the $TiCl_4$ growth mechanism is escalated due to the possibility of HCl adsorption on to the TiO_2 surface.[35] These are reversible reactions as displayed below whose equilibria is temperature dependent:

$$\mathrm{Ti-OH} + \mathrm{HCl}(g) \leftrightarrow \mathrm{Ti(H_2O)-Cl} \leftrightarrow \mathrm{Ti-Cl} + \mathrm{H_2O}(g) \qquad \textbf{3.14}$$

$$Ti(-O-)_2\mathrm{Ti} + \mathrm{HCl}(g) \leftrightarrow \mathrm{Ti(OH)-O-Ti-Cl} \qquad \textbf{3.15}$$

The equilibria of these reactions have been observed to take place on the right at low deposition temperatures for rutile TiO_2.[35] Residuals of chlorine have been observed to increase the amount of water adsorbed on the surface material at low temperatures, whereas at higher temperatures they assist dihydroxylation.[33]

Due to the complexity of all these reactions the realistic growth mechanism consists of competitive, simultaneous reactions. The hydroxyl groups at the surface of the deposition material can either react with $TiCl_4$ (equation 3.9) or with HCl (equation 3.14) when the reactor is pulsed with the $TiCl_4$ precursor. Successful film growth can only occur as per equations 3.9 and 3.13. The effects of equations 3.11 and 3.12 must be taken into account for dehydroxylation.

The use of halide ligands such as chlorides, bromides and iodides are common in ALD precursors. These halides are usually solids with low volatility but due to their high reactivity are efficient as ALD precursors. As previously mentioned in section 3.2.2, a distinct advantage of halide ligands is their small size which provide low steric hindrance and do not block active surface sites. Conversely, the halide atoms can unintentionally be incorporated into the deposited material producing doped films.[20] These halide ligands also tend to produce reactive by-products such as HCl. The corrosive nature of HCl formed from the reaction of $TiCl_4$ and H_2O is undesireable for ALD reactors and often the grown materials, thus the investigation of other possible titanium precursors was necessary.

An alternative titanium halide precursor, TiI_4, has been reported which has a lower bond energy compared to $TiCl_4$ with a larger ionic radius of iodine.[36] This precursor has been shown to release ligands more easily than $TiCl_4$ in the ALD process.[37-42] Titanium precursors with alkoxide ligands such as titanium methoxide, Ti(OMe)4,[43-45] titanium ethoxide, $Ti(O(CH_3)_2)_4$,[46-50] and titanium isopropoxide, $Ti(OCH(CH_3)_2)_4$ (TTIP)[51-57] have been used to deposit ALD TiO_2 films along with titanium alkylamides such as tetrakis (dimethylamido) titanium, $Ti(N(CH_3)_2)_4$ (TDMAT)[57-63] and tetrakis (diethylamido) titanium, $Ti(N(C_2H_5)_2)_4$ (TDEAT).[63-65] Several criteria need to be considered before the selection of a titanium precursor such as chemistry with the desired reactant, GPC, range and upper limit of the temperature window process, and precursor volatility. Depending on the desired application electronic and optical properties of the resulting thin film also need to be taken into account. The use of titanium precursors TTIP and TDMAT will be discussed in further detail herein.

3.4.2 Titanium precursor TTIP

The titanium precursor TTIP is widely used in ALD processes due to the desirable electrical properties produced in resultant TiO_2 thin films. When applied with a H_2O reactant the process is self-limited at deposition temperatures in the approximate range of 200°C to 250°C. When H_2O_2 is applied as a reactant the self-limited growth can be obtained from 100°C to 250°C.[52] The growth mechanism of TiO_2 through use of the TTIP precursor is given in the following equations where -OH indicates a surface hydroxyl and n=1-3:[66]

$$\mathrm{n-OH} + \mathrm{Ti(OCH(CH_3)_2)_4} \rightarrow \mathrm{(-O-)_nTi(OCH(CH_3)_2)_{4-n}} + \mathrm{nCH_3CH_2OH} \quad \textbf{3.16}$$

$$\mathrm{(-O-)_nTi(OCH(CH_3)_2)_{4-n}} + \mathrm{(4-n)H_2O} \rightarrow \mathrm{(-O-)_nTi(OH)_{4-n}} + \mathrm{(4-n)CH_3CH_2OH} \quad \textbf{3.17}$$

From equations 3.16 and 3.17 the ethanol (CH_3CH_2OH) may be dehydrated after its formation. An alternative growth mechanism would be the chemisorption of TTIP

followed by its hydrolysis once the surface of the deposition material has undergone complete hydroxylation with the introduction of a H_2O pulse. This is provided in equations 3.18 and 3.19:

$$\mathrm{Ti(OCH(CH_3)_2)_4} \rightarrow \mathrm{Ti(OCH(CH_3)_2)_4}\ [chemisorption] \quad \textbf{3.18}$$

$$\mathrm{Ti(OCH(CH_3)_2)_4}\ [chemisorption] + 2\mathrm{H_2O} \rightarrow \mathrm{TiO_2} + \mathrm{CH_3CH_2OH} \quad \textbf{3.19}$$

It has been reported that between deposition temperatures range of 150°C to 200°C, two ligands per TTIP molecule are released upon reaction with the hydroxylated surface of the deposition material.[53,67] In addition, TTIP is a large bulky molecule which can cause high steric hindrance. For these reasons a lower amount of the TTIP molecules are likely to saturate a hydroxylated surface leading to a low growth rate.

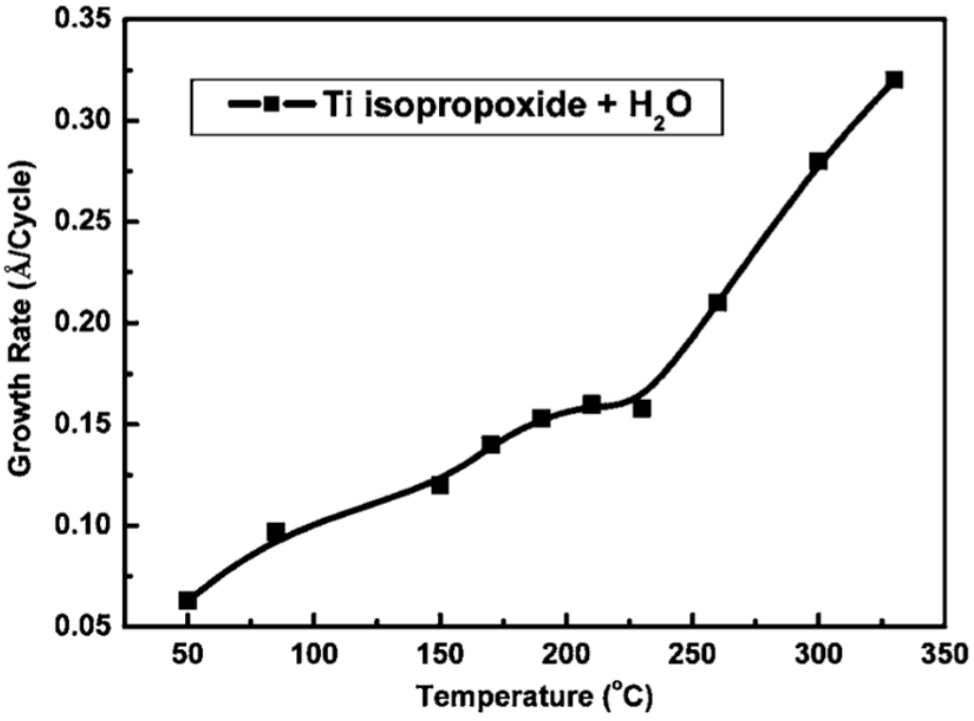

Figure 3. 4: *GPC of TiO_2 deposited using TTIP and H_2O as a function of deposition temperatures* [60]

As observed in Figure 3.4 the GPC of TTIP with H_2O is low at reduced temperatures reaching 0.12 Å/cycle at a deposition temperature of 150°C.[60] At low deposition temperatures the reactant H_2O_2 has provided an improved TiO_2 GPC compared to H_2O with use of TTIP. This is due to the H_2O_2 reactant being better able to eliminate alkoxide ligands. At higher deposition temperatures, the growth rate was found to be independent of oxygen reactants.[52] PEALD of TiO_2 with TTIP has also been reported to improve GPC at low deposition temperatures. A growth rate of 0.45 Å/cycle was reported by Jeong et al. when TiO_2 was deposited on an Al bottom electrode patterned on SiO_2.[68]

3.4.3 Titanium precursor TDMAT

The titanium precursor TDMAT is also commonly used in ALD processes due to the desirable electrical properties in resulting TiO_2 films.[60,63] The bond energy of metal halide precursors such as $TiCl_4$ are much stronger than those of metal-nitrogen bonds. Metal amide compounds such as TDMAT have a much higher reactivity when used in conjunction with H_2O.[69] This precursor is more reactive than TTIP allowing for better coverage approaching ideal monolayer growth at low deposition temperatures.[60] In contrast, at higher deposition temperatures above 250°C the TDMAT precursor has been reported to begin decomposing.[63] A wide ALD temperature window is observed between 100°C and 250°C with a self-limiting saturated growth rate of 0.46 Å/cycle when TDMAT is employed with either H_2O or O_3 as reactants.[63, 69]

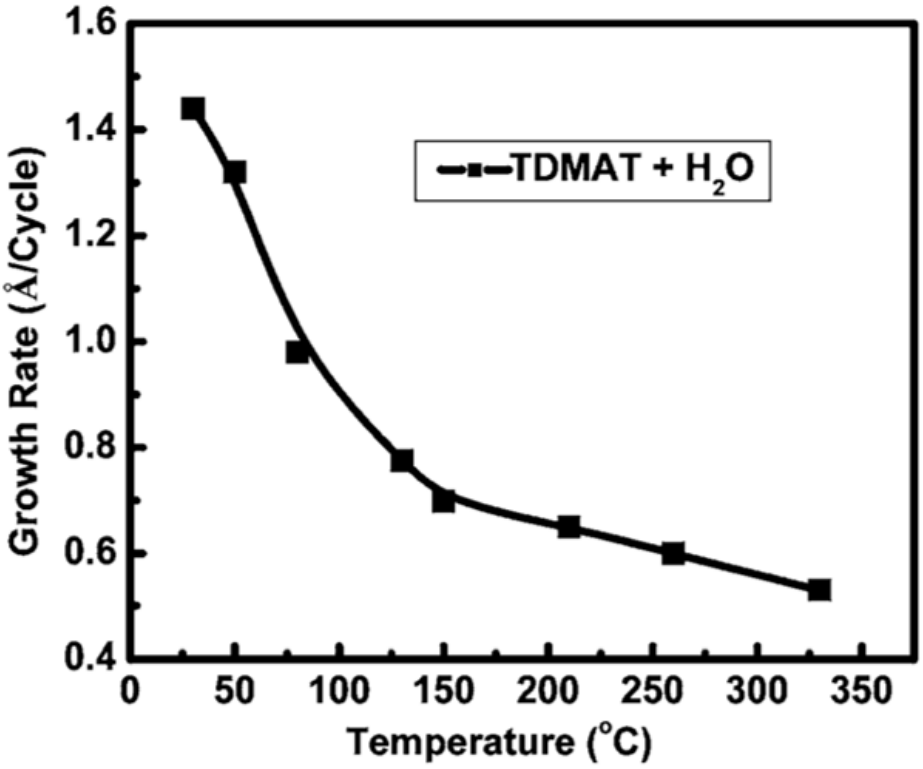

Figure 3. 5: *GPC of TiO_2 deposited using TDMAT and H_2O as a function of deposition temperatures* [60]

Figure 3.5 displays the GPC of TiO_2 using TDMAT and H_2O increasing with decreasing deposition temperature. The ALD growth mechanism of TDMAT with H_2O is shown below in equations 3.20 and 3.21 where *n* = 1-3: [60]

$$Ti(N(CH_3)_2)_4 \ + \ \mathrm{n} - \mathrm{OH} \rightarrow \qquad \textbf{3.20}$$

$$nNH(CH_3)_2 + (-O-)_nTi(N(CH_3)_2)_{4-n}$$

$$(-O-)_nTi(N(CH_3)_2)_{4-n} \ + (4 - \mathrm{n})H_2\mathrm{O} \rightarrow \qquad \textbf{3.21}$$

$$(4 - \mathrm{n})NH(CH_3)_2 + (-O-)_nTi(OH)_{4-n}$$

3.5 ALD of Tin(IV) Oxide

Tin (IV) oxide, also referred to as tin dioxide, is a wide band-gap semiconductor material. This metal oxide has gathered significant attention due to its high conductivity, transparency and superior stability.[70-71] As well as these desirable optical and electrical properties, SnO_2 also exhibits favourable magnetic and chemical properties.[72-74] As a consequence SnO_2 is widely used in gas sensors,[72-78] ion-sensitive field effect transistors,[79-81], catalysts,[82-84] and transparent electrodes for flat panel displays.[85] SnO_2 become a key area of interest for application in DSSCs[86-89] due to its fast electron conductivity and stability under UV radiation. However, these types of solar cells exhibited poor device performance compared to their TiO_2 counterparts. The poor performance due to SnO_2 has been attributed to its faster electron recombination as well as a weaker adsorption of dyes with acidic carboxyl groups.[90, 91] SnO_2 has more recently been applied as an ETL in PSCs.[92-97] As well as improved stability over TiO_2,[98,99] SnO_2 has a deep conduction band which enables a barrier-free band alignment between the perovskite light harvester and the ETL in planar PSCs.[100]

3.5.1 Tin precursor $SnCl_4$

The first reported ALD growth of SnO_2 was carried out in 1994 by H. Viirola and L. Niinisto.[101] Film growth was carried out between 300°C and 600°C using $SnCl_4$ and H_2O as respective precursor and reactant. A narrow ALD window was found to be within the deposition temperature range of 500°C and 550°C with a GPC of 0.35 Å/cycle. Further studies found the GPC to increase to 0.6 Å/cycle with an increased H_2O pulse.[102] Films deposited above 500°C were found to be polycrystalline in nature with a preferred orientation depending on thickness obtained and deposition temperature.[101]

In the early 2000s Tarre and Rosental succeeded in depositing amorphous SnO_2 films at the low deposition temperature of 180°C, while amorphous with small amounts of rutile SnO_2 films were deposited at 300°C.[103, 104] The GPC of these thin films was found to be notably low with 0.04 Å/cycle and 0.17 Å/cycle achieved at 180°C and 300°C respectively. Significant contamination of chlorine was found at low deposition temperatures effecting stoichiometry. 8-9% chlorine was found to be present in films deposited at 180°C[103] while the chlorine content was reduced to 3.6 % in films

deposited at 500°C.[102] The ALD growth mechanism for SnO_2 using $SnCl_2$ and H_2O resembles that outlined for $TiCl_4$ in section 3.4.1.

The ALD process employing $SnCl_4$ with O_2 was found not to permit any SnO_2 film growth.[102] In contrast, when O_3 was used in conjunction with H_2O as a reactant, an increase in the SnO_2 GPC to 0.74 Å/cycle could be observed at a deposition temperature of 500°C.[102] This is due to a high concentration of hydroxyl groups forming on the surface of the deposition material through use of O_3 assisted H_2O dissociation. Likewise, an improved GPC of 0.7 Å/cycle at 325°C was observed when H_2O_2 was employed as a reactant.[105, 106]

Overall, the chlorine contamination and non-stoichiometry combined with the narrow ALD window of SnO_2 deposited using $SnCl_4$ produces poor films. The HCl by-product of the ALD process has also been shown to produce rough films due to etching.[107] Among inorganic precursors, SnI_4 has a greater potential for obtaining SnO_2 films with a uniform thickness and a low defect density when employed with O_2 or H_2O_2 reactants.[107, 108] While the use of $SnCl_4$ as a precursor has the advantage of being a low cost material with high availability, SnI_4 has proved itself to be a superior choice precursor.

3.5.2 Tin precursor TDMASn

Both $SnCl_4$ and SnI_4 can form agglomerates when large exposure times are used to infiltrate porous substrates such as powders or nanoporous membranes. This leads to non-uniform coatings.[109] The use of stable non-halogenated tin precursors is necessary to achieve high growth rates without the requirement of high deposition temperatures. TDMASn was first applied to the SnO_2 ALD process in 2008 by Elam et al.[110] TDMASn was used in conjunction with a H_2O_2 reactant to produce thin films in the temperature range of 50 to 300°C with an average growth rate of 1.2 Å/cycle.

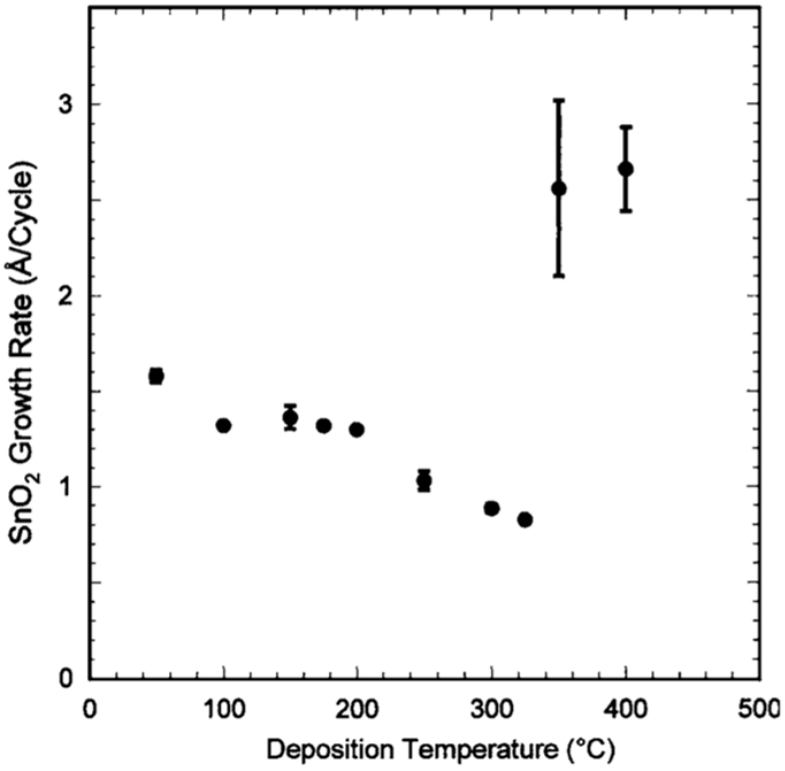

Figure 3. 6: *GPC of SnO_2 deposited using TDMASn and H_2O_2 as a function of deposition temperatures from 50°C to 400°C* [110]

From Figure 3.6 it can be observed that the SnO_2 GPC decreases steadily with increased deposition temperature. The authors suggested that the thermal decomposition of TDMASn takes place at temperatures above 325°C leading to non-ALD type growth.[110] Separately however, the TDMASn thermal decomposition has also been reported to be above 230°C which also leads to an increase in GPC.[111] The ALD temperature window for TDMASn with H_2O_2 is within the range of 100°C to 200°C.

While TDMASn with H_2O_2 provides a relatively high GPC of 1.2 Å/cycle, when the same precursor is employed with H_2O the GPC is reduced to 0.6 Å/cycle. The use of H_2O as a reactant allows the production of SnO_2 films with a very high growth rate at low deposition temperatures as displayed in Figure 3.7.[112] At 30°C the GPC was a significantly high 2.0 Å/cycle, while at 150°C the GPC was reduced to 0.7 Å/cycle. This ALD process was found to be saturated even at low deposition temperatures. Further studies into surface chemistry and growth characteristics of ALD SnO_2

through TDMASn and H_2O were investigated by density functional theory and second-order Møller−Plesset perturbation theory calculations.[113] These suggested that the increased growth rate for films deposited below 100°C was due to physisorbed H_2O as the energetics for the TDMASn reaction with surface OH groups is similar to that with H_2O molecules. Therefore, TDMASn can react with physisorbed water as well as surface hydroxyl groups and the summary process can be considered "mixed CVD/ALD" or "controlled CVD". Using H_2O as a reactant gives the possibility to obtain SnO_2 films at temperatures lower than 100°C. This is crucial for the production of thermally sensitive materials such as photovoltaic cells.

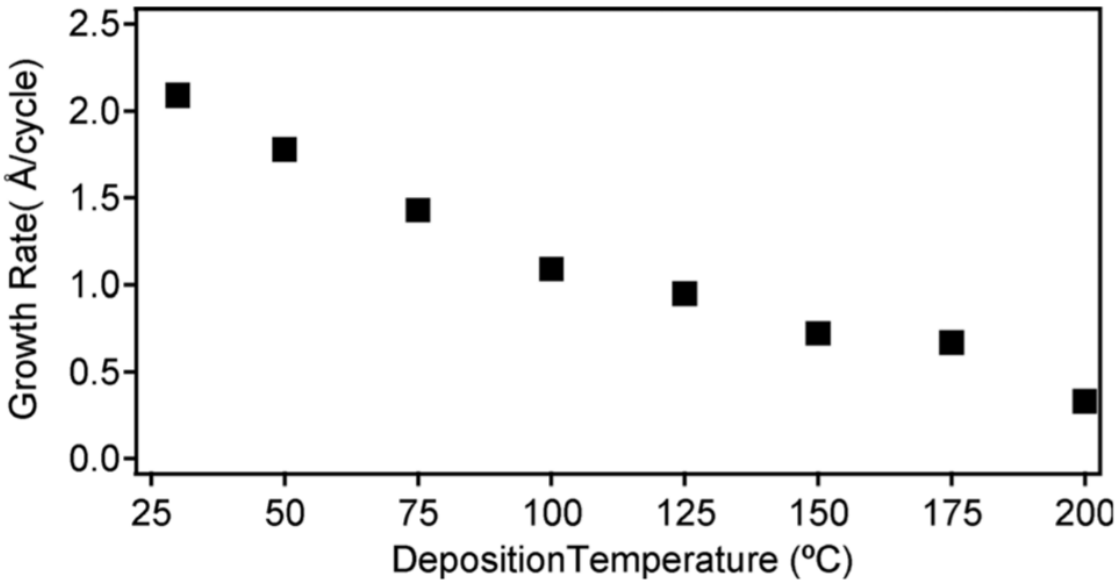

Figure 3. 7: *GPC of SnO_2 deposited using TDMASn and H_2O as a function of deposition temperatures from 25°C to 200°C* [112]

Considering the surface reactions involved in ALD processes is important for understanding film growth. A reaction mechanism for the growth of SnO_2 using TDMASn and H_2O is shown in equations 3.22 and 3.23 where n =1-3: [112]

$$Sn(N(CH_3)_2)_4 \ + \ \mathrm{n-OH} \rightarrow \qquad \textbf{3.22}$$

$$nNH(CH_3)_2 + (-O-)_nSn(N(CH_3)_2)_{4-n}$$

$$(-O-)_n Sn(N(CH_3)_2)_{4-n} + (4-\mathrm{n})H_2O \rightarrow \quad \textbf{3.23}$$

$$(4-\mathrm{n})NH(CH_3)_2 + (-O-)_n Sn(OH)_{4-n}$$

In-situ quartz crystal microbalance (QCM) analysis indicates that n = 2.5 with H_2O as the reactant, compared to a higher value of n = 3 when using H_2O_2. This reaction stoichiometry is consistent with the lower growth rate observed with H_2O at higher temperatures and reflects a lower degree of surface hydroxylation.[110]

3.6 Electron Transport layers by ALD for use in perovskite solar cells

In perovskite devices the ETL has a number of roles. It is required to selectively extract electrons from the perovskite material whilst simultaneously blocking holes, to transport electrons through the ETL to be collected by the electrode, to minimise carrier recombination between the ETL and the perovskite interface as well as between the electrode and ETL interface, and to be electrically continuous in order to prevent shunt pathways. A successful ETL has a conduction band aligned with or slightly lower than that of the perovskite material. TiO_2,[114-117] SnO_2,[92, 93, 118, 119] ZnO[120-123], and Zn_2SnO_4[124,125] are all n-type metal oxides which demonstrate the desired conduction band alignment along with deep valence bands to adequately extract electrons and block holes from the perovskite material.

To reduce series resistance and optimise electron extraction an ETL is also required to exhibit excellent electrical properties. Series resistance can be reduced by reducing the thickness of the ETL on the condition that the layer remains continuous and pinhole free. Deposition of these charge contacts are often carried out using techniques such as spin coating[126-128] and spray pyrolysis[129,130]. Reducing the ETL thickness through these deposition processes generally results in films with poor uniformity and pinholes. As a result the hole blocking ability is reduced and shunt pathways are increased. This leads to a low V_{oc} and FF in the final device. Cell performance is further reduced by these deposition methods as the active area increases for large area

processing. In contrast, the conformality of ALD allows for the deposition of very thin blocking layers over large areas when compared to conventional techniques.

3.6.1 ALD TiO_2 as electron transport layer

In 2014 Wu et al.[131] compared TiO_2 compact layers deposited by spin coating, spray pyrolysis and ALD which were then fabricated into mesoporous perovskite devices. 50 nm of ALD TiO_2 was deposited at 200°C using TDMAT and H_2O as titanium precursor and reactant, respectively. Surface morphology and film resistance studies indicated that the ALD TiO_2 compact layer was dense containing a much lower density of pinholes than the TiO_2 layers deposited by alternative methods. Final cell performances achieved 12.56 % PCE for devices incorporating the ALD layer. This was substantially higher than the 8.76 % PCE reached from devices using spray pyrolysis and 6.52 % PCE with spin coating (Table IIII.I). In the same year a 30 nm ALD TiO_2 layer was deposited as a compact layer using TTIP and H_2O and fabricated into a mesoporous lead free cell.[132] This was the first report of $CH_3NH_3SnI_{3-x}Br_x$ being used as a lead free light harvester. This perovskite material featured the ideal band gap of 1.3 eV and final device performance reached 5.73 % PCE.

Table III. I: *Photovoltaic performance of perovskite solar cells based on different compact TiO_2 blocking layers*[131]

c-TiO_2	*J_{sc} (mA cm^{-2})*	*V_{oc} (V)*	*FF (%)*	*η (%)*	*R_{sh} (Ω cm^2)*	*R_s (Ω cm^2)*
ALD	18.74	0.93	0.72	12.56	4202	5.6
Spray pyrolysis	17.37	0.87	0.58	8.76	1182	7.1
Spin coating	15.30	0.79	0.54	6.52	567	11.3
Without	2.44	0.51	0.26	0.32	247	157.9

Thin ALD TiO_2 overlayers have also been successfully deposited over mesoporous TiO_2. Chandiran et al.[133] deposited various thicknesses of ALD TiO_2 from 1 nm to 4 nm on top of a mesoporous TiO_2 layer. The 2 nm film was found to provide the best performance in final devices reaching a PCE of 11.5 % by effectively blocking parasitic back reaction from the FTO and mesoporous TiO_2 surface. When the ALD passivation layer was increased to 4 nm the final cell dropped in PCE to 9.1 %. It was concluded that this thicker ALD TiO_2 overlayer reduced the pore diameter leading to improper pore filling by the perovskite material. As displayed in Figure 3.8, the mesoporous TiO_2/ALD TiO_2 film is infiltrated with the $CH_3NH_3PbI_3$ perovskite.

When the ALD TiO_2 overlayer is too thick the pore diameter for perovskite infiltration is reduced leading to improper pore filling. These ALD TiO_2 layers were deposited at the low temperature of 120°C using TDMAT and H_2O. Approximately 15 cycles was found to produce 1 nm of TiO_2.

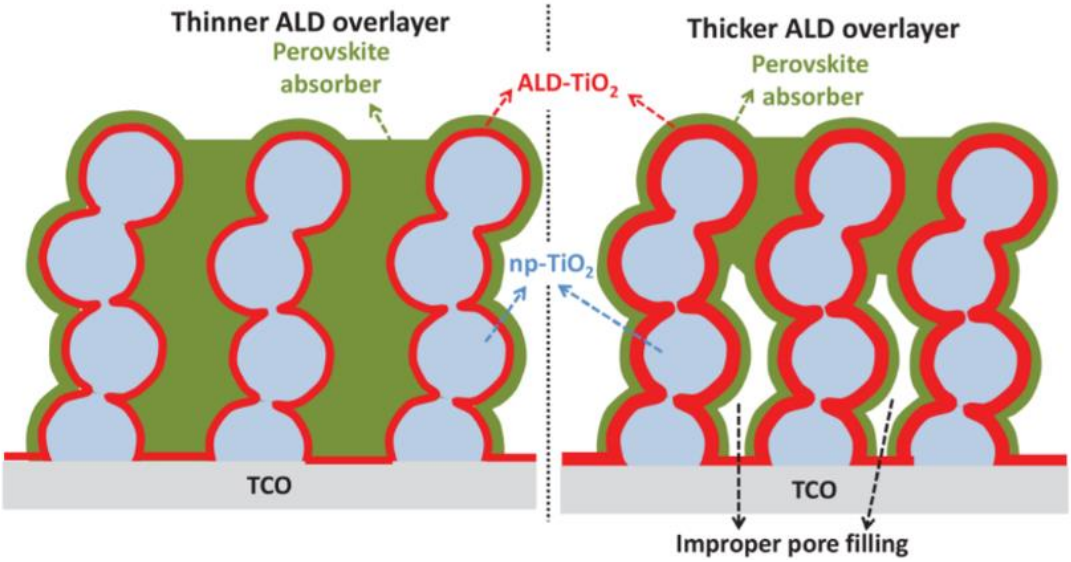

Figure 3. 8: *Block diagrams of mesoscopic photoanodes with thinner (left) and thicker (right) ALD TiO_2 overlayer deposited on the mesoporous nanoparticle TiO_2.*[133]

PEALD of TiO_2 has also been well established for low temperature deposition of compact TiO_2 layers. Di Giacomo et al.[134] deposited 11 nm TiO_2 on flexible ITO coated plastic substrates at 150°C using $Ti(CpMe)(NMe_2)_3$ and O_2 plasma as the respective titanium precursor and reactant. The plasma approach enables the deposition of higher quality films in terms of low pinhole density in a low temperature range which is compatible with conductive plastic substrates.[135] The final mesoporous perovskite devices achieved a PCE of 8.4 %. A screen-printable procedure for the mesoporous layer was then developed producing large area flexible modules of 8 cm^2 composed of four series connected cells. The PCE over the module was 3.1 % with the best cell exhibiting 4.3 %. Di Giacomo et al.[136] went on to develop mesoporous perovskite cells which consisted of PEALD TiO_2 on ITO coated PET. These devices reached 15.9 % PCE under one sun and 24 % PCE under indoor lighting of 200 lux.

A later study by the same group compared a thickness series of PEALD TiO_2 of between 2.5 nm and 44 nm in mesoporous flexible PSCs.[137] The resulting devices were then compared in terms of J-V characteristics to identical mesoporous cells incorporating a conventional sol-gel TiO_2 ETL. The dense and conformal nature of PEALD allowed TiO_2 films as thin as 5.5 nm to successfully reduce charge recombination. The ideal ALD thickness was found to be 11 nm deposited at 150°C using $Ti(CpMe)(NMe_2)_3$ and RF O_2 plasma as titanium precursor and reactant. When fabricated into mesoporous devices these cells produced a maximum PCE of 9.2 %. In contrast, an identical cell using sol gel TiO_2 as the ETL achieved a max PCE of just 4.0 %. Electrochemical characterisation and XPS analysis confirmed the higher quality of PEALD TiO_2, which was shown to contain a lower defect density with a low level of impurities compared to sol gel TiO_2. A thickness series comparison of thermal ALD TiO_2 of between 10 nm and 400 nm was also conducted for use in mesoporous PSCs with contrasting results.[138] ALD TiO_2 thin films were grown on FTO coated glass at a high deposition temperature of 300°C using $TiCl_4$ and H_2O as respective titanium precursor and reactant. The ALD TiO_2 layer was found to be most conductive at a thickness of 200 nm. Photoluminescence (PL) quenching demonstrated that most efficient interfacial electron transfer occurred at this thickness as the TiO_2 film was rough, increasing surface area contact with the $CH_3NH_3PbI_3$ perovskite. 200 nm was determined to be the superior thickness for use in PSCs as well, reaching a maximum PCE of 15.41 %. While these results differ greatly from those derived from the PEALD thickness series deposited by Zardetto et al.[137], it should be noted that the cell architectures employed were dissimilar. As well as this, different titanium precursors and reactants were used and deposited at significantly different temperatures. As previously discussed in section 3.4, individual titanium precursors and reactants tend to undergo distinct and competing surface reactions with diverse surface chemistry.

ALD of TiO_2 compact layers in mesoporous PSCs have shown improvement in performance compared to conventional deposition techniques. For planar PSCs however the results have been more complicated. Flexible planar PSCs comprising of PEALD compact TiO_2 layers were fabricated by Kim et al.[139] obtaining an impressive PCE of 12.2 % with little hysteresis. In this case TTIP was employed as the titanium precursor and O_2 plasma as the reactant to deposit 20 nm TiO_2 at 100°C. Identical

planar devices were fabricated incorporating solution processed TiO_2 ETLs which produced poor efficiencies of 4.3 %. XPS analysis detected fewer Ti^{3+} in the ALD film compared to the solution based TiO_2, while FTIR displayed a lower carbon content for the ALD TiO_2. The higher quality of ALD TiO_2 lead to faster charge injection at the ETL/$CH_3NH_3PbI_{3-x}Cl$ interface. In contrast to these results, ALD TiO_2 deposited thermally[100] and through plasma assistance[132] have been reported to exhibit low PCEs and high hysteresis when fabricated into planar PSCs. While these ETLs have displayed excellent hole blocking properties due to the conformal nature of ALD, poor electron injection at the ETL/perovskite interface has been attributed to the low performance. Correa Baena et al.[100] reported a conduction band misalignment between the TiO_2 ETL and the $CH_3NH_3PbI_3$ perovskite layer of 80 meV. This extends to 300 meV with the mixed perovskite $(FAPbI_3)_{0.85}(MAPbBr_3)_{0.15}$ (Figure 3.9). Undesired charge accumulation at the interface is caused by this band offset leading to poor electron injection. The scan rate during J-V measurements was found to dictate this electron extraction.

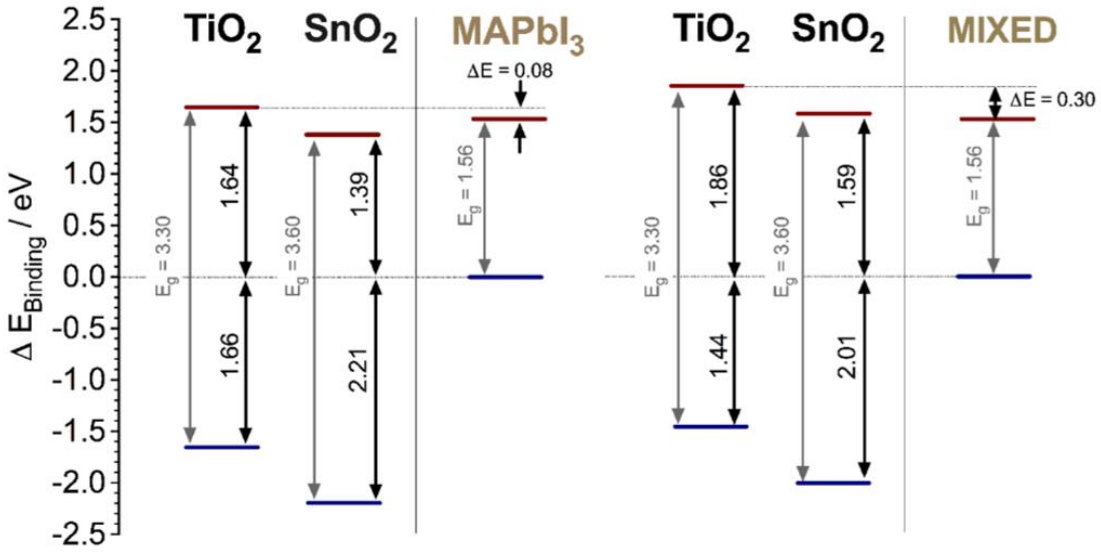

***Figure 3. 9**: Schematic energy level diagram of the perovskite films and the electron selective layers, TiO_2 and SnO_2 for $MAPbI_3$ and $(FAPbI_3)_{0.85}(MAPbBr_3)_{0.15}$ labelled as mixed [100]*

Zardetto et al.[140] have recently proposed a solution to the conduction band misalignment between the ALD TiO_2 ETL and the $CH_3NH_3PbI_3$ perovskite. A post treatment of CF_4 has been demonstrated to effectively modify the chemical surface composition of PEALD TiO_2 improving adhesion with the perovskite layer. In this study 20 nm TiO_2 thin films were deposited at 130 °C using TTIP and O_2 plasma. A post treatment of CF_4 exposure lasting between 1 and 5 minutes was carried out using a plasma etcher. In the resulting planar cells the effect of only 2 minutes CF_4 exposure was found to boost J-V characteristics and significantly reduce hysteresis compared to devices which did not undergo the same ETL post treatment (Table III.II). The CF_4 plasma treated device achieved a stable PCE of 14.8% after 5 minutes of steady state tracking. This PCE was found to remain stable at 14.6% after 15 hours of light exposure. In contrast, the reference device which did not undergo a CF_4 treatment produced a poor stabilised PCE of 4 % after 5 minutes of steady state tracking.

Table III. II: *Photovoltaic parameters calculated according to the direction of the J-V scan for the devices with and without CF_4 plasma treatment* [140]

	Reference ALD TiO_2		*ALD TiO_2 with CF_4 treatment*	
	Reverse	*Forward*	*Reverse*	*Forward*
J_{sc} *(mA cm^2)*	19.7	19.2	20.3	20.3
V_{oc} *(V)*	0.824	0.704	1.033	1.010
FF (%)	54.5	29.6	75.5	65.4
η (%)	8.8	4.0	15.8	13.4
η after 5 min (%)	3.9		14.8	

At an increased CF_4 exposure time of 5 minutes, PEALD TiO_2 layers were found to be discoloured and inhomogeneous due to etching. As a result these devices performed poorly when fabricated into planar PSCs. XPS analysis showed that the ideal post treatment time of 2 minutes produced a fluorine-rich TiO_2 surface. A third of the oxygen atoms on the surface were replaced with fluorine when compared to the reference PEALD TiO_2. This fluorine content was only found to be present at the surface of post treated samples as XPS analysis after sputtering produced no fluorine signal. Ultraviolet photoelectron spectroscopy (UPS) also showed that the CF_4 treatment modified the PEALD TiO_2 energy levels allowing better alignment with the conduction band of the perovskite.

3.6.2 ALD SnO_2 as electron transport layer

SnO_2 has a deep conduction band which allows for barrier free alignment between the ETL and the perovskite material. ALD SnO_2 was first applied as an ETL to planar PSCs by Correa Baen et al.[100] which achieved a notably high 18.4 % PCE in the reverse scan and voltages exceeding 1.19 V displayed in J-V characterisation. Femtosecond transient absorption (TA) measurements showed that ALD SnO_2 was able to effectively extract electrons from the mixed perovskite material, $(FAPbI_3)_{0.85}(MAPbBr_3)_{0.15}$. This was not observed with ALD TiO_2. It was concluded that the ALD SnO_2/perovskite interface provided efficiently high and stable current densities regardless of sweep rate. The ALD SnO_2 layer was deposited at 120°C using TDMASn and O_3 while the TiO_2 layer was deposited at the same temperature using TDMAT and H_2O_2.

Following this, studies on PEALD SnO_2 for planar PSCS were carried out by Wang et al.[141] 15 nm thin films were deposited on both glass and flexible ITO/PET substrates using the tin precursor TDMASn and the reactant O_2 plasma at 100°C by. The average GPC was found to be 1.7 Å/cycle as determined by spectroscopic ellipsometry. Devices were fabricated with and without ETL passivation. A thin C_{60}-SAM layer was spin coated on top of the PEALD SnO_2 layer as thin fullerenes have the ability to passivate metal oxide surfaces promoting electron transfer. Once were fabricated into planar cells an improvement in V_{oc}, J_{sc}, FF and thus PCE could be observed for devices incorporating the C_{60}-SAM passivation layer compared to devices without a passivation layer (Figure 3.10).

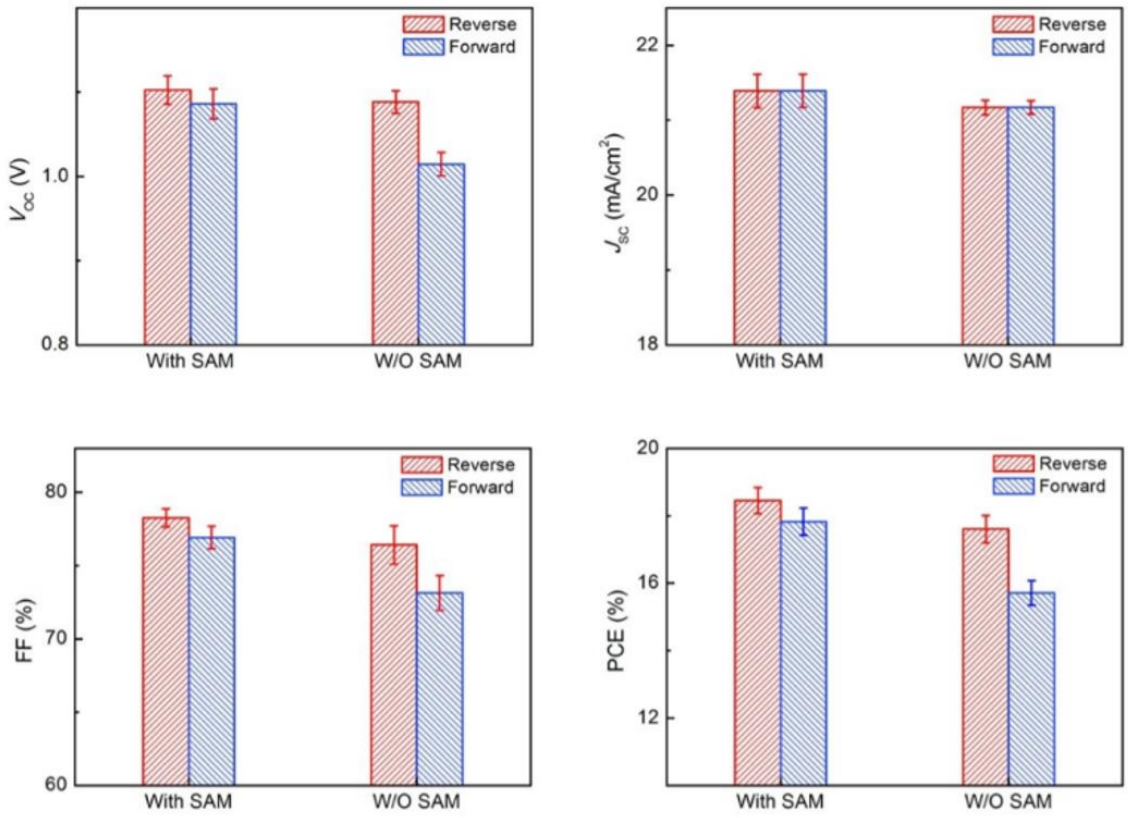

Figure 3. 10: *Statistical device performance results of 20 cells with and without C_{60}-SAM interlayers. Error bars represent the standard deviation calculated from 20 devices prepared at the same conditions (Supplementary Information)* [141]

A max PCE of 19.03 % was achieved by devices incorporating the C_{60}-SAM passivation layer with PEALD SnO_2 on glass substrates. A similarly high maximum of 16.80 % PCE was reached using the same device architecture on ITO/PET flexible substrates. This study demonstrated the potential of low temperature processing with high efficiency suitable for large-scale manufacturing.

A comparative study was carried out on ALD SnO_2 thin films deposited using various reactants in 2017.[142] The deposition temperature was maintained at 100°C for the growth of ALD SnO_2 films while the tin precursor employed was TDMASn. All films were deposited at a thickness of 20 nm on ITO coated glass and fabricated into planar PSCs. Their J-V characteristics were compared and the maximum values from a sample set of 20 are outlined in Table III.III.

Table III. III: *Device characteristics of cells based on ozone-SnO_2, plasma-SnO_2 and H_2O SnO_2 in forward and reverse directions* [142]

ALD SnO_2 Reactant	*Scan direction*	*J_{sc} (mA cm^{-2})*	*V_{oc} (V)*	*FF (%)*	*η (%)*
O_3	Reverse	20.5	1.186	67	15.3
	Forward	20.3	1.186	68	15.4
O_2 plasma	Reverse	20.5	1.164	63	14.6
	Forward	20.3	1.164	61	13.6
H_2O	Reverse	20.9	1.110	59	12.7
	Forward	20.4	1.100	48	9.8

The best J-V characteristics were achieved using ALD SnO_2 deposited by an O_3 reactant achieving a PCE of 15.3 % and a remarkably high V_{oc} of 1.186. Photoelectron spectroscopy showed the presence of a PbI_2 layer between the ALD SnO_2 and the perovskite layer for all ALD variants. This layer was largest for SnO_2 deposited using TDMASn and H_2O providing a barrier for electron extraction and reducing the obtainable PCE. From these results an ITO-free perovskite device was assembled employing SnO_2/Ag/SnO_2 as the bottom electrode. This semi-transparent ITO-free cell obtained a high PCE of 11 %.

While the ALD process provided the most compact films compared to alternative deposition processes, an issue with hysteresis was observed with ALD SnO_2 in planar perovskite devices.[141, 143] As previously discussed, this was found to be slightly reduced and performance enhance by deposition of a fullerene passivation layer on top of the ETL.[141] To identify the origin of this hysteresis Kelvin Probe Microscopy (KPFM) characterisation and trap density of states (tDOS) measurements were carried out by Wang et al.[144] From this report it was suggested that the hysteresis observed was attributed to an imbalance of charge transportation between the PEALD SnO_2 and the perovskite interface, and the HTL and perovskite interface. The poor electrical conductivity of low temperature PEALD SnO_2 was found to be the source of this charge transport imbalance. To increase electrical conductivity a study on post annealing the PEALD layers at 100°C, 150°C and 200°C was carried out. All thin films were found to remain amorphous by XRD characterisation post annealing. These layers were then fabricated into planar PSCs employing C_{60}-SAM as a passivation layer. The device incorporating PEALD SnO_2 annealed at 100°C performed the best reaching a maximum PCE of an impressive 20.41 % with hysteresis significantly reduced compared to an identical device incorporating an unannealed ETL. This study

outlined the importance of optimising electrical conductivity in ETLs to obtain improved PCEs. Recent work by Lee et al[145] demonstrated that surface passivation of ALD SnO_2 followed by post annealing could reduce interfacial recombination and improve the electrical properties of the thin film. When used in conjunction with an ALD TiO_2 layer improved PCEs reaching 20.03 % were achieved with enhanced ETL hole blocking properties. These thermal ALD SnO_2 thin films were deposited at 100°C using TDMASn and O_3 as the tin precursor and reactant. The film was then post-annealed at 180°C to improve crystallinity. The low temperature ALD SnO_2 film was found to be self-passivating by unreacted TDMASn within the film. This study shows that low temperature ALD deposition followed by post-annealing can enhance PCEs compared to high temperature ALD deposition.

ALD SnO_2 has successfully been employed in *p-i-n* architecture PSCs as part of a bilayered aluminium doped zinc oxide (AZO)/SnO_2 ETL.[146] In this report 20 nm ALD SnO_2 was deposited at the low temperature of 80°C using TDMASn and H_2O as respective precursor and reactant. The average GPC obtained was 1.1 Å/cycle. The SnO_2 was deposited on top of a nanoparticle dispersion spin coated AZO layer. This AZO layer was porous and so the conformal nature of ALD SnO_2 was able to successfully infiltrate the pores. In this study ALD SnO_2 was employed not only as an ETL but more importantly as a moisture barrier layer which also suppressed out-diffusion of decomposition products at elevated temperatures. The decomposition of the perovskite was significantly mitigated even after 41, 000 hours. ALD SnO_2 has also been deposited in conjunction with ALD zinc tin oxide (ZTO) on top of a PCBM/perovskite layer for monolithic perovskite/silicon tandem solar cells (Figure 3.11).[147] Both SnO_2 and ZTO were deposited at 100°C using TDMASn and diethyl zinc (DEZ) as the respective tin and zinc precursors, and deionised H_2O as the reactant. Both pulsed CVD and ALD were successfully tested for the deposition of the SnO_2/ZTO bilayer. This highly transparent bilayer was found to be conformal, uniform and pinhole free on 1cm^2 devices. The final monolithic perovskite/silicon tandem solar device achieved a high PCE of 23.6 % with no hysteresis while the steady state tracking of PCE was stable for over 30 minutes under illumination. This report presented ALD SnO_2/ZTO as a promising method toward achieving industry-standard operational lifetimes due to its thermal and ambient stability.

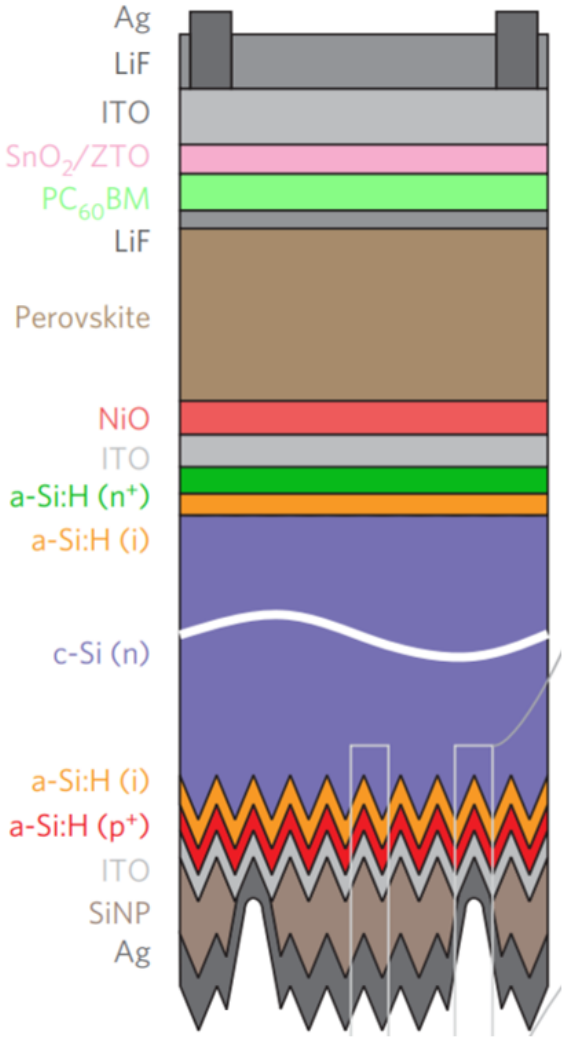

Figure 3. 11: *Schematic of the perovskite/silicon tandem solar cell consisting of a ALD SnO_2/ZTO bilayer*[147]

Recently spatial ALD at atmospheric pressure has been employed for the deposition of SnO_2 in *p-i-n* PSCs.[148] Thin film deposition carried out by this method overcomes the vacuum limitation from classical thermal and plasma enhanced ALD (Figure 3.12). ALD SnO_2 was deposited at various temperatures between 80°C and 150°C using TDMASn and H_2O as the precursor and reactant. The substrate velocity was also varied between 0.3 m min^{-1} and 9.6 m min^{-1}. From this study it was concluded that spatial ALD (S-ALD) could deposit SnO_2 layers in a continuous fashion at the low temperature of 80°C at a web speed of up to 2.4 m min^{-1}. S-ALD was used to deposit 20 nm SnO_2 on top of a AZO/ PCBM/ $CH_3NH_3PbI_3$/ PEDOT:PSS/ ITO coated glass

architecture. An 11.2 % PCE was achieved in the final device matching the performance of an identical cell containing SnO_2 deposited by classical ALD. SnO_2 was found to act as an excellent permeation barrier which limited the ingress of moisture into the photovoltaic device. The 11.2 % PCE achieved showed stable characteristics beyond 1,000 hours in ambient air and over 3,000 hours when held at 60°C in an inert atmosphere. The use of S-ALD shows promise for PSC commercialisation in roll-to-roll manufacturing.

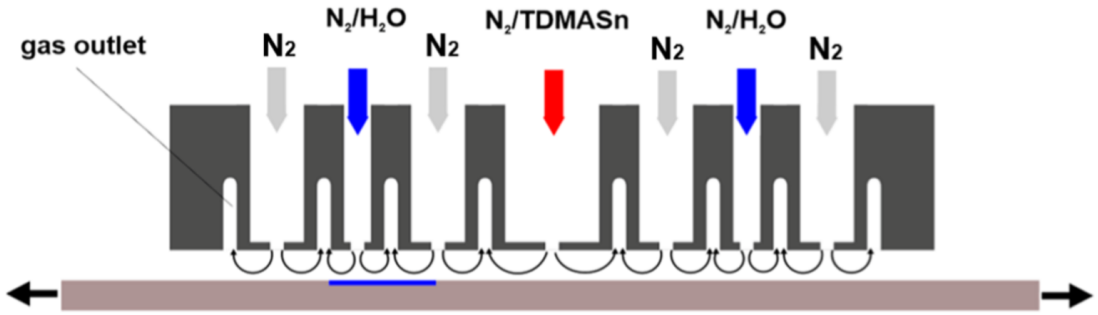

Figure 3. 12: *Schematic of spatial ALD assembly* [148]

A recent report investigated the effect of PEALD SnO_2 deposition temperature when fabricated into planar PSCs.[149] Films were deposited between 50°C and 200°C using TDMASn and RF O_2 plasma as the tin precursor and reactant. The as deposited films were found to be resistive at a deposition temperature of 50°C and electrically conductive when deposited at 200°C. Moreover, UPS indicated a notable 0.69 eV conduction band minimum mismatch at the interface between SnO_2 deposited at 50°C and the perovskite, $Cs_{0.05}(MA_{0.17}FA_{0.83})_{0.95}Pb(I_{2.7}Br_{0.3})$. In contrast, an excellent conduction band minimum alignment was exhibited for the SnO_2 deposited at 200°C and the same perovskite. This finding is displayed below in Figure 3.13.

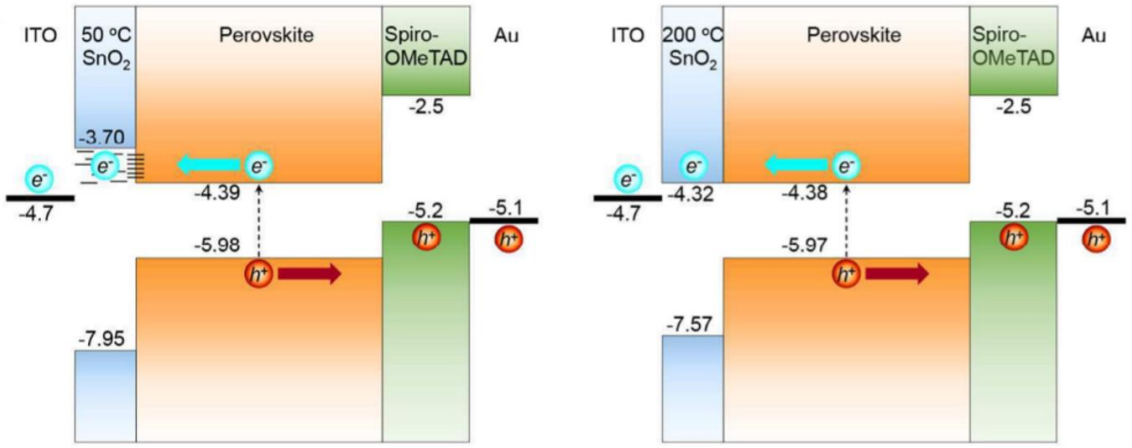

***Figure 3. 13**: Energy levels (in eV) of the applied layers in a $Cs_{0.05}(MA_{0.17}FA_{0.83})_{0.95}Pb(I_{2.7}Br_{0.3})$ perovskite solar cell using PEALD SnO_2 ETLs deposited at 50°C (left) and 200°C (right)* [149]

15 nm of these PEALD SnO_2 thin films were then fabricated into planar PSCs and the J-V characteristics compared. Comparable PCEs of 17.5 % and 17.8 % were demonstrated for cells containing SnO_2 deposited at 50°C and SnO_2 deposited at 200°C respectively. Despite these similar initial performances the device containing SnO_2 deposited at 50°C was shown to dramatically drop in PCE by 50 % over 16 hours with one sun illumination in an inert atmosphere. In contrast the device containing SnO_2 deposited at 200°C retained its initial performance under the same test. By employing PCBM as a passivation layer the decrease in PCE for the device containing SnO_2 deposited at 50°C was significantly reduced under the same 16 hour illumination test. This result could be due to the PCBM layer providing a more favourable band alignment at the ETL/perovskite interface compared to the 0.69 eV conduction band mismatch with SnO_2 deposited at 50°C.

ALD has been well established as a versatile technique for the deposition of inorganic thin films. The self-limiting nature of this process allows continuous, dense and virtually pinhole-free layers to be grown. The low deposition temperatures employed by ALD combined with its unrivalled film conformality have allowed the process to be adopted by the photovoltaics field. Both ALD TiO_2 and ALD SnO_2 have been employed as successful ETLs for PSCs. With further studies on alignment and passivation at the ALD ETL/perovskite interface their performance in perovskite devices can be optimised.

The objective of this thesis is to investigate metal oxide ETLs deposited using the conformal ALD technique for use in both planar and mesoporous perovskite solar devices.

3.7 Bibliography

[1] A. M. Shevjakov, G. N. Kuznetsova, V. B. Aleskovskii, Chemistry of high temperature materials, Proceedings of 2nd USSR conference on high temperature chemistry of oxides, 26-29, Leningrad, USSR (Nauka, Leningrad, USSR, 1967) 149–155, 1965

[2] S. I. Kol'tsov, Production and investigation of reaction products of titanium tetrachloride with silica gel, Zh. Prikl. Khim., J. Appl. Chem. USSR, 42, 1023, 1969

[3] G. V. Sveshnikova, S. I. Kol'tsov, V. B. Aleskovskii, Formation of a silica layer of predetermined thickness on silicon by the molecular layering method, Zh. Prikl. Khim., J. Appl. Chem. USSR., 43, 1150, 1970

[4] G. V. Sveshnikova, S. I. Kol'tsov, V. B. Aleskovskii, Interaction of titanium tetrachloride with hydroxylated silicon surfaces, Zh. Prikl. Khim, J. Appl. Chem. USSR., 43, 432- 434, 1970

[5] S. I. Kol'tsov, V. B. Aleskovskii, A. N. Volkova, V. M. Smirnov, Change in the structure of silica gel in the process of the formation of a layer of phosphorus pentoxide on its surface, Zh. Prikl. Khim, J. Appl. Chem. USSR., 47, 1292-1295, 1974

[6] S. I. Kol'tsov, V. B. Kopylov, V. M. Smirnov, and V. B. Aleskovskii, Synthesis and investigation of aluminum-oxygen layers on the surface of silica, Zh. Prikl. Khim., J. Appl. Chem. USSR., 49, 525-528, 1976

[7] A. P. Nechiporenko, T. M. Sukhareva, A. A. Malygin, S. I. Kol'tsov, V. B. Aleskovskii, Ultramicrochemical investigation of chromium oxide layers synthesized by molecular layering on single-crystal germanium and silicon surfaces, Zh. Prikl. Khim., J. Appl. Chem. USSR., 51 (11), 2333-2337, 1978

[8] S. I. Kol'tsov, T. V. Tuz, and A. N. Volkova, Molecular layering of boron oxide on the surface of silica, Zh. Prikl. Khim., J. Appl. Chem. USSR., 52, 2074-2077, 1979

[9] T. Suntola, J. Antson, Method for producing compound thin films, US Patent 4058430, November 15, 1977

[10] T. Suntola, A. Pakkala, S. Lindors, Apparatus for performing growth of compound thin films, U.S. Patent No. 4,389,973, 1983

[11] S. M. Bedair, M. A. Tischler, T. Katsuyama, N. A. El-Masry, Atomic layer epitaxy of III- V binary compounds, Appl. Phys. Lett., 47, 51, 1985

[12] J. Nishizawa, H. Abe, T. Kurabayashi, Molecular Layer Epitaxy, J. Electrochem. Soc., 132, 5, 1197-1200, 1985

[13] T. Takeda, T. Kurosu, M. Lida, T. Yao, Growth of ZnS/ZnTe and ZnSe/ZnTe superlattices by molecular beam epitaxy and atomic layer epitaxy, Surf. Sci. 174 (1-3), 548 (1986).

[14] M. A. Tischler, S. M. Bedair, Self-limiting mechanism in the atomic layer epitaxy of GaAs, Appl. Phys. Lett, 48 (24), 1681-1683 (1986).

[15] M. Leskel, M. Ritala, Atomic Layer Deposition Chemistry: Recent Developments and Future Challenges, Angew. Chem. Int. Ed., 42, 5548 –5554, 2003

[16] M. Ritala, K. Kukli, A. Rahtu, P. I. Raisanen, M. Leskela, T. Sajavaara, J. Keinonen, Atomic layer deposition of oxide thin films with metal alkoxides as oxygen sources, Science, 288, 319, 2000

[17] R. Puurunen, Growth Per Cycle in Atomic Layer Deposition: A Theoretical Model, Chem. Vap Deposition, 9, 5, 249, 2003

[18] M. Leekelti, L Niinisto, In Atomic Layer Epitaxy; Suntola, T.; Simpeon, M.; Me.; Blackie and Son Ltd.: Glasgow, 1990

[19] M. Ritala, M. Leskela, L. Niinisto, P. Haussalo, Titanium Isopropoxide as a Precursor in Atomic Layer Epitaxy of Titanium Dioxide Thin Films, Chemistry of Materials, 5, 8, 1174-1181, 1993

[20] R. W. Johnson, A. Hultqvist, S. F. Bent, A brief review of atomic layer deposition: from fundamentals to applications, Materials Today, 17, 5, 236-246, 2014

[21] C. Argile, G. E. Rhead, Adsorbed layer and thin film growth modes monitored by Auger electron spectroscopy, Surf. Sci. Rep., 10, 277, 1989

[22] C. H. L. Goodman, M. V. Pessa, Atomic layer epitaxy, J. Appl. Phys., 60, 3, R65-R81, 1986

[23] K. Kukli, T. Pilvi, M. Ritala, T. Sajavaara, J. Lu, M. Leskelä, Atomic layer deposition of hafnium dioxide thin films from hafnium tetrakis(dimethylamide) and water, Thin Solid Films, 491, 328-338, 2005

[24] J. S. M. Lehn, S. Javed, D. M. Hoffman, New precursors for the CVD of zirconium and hafnium oxide films, Chem. Vap. Deposition, 12, 5, 280-284, 2006

[25] E. Langereis, S. B. S. Heil, H. C. M. Knoops, W. Keuning, M. C. M. van de Sanden, W. M. M. Kessels, In situ spectroscopic ellipsometry as a versatile tool for studying atomic layer deposition, J. of Physics D: Applied Physics, 42, 073001, 2009

[26] S. M. George, Atomic Layer Deposition: An Overview, Chemical Reviews, 110, 111-131, 2010

[27] T. O. Kääriäinen, D. C. Cameron, Plasma-assisted atomic layer eposition of Al_2O_3 at room temperature, Plasma Processes and Polymers, 6, 237-241, 2009

[28] T. O. Kääriäinen, S. Lehti, M.-L. Kääriäinen, D. C. Cameron, Surface modification of polymers by plasma-assisted atomic layer deposition, Surf Coatings Techn., 205, 475–479, 2011

[29] T. Suntola, J. Hyviirinen, Atomic Layer Epitaxy, Ann. Rev. Mater. Sci., 15, 177-195, 1985

[30] E.-L. Lakomaa, S. Haukka, T. Suntola, Atomic layer growth of TiO_2 on silica, Applied Surface Science, 60, 742–748, 1992

[31] M. Ritala, M. Leskela, E. Nykanen, P. Soininen, L. Niinisto, Growth of titanium dioxide thin films by atomic layer epitaxy, Thin Solid Films, 225, 288–295, 1993

[32] M. Primet, P. Pichat, M.-V. Mathieu, Infrared study of the surface of titanium dioxides. I. Hydroxyl groups, J. Phys. Chem., 75, 9, 1216-1220, 1971

[33] G. D. Parfitt, The surface of titanium dioxide, Progr. Surf. Membrane Sci., I1, 181-226, 1976

[34] J. B. Kimney, R. H. Staley, Reactions of titanium tetrachloride and trimethylaluminum at silica surfaces studied by using infrared photoacoustic spectroscopy, J. Phys. Chem., 87, 3735-3740, 1983

[35] G. D. Parfitt, J. Ramsbotham, C. H. Rochester, Infra-red study of ammonia adsorption on rutile surfaces, Trans. Faraday Soc., 67, 841-847, 1971

[36] K. Kukli, M. Ritala, M. Schuisky, M. Leskela, T. Sajavaara, J. Keinonen, T. Uustare, A. Harsta, Atomic Layer Deposition of Titanium Oxide from TiI_4 and H_2O_2, Chemical Vapor Deposition, 6, 303–310, 2000

[37] K. Kukli, A. Aidla, J. Aarik, M. Schuisky, A. Harsta, M. Ritala, M. Leskela, Real-Time Monitoring in Atomic Layer Deposition of TiO_2 from TiI_4 and $H_2O{-}H_2O_2$ Langmuir, 16, 8122–8128, 2000

[38] M. Schuisky, A. Harsta, A. Aidla, K. Kukli, A.-A. Kiisler, J. Aarik, Atomic Layer Chemical Vapor Deposition of TiO_2 Low Temperature Epitaxy of Rutile and Anatase, J. Electrochem. Society, 147, 9, 3319–3325, 2000

[39] M. Schuisky, J. Aarik, K. Kukli, A. Aidla, A. Harsta, Atomic Layer Deposition of Thin Films Using O_2 as Oxygen Source, Langmuir, 17, 5508–5512, 2001

[40] J. Aarik, A. Aidla, T. Uustare, K. Kukli, V. Sammelselg, M. Ritala, M. Leskela, Atomic layer deposition of TiO_2 thin films from TiI_4 and H_2O, Applied Surface Science, 193, 277–286, 2002

[41] M. Schuisky, K. Kukli, J. Aarik, J. Lu, A. Harsta, Epitaxial growth of TiO_2 films in a hydroxyl-free atomic layer deposition process, J. Crystal Growth, 235, 293–299, 2002

[42] Z. Hu, C. H. Turner, Atomic Layer Deposition of TiO_2 from TiI_4 and H_2O onto SiO_2 Surfaces: Ab Initio Calculations of the Initial Reaction Mechanisms, J. Am. Chem. Soc., 129, 13, 3863–3878, 2007

[43] V. Pore, A. Rahtu, M. Leskela, M. Ritala, T. Sajavaara, J. Keinonen, Atomic Layer Deposition of Photocatalytic TiO_2 Thin Films from Titanium Tetramethoxide and Water, Chem. Vap. Deposition, 10, 143–148, 2004

[44] A. Niskanen, K. Arstila, M. Leskelä, M. Ritala, Radical Enhanced Atomic Layer Deposition of Titanium Dioxide, Chem. Vap. Deposition, 13, 152-157, 2007

[45] A. P. Alekhin, S. A. Gudkova, A. M. Markeev, A. S. Mitiaev, A. A. Sigarev, V. F. Toknova, Structural properties of the titanium dioxide thin films grown by atomic layer deposition at various numbers of reaction cycles, 257, 1, 186-191, 2010

[46] M. Ritala, M. Leskela, E. Rauhala, Atomic layer epitaxy growth of titanium dioxide thin films from titanium ethoxide, Chemistry of Materials, 6, 556–561, 1994

[47] J. Aarik, A. Aidla, V. Sammelselg, T. Uustare, M. Ritala, M. Leskela, Characterization of titanium dioxide atomic layer growth from titanium ethoxide and water, Thin Solid Films, 370, 163–172, 2000

[48] J. Aarik, J. Karlis, H. Mandar, T. Uustare, V. Sammelselg, Influence of structure development on atomic layer deposition of TiO_2 thin films, Applied Surface Science, 181, 339–348, 2001

[49] A. Rahtu, K. Kukli, M. Ritala, In Situ Mass Spectrometry Study on Atomic Layer Deposition from Metal (Ti, Ta, and Nb) Ethoxides and Water, Chemistry of Materials, 13, 3, 817– 823, 2001

[50] I.-D. Kim, H. L. Tuller, H.-S. Kim, J.-S. Park, High tunability (Ba,Sr)TiO_3 thin films grown on atomic layer deposited TiO_2 and Ta_2O_5 buffer layers, Applied Physics Letters, 85, 4705–4707, 2004

[51] H. Doring, K. Hashimoto, A. Fujishima, TiO_2 Thin Films Prepared by Pulsed Beam Chemical Vapor Deposition from Titanium Tetraisopropoxide and Water, Berichte der Bunsengesellschaft fur Physikalische Chemie, 96, 620–622, 1992

[52] J. Aarik, A. Aidla, T. Uustare, M. Ritala, M. Leskela, Titanium isopropoxide as a precursor for atomic layer deposition: characterization of titanium dioxide growth process, Applied Surface Science, 161, 385–395, 2000

[53] A. Rahtu, M. Ritala, Reaction Mechanism Studies on Titanium Isopropoxide–Water Atomic Layer Deposition Process, Chemical Vapor Deposition, 8, 21–28, 2002

[54] H. Shin, D.-K. Jeong, J. Lee, M. M. Sung, J. Kim, Formation of TiO_2 and ZrO_2 Nanotubes Using Atomic Layer Deposition with Ultraprecise Control of the Wall Thickness, Advanced Materials, 16, 1197–1200, 2004

[55] D. K. Jeong, N. Park, S.-H Jung, W. G. Jung, H. Shin, J. Lee, J. Kim, Fabrication of Oxide/Semiconducting Coaxial Nanotubular Materials Using Atomic Layer Deposition, Materials Science Forum, 449, 1165–1168, 2004

[56] D. K. Jeong, J. Lee, H. Shin, J. Lee, J. Kim, M. Sung, Synthesis of Metal Oxide Nanotubular Structure Using Atomic Layer Deposition on Nanotemplates, J. Korean Phy. Soc., 45, 5, 1249–1252, 2004

[57] J. W. Lim, S. J. Yun, J. H. Lee, Characteristics of TiO_2 Films Prepared by ALD With and Without Plasma, Electrochem. Solid-State Lett., 7, F73–F76, 2004

[58] W. Maeng, H. Kim, Thermal and Plasma-Enhanced ALD of Ta and Ti Oxide Thin Films from Alkylamide Precursors, Electrochem. Solid-State Lett., 9, G191–G194, 2006

[59] R. Pheamhom, C. Sunwoo, D.-H. Kim, Characteristics of atomic layer deposited TiO_2 films and their photocatalytic activity, J. Vacuum Science and Technology A: Vacuum, Surfaces and Films, 24, 1535-1539, 2006

[60] Q. Xie, Y.-L. Jiang, C. Detavernier, D. Deduytsche, R. L. Van Meirhaeghe, G.-P. Ru, B.-Z. Li, X.-P. Qu, Atomic layer deposition of TiO_2 from tetrakis-dimethyl-amido titanium or Ti isopropoxide precursors and H_2O, J. App. Phy., 102, 8, 2007

[61] Q. Xie, J. Musschoot, D. Deduytsche, R. Van Meirhaeghe, C. Detavernier, S. Van Den Berghe, Y.-L. Jiang, G.-P. Ru, B.-Z. Li, X.-P. Qu, Growth Kinetics and Crystallization Behavior of TiO_2 Films Prepared by Plasma Enhanced Atomic Layer Deposition, J. Electrochem. Soc., 155, 9, H688-H692, 2008

[62] A. I. Abdulagatov, Y. Yan, J. R. Cooper, Y. Zhang, Z. M. Gibbs, A. S. Cavanagh, R. G. Yang, Y. C. Lee, S. M. George, Al_2O_3 and TiO_2 Atomic Layer Deposition on Copper for Water Corrosion Resistance, ACS Appl. Mater. Interfaces, 3, 12, 4593-4601, 2011

[63] M. Reiners, K. Xu, N. Aslam, A. Devi, R. Waser, S. Hoffmann-Eifert, Growth and Crystallization of TiO_2 Thin Films by Atomic Layer Deposition Using a Novel Amido Guanidinate Titanium Source and Tetrakis-dimethylamido-titanium, Chem. Mat., 25, 2934–2943, 2013

[64] J. Y. Yun, M. Y. Park, S. W. Rhee, Comparison of Tetrakis(dimethylamido)titanium and Tetrakis(diethylamido)titanium as Precursors for Metallorganic Chemical Vapor Deposition of Titanium Nitride, J. Electrochem. Soc., 146, 5, 1804-1808, 1999

[65] G. Cho, S.-W. Rhee, Effect of the amido Ti precursors on the atomic layer deposition of TiN with NH_3, J. Vac. Sci. Tech. A, 31, 1, 2013

[66] J. S. Ponraj, G. Attolini, M. Bosi, Review on Atomic Layer Deposition and Applications of Oxide Thin Films, Critical Reviews in Solid State and Materials Sciences, 38, 203–233, 2013

[67] A. Sinha, D. W. Hess, C. L. Henderson, Area selective atomic layer deposition of titanium dioxide: Effect of precursor chemistry, J. Vac. Sci. Technol. B 24, 6, 2006

[68] H. Y. Jeong, J. Y. Lee, M.-K. Ryu, S.-Y. Choi, Bipolar resistive switching in amorphous titanium oxide thin film, Phys. Status Solidi RRL 4, 1–2, 28–30, 2010

[69] C. Jin, B. Liu, Z. Lei, J. Sun, Structure and photoluminescence of the TiO_2 films grown by atomic layer deposition using tetrakis-dimethylamino titanium and ozone, Nanoscale Research Letters, 10, 95, 2015

[70] R. G. Gordon, Criteria for Choosing Transparent Conductors, MRS Bull, 25, 8, 52–57, 2000

[71] T. Minami, Transparent conducting oxide semiconductors for transparent electrodes, Semicond. Sci. Technol., 20, 4, S35–S44, 2005

[72] M. Batzill, U. Diebold, The surface and materials science of tin oxide, Progress in Surface Science, 79, 47, 2005

[73] Z. Chen, D. Pan, Z. Li, Z. Jiao, M. Wu, C.-H. Shek, C. M. L. Wu, J. K. L. Lai, Recent Advances in Tin Dioxide Materials: Some Developments in Thin Films, Nanowires, and Nanorods, Chem. Rev., 114, 15, 7442-7486, 2014

[74] S. Das, V. Jayaraman, SnO_2: A comprehensive review on structures and gas sensors, Progress in Materials Science 66, 112-255, 2014

[75] M. N. Rumyantseva, O. V. Safonova, M. N. Boulova, L. I. Ryabova, A. M. Gas'kov, Dopants in nanocrystalline tin dioxide, Rus. Chem. Bull. Int. Ed. 52, 6, 2003

[76] M. M. Arafat, B. Dinan, S. A. Akbar, A. S. M. A. Haseeb, Gas Sensors Based on One Dimensional Nanostructured Metal-Oxides: A Review, Sensors, 12, 6, 2012

[77] G. Choi, L. Satyanarayana, J. Park, Effect of process parameters on surface morphology and characterization of PE-ALD SnO_2 thin films for gas sensing, Appl. Surf. Sci. 252, 22, 2006

[78] D. H. Kim, W.-S.Kim, S. B. Lee, S.-H. Hong, Gas sensing properties in epitaxial SnO_2 films grown on TiO_2 single crystals with various orientations, Sens. Actuators B, 147, 2, 2010

[79] Y. Cheng, P. Xiong, Mechanism and Optimization of pH Sensing Using SnO_2 Nanobelt Field Effect Transistors, Nano Lett., 8, 12, 4179-4184, 2008

[80] P. D. Batista, M. Mulato, C. F. de O. Graeff, F. J. R. Fernandez, F. das C. Marques, SnO_2 extended gate field-effect transistor as pH sensor, Braz. J. Phys., 36, 2a, 478-481, 2006

[81] J.-C. Chou, P.-K. Kwan, Z.-J. Chen, SnO_2 Separative Structure Extended Gate H+-Ion Sensitive Field Effect Transistor by the Sol–Gel Technology and the Readout Circuit Developed by Source Follower, Japanese J. App. Phys., 42, 11, 2003

[82] J. Xu, G. Liu, J. Li, X. Wang, The electrocatalytic properties of an IrO_2/SnO_2 catalyst using SnO_2 as a support and an assisting reagent for the oxygen evolution reaction, Electrochimica Acta, 59, 105-112, 2012

[83] K. Matar, D. Zhao, D. Goldfarb, W. Azelee, W. Daniel, P. G. Harrison, Characterization of Cu(II) Sites in Cu/SnO_2 Catalysts by Electron Spin Echo Envelope Modulation Spectroscopy, J. Phys. Chem., 99, 24, 9966-9973, 1995

[84] N. S. Fallah, M. Mokhtary, Tin oxide nanoparticles (SnO_2-NPs): An efficient catalyst for the one-pot synthesis of highly substituted imidazole derivatives, J. Taibah University for Science, 9, 4, 531-537, 2015

[85] T. Isono, T. Fukuda, K. Nakagawa, R. Usui, R. Satoh, E. Morinaga, Y. Mihara, Highly conductive SnO_2 thin films for flat- panel displays, J. Society for Information Display, 15, 161-166, 2007

[86] T.-T. Duong, H.-J. Choi, Q.-J. He, A.-T. Le, S.-G. Yoon, Enhancing the efficiency of dye sensitized solar cells with an SnO_2 blocking layer grown by nanocluster deposition, J. Alloys and Compounds, 561, 5, 206-210, 2013

[87] A. Birkel, Y.-G. Lee, D. Koll, X. Van Meerbeek, S. Frank, M. J. Choi, Y. S. Kang, K. Char, W. Tremel, Highly efficient and stable dye-sensitized solar cells based on SnO_2 nanocrystals prepared by microwave-assisted synthesis, Energy Environ. Sci.,5, 5392-5400, 2012

[88] Y. Duan, J. Zheng, N. Fu, Y. Fang, T. Liu, Q. Zhang, X. Zhou, Y. Lin, F. Pan, Enhancing the performance of dye-sensitized solar cells: doping SnO_2 photoanodes with Al to simultaneously improve conduction band and electron lifetime, J. Mater. Chem. A,3, 3066-3073, 2015

[89] X. Mao, R. Zhou, S. Zhang, L. Ding, L. Wan, S. Qin, Z. Chen, J. Xu, S. Miao, High Efficiency Dye-sensitized Solar Cells Constructed with Composites of TiO_2 and the Hot-bubbling Synthesized Ultra-Small SnO_2 Nanocrystals, Scientific Reports, 6, 19390, 2016

[90] A. N. M. Green, E. Palomares, S. A. Haque, J. M. Kroon, J. R. Durrant, Charge Transport versus Recombination in Dye-Sensitized Solar Cells Employing Nanocrystalline TiO2 and SnO2 Films, J. Phys. Chem. B, 109, 25, 2005

[91] A. Kay and M. Grätzel, Dye-Sensitized Core−Shell Nanocrystals: Improved Efficiency of Mesoporous Tin Oxide Electrodes Coated with a Thin Layer of an Insulating Oxide Chem. Mater., 14, 7, 2002

[92] Z. Zhu, Y. Bai, X. Liu, C.-C. Chueh, S. Yang, A. K. Y. Jen, Enhanced Efficiency and Stability of Inverted Perovskite Solar Cells Using Highly Crystalline SnO_2 Nanocrystals as the Robust Electron- Transporting Layer, Adv. Mater., 28, 6478-6484, 2016

[93] Q. Dong, Y. Shi, K. Wang, Y. Li, S. Wang, H. Zhang, Y. Xing, Y. Du, X. Bai, T. Ma, Insight into Perovskite Solar Cells Based on SnO_2 Compact Electron-Selective Layer, J. Phys. Chem. C, 119, 19, 10212–10217, 2015

[94] W. Ke, G. Fang, Q. Liu, L. Xiong, P. Qin, H. Tao, J. Wang, H. Lei, B. Li, J. Wan, G. Yang, Y. Yan, Low-Temperature Solution-Processed Tin Oxide as an Alternative Electron Transporting Layer for Efficient Perovskite Solar Cells, J. Am. Chem. Soc., 137, 21, 6730–6733, 2015

[95] H.-S. Rao, B.-X. Chen, W.-G. Li, Y.-F. Xu, H.-Y. Chen, D.-B. Kuang, C.-Y. Su, Improving the Extraction of Photogenerated Electrons with SnO_2 Nanocolloids for Efficient Planar Perovskite Solar Cells, Adv. Funct. Mater., 25, 7200-7207, 2015

[96] M. Park, J.-Y. Kim, H. J. Son, C.-H. Lee, S. S. Jang, M. J. Ko, Low-temperature solution-processed Li-doped SnO_2 as an effective electron transporting layer for high-performance flexible and wearable perovskite solar cells, Nano Energy, 26, 208-215, 2016

[97] J. Dagar, S. Castro-Hermosa, G. Lucarelli, F. Cacialli, T. M. Brown, Highly efficient perovskite solar cells for light harvesting under indoor illumination via solution processed SnO2/MgO composite electron transport layers, Nano Energy, 49, 290, 2018

[98] J. Song, E. Zheng, J. Bian, X.-F. Wang, W. Tian, Y. Sanehira, T. Miyasaka, Low-temperature SnO_2-based electron selective contact for efficient and stable perovskite solar cells, J. Mater. Chem. A, 3, 10837, 2015

[99] X. Qin, Z. Zhao, Y. Wang, J. Wu, Q. Jiang, J. You, Recent progress in stability of perovskite solar cells, J. Semicond., 38, 011002, 2017

[100] J.-P. Correa Baena, L. Steier, W. Tress, M. Saliba, S. Neutzner,T. Matsui, F. Giordano, T. J. Jacobsson, A. R. S. Kandada, S. M. Zakeeruddin, A. Petrozza, A. Abate, M. K. Nazeeruddin, M. Grätzel, A. Hagfeldt, Highly efficient planar perovskite solar cells through band alignment engineering, Energy Environ. Sci., 8, 2928, 2015

[101] H. Viirola, L. Niinistö, Controlled growth of tin dioxide thin films by atomic layer epitaxy, Thin Solid Films, 249, 2, 1994

[102] M. Utriainen, K. Kovács, J. M. Campbell, L. Niinistö, F. Réti, Controlled Electrical Conductivity in SnO_2 Thin Films by Oxygen or Hydrocarbon Assisted Atomic Layer Epitaxy, J. Electrochem. Soc., 146, 1, 189-193, 1999

[103] A Tarre, A Rosental, V Sammelselg, T Uustare, Comparative study of low-temperature chloride atomic-layer chemical vapor deposition of TiO_2 and SnO_2, App. Surf. Sci., 175–176, 111-116, 2001

[104] A Rosental, A Tarre, A Gerst, T Uustare, V Sammelselg, Atomic-layer chemical vapor deposition of SnO_2 for gas-sensing applications, Sens. and Actuators B: Chemical, 77, 1–2, 297-300, 2001

[105] X. Du, Y. Du, S. M. George, In situ examination of tin oxide atomic layer deposition using quartz crystal microbalance and Fourier transform infrared techniques, J. Vac. Sci. Technol. A, 23, 581, 2005

[106] X. Du, S. M. George, Thickness dependence of sensor response for CO gas sensing by tin oxide films grown using atomic layer deposition, Sens. Actuators B, 135, 152, 2008

[107] J. Sundqvist, A. Tarre, A. Rosental, A. Hårsta, Atomic Layer Deposition of Epitaxial and Polycrystalline SnO_2 Films from the SnI_4/O_2 Precursor Combination, Chem. Vap. Deposition, 9, 21, 2003

[108] A. Tarre, A. Rosental, J. Sundqvist, A. Hårsta, T. Uustare, V. Sammelselg, Nanoepitaxy of SnO_2 on α-Al_2O_3(0 1 2), Surf. Sci., 514, 532, 2003

[109] R. L. Puurunen, Surface chemistry of atomic layer deposition: A case study for the trimethylaluminum/water process, Chem. Vap. Deposition 11, 79, 2005.

[110] J. W. Elam, D. A. Baker, A. J. Hryn, A. B. F. Martinson, M. J. Pellin, J. T. Hupp, Atomic layer deposition of tin oxide films using tetrakis(dimethylamino) tin, J. Vac. Sci. Technol. A, 26, 244, 2008

[111] D.-W. Choi, W. J. Maeng, J.-S. Park, The conducting tin oxide thin films deposited via atomic layer deposition using Tetrakis-dimethylamino tin and peroxide for transparent flexible electronics, Appl. Surf. Sci., 313, 585, 2014

[112] M. N. Mullings, C. Hägglund, S. F. Bent, Tin oxide atomic layer deposition from tetrakis(dimethylamino)tin and water, J. Vac. Sci. Technol. A, 31, 061503, 2013

[113] J. T. Tanskanen, S. F. Bent, Insights into the Surface Chemistry of Tin Oxide Atomic Layer Deposition from Quantum Chemical Calculations, J. Phys. Chem. C, 117, 37, 19056–19062, 2013

[114] J. T.-W. Wang, J. M. Ball, E. M. Barea, A. Abate, J. A. Alexander-Webber, J. Huang, M. Saliba, I. Mora-Sero, J. Bisquert, H. J. Snaith, R. J. Nicholas, Low-Temperature Processed Electron Collection Layers of Graphene/TiO_2 Nanocomposites in Thin Film Perovskite Solar Cells, Nano Lett., 14, 2, 724-730, 2014

[115] K. Cao, Z. Zuo, J. Cui, Y. Shen, T. Moehl, S. M. Zakeeruddin, M. Grätzel, M. Wang, Efficient screen printed perovskite solar cells based on mesoscopic TiO_2/Al_2O_3/NiO/carbon architecture, Nano Energy, 17, 171-179, 2015

[116] D. Liu, S. Li, P. Zhang, Y. Wang, R. Zhang, H. Sarvari, F. Wang, J. Wu, Z. Wang, Z. D. Chen, Efficient planar heterojunction perovskite solar cells with Li-doped compact TiO_2 layer, Nano Energy, 31, 462-468, 2017

[117] J.- Y. Seo, R. Uchida, H.- S. Kim, Y. Saygili, J. Luo, C. Moore, J. Kerrod, A. Wagstaff, M. Eklund, R. McIntyre, N. Pellet, S. M. Zakeeruddin, A. Hagfeldt, M. Grätzel, Boosting the Efficiency of Perovskite Solar Cells with CsBr- Modified Mesoporous TiO_2 Beads as Electron- Selective Contact, Adv. Funct. Mater., 28, 1705763, 2018

[118] X. Ren, D. Yang, Z. Yang, J. Feng, X. Zhu, J. Niu, Y. Liu, W. Zhao, S. F. Liu, Solution-Processed Nb:SnO_2 Electron Transport Layer for Efficient Planar Perovskite Solar Cells, ACS App. Mat. & Int., 9, 3, 2421-2429, 2017

[119] G. Yang, C. Chen, F. Yao, Z. Chen, Q. Zhang, X. Zheng, J. Ma, H. Lei, P. Qin, L. Xiong, W. Ke, G. Li, Y. Yan, G. Fang, Effective Carrier Concentration Tuning of SnO_2 Quantum Dot Electron Selective Layers for High Performance Planar Perovskite Solar Cells, Adv. Mater., 30, 1706023, 2018

[120] M. H. Kumar, N. Yantara, S. Dharani, M. Graetzel, S. Mhaisalkar, P. P. Boix, N. Mathews, Flexible, low-temperature, solution processed ZnO-based perovskite solid state solar cells, Chem. Commun., 49, 11089-11091, 2013

[121] D. Liu, T. L. Kelly, Perovskite solar cells with a planar heterojunction structure prepared using room-temperature solution processing techniques, Nature Photonics 8, 133–138, 2014

[122] J. You, L. Meng, T.-B. Song, T.-F. Guo, Y. Yang, W.-H. Chang, Z. Hong, H. Chen, H. Zhou, Q. Chen, Y. Liu, N. De Marco, Y. Yang, Improved air stability of perovskite solar cells via solution-processed metal oxide transport layers, Nature Nanotechnology, 11, 75–81, 2016

[123] J. Cao, B. H. Wu, R. H. Chen, Y. Y. Q. Wu, Y. Hui, B.-W. Mao, N. F. Zheng, Efficient, Hysteresis-Free, and Stable Perovskite Solar Cells with ZnO as Electron Transport Layer: Effect of Surface Passivation, Adv. Mater., 30, 1705596, 2018

[124] S. S. Shin, W. S. Yang, J. H. Noh, J. H. Suk, N. J. Jeon, J. H. Park, J. S. Kim, W. M. Seong, S. I. Seok, High-performance flexible perovskite solar cells exploiting Zn_2SnO_4 prepared in solution below 100 °C, Nat. Commun., 6, 7140, 2015

[125] S. S. Shin, W.-S. Yang, E. J. Yeom, S. J. Lee, N. J. Jeon, Y.-C. Joo, J. H. Noh, S. I. Seok, I. J. Park, Tailoring of Electron-Collecting Oxide Nanoparticulate Layer for Flexible Perovskite Solar Cells, J. Phys. Chem. Lett., 7, 1845, 2016

[126] W. S. Yang, J. H. Noh, N. J. Jeon, Y. C. Kim, S. Ryu, J. Seo, S. I. Seok, High performance photovoltaic perovskite layers fabricated through intramolecular exchange, Science, 348, 1234-1237, 2015

[127] D. Bi, C. Yi, J. Luo, J.-D. Décoppet, F. Zhang, S. M. Zakeeruddin, X. Li, A. Hagfeldt, M. Grätzel, Polymer-templated nucleation and crystal growth of perovskite films for solar cells with efficiency greater than 21%, Nat. Energy, 1, 16142, 2016

[128] J. Kim, J. S. Yun, X. Wen, A. M. Soufiani, C.-F. J. Lau, B. Wilkinson, J. Seidel, M. A. Green, S. Huang, A. W.-Y. Ho-Baillie, Nucleation and growth control of $HC(NH_2)_2PbI_3$ for planar perovskite solar cell, J. Phys. Chem. C, 120, 11262, 2016

[129] X. Li, J. Yang, Q. Jiang, W. Chu, D. Zhang, Z. Zhou, J. Xin, Synergistic Effect to High-Performance Perovskite Solar Cells with Reduced Hysteresis and Improved Stability by the Introduction of Na-Treated TiO_2 and Spraying-Deposited CuI as Transport Layers, ACS App. Mat. & Int., 9, 47, 41354-41362, 2017

[130] H. Krýsová, J. Krýsa, L. Kavan, Semi-automatic spray pyrolysis deposition of thin, transparent, titania films as blocking layers for dye-sensitized and perovskite solar cells, Beilstein J Nanotechnol, 9, 1135-1145, 2018

[131] Y. Wu, X. Yang, H. Chen, K. Zhang, C. Qin, J. Liu, W. Peng, A. Islam, E. Bi, F. Ye, M. Yin, P. Zhang, L. Han, Highly compact TiO_2 layer for efficient hole-blocking in perovskite solar cells, Appl. Phys. Express, 7, 052301, 2014

[132] F. Hao, C. C. Stoumpos, D. H. Cao, R. P. H. Chang, M. G. Kanatzidis, Lead-free solid-state organic–inorganic halide perovskite solar cells, Nature Photonics, 8, 489–494, 2014

[133] A. K. Chandiran, A. Yella, M. T. Mayer, P. Gao, M. K. Nazeeruddin, M. Grätzel, Sub-Nanometer Conformal TiO_2 Blocking Layer for High Efficiency Solid-State Perovskite Absorber Solar Cells, Adv. Mat., 26, 25, 2014

[134] F. Di Giacomo, V. Zardetto, A. D'Epifanio, S. Pescetelli, F. Matteocci, S. Razza, A. Di Carlo, S. Licoccia, W. M. M. Kessels, M. Creatore, T. M. Brown, Flexible Perovskite Photovoltaic Modules and Solar Cells Based on Atomic Layer Deposited Compact Layers and UV- Irradiated TiO_2 Scaffolds on Plastic Substrates, Adv. Energy Mat., 5, 8, 2015

[135] H. B. Profijt, S. E. Potts , M. C. M. van de Sanden , W. M. M. Kessels , Plasma-assisted atomic layer deposition: basics, opportunities and challenges, J. Vacuum Sci. Technol. A., 29 , 050801, 2011

[136] F. Di Giacomo, V. Zardetto, G. Lucarelli, L. Cin`a, A. Di Carlo, M. Creatore, T. M. Brown, Mesoporous perovskite solar cells and the role of nanoscale compact layers for remarkable all-round high efficiency under both indoor and outdoor illumination, Nano Energy, 30, 460–469, 2016

[137] V. Zardetto, F. Di Giacomo, G. Lucarelli, W. M. M. Kessels, T.M. Brown, M. Creatore, Plasma-assisted atomic layer deposition of TiO_2 compact layers for flexible mesostructured perovskite solar cells, Solar Energy, 150, 447–453, 2017

[138] A. E. Shalan, S. Narra, T. Oshikiri, K. Ueno, X. Shi, H.-P. Wu, M. M. Elshanawany, E. W.-G. Diau, H. Misawa, Optimization of a compact layer of TiO2via atomic-layer deposition for high-performance perovskite solar cells, Sustainable Energy Fuels, 1, 1533, 2017

[139] B. J. Kim, D. H. Kim, Y.-Y. Lee, H.-W. Shin, G. S. Han, J. S. Hong, K. Mahmood, T. Ahn, Y.-C. Joo, K. S. Hong, N.-G. Park, S. Lee and H. S. Jung, Highly Efficient and Bending Durable Perovskite Solar Cells: Toward Wearable Power Source Energy Environ. Sci., 8, 916–921, 2015

[140] V. Zardetto, F. di Giacomo, H. Lifka, M. A. Verheijen, C. H. L. Weijtens, L. E. Black, S. Veenstra, W. M. M. Kessels, R. Andriessen, M, Creatore, Surface Fluorination of ALD TiO_2 Electron Transport Layer for Efficient Planar Perovskite Solar Cells, Adv. Mater. Interfaces, 5, 1701456, 2018

[141] C. Wang, D. Zhao, C. Grice, W. Liao, Y. Yu, A. Cimaroli, N. Shrestha, P. J. Roland, J. Chen, Z. Yu, P. Liu, N. Cheng, R. Ellingson, X. Zhao and Y. Yan, Low-temperature plasma-enhanced atomic layer deposition of tin oxide electron selective layers for highly efficient planar perovskite solar cells, J. Mater. Chem. A, 4, 12080–12087, 2016

[142] T. Hu, T. Becker, N. Pourdavoud, J. Zhao, K. O. Brinkmann, R. Heiderhoff, T. Gahlmann, Z. Huang, S. Olthof, K. Meerholz, D. Többens, B. Cheng, Y. Chen, T.

Riedl, Indium-Free Perovskite Solar Cells Enabled by Impermeable Tin-Oxide Electron, Extraction Layers, Adv. Mater., 29, 1606656, 2017

[143] E. H. Anaraki, A. Kermanpur, L. Steier, K. Domanski, T. Matsui, W. Tress, M. Saliba, A. Abate, M. Gratzel, A. Hagfeldt, J.-P. Correa-Baena, Highly efficient and stable planar perovskite solar cells by solution-processed tin oxide, Energy Environ. Sci., 9, 3128, 2016

[144] C. Wang, C. Xiao, Y. Yu, D. Zhao, R. A. Awni, C. R. Grice, K. Ghimire, D. Constantinou, W. Liao, A. J. Cimaroli, P. Liu, J. Chen, N. J. Podraza, C.-S. Jiang, M. M. Al-Jassim, X. Zhao, Y. Yan, Understanding and Eliminating Hysteresis for Highly Efficient Planar Perovskite Solar Cells, Adv. Energy Mater., 7, 1700414, 2017

[145] Y. Lee, S. Lee, G. Seo, S. Paek, K. T. Cho, A. J. Huckaba, M. Calizzi, D. Choi, J. S. Park, D. Lee, H. J. Lee, A. M. Asiri, M.K. Nazeeruddin, Efficient Planar Perovskite Solar Cells Using Passivated Tin Oxide as an Electron Transport Layer, Adv. Sci., 1800130, 2018

[146] K. O. Brinkmann, J. Zhao, N. Pourdavoud, T. Becker, T. Hu, S. Olthof, K. Meerholz, L. Hoffmann, T. Gahlmann, R. Heiderhoff, M. F. Oszajca, N. A. Luechinger, D. Rogalla, Y. Chen, B. Cheng, T. Riedl, Suppressed Decomposition of Organometal Halide Perovskites by Impermeable Electron-extraction Layers in Inverted Solar Cells, Nat. Commun., 8, 13938, 2017

[147] K. A. Bush, A. F. Palmstrom, Z. J. Yu, M. Boccard, R. Cheacharoen, J. P. Mailoa, D. P. Mcmeekin, R. L. Z. Hoye, C. D. Bailie, T. Leijtens, I. M. Peters, M. C. Minichetti, N. Rolston, R. Prasanna, S. Sofia, D. Harwood, W. Ma, F. Moghadam, H. J. Snaith, T. Buonassisi, Z. C. Holman, S. F. Bent, M. D. Mcgehee, 23.6% Efficient Monolithic Perovskite/Silicon Tandem Solar Cells with Improved Stability, Nat. Energy, 2, 17009, 2017

[148] L. Hoffmann, K. O. Brinkmann, J. Malerczyk, D. Rogalla, T. Becker, D. Theirich, I. Shutsko, P. Görrn, T. Riedl, Spatial Atmospheric Pressure Atomic Layer Deposition of Tin Oxide as an Impermeable Electron Extraction Layer for Perovskite Solar Cells with Enhanced Thermal Stability, ACS Appl. Mater. Int., 10, 6006-6013, 2018

[149] Y. Kuang, V. Zardetto, R. van Gils, S. Karwal, D. Koushik, M. A. Verheijen, L. E. Black, C. Weijtens, S. Veenstra, R. Andriessen, W. M.M. Kessels, M. Creatore, Low-Temperature Plasma-Assisted ALD SnO_2 as Electron Transport Layer in Planar Perovskite Solar Cells, ACS Appl. Mater. Int., 10, 36, 30367-30378, 2018

CHAPTER 4:

Investigation into effects of FTO electrodes and TiO_2 BLs in mesoporous PSCs

4.1 Introduction

The majority of literature published on the subject of PSCs concentrates on the perovskite layer itself, with studies on its deposition,[1–3] composition, structure,[4] stability,[5] and how they affect cell characteristics.[6,7] However, there is much less discussion on the influence of other layers. In this chapter, the effects of F-doped SnO_2 (FTO) electrodes and TiO_2 blocking layers (BLs) are investigated in a mesoporous perovskite solar device through collaborations with the University of Salford, CSEM and EPFL.[8]

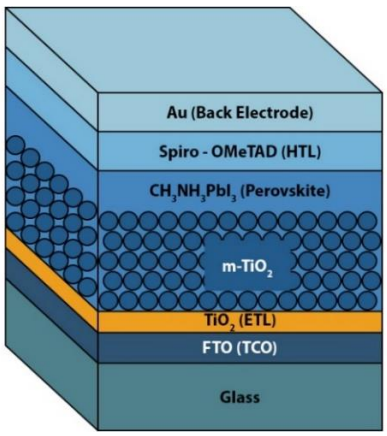

Figure 4. 1: *Schematic illustration of a mesoporous perovskite solar device*

The mesoscopic form of a PSC as depicted in Figure 4.1 shows the metal halide perovskite absorber permeating a charge-conducting mesoporous scaffold, often TiO_2. The photogenerated electrons from the perovskite layer are transferred to the

mesoporous sensitised layer through which they are transported to the electrode and extracted into the circuit. This active perovskite layer is contacted with an n-type material for electron extraction (ETL) and a p-type material for hole extraction (HTL). The ETL layer also acts as a BL to block recombination between the electrons in the front electrode and the holes in the perovskite. Usually a transparent conducting oxide (TCO), often F-doped tin oxide or indium tin oxide, is used for the front electrode contact and gold is used for the back contact.

A good BL not only blocks recombination between the TCO electrons and perovskite holes, but also needs to provide efficient electron extraction from the perovskite to TCO. A thicker BL decreases the charge recombination between the perovskite holes and TCO electrons, but also reduces the electron flow to the TCO due to a higher series resistance in the cell. Thus a balance of conditions is required. A detailed study by Choi et al.[9] investigated the deposition methods and resulting properties of BLs in the production of planar solar cells, emphasising the importance of well-defined, defect free morphologies and uniform thickness. Most cells reported use TiO_2, although alternatives materials have been tested such as SnO_2,[10] composite graphene/TiO_2[11] and ZnO.[12]

The role of TCO characteristics has had very limited discussion, with researchers commonly using a commercially supplied standard material. The most utilised TCO is FTO such as TEC-7, TEC-8 (NSG), or TCO22-15 (Solaronix). Previous work by the University of Salford[13] concentrated on FTOs optimised for use in thin film silicon (Si) PV cells, which require high optical transparency, low resistivity and high surface roughness. High surface roughness is critical to increase internal light trapping and improve the efficiency of light use by the absorbing layers because Si (especially a-Si) has a low absorption efficiency. In the case of perovskite solar devices, high optical transparency and low resistivity are considerations, but as the perovskite absorber already has excellent absorption coefficients[14] the main goal is to achieve a suitable uniform surface to enable good adhesion and no pinholes through the BL and hence direct perovskite contact. The FTO morphology directs that of the BL and hence that of the perovskite, so it is an important factor affecting cell efficiency. Too rough a surface tends to lead to FTO spikes or pinholes in the perovskite and hence fast electron/hole recombination. A non-uniform, rough surface can also lead to lower adhesion between the various layers, resulting in poorer films and much lower cell

efficiencies. Another important factor is the wettability of the TiO_{2-x} surface to the perovskite precursor solution, and hence the solid surface coverage and crystallinity of the perovskite. A rougher TiO_{2-x} surface has previously been shown to result in increased wettability and hence a lower energy barrier to heterogeneous nucleation on the liquid/solid interface.[15] An improvement in the perovskite layer (coverage, adhesion and crystallinity) in turn leads to improved cell properties. Hence, it may be advantageous to start with a relatively rough TCO surface which can lead to the formation of a similar BL morphology.

In this chapter a collaborative study on cell performance and how it relates to the deposition methods was made for the FTO electrode and the TiO_{2-x} blocking layer. FTO was grown by atmospheric pressure chemical vapour deposition (APCVD) at the University of Salford and compared to commercially available FTO (Solaronix TCO22-15). This was carried out to establish if the TCO could be improved upon and optimised in terms of optical transparency, resistivity and morphology compared to what was accessible on the market. Bocking layers were deposited by ALD at Tyndall National Institute and RF sputtering or spin coating at CSEM. In addition, some changes to the perovskite precursor composition were considered by CSEM, and their effects on the overall properties of the PV cell were investigated. The optimised layers from each group were combined and fabricated into mesoporous PSCs leading to improved cell efficiencies.

For FTO films, the effects of roughness, dopant level and resistivity on cell characteristics were considered. The combination of FTO properties required to give low resistivity, high optical transparency and uniform surfaces were found to improve cell efficiency. The effects of different deposition methods for BL films, namely ALD, spin coating and sputter coating, were studied to show the importance of technique chosen, layer thickness and the production of dense, pinhole free, conformal films. In addition, optimisation of the spin coating method for the perovskite layer via precursor/solvent changes was also considered.

4.2 Experimental

4.2.1 CVD FTO

Thin films were deposited by APCVD at a deposition temperature of 600°C using monobutyl tin trichloride (MBTC) with 0.2, 0.6 or 1.0 M aqueous trifluoroacetic acid (TFAA), delivered with a Sn precursor to H_2O molar ratio of 1:5 or 1:30. Precursors were vapourised using either a bubbler (MBTC at 125°C, 0.7 L min^{-1} carrier gas) or flash evaporation (TFAA/water mix, 0.6 L min^{-1} carrier gas). N_2 was used as the carrier gas. The process flow was set to 7 L min^{-1} with oxygen (1.5 L min^{-1}) giving a total flow of ~9.8 L min^{-1}. Deposition was on 1 mm thick borosilicate (Corning Eagle 2000) glass. The heated substrate is translated, on an automated stage, beneath a static, non-contact CVD head (i.e. gas distributor) in an extracted, open atmosphere, enclosure.[16] This allows the deposition of extended area films with high uniformity over 100 mm width (± 2%) and the length is only limited by the translation table size. For these experiments, samples of 100 mm x 100 mm were provided for cell fabrication. The film thickness was varied by changing the number of passes under the coating head. For each type of deposition parameter several samples were prepared. This then enabled the fabrication of a greater number of cells and hence increased confidence in the resulting data.

4.2.2 TiO_{2-x} blocking layers

Spin coated blocking layers of 10 to 15 nm were prepared by using a precursor solution of 0.15 M titanium diisopropoxide bis(acetylacetonate) (Sigma-Aldrich, 75 wt% in isopropanol) in 1-butanol (Sigma-Aldrich, 99.8%). The precursor solution was spin-coated on a FTO glass substrate at 1000 rpm for 10 seconds and then 2000 rpm for 20 seconds. This was followed by sintering at 450°C for 30 minutes.

Thin films of TiO_{2-x} of 23 nm in thickness were deposited by RF sputtering at 60°C on FTO coated glass substrates. These substrates were first patterned with 0.6 mm kapton tape prior to deposition as described in Appendix I, Figure 1. The stoichiometry of the thin films could be controlled by adjusting the Ar and Ar:O_2 flows in the sputtering chamber. Thus the electrical conductivity and transparency of the TiO_{2-x} films could be tuned in order to achieve optimal optoelectronic properties in the solar cells.

Nominally undoped TiO_2 thin films of a range of thicknesses (10 nm, 20 nm, 30 nm) were deposited on kapton tape patterned FTO coated glass by employing a Cambridge Nanotech Fiji ALD system. The titanium precursor and reactant used for these depositions were tetrakis dimethylamido titanium (TDMAT) and H_2O respectively. The precursor vessel for TDMAT was maintained at 75°C while the H_2O vessel was not directly heated but maintained at 35°C due to its proximity to nearby heated components on the system. Adequate vapour pressures to give saturated coverage were achieved at these precursor temperatures. The deposition temperature employed was 200°C. The nominal growth rate of TiO_2 was assumed to be 0.05 nm per cycle on FTO coated glass. An example pulse/purge sequence for a nominally undoped 20 nm thin film is outlined in Table IV.I.

Table IV. I: Experimental parameters for deposition of thermal 20 nm TiO_2 ALD by Cambridge Nanotech Fiji

Step	*Instruction*	*Number*	*Value*	*Unit*	*Description*
0	Flow	0	40	sccm	Ar carrier gas in lines ON
1	Flow	1	180	sccm	Ar carrier dilution in reactor ON
2	Wait		20	s	Stabilisation
3	Pulse	1	0.3	s	TDMAT pulse
4	Wait		10	s	Purge
5	Pulse	0	0.1	s	H_2O pulse
6	Wait		10	s	Purge
7	Goto	3	400	-	Number of cycles
8	Flow	0	20	sccm	Ar carrier gas in lines OFF
9	Flow	1	20	sccm	Ar carrier dilution in reactor OFF

In steps (0) and (1), the precursor manifold carrier flow and plasma source purge flow rates are set to values in standard cubic centimetres per minute (sccm) at atmospheric pressure and temperature. Step (2) involves waiting a total of 20 seconds for the Ar flow rates to stabilize. At (3) the loop begins as the precursor, TDMAT, is pulsed for 0.3 seconds. A wait of 10 seconds in (4) allows for a purge of the TDMAT and reaction by-products. At step (5) the reactant, H_2O, is introduced and pulsed for 0.1 seconds. A waiting period of 10 seconds in step (6) allows for a purge of any remaining H_2O

and by-products. Step (7) stands for “go to” next cycle, where the recipe returns to step 3 and repeats for a total of 400 cycles. In step (8) and (9) the precursor manifold carrier and plasma source purge flow rates are set to stand-by conditions in sccm.

Table IV. II: *Cambridge Nanotech Fiji system temperatures*

Cambridge Fiji Nanotech	*Temperature (°C)*
Reactor	200
Substrate heater	200
Trap	200
Precursor inlet line	105
TDMAT precursor	75

4.2.3 Cell Fabrication

Following the deposition of TiO_{2-x} blocking layers on FTO coated glass substrates, the remainder of the stack was fabricated into devices by collaborators at CSEM and EPFL. The mesoporous TiO_2 (m-TiO_2) layer was deposited on top of the TiO_{2-x} blocking layers/FTO coated substrates outside of the glovebox by spin coating TiO_2 paste (Dyesol 18NRT) diluted in isopropanol (1 g in 10 ml) at 2000 rpm for 30 seconds before annealing at 500°C for 30 minutes. This sintering step at 500°C was found to affect the underlying ALD TiO_2 layer by increasing resistivity as discussed later in section 6.3.3.2.

Three different perovskite recipes were used for the optimisation of the perovskite layer. The same $CH_3NH_3PbI_3$ ($MAPbI_3$) precursor solution was used for recipes one and two but the amount of solvent quenching toluene was increased from 60 µl to 1 ml in recipe two. 1.2 M PbI_2 (TCI) and CH_3NH_3I (Dyesol) were dissolved in a mixture of γ-butyrolactone (GBL) and dimethyl sulfoxide (DMSO) (7:3 volume ratios) at 70°C. A $MAPbI_3$ precursor solution was then spin coated on the m-TiO_2 substrate at 1000 rpm and 5000 rpm for 10 seconds and 30 seconds, respectively outside of the glovebox. During the second step of spin coating, toluene was dripped on to the substrate and the perovskite layer was dried at 100°C for 10 minutes. In recipe three,

461 mg of PbI_2, 159 mg of CH_3NH_3I, and 78 mg of DMSO (molar ratio 1:1:1) were mixed in 600 mg of dimethylformamide (DMF) at room temperature and stirred for 1 hour in a N_2 glovebox in order to prepare the $CH_3NH_3PbI_3$ precursor solution. The precursor solution was then spin coated outside of the glovebox on to the m-TiO_2 substrate in a two-stage sequence (1000 rpm for 10 seconds followed by 5000 rpm for 45 seconds) and 0.75 ml of diethyl ether was employed as a solvent quenching technique 12 seconds before the end of the procedure. The substrate was then heated at 50°C for 2 minutes and 100°C for 10 minutes.[17]

For the hole transport layer, Spiro-OMeTAD solution was prepared by dissolving 72.3 mg spiro-OMeTAD (Merck), 28.8 µl 4-tert-butylpyridine (Sigma-Aldrich), 17.5 ml of a stock solution of 520 mg ml^{-1} lithium bis(trifluoromethylsulfonyl)imide (Sigma-Aldrich) in 1 ml chlorobenzene and this was spin coated on top of the perovskite layer at 4000 rpm for 30 seconds inside of the N_2 glovebox. The cells were then left for 3 hours in a desiccator cabinet in an attempt to promote oxidation of the Spiro-OMeTAD layer prior to pumping down in an evaporation chamber overnight. The devices were then finished with the evaporation of a 100 nm thick gold electrode. It is common practice to expose both DSSCs and perovskite devices which employ doped Spiro-OMeTAD as the HTL to air for several hours prior to the deposition of the electrode. An enhancement in electrical conductivity, FF and PCEs can be observed in final devices after oxidation. Abate et al. proposed a two-step mechanism to describe the oxidation of Spiro-OMeTAD as outlined below:[18]

$$Spiro - OMeTAD + O_2 \leftrightarrow Spiro - OMeTAD^{\cdot +} O_2^{\cdot -} \quad \textbf{4.1}$$

$$Spiro - OMeTAD^{\cdot +} O_2^{\cdot -} + LiTFSI \rightarrow$$

$$Spiro - OMeTAD^{\cdot +} TFSI^{-} + Li_xO_y \quad \textbf{4. 2}$$

Equation 4.1 illustrates an equilibrium between Spiro-OMeTAD and oxidised Spiro-OMeTAD while equation 4.2 shows the equilibrium to move forward in the presence of the LiTFSI dopant as Li^+ reacts with the superoxide O_2^- to form Li_2O and Li_2O_2. This produces a stabilised Spiro-$OMeTAD^{\cdot +}TFSI^-$ which along with Spiro-

$OMeTAD^{\cdot+}O_2^{\cdot-}$ is associated with high conductivities.[19]

4.3 Results and Discussion

4.3.1 FTO sets A, B and C

Thin films of FTO were deposited by APCVD at the University of Salford. Changes to the F dopant level, tin precursor to H_2O molar ratio, and thickness via the number of coater head passes were investigated. FTO film thickness was determined by etching the films with a mixture of zinc and HCl to provide a step edge. This was followed by surface profiling on a Dektak 3ST. Resistivity of films was measured using a Jandel Universal four point probe. Hall Effect measurements were also performed on the TCO films to determine the carrier concentration and electron mobility. This was carried out with a lab built system using an electromagnet with a probe separation of 12.5 mm and a current of 1.1 A to produce a magnetic flux density of 0.66 T. The results of these measurements are given in Table IV.III where d represents average film thickness (determined by SEM), root mean square (*RMS*) roughness (AFM), R_s sheet resistance, p resistivity, μ mobility, and N carrier concentration.

Table IV. III: *Deposition conditions and electrical properties for FTO sets A, B and C*

Set	*H_2O:MBTC*	*TFAA (M)*	*d (nm)*	*RMS Roughness (nm)*	*R_s (Ω sq^{-1})*	*$p/x10^{-4}$ (Ω cm^{-1})*	*μ ($cm^2V^{-1}s^{-1}$)*	*$N/x10^{20}$ (cm^{-3})*
Ref	N/A	N/A	400	14	13	5.2	28	4.2
A	5:1	0.2	1042	33	19	20	22	2.4
B	30:1	0.2	550	22	18	10	22	3.4
C1	30:1	0.6	365	16	21	7.6	28	2.7
C2	30:1	0.6	483	20	14	6.7	31	3.4
C3	30:1	1	410	20	14	5.6	23	4.0
C4	30:1	1	326	17	23	7.6	25	3.7

Sets A and B are two types of deposited FTO which contained similar sheet resistance (~20 Ω sq^{-1}) but differing surface roughness (RMS 33 nm, 22nm). The roughness of films was obtained by atomic force microscopy (AFM) using a Nanoscope IIIa, Digital Inst. Ltd. The reduction in thickness from film A to B while maintaining sheet resistance was achieved by reducing film thickness and increasing the H_2O:MBTC precursor ratio. Set C is evaluated later in section 4.3.4.

Batch A of FTO thin films were produced using a 5:1 H_2O:MBTC precursor ratio which had a thickness of 1042 nm. In contrast, batch B of FTO thin films were produced using a 30:1 H_2O:MBTC ratio which had a thickness of 550 nm. A third sample was deposited at the higher H_2O:MBTC precursor ratio, but had a similar thickness to set A. This had a similar roughness to set A but a much lower sheet resistance. For the three FTO films discussed in this section it can be seen that if only the film thickness is increased (H_2O:MBTC fixed), then roughness increases. However, if only the precursor ratio is increased (thickness fixed), then the roughness does not change. Therefore the roughness of the film depends on the film thickness not the precursor ratio. However, at the higher ratio the slightly increased doping level (as the TFAA is transported with the water) kept the resistance down.

These APCVD FTO samples were fabricated into mesoporous PSCs and compared to a high quality commercially available FTO thin film (Solaronix TCO22-15). This was

found to have a 400 nm thick FTO layer with an RMS roughness of 14 nm. The electrical properties, as measured on Salford instrumentation, gave a sheet resistance of 13 Ω sq^{-1}, a carrier concentration of 4.2 x 1020 cm^3, and a mobility of 28 cm^2 V^{-1} s^{-1}. The commercial FTO was thinner with a much lower roughness than the APCVD deposited FTO, with lower sheet resistance and higher mobility. The electrical properties of this commercial product are in line with its much higher carrier concentration. A lab built spectrometer consisting of a 75 W xenon lamp and a series of filters allowing measurement at 800 nm, 650 nm, 531 nm, and 450 nm was used to determine optical properties. Optical scattering measurements confirmed the variation in sample roughness showing an increase in haze with surface roughness. The devices containing APCVD FTOs were made simultaneously to the devices containing the reference Solaronix TCO22-15 FTO coated glass to avoid variations in the preparation method and hence allow the TCOs to be directly compared.

The solar cell devices were composed of a conductive APCVD FTO (set A and B) or a TCO22-15 FTO (reference) coated glass, a spin coated TiO_2 blocking layer, a mesoporous TiO_2 scaffold, a $MAPbI_3$ perovskite layer, a Spiro-OMeTAD hole transport layer and an Au counter electrode. 16 devices for each variation of FTO were fabricated using spin coated TiO_2 as the blocking layer. Interestingly, both A and B batches of APCVD FTO derived cells performed well, exceeding the efficiency achieved with use of the commercial TCO, used as a reference, by over 1% abs. in each case (Table IV.IV), representing an improvement in the order of 10%. This is particularly noticeable as the commercial TCO reference despite the lower sheet resistance and higher carrier mobility, which would be expected to give the cell a higher efficiency in removing the generated current, does not perform as well overall. However, it does have higher carrier concentration (N) than the other FTO samples. This will decrease the optical transmission via free carrier absorption and hence reduce the amount of light reaching the absorber parts of the cell. The relationship between carrier concentration and transmission has been seen previously for TCO ZnO electrodes in thin film silicon solar cells.[20] In addition the reference cell has a lower short circuit current density (J_{sc}), which in previous cell literature has been related to lower internal light scattering due to the TCO increased smoothness.[21, 22] The higher PCE values for set A and B cells suggested that while using a mesoporous scaffold layer the level of FTO roughness is not an issue. Previously it has been shown that

addition of a scaffold layer tends to reduce series resistance (R_{oc}) and hence increase the fill factor (FF), along with the open circuit voltage (V_{oc}) and shunt resistance (R_{sc}).[23]

Table IV. IV: *Cell data for APCVD FTO set A and B compared to reference Solaronix TCO22-15 when incorporated into mesoporous PSCs*

Sample ID	*BL method*	*PCE (%)*	*V_{oc} (mV)*	*J_{sc} (mA cm^{-2})*	*FF (%)*	*R_{sc} (Ω cm^2)*	*R_{oc} (Ω cm^2)*
Reference	Spin coated	8.436	887	16.06	59.2	925	7.67
A1	Spin coated	9.858	911.8	17.4	62.12	1924	7.711
B1	Spin coated	9.776	878.3	17.58	63.31	786.1	7.139

4.3.2 BL deposition method – spin coating versus ALD

Following on from the promising results obtained from APCVD FTO above, studies on a blocking layer deposition method were carried out. ALD was utilised to deposit nominally undoped TiO_2 in a range of thicknesses (10 nm, 20 nm, 30 nm) at 200°C on a batch of A1 APCVD FTO coated glass substrates. 16 devices for each variation of blocking layer were fabricated for this study. Both 10 nm and 20 nm ALD TiO_2 as the BL ETLs were found to boost the PCE of a mesoporous cell when compared to spin coated TiO_2 on the same APCVD FTO coated glass substrate. The optimal thickness of 20 nm ALD TiO_2 achieved 10.37 % PCE when incorporated into a mesoporous PSC on a 0.43 cm^2 active area. 30 nm ALD TiO_2 proved to be too thick a coating when incorporated into a device reducing the obtained R_{sc} as shown in Table IV. V.

Table IV. V: *Cell data comparing spin coated TiO_2 and ALD TiO_2 (10 nm, 20 nm, 30 nm) deposited on APCVD FTO set A when incorporated into mesoporous PSCs*

Sample ID	*BL method*	*PCE (%)*	*V_{oc} (mV)*	*J_{sc} (mA cm^{-2})*	*FF (%)*	*R_{sc} (Ω cm^2)*	*R_{oc} (Ω cm^2)*
A1	Spin coated	9.858	911.8	17.4	62.12	1924	7.711
A1	ALD (10 nm)	10.06	921.6	18.38	59.42	6662	9.943
A1	ALD (20 nm)	10.37	946.5	18.44	59.40	3604	11.83
A1	ALD (30 nm)	6.156	858.7	17.64	40.65	695.2	29.74

A comparison of the methods used to deposit the BL showed an advantage in using ALD opposed to spin coating with better V_{oc}, J_{sc} and hence device efficiency. This improvement relates to the increased film density generally found with the ALD process, conformal behaviour and better control of thickness uniformity (10.00 nm ± 0.86 nm, 20.00 nm ± 1.05 nm) which for the spin coated samples was between 10 nm and 15 nm. ALD is a surface controlled, chemically self-limiting technique for depositing thin films. It is well documented for its ability to produce conformal and pinhole free layers with high thickness uniformity.[24] Using the same ALD process as described here, Chen et al.[25] demonstrated pinhole free, conformal deposition of only 2 nm TiO_2 over Si layers. Other studies[26] on the effect of the BL deposition method, this time ALD, spray pyrolysis and sol–gel also concluded that the improved cell efficiency was due to the ALD dense, pinhole free TiO_2. Despite this, a lower FF for the ALD opposed to spin coated samples was observed in these mesoporous PSCs as depicted in Table IV. V. This result may be due to increased series resistance from the FTO contact.

4.3.3 Perovskite deposition method – increased solvent quenching

The $MAPbI_3$ absorber layer was investigated by increasing the solvent quenching treatment with toluene from 60 µl to 1 ml. Mesoporous devices were then fabricated using various FTO coated glass substrates as the TCO (reference TCO22-15, set A2 and set B2) and spin coated TiO_2 as the BL.

Increasing the amount of solvent quenching toluene for the perovskite layer deposition led to an increase in the overall cell efficiency for mesoporous devices containing both reference FTO and set A2 APCVD FTO, as observed in Table IV. VI. Batch B2 of APCVD FTO was a smoother and thinner FTO coated glass substrate and the final mesoporous device showed a reduced V_{oc} and FF with no improvement in overall PCE, despite a much larger R_{sc}. Use of a greater amount of toluene led to improved perovskite coverage, a denser structure with a more controllable grain structure and higher reproducibility. Solvent engineering for PSCs using toluene was first reported by Jeon et al., who used it to produce uniform and dense perovskite layers with low surface roughness. This quenching causes the formation of an intermediate phase of MAI-PbI_2-DMSO by washing the precursor solvent, DMF, away. Upon heating, the residual DMSO is then removed and the perovskite film is formed. Without this solvent quenching treatment, an inhomogeneous perovskite layer is formed which does not fully cover the substrate.[27] Since the initial report, toluene has been extensively investigated for its use as a solvent quenching method in the fabrication of PSCs. The optimal volume of toluene has been observed to vary from 20 µl to 800 µl depending on perovskite composition and researchers' own preferences.[28, 29] While toluene, chlorobenzene, ethyl acetate and diethyl ether have all been reported to enhance perovskite film quality as anti-solvent treatments, ethyl acetate's higher affinity for scavenging moisture does not produce poor films at higher processing humidities. This presents the possibility of processing perovskite films outside the glovebox for commercial scale.[30]

Table IV. VI: *Cell data for APCVD FTO set A and B compared to reference Solaronix TCO22-15 when incorporated into mesoporous PSCs with an increased toluene dripping on $MAPbI_3$*

Sample ID	*BL method*	*Scan Direction*	*PCE (%)*	*V_{oc} (mV)*	*J_{sc} (mA cm^{-2})*	*FF (%)*	*R_{sc} (Ω cm^2)*	*R_{oc} (Ω cm^2)*
Reference	Spin coated	Reverse	13.37	1040	19.92	64.43	1175	3.783
A2	Spin coated	Reverse	14.68	1029	20.29	70.34	1672	5.464
		Forward	13.37	1023	18.96	68.90	1043	5.473
B2	Spin coated	Reverse	9.276	786.9	20.40	57.78	2786	8.112

4.3.4 FTO set C with improved perovskite comparing ALD to spin coated BLs

Batch C of FTO APCVD samples were deposited and through AFM were found to be slightly smoother than set B deposited previously. Set C was also found to be thinner in FTO thickness which increases percentage transmission, and of a much lower resistivity than both sets A and B (Table IV. III). Set C was fabricated into mesoporous PSCs using the improved perovskite recipe (Section 4.3.3) as well as two different blocking layers, 20 nm nominally undoped TiO_2 by ALD and 10 nm – 15 nm TiO_2 by spin coating, for comparison.

Table IV. VII: *Cell data comparing 20 nm ALD TiO_2 deposited on reference Solaronix TCO22-15 and APCVD FTO set C and incorporated into mesoporous PSCs*

Sample ID	*BL method*	*Scan Direction*	*PCE (%)*	*V_{oc} (mV)*	*J_{sc} (mA cm^{-2})*	*FF (%)*	*R_{sc} (Ω cm^2)*	*R_{oc} (Ω cm^2)*
Reference	ALD (20nm)	Reverse	15.00	1036	18.81	76.98	8274	5.441
		Forward	14.84	1043	19.19	74.18	2860	5.729
C1	ALD (20nm)	Reverse	4.569	761	18.71	32.09	72.07	17.39
C2	ALD (20nm)	Reverse	14.68	1047	19.86	70.58	2203	5.153
		Forward	14.33	1043	19.27	71.33	1826	4.282
C3	ALD (20nm)	Reverse	14.70	1057	19.77	70.34	1640	4.614
		Forward	11.34	1020	19.40	56.61	447.7	8.169
C4	ALD (20nm)	Reverse	14.66	1049	19.37	72.14	3330	7.565
		Forward	13.29	1075	19.50	63.40	898.7	7.076

ALD TiO_{2-x} coated FTO samples showed improved PCEs when compared to spin coated BLs. ALD coated APCVD FTO samples exhibited greater efficiencies than similarly coated commercial TCOs even when re-characterised three days later as depicted in Table IV. VII and IV. VIII. Samples with a spin coated blocking layer generally shunted or yielded low PCE values. This was likely due to post growth

particles and debris on the FTO surfaces, as observed by SEM (not given), which were not fully covered by the thin spin coated BL. The resulting direct contact between the FTO and perovskite absorber layer may account for the poor efficiency of the complete devices. This may also explain the lower efficiencies previously obtained from set B FTO which was spin coated with a TiO_{2-x} BL followed by the improved perovskite recipe. Furthermore, those samples in set C which showed enhanced cell efficiency were subjected to an additional cleaning step whereby the FTO coated glass substrates were annealed for 1 hour at 500°C to help remove organic debris. This high temperature anneal did not prove detrimental to the optical or electrical properties of the FTO films. The higher conformality achieved by ALD over the spin coating method reduces the number of pinholes resulting from large FTO particles or debris. Moreover, the less conformal spin coating process described elsewhere[9] can lead to a smoother top surface and hence a smaller contact area between BL and perovskite. These shortcomings of the spin coating method resulted in increased shunting pathways within the devices and thus lower device performance.

Table IV. VIII: *Cell data comparing 20 nm ALD TiO_2 deposited on reference Solaronix TCO22-15 and APCVD FTO set C and incorporated into mesoporous PSCs re-measured after 3 days*

Sample ID	*BL method*	*Scan Direction*	*PCE (%)*	*V_{oc} (mV)*	*J_{sc} (mA cm^{-2})*	*FF (%)*	*R_{sc} (Ω cm^2)*	*R_{oc} (Ω cm^2)*
Reference	ALD (20 nm)	Reverse	15.18	1028	20.20	73.09	2106	5.015
		Forward	14.62	1023	20.35	70.18	2550	4.915
C2	ALD (20 nm)	Reverse	15.40	1031	20.54	72.69	1830	4.927
C3	ALD (20 nm)	Reverse	15.20	1049	20.25	71.67	4049	6.088
C4	ALD (20 nm)	Reverse	14.13	1055	20.71	64.64	2047	9.39

A comparison of the cell data from set C (Table IV. III) showed that a higher film thickness in the APCVD FTO produced lower sheet resistance and, thus, marginally improved cell efficiencies when the same doping level was present. Increasing the doping level from 0.6 M to 1 M of TFAA made no conclusive improvement in the cell properties of these samples.

4.3.5 FTO set D

Based on the previous results, a new batch of APCVD FTO was deposited, taking additional care to ensure no particles or debris were incorporated into the films. For this batch, set D, all deposition parameters were fixed (H_2O:MBTC 5:1, 1 M TFAA) except for the number of passes of the coating head over the substrate. The result was a set of FTO samples with three separate thicknesses, thereby altering the sheet resistance and roughness for each (Table IV. IX). As expected the sheet resistance decreases and roughness increases as the film thickness increases.[16]

Table IV. IX: *Physical and electrical properties of Set D*

Set D	*d* (nm)	*RMS Roughness (nm)*	*R_s* ($\Omega\ sq^{-1}$)	*μ* ($cm^2V^{-1}s^{-1}$)	*$N/x10^{20}$* (cm^{-3})
D1	350	13	20	28	3.3
D2	523	21	11	31	3.8
D3	745	25	7	34	3.5

The carrier mobility of set D is seen to be fractionally greater than that of the reference TCO sample (Table IV.III), while the carrier concentration is lower. The greater optical scatter with increased film thickness confirms the increased surface roughness, as shown in Figure 4.2 (a). The reference FTO gave haze values comparable to its thickness and surface roughness i.e. between the APCVD samples with thicknesses of 350 nm and 523 nm. As can be seen in Figure 4.2 (b) and (c) there is a general decrease in percentage transmission and an increase in percentage absorption as the films increase in thickness, particularly at the higher wavelengths. The reference FTO generally lies within the band of optical values, except for a much increased reflectance at wavelengths > 1500 nm.

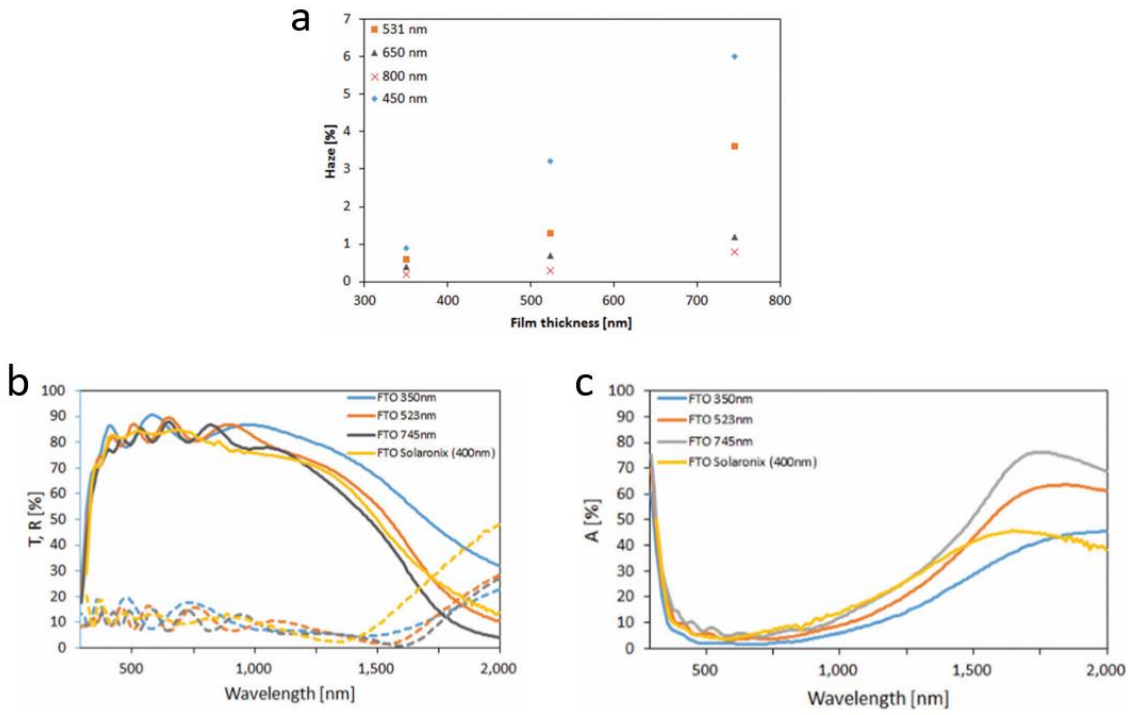

Figure 4. 2: (a) *Optical haze for set D at 4 different wavelengths,* ***(b)*** *Percentage transmittance (solid line) and reflectance (dotted line),* ***(c)*** *percentage absorption comparing set D to reference FTO*

In all cases the improved quality of the FTO gave cell efficiencies comparable to or better than the cells fabricated from the commercial FTO (Table IV. X). This must have arisen from a combination of properties as although samples in set D all had a lower carrier concentration and higher mobility than the reference, they only had lower sheet resistance in two out of three samples. An important factor in the efficiency of the cells containing APCVD FTO was their higher optical transmittance.

Interestingly, as the FTO increased in thickness there was a corresponding increase in cell FF and a decrease in R_{oc} leading to increased efficiency. This was despite decreased transmission, particularly in wavelengths above 1200 nm, and a possible issue with increased roughness from D1 (13 nm) to D3 (25 nm). This again suggests that FTO roughness does not negatively impact cell efficiency as long as the BL is both conformal and pinhole free, preventing shunt pathways. This set of results establishes that the pivotal FTO property which contributes to cell efficiency is sheet resistance.

4.3.6 BL deposition method – sputtering versus ALD

As previously discussed in this chapter, deposition of the ETL BL via ALD improved the overall PCE of mesoporous perovskite devices when compared to those containing an ETL BL deposited by spin coating. A third TiO_{2-x} BL deposition method of magnetron sputtering was investigated with FTO set D and compared to ALD. For both deposition methods, sputtering and ALD, the TiO_{2-x} layers deposited were 20 nm in thickness.

Sigma dark measurements from sputtered TiO_{2-x} on glass substrates exhibited semi-conducting behaviour for all films with conductivity increasing as temperature increased in Figure 4.3 (a). This indicates that oxygen vacancies act as a dopant in TiO_{2-x} as smaller activation energies are found for deposited TiO_{2-x} films with increased reducing conditions, Figure 4.3 (b). Such behaviour is ascribed to electrical conduction through mid-gap defect states induced by Ti^{3+} sites. The dark conductivity was also shown to depend on the degree of reduction within the sputtered TiO_{2-x} films, with a larger electrical conductivity measured for films deposited without the introduction of O_2 during the sputtering process.

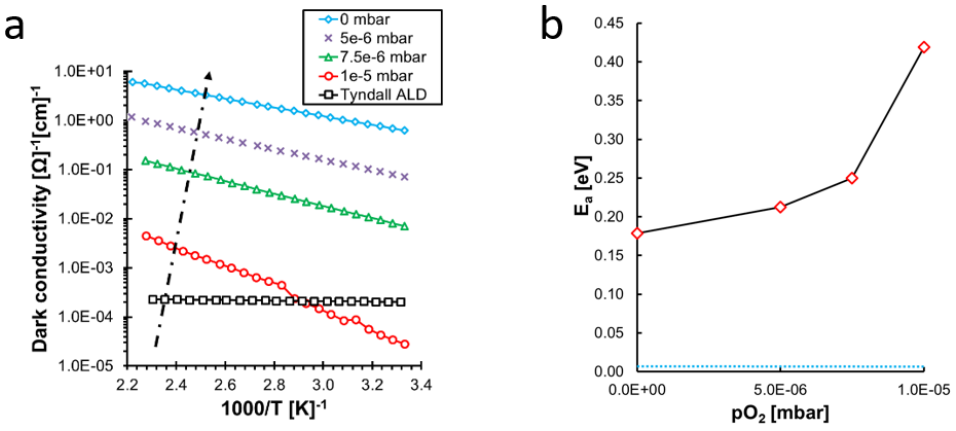

Figure 4. 3: (a) *Arrhenius plot of the surface conductivity of sputtered TiO_{2-x} and ALD TiO_2,* ***(b)*** *Activation energy (E_a) as a function of the partial O_2 pressure (pO_2) with the blue line corresponding to 7 meV of ALD TiO_2*

In contrast, 20 nm ALD TiO_2 on glass was found to exhibit a low E_a of 7 meV when measured using sigma dark characterisation. This measurement is consistent with a

degenerately doped semiconductor. TiO_2 films deposited by ALD at 200°C were found to be amorphous as grown by XRD characterisation.

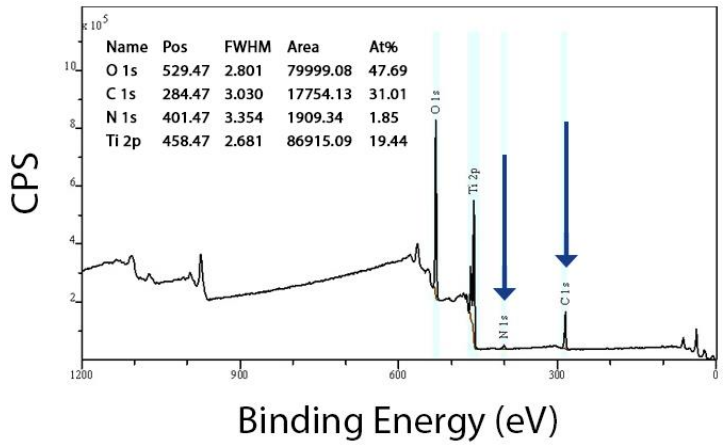

Figure 4. 4: *XPS showing binding energy of as grown 20 nm ALD TiO_2*

XPS analysis of the ALD film on the reference FTO substrate exhibited significant Ti^{3+} content, indicating non-stoichiometric TiO_2. Ti $2p_{3/2}$ and Ti $2p_{1/2}$ peaks correspond to Ti^{4+} states and can be found at ~ 458.6 eV and ~ 464 eV respectively. A shoulder associated with Ti^{3+} species is found at 456.9 eV indicating the presence of a defect density of states. A common source of Ti^{3+} states in TiO_2 is oxygen vacancies. The variation in the chemical state of elements 'O' and 'Ti' can be analysed by comparing the intensities of the O 1s (~539.3 ev) and Ti 2p peaks. As well as being non-stoichiometric, measurable quantities of both nitrogen and carbon from unreacted precursors were present in ALD TiO_2 as displayed in Figure 4.4. This film was found to have improved resistivity over stoichiometric TiO_2 which may be attributed to the higher density in ALD deposited films. Despite this, the impurities caused by carbon and nitrogen lead to a reduction in film conductivity.

Sputtered TiO_{2-x} was also found to be non-stoichiometric from Figure 4.3 and Figure 4.4, producing a higher conductivity and larger optical absorption than ALD TiO_2. This suggests that sputtered TiO_2 contains a greater number of oxygen vacancies which can be controlled by adjusting the Ar and Ar:O flow on deposition.

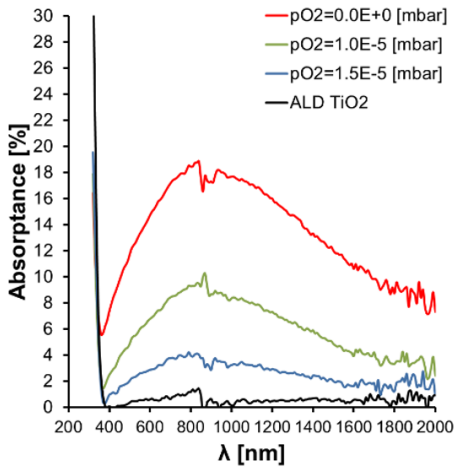

Figure 4. 5: *Optical absorption of TiO_{2-x} thin films with different pO_2*

Optical absorption of sputtered TiO_2 films was found to increase with increased degree of reduction. A broad peak centred around the 900 nm wavelength was related to mid-gap optical losses. Following this result, sputtered TiO_2 thin films with pO_2 = 7.5 x 10^{-6} mbar were selected to be fabricated into mesoporous perovskite devices using set D FTO due to their optimal conductivity-transparency trade-off.

Table IV. X: Cell data for set D comparing sputtered TiO_{2-x} to ALD TiO_2 *on a 1.04 cm^2 active cell area*

Sample ID	*BL method*	*Scan Direction*	*PCE (%)*	*V_{oc} (mV)*	*J_{sc} (mA cm^{-2})*	*FF (%)*	*R_{sc} (Ω cm^2)*	*R_{oc} (Ω cm^2)*
Reference	Sputter	Reverse	15.66	1069	20.00	73.26	21767	7.97
		Forward	14.31	1067.7	20.22	66.29	6470	10.4
Reference	ALD (20 nm)	Reverse	10.98	1044	19.15	54.91	1014	30.97
		Forward	10.22	1084	18.35	51.38	3144	48.65
D1	Sputter	Reverse	13.82	1088	21.12	60.07	2047	14.02
		Forward	13.50	1092	21.15	58.46	1027	12.75
D2	Sputter	Reverse	15.43	1067	20.95	69.01	5472	8.87
		Forward	12.80	1064	20.07	59.90	1249	9.59
D3	Sputter	Reverse	16.66	1093	20.75	73.46	24225	6.92
		Forward	16.46	1052	21.38	73.18	11153	6.23
D1	ALD	Reverse	13.96	1039	22.59	59.49	2668	11.6
		Forward	13.54	1074	21.20	59.47	13.80	13.52
D2	ALD	Reverse	10.54	1073	15.49	63.39	479.2	10.60
		Forward	10.37	1040	20.15	49.44	127.8	10.29
D3	ALD	Reverse	16.45	1073	20.76	73.85	3453	5.91
		Forward	16.33	1085	20.57	73.16	23995	6.81

Data comparing BLs of sputtered TiO_{2-x} to ALD TiO_2 in mesoporous cells using reference FTO is presented at the top of Table IV. X. From this data it is clear that despite the lower transparency of sputtered TiO_{2-x}, these films contributed to a higher J_{sc} and lower R_{oc}, which lead to an improved PCE compared to the same cells incorporating ALD TiO_2. This result is consistent with the observed electrical conductivities achieved through the BL deposition methods.

When comparing the BL deposition methods of sputtering and ALD on APCVD FTO, the ALD TiO_2 was seen to outperform sputtered TiO_{2-x} on the thinner FTO set, D1. A higher J_{sc} and lower R_{oc} for the cells containing ALD TiO_2 lead to an improved PCE of 13.96 %. For the intermediate FTO thickness, D2, efficiencies from both types of BL depositions were found to be poor. Devices containing sputtered TiO_{2-x} reached a PCE of 12.80 %, while the devices containing ALD TiO_2 were even lower, only reaching 10.54 % PCE. This lower PCE in devices containing ALD was due to the perovskite layer being less compact due to evaporation of the solvent taking place too quickly and leaving voids and/or a higher resistance in the ALD layer hindering the extraction of electrons. The increased resistance could be a product of the high scaffold annealing temperature of 500°C changing the TiO_2 structure more negatively for ALD than sputtering. It is possible that on annealing the thin, amorphous TiO_2 deposited by ALD undergoes partial crystallisation and hence the formation of poor grain boundaries due to the higher level of impurities as compared to the sputtered film. In addition the annealing could have induced cracking of the thin 20 nm film.

The BL deposition methods of sputtering and ALD both provided improved uniformity on the FTO coated glass compared to spin coating, aiding in the formation of a more uniform and well adhered perovskite absorber layer. This enhanced uniformity allowed an increase in cell dimension from a 0.43 cm^2 active area to a 1.04 cm^2 active area in set D. As observed in Table IV. X, the PCEs obtained on the larger active areas are as high if not higher than the PCEs achieved by earlier batches on the smaller 0.43 cm^2 active areas.

Table IV. X shows that with increased FTO thickness from D1 to D3 there is a corresponding improvement in FF and efficiency, with a decrease in R_{oc}. This is attributed to the decrease in FTO sheet resistance, as demonstrated in Figure 4.6.

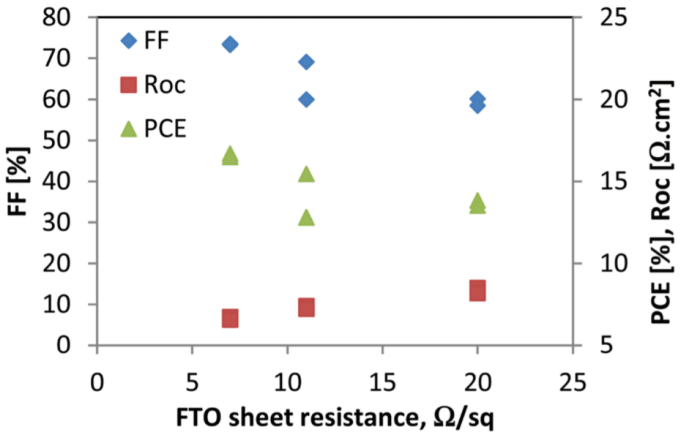

Figure 4. 6: *Plot showing the trend in mesoporous cell parameters which incorporated set D FTO with a sputtered TiO_{2-x} BL.*

The best cell result was obtained from the thickest and hence lowest resistance APCVD FTO layer (7 Ω sq^{-1}), with a sputtered 20 nm BL, a mesoporous scaffold, and a 300 nm perovskite absorber layer, resulting in an overall PCE value of 16.66 %. This PCE was only slightly higher than that obtained by the same cell incorporating ALD TiO_2, 16.45 %. This result implies that ALD TiO_2 is comparable to that of RF sputtered TiO_{2-x}.

These results compare well with literature values for similar cells. Lee et al.[7] obtained a similar 16.6 % efficiency with a much smaller cell active area of 0.16 cm^2, while Japan's National Institute for Materials Science achieved a certified value of 15 % on a similar cell size of 1.017 cm^2.[31] Higher values have also been reported by Yang et al.[32] at 20 % for a 0.096 cm^2 cell and Li et al.[33] at 19.6 %, however these efficiencies are not directly comparable as Yang et al. utilised a formamidinium lead triiodide perovskite while Li et al. incorporated a mixed anion as well as mixed halide perovskite.

4.4 Summary

A number of sets of the TCO, FTO, varying in thickness, roughness, sheet resistance, resistivity, mobility and the H_2O:MBTC precursor ratio were successfully deposited by APCVD. These APCVD FTO samples were fabricated into mesoporous PSCs and compared to a high quality commercially available FTO thin film (Solaronix TCO22-15). It was observed that uniform thin films of FTO with low sheet resistance are

necessary to aid in the formation of uniform, pinhole free blocking layers and hence well adhered perovskite absorber layers.

Blocking layer deposition methods of spin-coating, ALD, and sputtering were also investigated and synthesised into mesoporous PSCs on both APCVD FTO and reference FTO. In addition some changes to the perovskite precursor composition were considered, and their effects on the overall properties of the PV cell were investigated. The optimised layers were then combined and fabricated into mesoporous PSCs leading to improved cell efficiencies.

ALD was utilised to deposit nominally undoped TiO_2 in a range of thicknesses (10 nm, 20 nm, 30 nm) at 200°C on a batch of A1 APCVD FTO coated glass substrates. Both 10 nm and 20 nm ALD TiO_2 were found to boost the PCE of a mesoporous cell when compared to spin coated TiO_2 on the same APCVD FTO coated glass substrate due to an increase in both V_{oc} and J_{sc}. 30 nm ALD TiO_2 proved to be too thick reducing the obtained $R_{sc.}$ The optimal thickness of 20 nm ALD TiO_2 achieved 10.37 % PCE when incorporated into a mesoporous PSC. This improvement related to the increased film density, conformal behaviour and better control of thickness uniformity, which for the spin coated samples was between 10 nm and 15 nm. ALD is a surface controlled, chemically self-limiting technique for depositing thin films. From this result, 20 nm ALD was chosen to be used for the remainder of the study.

20 nm thermal TiO_2 was deposited by ALD at 200°C on set C APCVD deposited FTO and reference FTO. This APCVD FTO set was smoother with a reduced thickness than previous set B. These samples were then fabricated into mesoporous PSCs using a modified $MAPbI_3$ deposition process which had increased the amount of dripped toluene. Similarly to results from cells using set A, ALD outperformed spin coating as a BL deposition method. For devices using the reference FTO with ALD, high efficiencies of 15.00 % PCE were obtained which increased to 15.18 % PCE when re-measured three days later. The ALD TiO_2 thin films achieved similarly high results on APCVD FTO with set C3 reaching 14.68 % PCE when fabricated into a mesoporous PSC which was found to increase to 15.4 % PCE after three days.

The ALD method was then compared to RF sputtering. Nominally undoped 20 nm TiO_2 was deposited by ALD on set D APCVD FTO and reference FTO. 20 nm sputtered TiO_{2-x} with 7.5 x 10^{-6} mbar of O_2 introduced to the sputtering process was

selected for fabrication into mesoporous devices as this amount of partial O_2 provided the optimal conductivity-transparency trade-off. The best cell result was obtained from the thickest and hence lowest resistance APCVD FTO layer (7 Ω sq^{-1}), with a sputtered 20 nm BL, a mesoporous scaffold, and a 300 nm perovskite absorber layer, resulting in an overall PCE value of 16.66 %. This PCE was only slightly higher than that obtained by the same cell incorporating ALD TiO_2, 16.45 %. This result implies that ALD TiO_2 is comparable to that of RF sputtered TiO_{2-x} and may be improved on for use in mesoporous PSCs.

This study demonstrates that both ALD and sputtering are viable techniques for scaled up systems. While the application of ALD has predominantly been associated with the microelectronic and the nanotechnology industries, ALD shows great potential for the fabrication of photovoltaic devices. Its unrivalled conformality combined with its mild, low-temperature deposition technique could make it an ideal candidate for tandem cells. These factors may also aid in minimising sputter damage to the perovskite during the sputtering process. Overall, these two vacuum techniques show great promise for scalable devices.

4.5 Bibliography

[1] D. S. Bhachu, D. O. Scanlon, E. J. Saban, H. Bronstein, I. P. Parkin, C. J. Carmalt and R. G. Palgrave, Scalable route to $CH_3NH_3PbI_3$ perovskite thin films by aerosol assisted chemical vapour deposition, J. Mater. Chem. A, 3, 9071–9073, 2015

[2] S. Chen, J. Briscoe, Y. Shi, K. Chen, R. M. Wilson, S. Dunn, R. Binions, A simple, low-cost CVD route to high-quality $CH_3NH_3PbI_3$ perovskite thin films, Cryst Eng Comm, 17, 7486-7489, 2015

[3] D. Bi, S.-J. Moon, L. Haggman, G. Boschloo, L. Yang, E. M. Johansson, M. K. Nazeeruddin, M. Gratzel, A. Hagfeldt, Using a two-step deposition technique to prepare perovskite ($CH_3NH_3PbI_3$) for thin film solar cells based on ZrO_2 and TiO_2 mesostructures, RSC Adv., 3, 18762–18766, 2013

[4] M. Anaya, J. F. Galisteo-Lopez, M. E. Calvo, C. Lopez, H. Miguez, Photophysical Analysis of the Formation of Organic–Inorganic Trihalide Perovskite Films: Identification and Characterization of Crystal Nucleation and Growth, J. Phys. Chem. C, 120, 3071–3076, 2016

[5] A. M. A. Leguy, Y. Hu, M. Campoy-Quiles, M. I. Alonso, O. J. Weber, P. Azarhoosh, M. van Schilfgaarde, M. T. Weller, T. Bein, J. Nelson, P. Docampo, P. R. F. Barnes, The reversible hydration of $CH_3NH_3PbI_3$ in films, single crystals and solar cells, Chem. Mater., 27, 3397–3407, 2015

[6] W. Tress, N. Marinova, T. Moehl, S. M. Zakeeruddin, M. K. Nazeeruddin and M. Gratzel, Understanding the rate-dependent J–V hysteresis, slow time component, and aging in $CH_3NH_3PbI_3$ perovskite solar cells: the role of a compensated electric field, Energy Environ. Sci., 8, 995–1004, 2015

[7] Y. H. Lee, J. Luo, R. Humphry-Baker, P. Gao, M. Gratzel, M. K. Nazeeruddin, Unraveling the Reasons for Efficiency Loss in Perovskite Solar Cells, Adv. Funct. Mater., 25, 3925–3933, 2015

[8] H. M. Yates, M. Afzaal, A. Walter, J. L. Hodgkinson, S.-J. Moon, D. Sacchetto, M. Brauninger, B. Niesen, S. Nicolay, M. M. McCarthy, M. E. Pemble, I. M. Povey, C. Ballif, Progression towards high efficiency perovskite solar cells via optimisation of the front electrode and blocking layer, J. Mater. Chem. C, 4, 11269, 2016

[9] J. Choi, S. Song, M. T. Horantner, H. J. Snaith, T. Park, Well-Defined Nanostructured, Single-Crystalline TiO_2 Electron Transport Layer for Efficient Planar Perovskite Solar Cells, ACS Nano, 10, 6029–6036, 2016

[10] W. Ke, G. Fang, Q. Liu, L. Xiong, P. Qin, H. Tao, J. Wang, H. Lei, B. Li, J. Wan, Low-temperature solution-processed tin oxide as an alternative electron transporting layer for efficient perovskite solar cells, J. Am. Chem. Soc., 137, 6730–6733, 2015

[11] J. T.-W. Wang, J. M. Ball, E. M. Barea, A. Abate, J. A. Alexander-Webber, J. Huang, M. Saliba, I. Mora-Sero, J. Bisquert, H. J. Snaith, R. J. Nicholas, Low-temperature processed electron collection layers of graphene/TiO_2 nanocomposites in thin film perovskite solar cells, Nano Lett., 14, 724–730, 2014

[12] D. Liu, T. L. Kelly, Perovskite solar cells with a planar heterojunction structure prepared using room-temperature solution processing techniques, Nat. Photonics, 8, 133–138, 2014

[13] H. M. Yates, P. Evans, D. W. Sheel, S. Nicolay, L. Ding, C. Ballif, High-performance tandem silicon solar cells on F:SnO_2, Surf. Coat. Technol., 230, 228–233, 2013

[14] C. Zuo, H. J. Bolink, H. Han, J. Huang, D. Cahen, L. Ding, Advances in Perovskite Solar Cells, Adv. Sci., 3, 1500324, 2016

[15] P. Chen, Y. Wang, M. Wang, X. Zhang, L. Wang,Y. Liu, TiO_2 nanoparticle-based electron transport layer with improved wettability for efficient planar-heterojunction perovskite solar cell, J. Energy Chem., 24, 717–721, 2015

[16] H. M. Yates, P. Evans, D. W. Sheel, U. Dagkaldiran, A. Gordijn, F. Finger, Z. Remes, M. Vanecek, Optimum performance solar cells using atmospheric pressure chemical vapour deposition deposited TCOs, Int. J. Nanotechnol., 6, 816–827, 2009

[17] N. Ahn, D.-Y. Son, I.-H. Jang, S. M. Kang, M. Choi, N.-G. Park, Highly Reproducible Perovskite Solar Cells with Average Efficiency of 18.3 % and Best Efficiency of 19.7 % Fabricated via Lewis Base Adduct of Lead (II) Iodide, J. Am. Chem. Soc., 137, 8696–8699, 2015

[18] A. Abate, T Leijtens, S. Pathak, J. Teuscher, R. Avolio, M. E. Errico, J. Kirkpatrik, J. M. Ball, P. Docampo, I. McPherson, H. J. Snaith, Lithium salts as ‘‘redox active’’

p-type dopants for organic semiconductors and their impact in solid-state dye-sensitized solar cells, Phys. Chem. Chem. Phys., 15, 2572-2579, 2013

[19] Z. Hawash, L. K. Ono, Y. Qi, Moisture and Oxygen Enhance Conductivity of LiTFSI-Doped Spiro-MeOTAD Hole Transport Layer in Perovskite Solar Cells, Adv. Mater. Interfaces, 3, 1600117, 2016

[20] S. Fay, J. Steinhauser, S. Nicolay, C. Ballif, Polycrystalline ZnO: B grown by LPCVD as TCO for thin film silicon solar cells, Thin Solid Films, 518, 2961–2966, 2010

[21] H. M. Yates, P. Evans, D. W. Sheel, S. Nicolay, L. Ding, C. Ballif, The development of high performance SnO_2:F as TCOs for thin film silicon solar cells, Surf. Coat. Technol., 213, 167–174, 2012

[22] J. Springer, B. Rech, W. Reetz, J. Muller, M. Vanecek, Light trapping and optical losses in microcrystalline silicon pin solar cells deposited on surface-textured glass/ZnO substrates, Sol. Energy Mater. Sol. Cells, 85, 1–11, 2005

[23] J.-W. Lee, D.-J. Seol, A.-N. Cho, N.-G. Park, High-efficiency perovskite solar cells based on the black polymorph of $HC(NH_2)_2$ PbI_3, Adv. Mater., 26, 4991–4998, 2014

[24] M. Ritala, M. Leskela, Atomic layer epitaxy - a valuable tool for nanotechnology?, Nanotechnology, 10, 19–24, 1999

[25] Y. W. Chen, J. D. Prange, S. Duhnen, Y. Park, M. Gunji, C. E. D. Chidsey, P. C. McIntyre, Atomic layer-deposited tunnel oxide stabilizes silicon photoanodes for water oxidation, Nat. Mater., 10, 539–544, 2011

[26] F. Di Giacomo, V. Zardetto, G. Lucarelli, L. Cina, A. Di Carlo, M. Creatore, T. M. Brown, Mesoporous perovskite solar cells and the role of nanoscale compact layers for remarkable all-round high efficiency under both indoor and outdoor illuminiation, Nano Energy, 30, 460–469, 2016

[27] N. J. Jeon, J. H. Noh, Y. C. Kim, W. S. Yang, S. Ryu, S. I. Seok, Solvent engineering for high-performance inorganic-organic hybrid perovskite solar cells, Nat. Mater., 13, 897–903, 2014

[28] K. Kara, D. A. Kara, C. Kırbıyık, M. Ersoz, O. Usluer, A. L. Briseno, M. Kus, Solvent washing with toluene enhances efficiency and increases reproducibility in perovskite solar cells, RSC Adv., 6, 26606, 2016

[29] Y. Liao, H. Liu, W. Zhou, D. Yang, Y. Shang, B. Li, X. Jiang, L. Zhang, L. N. Quan, R. Quintero-Bermudez, B. R. Sutherland, Q. Mi, E. H. Sargent, Z. Ning, Highly Oriented Low-Dimensional Tin Halide Perovskites with Enhanced Stability and Photovoltaic Performance, J. Am. Chem. Soc, 139, 19, 6693-6699, 2017

[30] J. Troughton, K. Hooper, T. M. Watson, Humidity resistant fabrication of $CH_3NH_3PbI_3$ perovskite solar cells and modules, Nano Energy, 39, 60-68, 2017

[31] M. A. Green, K. Emery, Y. Hishikawa, W. Warta, E. D. Dunlop, Solar cell efficiency tables (version 48), Prog. Photovoltaics, 23, 3–11, 2016

[32] W. S. Yang, J. H. Yoh, N. J. Jeon, Y. C. Kim, S. Ryu, J. Seo, S. I. Seok, High-performance photovoltaic perovskite layers fabricated through intramolecular exchange, Science, 348, 1234–1237, 2015

[33] X. Li, D. Bi, C. Yi, J.-D. Decoppet, J. Luo, S. M. Zakeeruddin, A. Hagfeldt, M. Gratzel, A vacuum flash-assisted solution process for high-efficiency large-area perovskite solar cells, Science, 353, 58–62, 2016

CHAPTER 5:

A study into deposition optimisation of ALD TiO_2 thin films for mesoporous PSCs

5.1 Introduction

As discussed previously in Chapter 4, ALD was compared to alternative TiO_2 BL deposition methods, spin coating and RF sputtering, for use in mesoporous PSCs. ALD TiO_2 exhibited promising results on both commercially available FTO thin films (Solaronix TCO22-15) and APCVD deposited FTO. The conformal and uniform nature of ALD lead to the production of dense, pinhole free BLs which outperformed those produced by the spin coating method when fabricated into devices. RF sputtered TiO_2 produced a notably high PCE of 16.66 % on the D3 set of APCVD FTO, while ALD reached a similarly high PCE of 16.45 % on the same FTO in a mesoporous device.

In this chapter, an attempt to improve overall cell efficiency by altering the deposition of ALD TiO_2 BLs was investigated. The deposition temperature of all thin films deposited was further reduced from 200°C as utilised in Chapter 4 to 185°C. The effort to employ even lower deposition temperatures was motivated by the possibility of later integrating ALD layers into perovskite/silicon heterojunction tandem cells. Low-temperature processing conditions make it possible to monolithically integrate perovskite solar devices as the top component of tandem cells without damaging the bottom cell. Temperatures exceeding 200°C on the top cell can lead to severe junction deterioration in tandem structures employing a silicon heterojunction bottom cell. The growth of ALD TiO_2 was carried out on two commercial reactors, a Cambridge Nanotech Fiji F200 and a Picosun R200 system, to determine if a difference in film quality could be observed in films created by the two reactors or, alternatively, if the growths would be reproducible.

Two titanium precursors, titanium (IV) isopropoxide (TTIP) and tetrakis (diemthylamido) titanium (TDMAT), were investigated along with reactants of either H_2O or Ar/O_2 plasma for growth of TiO_2 films. Prior to growth, a 5 minute O_2 plasma treatment in situ to the ALD chamber was applied to all substrates, to which Ar/O_2 plasma would not be administered as a reactant, unless stated otherwise. This O_2 plasma clean prior to growth was carried out in order to provide more nucleation sites for the titanium precursor through an increased density of surface OH species, and to remove adventitious carbon species.

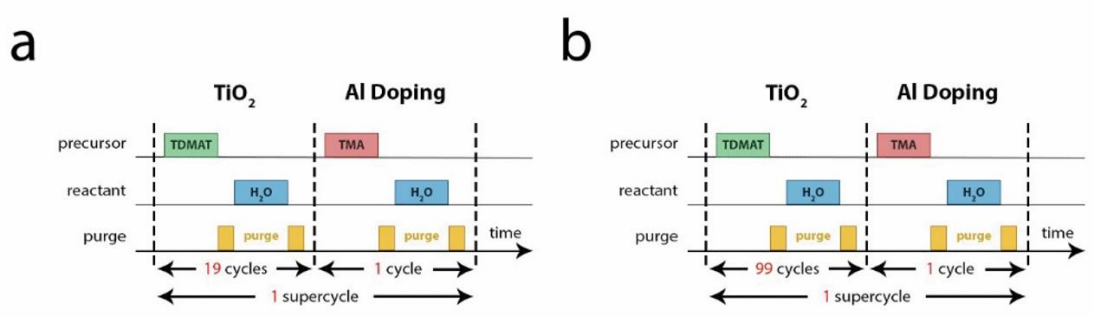

Figure 5. 1: *Schematic showing a typical ALD supercycle for TiO_2 doped with Al_2O_3 in* ***(a)*** *19:1 ratio and* ***(b)*** *99:1 ratio*

The influence of doping ALD TiO_2 was also investigated. Nanolaminate layers comprised of various metal oxides which could affect the electrical properties of the TiO_2 ETLs were introduced by ALD. The laminate doping was applied by introducing the secondary metal precursors in a 19:1 and 99:1 ratio of TiO_2:dopant pulses (Figure 5.1 where secondary metal precursor is trimethylaluminum). This was performed to establish whether there was a difference in electrical properties between the thin films depending on titanium precursor, reactant, dopant and ratio of applied dopant, any of which could enhance performance when incorporated into a mesoporous PSC.

5.2 Experimental

5.2.1 Substrate Cleaning and preparation

All perovskite solar devices were prepared on high temperature resistant alumino-boroscilicate glass coated with fluorine-doped tin oxide (FTO) which served as a transparent electrode (50 mm^2 TEC-15, 15 Ω cm^{-1} or TEC-7, 7 Ω cm^{-1} from Solaronix).

At Tyndall National Institute the FTO coated glass was diced into 25 mm^2 substrates prior to cleaning. The substrates were cleaned by successive ultra-sonication in Decon 90 (5 % in deionised water) for 30 minutes, followed by acetone and 2-propanol for 15 minute each. A N_2 gun was used to thoroughly dry samples between each step. Other substrates used for characterisation such as glass and quartz were also cleaned in this way. n-type Si(100) wafers, which were used as substrates to determine ALD film thickness, were treated with an initial surface clean using a Semitool Spray Acid. O_3, hot deionised water, NH_4OH and HF were used to remove organic contaminants and particles from the wafer surface prior to oxidation. This treatment produced a chemical passivation oxide of approximately 1.45 nm on the wafer surface.

Prior to ALD deposition, The FTO glass substrates were first etched with a laser to form two detached electrode patterns. This isolation of the FTO is commonly referred to as a P1 line and was scribed using a UV ArF excimer laser (193 nm Lasertechnik ATLEX 300i) 5 mm from the edge of each 25 mm^2 FTO coated glass substrate. The excimer laser focused on the front face of the FTO coated glass, isolating the FTO (Figure 5.2). FTO coated glass substrates were then patterned using 0.6 mm kapton tape as described in Appendix I, Figure 1 before ALD deposition.

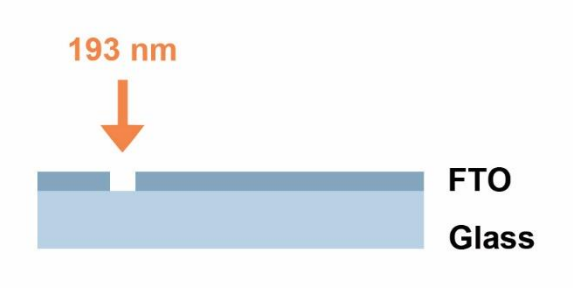

Figure 5. 2: *Interconnection schematic showing P1 line scribed from front face of FTO coated glass using ArF excimer laser*

At CSEM, large FTO coated glass sheets were cut into 100 mm^2 segments and cleaned using a dishwasher designated only for substrate cleaning. This cleaning procedure comprised of a basic solution, Deconex NS-X (Borer Chemie), followed by an acidic solution, Deconex Organacid (Borer Chemie), to suitably clean the Solaronix FTO coated glass. Subsequently, these segments were patterned using 0.6 mm kapton tape and then deposited with 20 nm TiO_{2-x} by RF sputtering to form the front electrode/hole blocking layer stack. A frequency tripled Nd:YAG laser (Newport BLS, 355 nm) was employed to scribe a P1 isolation line at 5 mm from the edge of each 25 mm^2 cell which would later be cut from a 100 mm^2 TiO_{2-x}/FTO coated glass segment. The P1 line was 20 µm in width.[1,2] The UV laser focused on the glass side of the FTO coated glass segments successfully isolating the transparent conductive oxide, FTO (Figure 5.3). The TiO_{2-x}/FTO coated glass segments were then diced into 25 mm^2 substrates and cleaned using a N_2 gun. For mesoporous PSCs incorporating ALD, 50 mm^2 FTO coated glass substrates were cleaned and deposited on at Tyndall National Institute before being P1 scribed, diced and fabricated at CSEM by the author.

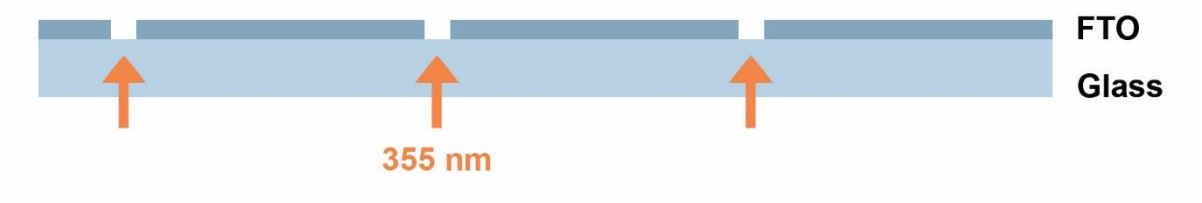

Figure 5. 3: *Interconnection schematic showing P1 line scribed from back face of FTO coated glass using Newport BLS, 355 nm, nanosecond pulse UV laser*

5.2.2 Deposition of nominally undoped and doped ALD TiO_2

Deposition of TiO_2 thin film ETLs was carried out on two commercial ALD reactors at Tyndall National Institute, a Cambridge Nanotech Fiji F200 and a Picosun R200 system. The growth methodologies employed in the Picosun and Cambridge Nanotech reactors differ due to their design characteristics. Both reactors feature different flow rates and chamber sizes which can affect growth. The heating of the precursors also varies from reactor to reactor causing reproducibility of literature experiments to become difficult as described in sections 5.2.2.1 and 5.2.2.2 respectively.

All metal oxides were deposited at 185°C to meet the thermal restrictions of perovskite/silicon heterojunction tandem cells, one of the promising applications for PSCs[3]. The Cambridge NanoTech Fiji F200 was employed for the growth of TiO_2 using titanium (IV) isopropoxide (TTIP) or tetrakis (diemthylamido) titanium (TDMAT) and H_2O or Ar/O_2 plasma in an argon carrier flow as the metal precursors and oxygen sources respectively, leading to a deposition rate of 0.2 Å per cycle with TTIP and 0.5 Å per cycle with TDMAT. The Picosun R200 grew TiO_2 using a N_2 carrier flow. TDMAT and H_2O or Ar/O_2 plasma were used as the Ti precursor and co-reactants. A study into the precursor TTIP was first carried out using the Cambridge NanoTech reactor. From the results consequently obtained and due to cost of precursor it was decided not to pursue TTIP as a titanium precursor on the Picosun reactor. The growth rate per cycle at 185°C for TDMAT was 0.5 Å using the Picosun R200 system. All growth rates were in agreement with literature values.[4-8]

Doping the ALD TiO_2 thin films in a nanolaminate mode was investigated using different metal oxides which could influence the electrical properties of the thin film. Hafnium was incorporated using the precursor, tetrakis (ethylmethylamino) hafnium (TEMAH).[9,10] The silver precursor, 2,2,6,6-tetramethyl-3,5-heptanedionate silver ($Ag(fod)(PEt_3)$), was also adopted for doping TiO_2.[11-13] The atomic masses of both hafnium and silver would likely cause stress because of their larger atom sizes when compared to titanium.[14] The tin precursor, tetrakis(dimethylamido)tin (TDMASn), was integrated as a dopant because of the similar atomic size of tin to titanium and bonds in the Sn^{4+} state similar to Ti^{4+}.[15-17] The vanadium precursor, tetrakis(dimethylamido)vanadium (TDMAV), was used to dope TiO_2. The vanadium ion is similar to that of titanium and should be easily incorporated into the thin film.[18-

[20] The smaller atom, aluminium (Al^{3+}), was included as a dopant using the precursor, trimethylaluminium (TMA). This was expected to fit into the structure without much distortion due to aluminium's smaller atomic size when compared to titanium.[21-23] These secondary oxides incorporated as dopants span a range of band gaps from the wide band gap Al_2O_3 (7-8 eV), to semiconducting oxides such as SnO_2, and the mid-range band gap of HfO_2 (~5.9 eV).

5.2.2.1 Cambridge Nanotech Fiji System

5.2.2.1 (i) Undoped thermal TiO_2

A nominally undoped TiO_2 thin film was first deposited on glass, quartz, n-Si(100) wafers, and FTO coated glass by ALD. To avoid run-by-run variation in growth experiments all substrate types were loaded together for each TiO_2 variation. Undoped thermal TiO_2 films were deposited at 185°C in a Cambridge Nanotech Fiji system using a thermal reaction. The titanium precursor and reactant used for this deposition were TDMAT and H_2O. The precursor vessel for TDMAT was maintained at 75°C while the H_2O vessel, as previously mentioned in Chapter 4, was not directly heated but maintained at 35°C due to its proximity to nearby heated components on the system. The nominal growth rate of TiO_2 is assumed to be 0.05 nm per cycle. An example pulse/purge sequence, for a nominally 20 nm film, is outlined in Chapter 4, Table IV.I.

Note that samples that included a plasma pre clean were subjected to a 5 minute 300 W Ar/O_2 plasma treatment in situ in the ALD chamber prior to deposition, as described in Table V.I.

Table V. I: *Cambridge Nanotech Fiji ramp to 20 sccm O_2 plasma at 300 W for 5 minutes prior to thermal growth*

Step	*Instruction*	*Number*	*Value*	*Unit*	*Description*
0	MFC valve	3	1	-	MFC valve open: O_2 flow
1	Flow	0	40	sccm	Ar carrier gas in lines ON
2	Flow	1	180	sccm	Ar carrier dilution in reactor ON
3	Wait		20	s	Stabilisation
4	Plasma		300	Watts	Plasma power ON
5	Wait		5	s	Purge
6	Flow	3	5	sccm	O_2
7	Wait		5	s	Purge
8	Flow	3	10	sccm	O_2
9	Wait		5	s	Purge
10	Flow	3	12	sccm	O_2
11	Wait		5	s	Purge
12	Flow	3	14	sccm	O_2
13	Wait		5	s	Purge
14	Flow	3	16	sccm	O_2
15	Wait		5	s	Purge
16	Flow	3	18	sccm	O_2
17	Wait		5	s	Purge
18	Flow	3	20	sccm	O_2
19	Wait		300	s	Stabilisation
20	Flow	3	0	sccm	
21	Plasma		0	Watts	Plasma power OFF
22	MFC valve	3	0	-	MFC valve closed

As shown in Table V.I above, the O_2 plasma required gentle ramping to stabilise from 5 sccm to 20 sccm and avoid plasma collapse.

5.2.2.1 (ii) Undoped plasma enhanced TiO_2

O_2 plasma was employed as a reactant for undoped plasma enhanced TiO_2 for both TDMAT and TTIP precursors. All depositions were performed at 185°C. For growth with TDMAT a 0.3 second pulse was employed for each cycle (Table V.II).

Table V. II: *Experimental parameters for deposition of TiO_2 by plasma enhanced ALD using TDMAT on Cambridge Nanotech Fiji*

Step	*Instruction*	*Number*	*Value*	*Unit*	*Description*
0	MFC valve	3	1	-	MFC valve open: O_2 flow
1	Flow	0	40	sccm	Ar carrier gas in lines ON
2	Flow	1	180	sccm	Ar carrier dilution in reactor ON
3	Wait		20	s	Stabilisation
4	Pulse	1	0.3	s	TDMAT Pulse
5	Wait		10	s	Purge
6	Plasma		300	Watts	Plasma power ON
7	Wait		5	s	Purge
8	Flow	3	10	sccm	O_2
9	Wait		5	s	Purge
10	Flow	3	15	sccm	O_2
11	Wait		10	s	Purge
12	Flow	3	0	sccm	O_2
13	Wait		5	s	Purge
14	Plasma		0	Watts	Plasma power OFF
15	Wait		10	s	Purge
16	Goto	4	400	-	Number of cycles
17	Flow	0	20	sccm	Ar carrier gas in lines OFF
18	Flow	1	20	sccm	Ar carrier dilution in reactor OFF

In step (0) the stop valve isolating the mass flow (MFC) is opened. In step (1) and (2) the precursor manifold carrier and plasma source purge flow rates are set. Step (3) involves waiting a total of 20 seconds for the Ar MFCs to stabilize. At (4) the loop begins as the precursor TDMAT is pulsed for 0.3 seconds. A wait of 10 seconds at (5) allows for a purge of the TDMAT and reaction by-products. At step (6) the plasma is turned on at 300 Watts. A wait of 5 seconds is allowed in step (7) before the O_2 flow stabilises at 10 sccm at (8) for 5 seconds. This is increased to 15 sccm in step (10). A wait of 10 seconds is allowed before the O_2 flow is turned off. At step (14) the plasma source is turned off and a waiting period of 10 seconds is allowed to purge any remaining O_2 and reaction by-products. Step (16) stands for "go to" next cycle where it returns to step 4 and repeats for a total of 400 cycles. In step (17) and (18) the precursor manifold carrier and plasma source purge flow rates are set to stand-by rates.

Figure 5.4 illustrates pressure versus time trace observed for the PEALD recipe in Table V.II.

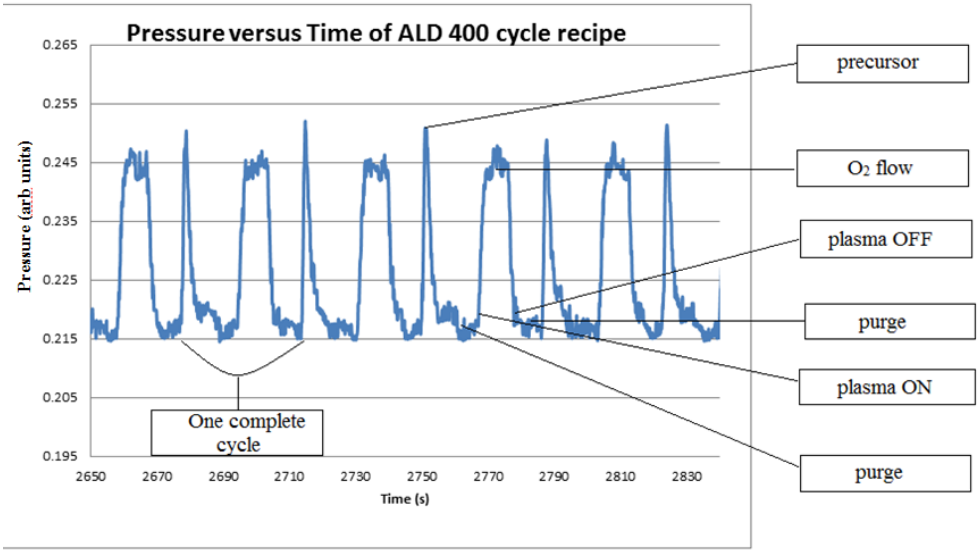

Figure 5. 4: *Graph of pressure versus time representing steps of ALD recipe for PEALD*

Note in this study TiO_2 grown by the precursor TTIP was only observed through use of PEALD as no growth was apparent when H_2O was used as a reactant. The precursor, TTIP, was gradually heated from 50°C in 5°C increments and tested until a pulse of precursor was obtained. The TTIP vessel was maintained at 110°C while four 0.6 second pulses were employed in quick succession between each pulse of an O_2 plasma reactant (Table V.III). The growth rate was found to be 0.02 nm per cycle, requiring 1000 cycles to reach 20 nm.

Table V. III: *Experimental parameters for deposition of TiO_2 by plasma enhanced ALD using TTIP on Cambridge Nanotech Fiji*

Step	*Instruction*	*Number*	*Value*	*Unit*	*Description*
0	MFC valve	3	1	-	MFC valve open: O_2 flow
1	Flow	0	40	sccm	Ar carrier gas in lines ON
2	Flow	1	180	sccm	Ar carrier dilution in reactor ON
3	Wait		20	s	Stabilisation
4	Pulse	4	0.6	s	TTIP Pulse
5	Wait		2	s	Purge
6	Goto	4	4	-	Number of TTIP pulses
7	Wait		10	s	Purge
8	Plasma		300	Watts	Plasma power ON
9	Wait		5	s	Purge
10	Flow	3	10	sccm	O_2
11	Wait		5	s	Purge
12	Flow	3	15	sccm	O_2
13	Wait		10	s	Purge
14	Flow	3	0	sccm	O_2
15	Wait		5	s	Purge
16	Plasma		0	Watts	Plasma power OFF
17	Wait		10	s	Purge
18	Goto	4	1000	-	Number of cycles
17	Flow	0	20	sccm	Ar carrier gas in lines OFF
18	Flow	1	20	sccm	Ar carrier dilution in reactor OFF

5.2.2.1 (iii) Doped TiO_2

All doped films in this study were grown in a nanolaminate mode and, to satisfy the thermal budget restrictions of perovskite/silicon heterojunction tandem cells,[3] at 185°C. Nanolamination in ALD refers to cycles of a secondary metal precursor and a reactant incorporated into the matrix of a thin film consisting of a separate material. This dopant laminate layer is nanoscale in thickness and may influence the electrical properties of the entire thin film structure. Doping was restricted to ratios of 19:1 and 99:1 of TiO_2:dopant pulses. Doping by ALD is unlike traditional doping as it forms laminate layers. This can dictate the crystallinity of the TiO_2 thin films and influence their resulting properties.[24, 25] Previous work by Wu et al. has shown that the conductivity of ZnO doped with Al atoms using ALD was improved by varying the doping level.[26] This improvement in conductivity can be limited by inhomogeneous distribution of the Al atoms within a supercycle growth.[26, 27] Too high a doping level will produce small spacing between the layers of dopant in the thin film matrix. This has been shown to produce overlaps of dopant profiles, which can affect conductivity and doping efficiency, by Atom Probe Tomography (APT) characterisation.[28] Too low

a doping level will not impact the conductivity of thin films. Low doping efficiency can be influenced by the dopant's solubility in the matrix material and suppression of ionisation of the dopant by adjacent dopant atoms. The 19:1 doping ratio was decided upon for this study due to its successful application in depositing conductive ZnO:Al in the literature.[27,29-31] Similarly, a 99:1 doping ratio has recently been reported for doping ZnO with aluminium-hydroquinine.[32] These ratios were chosen for use in a preliminary study to establish if any notable differences could be observed in the electrical properties of TiO_2 layers doped with a wide variety of dopants.

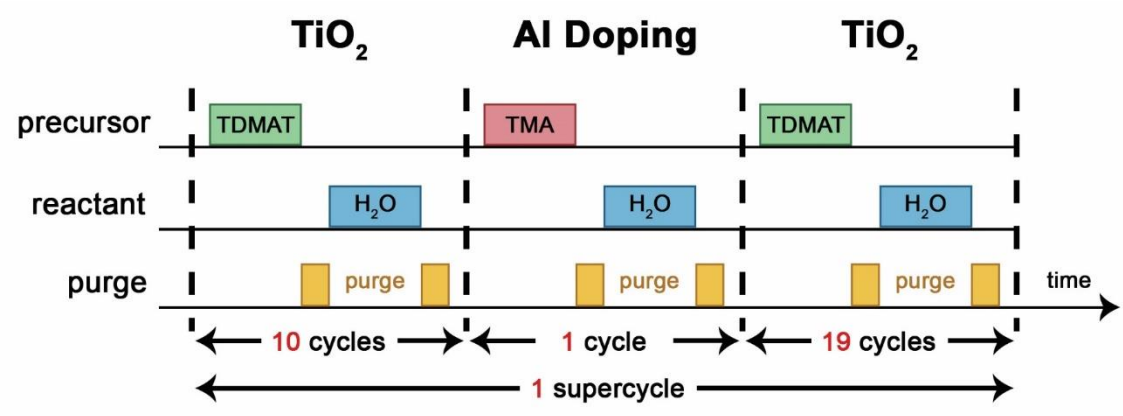

Figure 5. 5: *Schematic showing a typical ALD supercycle for TiO_2 doped with Al_2O_3 in a 19:1 ratio ensuring that the interfaces were not dominated by the dopant*

Prior to growth all substrates were subjected to a 5 minute O_2 plasma treatment in situ in the ALD chamber. In order to assess the bulk material the laminate method was adapted so as to not terminate on a doping cycle, for example, for the 19:1 ratio samples 10 cycles of TiO_2 were introduced through use of TDMAT or TTIP as the titanium precursor and H_2O or O_2 plasma as the reactant, this was followed by a cycle of the dopant and co-reagent and a further 19 cycles of TiO_2 (Figure 5.5).

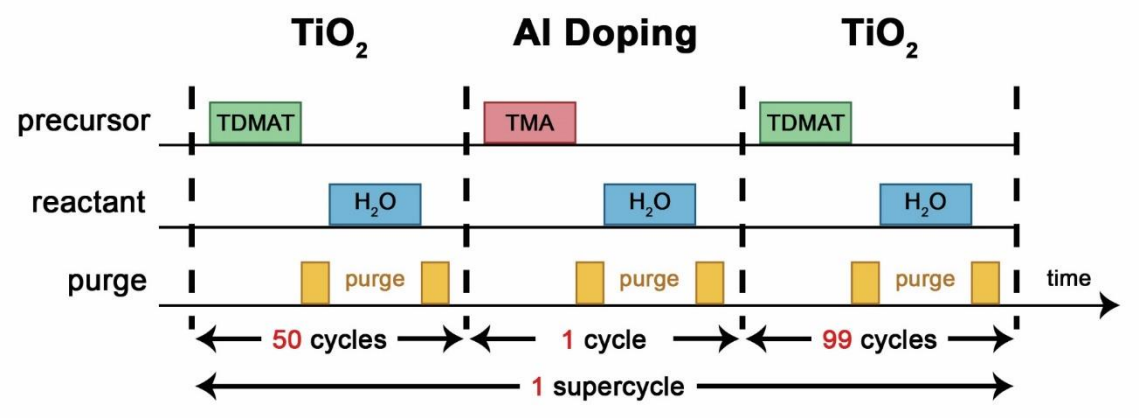

Figure 5. 6: *Schematic showing a typical ALD supercycle for TiO_2 doped with Al_2O_3 in a 99:1 ratio ensuring that the interfaces were not dominated by the dopant*

For the addition of dopants in the 99:1 ratio, 50 cycles of TiO_2 were introduced before a cycle of the dopant second precursor and reactant (Figure 5.6). These respective 10 and 50 cycles allowed nucleation of the TiO_2 and ensured that the dopant metal precursor was not at the interface of the material and would be contributing to the bulk growth regime and not the nucleation regime of the thin film. The supercycles continued until 400 cycles were deposited. Table V.IV below outlines the reaction conditions used for each variation of dopant and ratio incorporated into the TiO_2 films using the Cambridge Nanotech Fiji system.

Table V. IV: *Table showing titanium precursors, reactants, dopants and ratios used*

Ti precursor	*Ti pulse (s)*	*Reactant*	*Reactant pulse (s)*	*Purge time (s)*	*Dopant precursor*	*Dopant pulse (s)*	*Dopant reactant*	*Ratio*
TDMAT	0.3	H_2O	0.1	10	-	-	-	-
TDMAT	0.3	O_2 plasma	10	10	-	-	-	-
TDMAT	0.3	H_2O over O_2 plasma	0.1/10	10	-	-	-	-
TTIP	4 x 0.6	O_2 plasma	10	10	-	-	-	-
TTIP	4 x 0.6	O_2 plasma	10	10	TMA	0.1	O_2 plasma	19:1
TTIP	4 x 0.6	O_2 plasma	10	10	TMA	0.1	O_2 plasma	99:1
TDMAT	0.3	H_2O	10	10	TMA	0.1	H_2O	19:1
TDMAT	0.3	H_2O	0.1	10	TMA	0.1	H_2O	99:1
TDMAT	0.3	H_2O	0.1	10	TEMAH	0.3	H_2O	19:1
TDMAT	0.3	H_2O	0.1	10	TEMAH	0.3	H_2O	99:1
TDMAT	0.3	H_2O	0.1	10	Ag(fod)(PEt_3)	0.3	H_2O	19:1
TDMAT	0.3	H_2O	0.1	10	Ag(fod)(PEt_3)	0.3	H_2O	99:1
TDMAT	0.3	H_2O	0.1	10	TDMASn	0.3	H_2O	19:1
TDMAT	0.3	H_2O	0.1	10	TDMASn	0.3	H_2O	99:1
TDMAT	0.3	H_2O	0.1	10	TDMAV	0.3	H_2O	19:1
TDMAT	0.3	H_2O	0.1	10	TDMAV	0.3	H_2O	99:1

5.2.2.2 Picosun R200 System

5.2.2.2 (i) Undoped thermal TiO_2

A nominally undoped TiO_2 thin film was first deposited on glass, quartz, n-Si(100) wafers, and FTO coated glass by ALD. To avoid run-by-run variation in growth experiments all substrate types were loaded together for each TiO_2 variation. Undoped thermal TiO_2 films were deposited at 185°C in a Picosun R200 system using a thermal or plasma enhanced reaction. The titanium precursor and reactant used for the depositions were TDMAT and either an O_2 plasma at 2.95 kW or H_2O. The precursor vessel for the TDMAT was maintained at 65°C, while the vessel neck was held at 80°C. The H_2O reactant was maintained at a room temperature of approximately 27°C where an adequate vapour pressure was achieved. The nominal growth rate was assumed to be 0.05 nm per cycle. A pulse/purge sequence was adopted as outlined in Table V.V with a 1.6 second TDMAT pulse duration.

Due to the indirect heating of the substrate in the Picosun system, samples were given a 40 minute stabilisation time within the reaction chamber prior to processing. The

length of temperature stabilisation period was determined by the thermal-optical response of silicon as measured by in situ ellipsometry.

The Picosun R200 ALD system has a boost function which can be used for solid precursors with lower than ideal vapour pressures. The precursor vessel is equipped with a second precursor valve which allows the carrier gas (N_2) to flow through the precursor bottle when pulsing valves are active. This allows better transportation of the precursor chemical to the reactor. The carrier gas maintains a constant pressure for each pulse and allows the same sized pulse to be dosed consistently.

Table V. V: *Experimental parameters for deposition of thermal TiO_2 subjected to a 5 minute O_2 plasma treatment prior to deposition using TDMAT on Picosun R200*

Precursor	*Pulse*	*Purge*	*Repeat*
O_2 plasma	152 s		2
Purge		8 s	
TDMAT	1.6 s		400
Purge		8s	
H_2O	0.1 s		
Purge		8s	

Table V.V outlines the recipe used for the growth of thermal TiO_2 which was subjected to an in-situ O_2 plasma treatment prior to ALD growth at 185°C. The O_2 plasma (2.97 kW) was pulsed for 152 seconds before a break of 8 seconds to limit thermal effects. This was followed by a further 152 second pulse of plasma. This, when added to 4 seconds stabilisation time for each plasma pulse, gave a total of a 5 minute O_2 plasma clean. Following the plasma clean, a 10 second purge time was allowed before the first precursor, TDMAT, was introduced for 1.6 seconds using the boost function. After an 8 second purge a 0.1 second pulse of H_2O was introduced with another 8 second purge to complete the cycle. The cycle of TDMAT and H_2O was repeated for a total of 400 cycles. The nominal thickness of the thin film grown was 20 nm assuming a growth rate of 0.05 nm per cycle.

Similarly, nominally undoped TiO_2 thin films were deposited using PEALD. Here the H_2O was replaced with O_2 plasma, a 5 minute O_2 plasma treatment prior to ALD growth was not employed.

5.2.2.2 (ii) Doped TiO_2

As with the Cambridge Nanotech reactor all nanolaminate films were deposited at 185°C in a 19:1 ratio and a 99:1 ratio of TiO_2:dopant pulses.

Table V. VI: *Experimental parameters for deposition of TiO_2 with dopant in 19:1 ratio on Picosun R200 system*

	Precursor	*Pulse*	*Purge*	*Repeat*
	O_2 plasma	152s		2
	Purge		8s	
	TDMAT	1.8s		10
	Purge		8s	
	H_2O	0.1s		
	Purge		8s	
	Dopant precursor	1.8s/0.1s		1
Loop 20	Purge		8s	
	H_2O	0.1s		
	Purge		8s	
	TDMAT	1.8s		9
	Purge		8s	
	H_2O	0.1s		
	Purge		8s	

For example, the recipe for a 19:1 dopant ratio can be observed in Table V.VI. After a 40 minute stabilisation time in the reaction chamber, samples are subjected to the plasma clean. Following the plasma clean, as with the undoped samples a 10 second purge time was allowed before the first precursor, TDMAT, was introduced for 1.6 seconds using the boost function. After an 8 second purge a 0.1 second pulse of H_2O was introduced with another 8 second purge directly after to complete the cycle. As with the Cambridge Nanotech system, the supercycles were modified to ensure that the interfaces were not dominated by the dopant (Figure 5.5, 5.6).

A similar scheme was adopted for the 99:1 ratio, 50 cycles of TiO_2 were first introduced after 5 minutes of an O_2 plasma clean. A pulse of the second metal precursor was added followed by a purge and a pulse of H_2O reactant. This step was followed by 49 cycles of TiO_2 to complete the supercycle. The supercycles continued until a total of 400 cycles were deposited. The nominal thickness of all ALD TiO_2

films grown was 20 nm assuming a 0.05 nm per cycle growth rate. The growth parameters are outlined below in Table V.VII.

Table V. VII: *Table showing growth parameters with variations in reactants, dopants and ratios used on Picosun R200 system*

TDMAT pulse (s)	*Carrier (sccm)*	*TDMAT boost (sccm)*	*React*	*React pulse (s)*	*Purge time (s)*	*Dopant precursor*	*Dopant pulse (s)*	*Dopant boost (sccm)*	*Ratio*
1.6	80	600	H_2O	0.1	8	-	-	-	-
1.6	80	600	O_2 plasma	24	8	-	-	-	-
1.6	80	600	H_2O	0.1	8	TMA	0.1	-	19:1
1.6	80	600	H_2O	0.1	8	TMA	0.1	-	99:1
1.6	80	600	H_2O	0.1	8	TEMAH	1.6	600	19:1
1.6	80	600	H_2O	0.1	8	TEMAH	1.6	600	99:1
1.6	80	600	H_2O	0.1	8	TDMASn	1.6	600	19:1
1.6	80	600	H_2O	0.1	8	TDMASn	1.6	600	99:1

For doped samples grown by the laminate method ALD the doping process could be monitored by in situ spectroscopic ellipsometry (SE) using a Woollam M2000D system (193 - 998.9 nm). Although dopant levels could not be quantified, the growth mode could be verified in real time by sampling and analysing in dynamic capture mode the using CompleteEASE software (Woollam) coupled with a Cauchy model to describe the TiO_2 film deposited. In situ ellipsometry is a useful technique that is available to many commercial ALD systems on the market. Despite this, there are some drawbacks present with the system used in this study. The models used are based on room temperature fits for these measurements while the thin film in reality was deposited at 185°C. The refractive index is also assumed to be constant with increasing thickness which practically is unlikely.

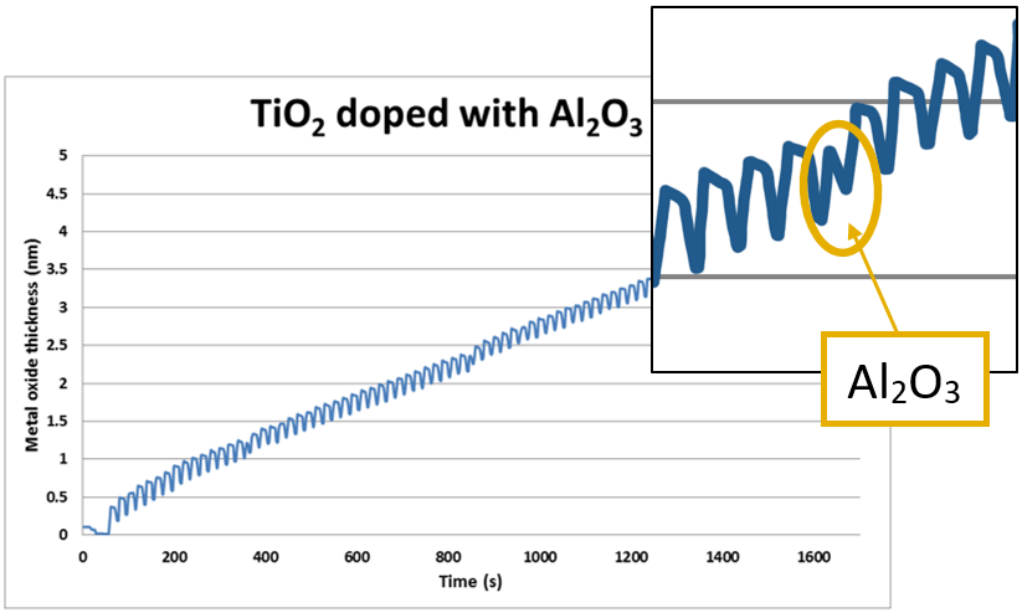

Figure 5. 7: *In situ SE of TiO_2 doped with Al_2O_3 in 24:1 supercycle*

For example, Figure 5.7 displays the fitted thickness with time plot from a real time observation of TiO_2:Al_2O_3 growth in the ratio 24:1. The measurement time was set to capture data at 1.6 second intervals, which allowed resolution of the cyclic nature of the precursor pulsing and purging. The step-wise nature of ALD TiO_2 film growth can be observed with the thickness increasing with increased number of cycles. The second precursor, TMA, is introduced every 24 cycles which is indicated by its smaller peak as displayed in the expanded view. The Al_2O_3 peak is notably smaller than that of TiO_2 due to its lower refractive index of 1.770 compared to 2.493 for TiO_2.

5.2.3 Fabrication of mesoporous PSCs

25 mm^2 TEC 15 FTO coated glass substrates (Solaronix TCO22-15) were cleaned and the metal oxide blocking/electron transport layer deposited via ALD as described in section 5.2.1 and 5.2.2.

The perovskite solution was prepared in the glove box, 225.05 mg of MAI (Dyesol) was added to 652.52 mg PbI_2 (TCI) in a 4 ml vial. A magnetic stirrer was added to the vial, followed by 1,000 µl of a 1:9 volume ratio of DMSO:DMF (Sigma Aldrich). This 1.4 M perovskite solution was allowed to stir overnight in the glove box.

Fifteen hours later, mesoporous TiO_2 (m-TiO_2) paste (Sharechem) was stirred into a dilution of IPA at a ratio of 1:5. A magnetic stir bar was placed in the m-TiO_2 paste and allowed to stir on a hot plate at 27°C for 15 minutes. Prior to spin coating, the ALD TiO_2 blocking layer/FTO coated glass substrates were blown with a N_2 gun to ensure any contaminants such as dust or loose particles could be removed. 4 drops of the m-TiO_2 solution were deposited from a dropper onto the centre of the substrate and spin coated at 4,500 rpm for 30 seconds to form the scaffold layer. The samples were immediately dried on a hot plate at 125°C for 5 minutes before being sintered. The sintering of the scaffold required the temperature to be ramped up from 125°C to 500°C in stages, Table V.VIII, and then allowed to cool for 1 hour before further processing. It should be noted that in Chapter 4 Dyesol 18NRT was utilised as the mesoporous TiO_2 paste while the brand Sharechem was processed for this study in Chapter 5. Collaborators were found to have their own preferences in terms of brands and the author adhered to their use for each chapter. This allowed like to be compared with like in each investigation with the sole variation being the ETL.

Table V. VIII: *Sintering process for mesoporous scaffold layer*

	Step 1	*Step 2*	*Step 3*	*Step 4*	*Step 5*
Ramp time	5 min	15 min	5 min	5 min	5 min
Temperature	125°C	325°C	375°C	450°C	500°C
Stabilised time	5 min	5 min	5 min	15 min	15 min

After stirring overnight, the perovskite solution was filtered into a clean vial using a 0.45 µm PTFE filter. This was then removed from the glove box and spin coated on the cooled m-TiO_2/ ALD TiO_2/ FTO coated glass substrates. The samples were again blown with a N_2 gun directly prior to spin coating to remove any contaminants from the environmental surroundings. 65 µl $MAPbI_3$ solution was micro-pipetted on the centre of the substrates before they were spun at 1,000 rpm for 10 seconds, followed by 5,000 rpm for 45 seconds. 0.75 ml of diethyl ether (Sigma Aldrich) was carefully used as an anti-solvent treatment 35 seconds before the end of the spin coating process. Samples were then dried for 2 minutes at 50°C and annealed for 10 minutes at 100°C.

The HTL was prepared by dissolving 43.4 mg 2,2',7,7'-tetrakis- (N,N-di-4-methoxyphenylamino) -9,9'spirobi-fluorenes (Spiro-OMeTAD) (Merck) in 17.3 µl/ml 4-tert-butylpyridine (tBP) (TCI), 10.5 µl/ml stock solution of 520 mg/ml lithium bis (trifluoromethylsulfonyl) imide (LiTFSI) (Sigma-Aldrich) in acetonitrile, in 600

µl chlorobenzene. This was spin coated on top of the perovskite layer at 4,000 rpm for 30 seconds. The devices were completed with the evaporation of a 100 nm gold electrode using a Lesker mini-spectros system, with substrate temperature of 80°C and a base pressure of 1.5 × 10−6 Torr. The spin coating steps carried out for the fabrication of mesoporous PSCs are outlined in Table V.IX.

Table V. IX: *Spin coating programmes for mesoporous PSC*

	m-TiO_2 scaffold	*$MAPbI_3$ Step 1*	*$MAPbI_3$ Step 2*	*HTL*
Rate (rpm)	4,500	1,000	5,000	4,000
Time (s)	30	10	45	30
Acceleration	1,500	200	1,000	1,650

All mesoporous device fabrication for both ALD and sputtered TiO_{2-x} ETLs in this chapter was carried out by the author while performing an internship at CSEM.

5.3 Results and Discussion

TiO_2 thin films were successfully deposited on a range of substrates using both thermal and plasma enhanced ALD by two different ALD systems, a Cambridge Nanotech Fiji system and a Picosun R200 system, at 185°C. Titanium precursors TDMAT and TTIP were studied with co-reactants water and oxygen plasma. A nanolaminate doping method was applied by introducing a range of second precursors in a 19:1 and 99:1 ratio of TiO_2:dopant. This was performed to establish whether there was a difference in electrical properties between the thin films depending on titanium precursor, reactant, dopant and ratio of applied dopant, any of which could enhance performance when incorporated into a mesoporous PSC. Mesoporous PSCs were then fabricated and their J-V characteristics were analysed in relation to the ALD ETLs.

5.3.1 Sigma Dark

Dark conductivity measurements of the 20 nm based ALD TiO_2 samples on glass were performed under a 1 mbar N_2 atmosphere. Evaporation of 200 nm thick Ag contacts, using a 1 mm x 8 mm mask, was performed prior to measurement. Samples were subjected to a temperature ramp from room temperature to 180°C at a rate of 10°C min^{-1} and then cooled at a rate of 1°C min^{-1}. Conductivity of the samples was measured during the cooling phase.

Table V. X: *Sample ID for Sigma Dark characterisation*

Sample ID	*Composition*	*ALD Reactor*
TT_a	Plasma Enhanced TiO_2 (TTIP)	Cambridge Nanotech Fiji
TT_b1	TiO_2:Al 19:1 (TTIP)	Cambridge Nanotech Fiji
TT_b2	TiO_2:Al 99:1 (TTIP)	Cambridge Nanotech Fiji
TD_a	Thermal TiO_2 (TDMAT)	Cambridge Nanotech Fiji
TD_b	O_2 plasma pre-clean, thermal TiO_2 (TDMAT)	Cambridge Nanotech Fiji
TD_c	Plasma Enhanced TiO_2 (TDMAT)	Cambridge Nanotech Fiji
TD_d	Plasma pulsed over water reactant, TiO_2 (TDMAT)	Cambridge Nanotech Fiji
TD_e1	O_2 plasma pre-clean, thermal TiO_2:Al 19:1 (TDMAT)	Cambridge Nanotech Fiji
TD_e2	O_2 plasma pre-clean, thermal TiO_2:Al 99:1 (TDMAT)	Cambridge Nanotech Fiji
TD_f1	O_2 plasma pre-clean, thermal TiO_2:V 19:1 (TDMAT)	Cambridge Nanotech Fiji
TD_f2	O_2 plasma pre-clean, thermal TiO_2:V 99:1 (TDMAT)	Cambridge Nanotech Fiji
TD_g1	O_2 plasma pre-clean, thermal TiO_2:Hf 19:1 (TDMAT)	Cambridge Nanotech Fiji
TD_g2	O_2 plasma pre-clean, thermal TiO_2:Hf 99:1 (TDMAT)	Cambridge Nanotech Fiji
TD_h1	O_2 plasma pre-clean, thermal TiO_2:Ag 19:1 (TDMAT)	Cambridge Nanotech Fiji
TD_h2	O_2 plasma pre-clean, thermal TiO_2:Ag 99:1 (TDMAT)	Cambridge Nanotech Fiji
TD_i1	O_2 plasma pre-clean, thermal TiO_2:Sn 19:1 (TDMAT)	Cambridge Nanotech Fiji
TD_i2	O_2 plasma pre-clean, thermal TiO_2:Sn 99:1 (TDMAT)	Cambridge Nanotech Fiji
PTD_j	O_2 plasma pre-clean, thermal TiO_2:Sn 19:1 (TDMAT)	Picosun R200
PTD_k	O_2 plasma pre-clean, thermal TiO_2:Hf 19:1 (TDMAT)	Picosun R200
PTD_l	O_2 plasma pre-clean, thermal TiO_2:Al 19:1 (TDMAT)	Picosun R200

In this section, the ALD thin films which underwent characterisation were provided with sample ID labels for ease of illustration. The corresponding composition is outlined in Table V.X.

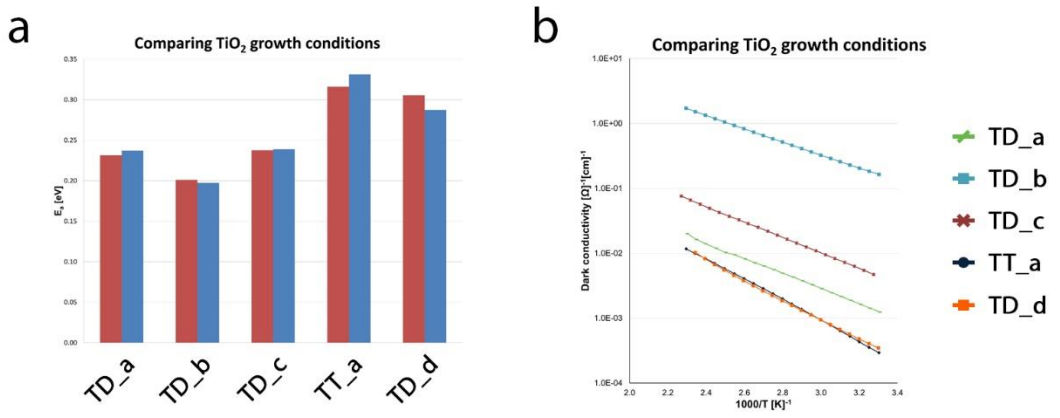

Figure 5. 8: (a) *Bar chart showing activation energy and* ***(b)*** *Arrhenius plot of the surface conductivity of ALD TiO_2 thin films comparing titanium precursor and reactant. TiO_2 deposited using TDMAT and H_2O with a 5 minute plasma clean prior to growth is observed to be the most conductive*

A bar chart comparing E_a, as well as an Arrhenius plot of the surface conductivity for undoped ALD TiO_2 thin films deposited by the Cambridge Nanotech Fiji system on glass are illustrated in Figure 5.8, demonstrating semi-conducting behaviour for all films with conductivity increasing as temperature increases. In addition, it can be seen that the bulk conductivity of the thin films is precursor dependent. The titanium precursor, TTIP, was found to be a less reactive precursor at the low deposition temperature of 185°C, requiring O_2 plasma as a reactant for growth (sample ID TT_a). The growth rate was quite low at 0.2 Å per cycle, implying either sub monolayer growth from a non-limiting reaction, or stearic hindrance by the ligands.

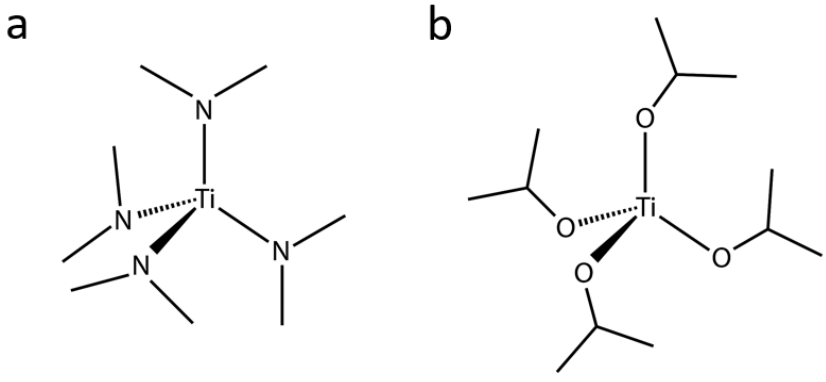

Figure 5. 9: *Illustration of chemical structures for (a) TDMAT and (b) TTIP*

It can be observed in Figure 5.9 that TTIP is a notably larger molecule than TDMAT. Reaction mechanism studies indicate that between deposition temperatures of 150°C to 200°C, two ligands per TTIP molecule are released during the exchange reaction with a hydroxylated surface.[33, 34] Combined with steric hindrance, a lower amount of TTIP molecules are likely to saturate the surface compared to TDMAT. This could lead to a difference in density between TiO_2 films deposited by TDMAT and TTIP.

There are discrepancies in the literature regarding the growth rate of TiO_2 thin films using the precursor, TTIP, underlining the complexity of ALD and its dependence on reactor design. A growth rate as high as 0.15 nm per cycle by pulsed beam CVD at a deposition temperature of 150°C has been reported by Döring et al.[35] Adversely, at the same deposition temperature, a growth rate of 0.015 nm per cycle was obtained using ALD by Ritala et al.[36] while a temperature-independent growth rate of 0.03 nm per cycle was exhibited between 250°C and 350°C. TiO_2 using TTIP and H_2O_2 below reaction temperatures of 150°C have been shown to have a higher growth rate than TiO_2 films deposited using TTIP and H_2O. This is due to the H_2O_2 reactant being better able to eliminate alkoxide ligands. At higher deposition temperatures, the growth rate was found to be independent of oxygen reactants.[37] Previous work by Jeong et al. found PEALD of TTIP to have a growth rate of 0.045 nm per cycle when deposited at 180°C on an Al bottom electrode of 60 nm patterned on SiO_2 substrates.[38] Stearic hindrance and kinetic limitation have been suggested as the main reasons for low growth rate using the precursor TTIP.[34]

The titanium precursor, TDMAT, was found to be more reactive as it only required H_2O as a reactant and provided the higher growth rate of 0.5 Å per cycle at 185°C. TDMAT allows for better coverage approaching ideal monolayer growth, resulting in a more uniform microstructure. It is expected that this is the reason for better resultant electrical properties. As described by Xie et al., TDMAT is more reactive at this lower temperature and would be the superior choice for ALD growth.[5] It is of significance that samples subjected to an O_2 plasma treatment prior to being deposited using TDMAT and H_2O demonstrate a marked improvement in conductivity over all other methods of depositing TiO_2 by ALD (sample ID TD_b). This plasma clean immediately preceding the deposition is likely to provide more nucleation sites for

ALD. With the introduction of TDMAT, these reactive sites form an increased number of chemisorbed species upon surface reaction, enhancing the ALD deposition. The use of an O_2 plasma is also known to remove adventitious carbon, which would result in a non-uniform growth, from the surface of the substrate.[39]

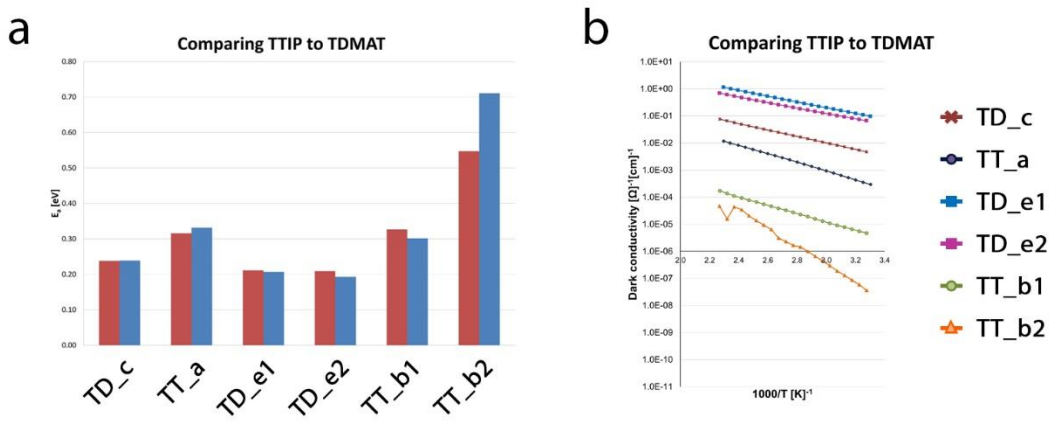

Figure 5. 10: (a) *Bar chart showing activation energy and* ***(b)*** *Arrhenius plot of the surface conductivity of ALD TiO_2 thin films comparing TDMAT to TTIP with doping of Al_2O_3 in a 19:1 and 99:1 ratio*

Figure 5.10 displays a comparison of TDMAT and TTIP growths. PEALD of TiO_2 using TDMAT (sample ID TD_c) shows an improved conductivity when compared to the same growth using TTIP (sample ID TT_a). Although TDMAT appears to outperform TTIP when doped with Al_2O_3 in a 19:1 and 99:1 ratio, it should be noted that this is not solely due to the TDMAT precursor. TDMAT was used in conjunction with a H_2O reactant for deposition of TD_e1 and TD_e2 thin films. TTIP was used in conjunction with an O_2 plasma reactant for deposition of TT_b1 and TT_b2 thin films. The O_2 plasma reactant has previously been shown to contribute to a less conductive thin film than H_2O when employed for TiO_2 films deposited using TDMAT. The TTIP precursor was only found to deposit TiO_2 through use of an O_2 plasma reactant in this study. TiO_2 doped with Al_2O_3 in a 19:1 ratio demonstrates improved conductivity when compared to the 99:1 doped thin films. Despite the 99:1 ratio TiO_2:Al films containing less dopant material, their semi-conducting behaviour was severely inhibited compared to the undoped and 19:1 doped versions.

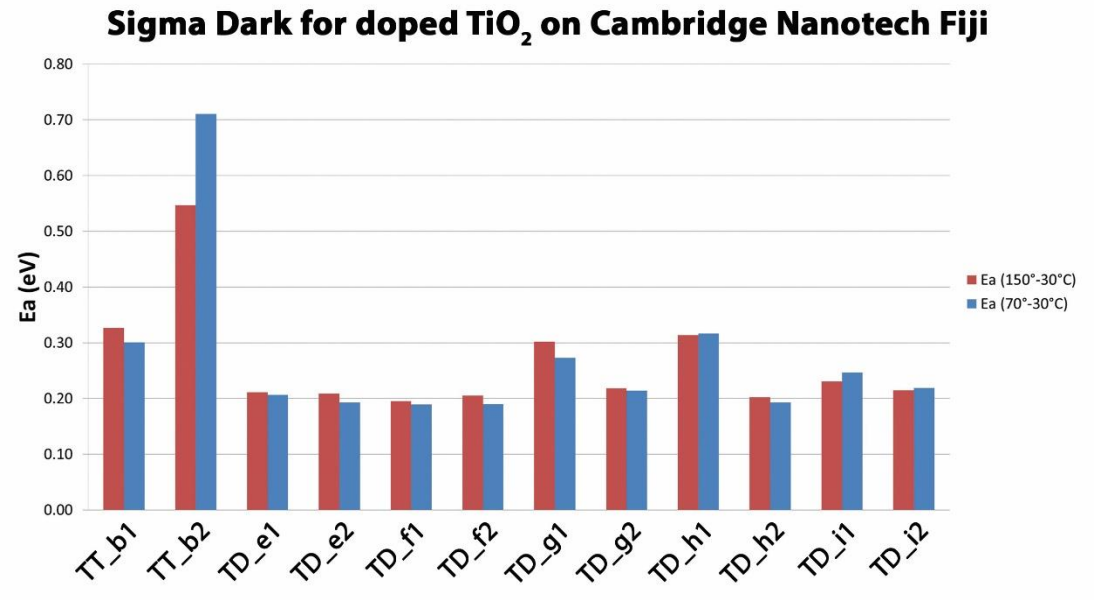

Figure 5. 11: *Bar chart showing electrical conductivity for all nanolaminate doped films on the Cambridge Nanocech Fiji system*

In Figure 5.11 a difference in electrical conductivity can be observed for all nanolaminate doped TiO_2 thin films deposited on the Cambridge Nanotech Fiji system. The secondary precursor dopants, the ratio in which they were injected, as well as the titanium precursor used have a significant effect on the semi-conducting behaviour. TiO_2 deposited by TTIP and O_2 plasma as precursor and reactant respectively which was doped in a 99:1 ratio with Al (TT_b2) is shown to be the most resistive film. This is due to the less reactive TTIP precursor, the O_2 plasma reactant which has proved to reduce semiconducting behaviour, and the 99:1 dopant ratio for the large band gap Al_2O_3.

TiO_2 deposited using TDMAT and H_2O as titanium precursor and reactant, which was doped in a 99:1 ratio with Ag (TD_h2), demonstrated the most conductive electrical behaviour out of all TiO_2 films doped by the Cambridge Nanotech Fiji system. Silver is known to enhance the photocatalytic properties and photo-electrochemical response of TiO_2. Silver particles can act as electron reservoirs by supressing e^- - h^+ recombination.[40, 41] Silver doped ZnO has been explored by solution emersion where 0 %, 1 %, 3 %, 5 % and 7 % concentrations of Ag doping were investigated. 1 % Ag produced the highest electrical conductivity by IV characterisation. The highly

orientated crystal growth and good morphology of the 1 % Ag doped ZnO films were found to be a good influence on the electrical properties.[42] Despite the initial results of improved conductivity with TiO_2:Ag in a 99:1 ratio, no evidence of Ag(fod)(PEt_3) was observed as a pressure pulse during ALD growth. Several attempts to grow an Ag_2O thin film using the Cambridge Nanotech Fiji were made but evidence of growth was difficult to determine. All XRD measurements showed films to be amorphous due to the thinness of any film that could be deposited and ellipsometry was deemed impractical due to the reflectivity of the samples. The TiO_2:Ag film in a 99:1 dopant ratio was found to be only marginally better than undoped TiO_2 with a 5 minute O_2 plasma pre clean using sigma dark characterisation (Figure 5.14). Further characterisation of the TiO_2:Ag film through XPS was necessary to ensure that silver was incorporated into the thin film and that this resulted in the improved electrical characteristics observed.

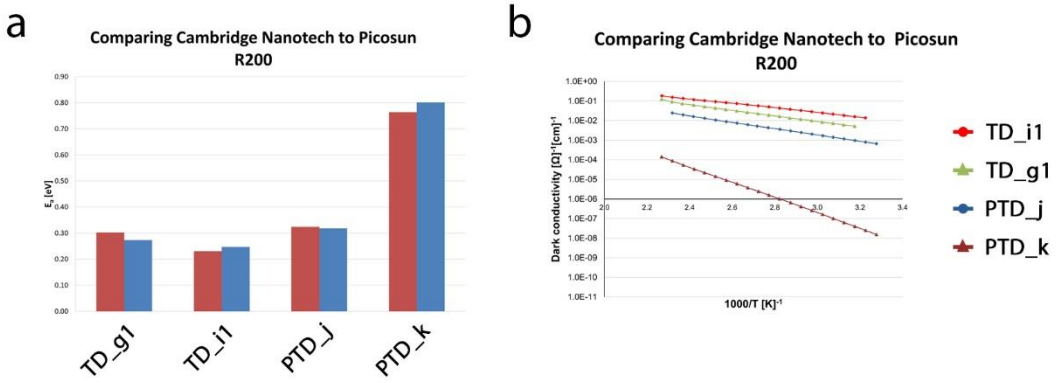

Figure 5. 12: (a) *Bar chart showing activation energy and* ***(b)*** *Arrhenius plot of the surface conductivity of ALD TiO_2 laminate doping from two different ALD systems*

When comparing the same TiO_2 depositions in different reactors using sigma dark, the Cambridge Nanotch Fiji system was observed to produce more conducting films than the Picosun R200 system (Figure 5.12). While both reactors produced thin films that had improved semi-conducting behaviour when doped with SnO_2 in a 19:1 ratio, the thin film produced by the Cambridge Nanotech Fiji (TD_i1) was an order of magnitude higher in terms of dark conductivity (Ω^{-1} cm^{-1}) when compared to the same film produced by the Picosun R200 (PTD_j). For TiO_2:Hf in a 19:1 ratio the film

deposited by the Nanotech system (TD_g1) was almost three orders of magnitude higher than the same film deposited by the Picosun (PTD_k). This is an interesting observation as it implies that films cannot be reproduced using different ALD systems. The reasoning behind this is that despite the same precursors and dopants being used in the same ratio, the reactors themselves adopt different pumps and vary in pressure. Both reactors utilise different flow rates and chamber sizes which can affect growth. The heating of the precursors also varies between reactors as TDMAT is set to 75°C for the Cambridge Nanotech Fiji system, while TDMAT was found to grow best when heated to 65°C with the accompaniment of a boost function on the Picosun R200 system. ALD reactors are reactor dependant and behave differently to one another making reproducibility extremely difficult using different reactors.

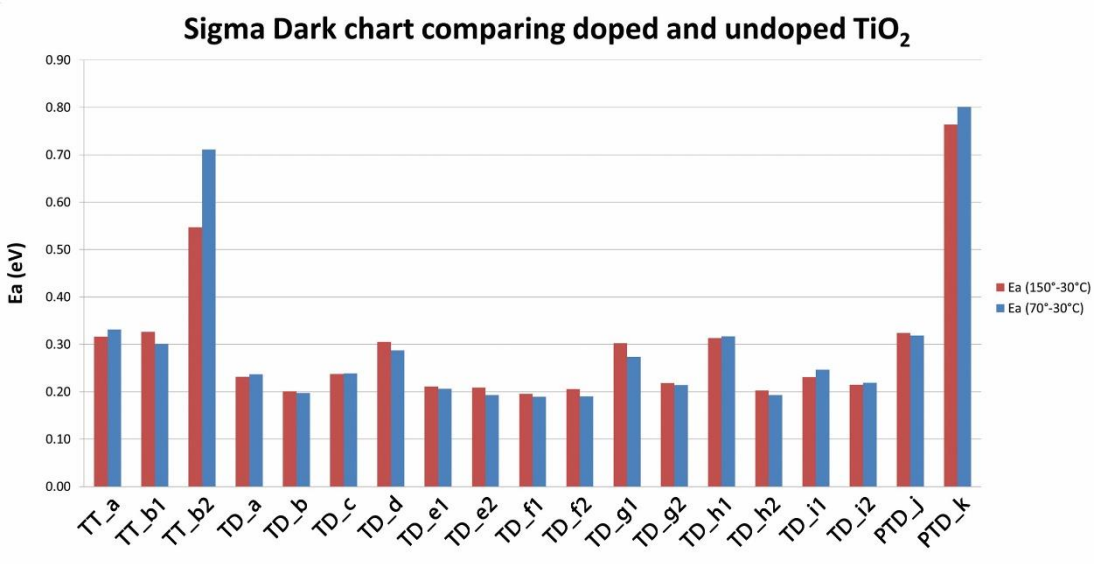

Figure 5. 13: *Bar chart showing electrical conductivity for all doped and undoped TiO_2 films measured for both ALD reactors*

When comparing all nominally doped and undoped TiO_2 films, TiO_2 doped with Ag in a 99:1 laminate ratio (TD_h2) and undoped TiO_2 which was subjected to an O_2 plasma treatment prior to ALD deposition (TD_b) performed the best in terms of dark conductivity. The plots of these two films' dark conductivity and corresponding activation energy are displayed in Figure 5.14. These two films demonstrated promise for fabrication into mesoporous PSCs, but as mentioned previously further

characterisation is required to clarify that silver was incorporated, and remained, in the TiO_2:Ag thin film.

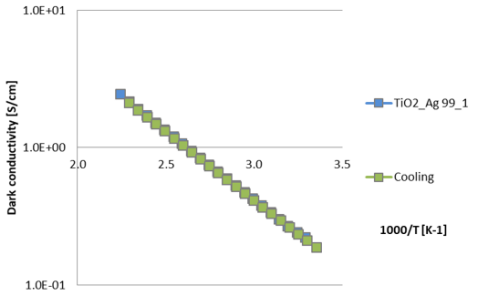

ALD 20nm TiO_2_Ag 99_1	
Conductivity at R.T	**1.96E-01**
Slope	-9.93E-01
Intercept	2.60E+00
A_e	**0.193**

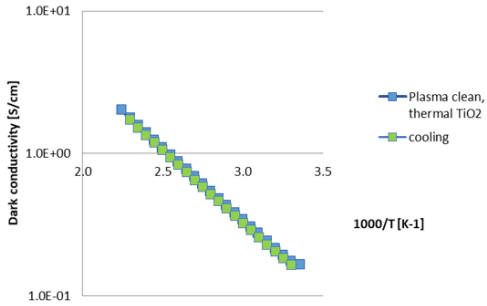

ALD 20nm Plasma pre-clean, thermal TiO_2	
Conductivity at R.T	**1.55E-01**
Slope	-1.01E+00
Intercept	2.55E+00
A_e	**0.200**

Figure 5. 14: *Plot of dark conductivity for best electrically conductive films* ***(a)*** *TiO_2:Ag_2O 99:1,* ***(b)*** *O_2 plasma pre clean, thermal TiO_2*

5.3.2 UV-visible spectrometry

The optical transmittance of the ALD TiO_2 thin films was measured with a Perkin-Elmer Lambda 900 spectrophotometer with a step size of 1 nm wavelength.

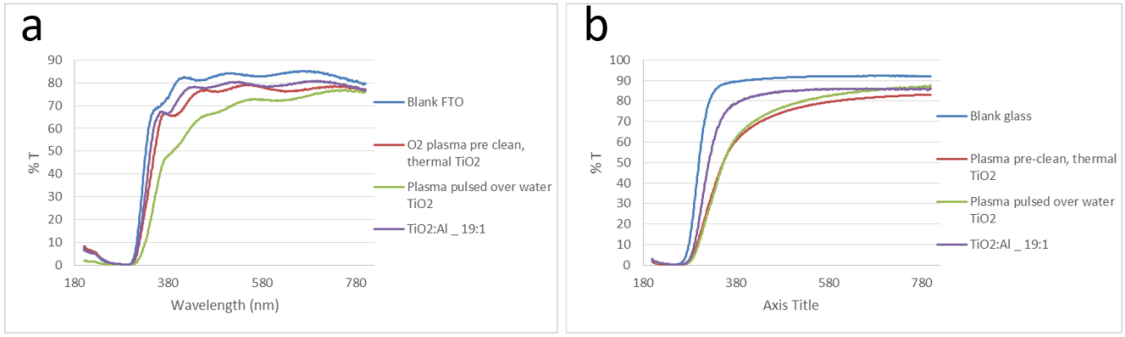

Figure 5. 15: *% Transmission spectra of the same 20 nm films on* ***(a)*** *FTO coated glass substrates and* ***(b)*** *glass substrates*

Optical transmittance on FTO coated glass and glass substrates is illustrated in Figure 5.15. In both of these cases TiO_2 doped with aluminium in a 19:1 ratio retains higher transmittance in the 300 nm – 800 nm range of the spectrum compared to undoped TiO_2 with a 5 minute O_2 plasma clean prior to growth. Transmittance values above 50 % are retained in all films deposited on FTO coated glass, and above 65 % in films deposited on glass in the 400 – 800 nm range of the spectrum.

UV-Vis is a useful technique to determine percentage transmission. However, the ALD method with its ability to coat high aspect ratios does not lend itself well to such measurements. Unless masked, “overlap” can be found on many ALD substrates, which involves deposits growing on the underside of the substrate. As a consequence, additional absorption can lead to a lower percentage transmission observed. For this reason these measurements on test samples, where masking is not essential, are for guidance only.

5.3.3 XPS

X-ray photoelectron spectroscopy (XPS) analysis was performed in order to obtain the elemental composition of the nominally undoped and doped TiO_2 films. The samples were first sputtered with an Argon Gas Cluster source (10 keV, Ar1000+ clusters) for 3 seconds in order to remove the carbon over layer. Then high-resolution X-ray photoelectron spectra were recorded using a Kratos AXIS instrument with a monochromatic Al Kα radiation of 1486.6 eV energy as the excitation source (10 mA, 15 kV). All the spectra were acquired with analyser pass energy of 20 eV and 100 ms

dwell time per step. Binding energy values were calibrated by employing the C 1s 284.80 eV. Construction and peak fitting of synthetic peaks in narrow region spectra used a Shirely type background and the synthetic peaks were of a mixed Gaussian-Lorenzian type. Relative sensitivity factors used were from CasaXPS library containing Scofield cross-sections.

Table V. XI: *XPS results detailing the percentage concentration of the Ti^{3+}, the Ti^{4+}, the nitrogen and the carbon contents in undoped and doped 20 nm TiO_2 films on FTO coated glass*

Sample ID	*C 1s %conc*	*N 1s %conc*	*Ti^{3+} %conc*	*Ti^{4+} %conc*	*Ti^{3+}/Ti^{4+}*	*O 1s %conc*
TD_b	8.9	0.6	3.7	14.4	0.257	63.4
TD_c	8.6	-	4.4	14.2	0.309	63.2
TD_d	7.2	-	4.6	13.5	0.341	63.6
PTD_1	9.0	0.9	3.1	12.6	0.246	58.6
TT_b1	5.7	-	3.9	12.3	0.317	62.2
TT_b2	4.8	-	4.4	14.1	0.312	64.3
PTD_j	5.1	-	4.3	13.8	0.311	64.6
TD_g1	-	-	4.5	13.5	0.333	65.81
TD_h1	9.3	-	5.5	12.5	0.440	61.6
TD_f1	6.8	-	4.7	13.9	0.338	63.6

Table V.XI displays the percentage concentration of Ti^{3+} and Ti^{4+} present in 20 nm ALD thin films deposited on FTO coated glass. The stoichiometry was estimated from the peak areas, Ti 2p peaks at 457.3 and 458.9 eV. XPS of the 20 nm thermal TiO_2 film deposited by the Cambridge Nanotech and pre-treated with a 5 minute O_2 plasma produced a Ti^{3+}:Ti^{4+} ratio of 0.257:1. This sample along with TiO_2 doped with aluminium in a 19:1 ratio deposited by the Picosun system contained the lowest ratio of Ti^{3+}:Ti^{4+} of all films measured. In general, the existence of Ti^{3+} in TiO_2 indicates that oxygen vacancies are generated to maintain an electrostatic balance. As discussed in Chapter 4, ALD TiO_2 from the TDMAT process at 200 °C was found to contain measurable quantities of N and C from unreacted precursors. This was also observed with as deposited TiO_2 from the TDMAT ALD process at 185°C which had been pre-treated with an O_2 plasma clean.

TiO_2 doped with silver in a 99:1 ratio has previously proved interesting due to its marginally improved electrical conductivity when compared to undoped TiO_2. XPS was carried out on the 19:1 version of this thin film to establish if any silver could be detected. The 19:1 TiO_2:Ag film would contain more silver than the 99:1 TiO_2:Ag film and so it would be easier to detect any incorporation through means of XPS. No evidence of silver was identified through XPS, however the increased carbon concentration for this film suggests that the carbon ligands from the silver precursor, Ag(fod)(PEt_3), may have been incorporated into the film. It is possible that conductivity of the film may have been improved by an increase in the carbon content. Under these low temperature growth conditions it appears that the precursor did not react as intended with residual ligands refusing to decompose and be purged through the extract. It has been reported in the literature that silver particles tend to diffuse into thin films and agglomerate forming large clusters upon heat treatments of 200°C.[43, 44] It is possible that if silver was incorporated, it may have diffused through the TiO_2 film and migrated to the FTO coated glass substrate. It was decided not to investigate the 99:1 ratio of TiO_2:Ag in mesoporous PSCs any further as incorporation of silver could not be verified.

No XPS signal was detected from the underlying FTO for any of the thin films characterised, supporting the claim of conformal and pinhole free ALD coverage.

Morphological and electrical comparisons between doped and undoped ALD TiO_2 thin films are displayed in Appendix I, Figures 10 to 14. XPS spectra of a 19:1 TiO_2:Al film on FTO coated glass is presented in Figures 15 and 16. A tauc plot of the same 19:1 TiO_2:Al film is also shown in Figure 17.

5.3.4 Mesoporous solar cell performance

Following the author's work depositing and characterising ALD ETLs at Tyndall National Institute, an internship was arranged at CSEM to study established methods with which to deposit the remaining PSC layers. Here the author fabricated mesoporous perovskite devices using the ALD ETLs and reference sputtered ETLs. Their performances are compared and discussed herein.

5.3.4.2 ALD plasma pre-clean, thermal TiO_2

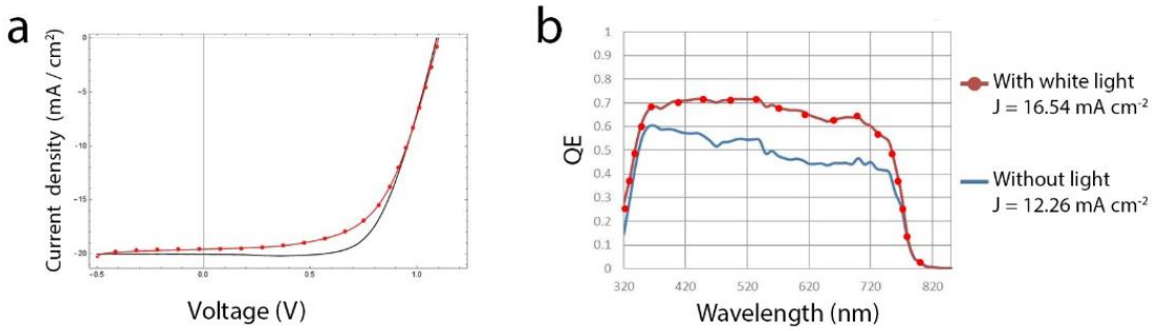

Figure 5. 18: (a) *J–V characteristics of mesoporous perovskite solar cell containing plasma pre clean, 20 nm thermal ALD TiO_2* ***(b)*** *External quantum efficiency of same perovskite solar cell containing plasma pre clean, 20 nm thermal ALD TiO_2 ETL*

Table V. XII: *Device performance parameters for a cell containing plasma pre clean, 20 nm thermal ALD TiO_2 ETL*

Scan Direction	*V_{oc} (mV)*	*J_{sc} (mA cm^{-2})*	*FF (%)*	*PCE (%)*
Reverse	1097	19.797	70.614	15.330
Forward	1088	19.541	68.784	14.621

The J-V characteristics of the best PSC based on undoped ALD TiO_2 (TD_b) is shown in Figure 5.18 (a) and the corresponding external quantum efficiency is displayed in Figure 5.18 (b). This device contained a 20 nm thermal ALD TiO_2 compact layer grown on an O_2 plasma cleaned substrate and reached a V_{oc}, J_{sc}, and FF of 1097 mV, 19.80 mA cm^{-2}, and 70.61 %, respectively, leading to a PCE of 15.33 %. EQE displayed a current density of 12.26 mA cm^{-2} without a light bias, which is not in agreement with J-V results. When a white light bias is applied the current density reaches 16.54 mA cm^{-2} which is still below the value predicted by J-V. There is a clear photo-doping effect observed in the ALD layer. This effect was exhibited in all ALD ETLs incorporated into mesoporous cells except that which was given a 5 minute O_2 plasma treatment after ALD deposition (Figure 5.19). It is speculated that the O_2 plasma treatment after ALD growth allowed for an improved interface between the compact ALD TiO_2 and the m-TiO_2 layers by improving wettability.[45] Fewer defects and charge traps from the interface suggests increased adhesion of the underlying

compact TiO_2 to the m-TiO_2 layer, resulting in a more ideal cell. While this procedure has not yet been optimised due to the low efficiency of the device (8.5 % PCE) as observed in Table V.XIV, it is thought to be the reason for removing the observed photo-doping effect.

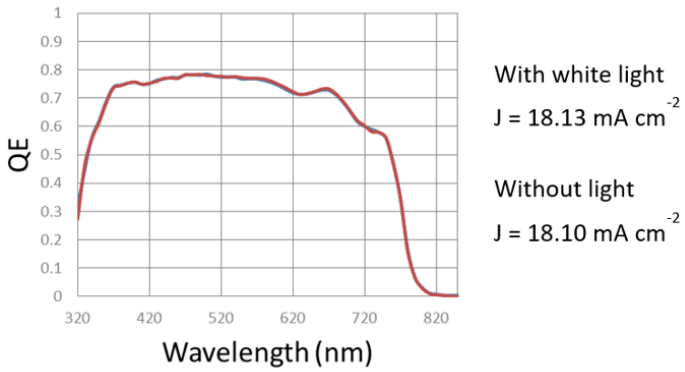

Figure 5. 19: *External quantum efficiency of perovskite solar cell containing 20 nm thermal ALD TiO_2 followed by a 5 minute O_2 plasma treatment ETL*

Table V.XIV summarises the IV parameters of mesoporous PSCs comprised of various undoped and laminate doped 20 nm ALD TiO_2 ETLs and compares them to a reference ETL of sputtered TiO_{2-x}. The ALD layer consisting of a 20 nm thermal ALD TiO_2 compact layer on an O_2 plasma cleaned substrate exhibits the best performance of all ALD TiO_2 layers tested in mesoporous devices. This is in accordance with the sigma dark characterisation of the ALD film on glass and the UV-Vis spectrometry of the ALD film on quartz. The resulting 15.33 % PCE is comparable to that of the reference cell containing sputtered TiO_{2-x} reaching 16.19 % PCE. The thermal TiO_2 ALD film reaches a slightly lower PCE of 14.42 % when incorporated into a cell. This indicates that the O_2 plasma clean prior to ALD growth is necessary to enhance overall device performance by removing adventitious carbon from the FTO coated glass substrate and enhancing ALD deposition by providing more –OH reactive sites on the surface. The cell fabricated from the thermal TiO_2 ALD film followed by a 5 minute O_2 plasma clean after deposition does not perform well attaining a low PCE of 8.5 % on a 1.04 cm^2 active area. However, the use of O_2 plasma after growth does correct the photo-doping effect observed in the remainder of cells utilising ALD TiO_2.

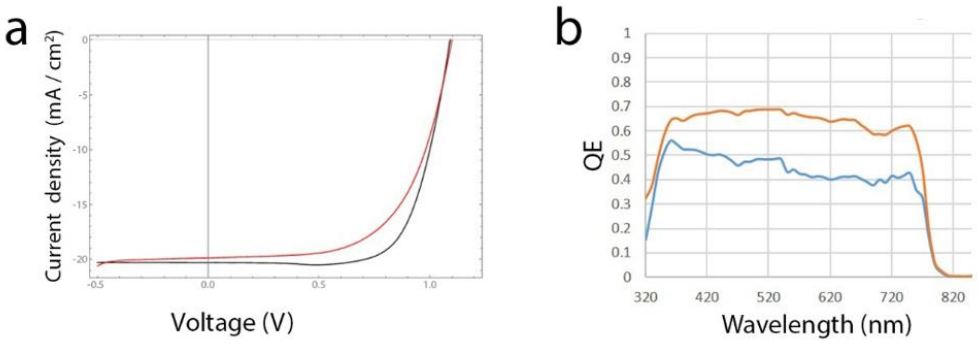

Figure 5. 20: (a) *J–V characteristics of mesoporous perovskite solar cell containing plasma pre clean, 20 nm thermal ALD TiO_2 doped with hafnium in 19:1 ratio.* ***(b)*** *External quantum efficiency of same perovskite solar cell containing plasma pre clean, 20 nm thermal ALD TiO_2 doped with hafnium in 19:1 ratio ETL.*

With regard to nanolaminate doped ALD TiO_2 thin films incorporated into mesoporous PSCs, TiO_2 doped with hafnium in a 19:1 ratio surprisingly performed the best out of all ALD films achieving 15.52 % PCE on a 1.04 cm^2 active area (Figure 5.20). This ALD film was deposited using the Picosun R200 ALD system and produced the worst semi-conducting behaviour out of all deposited films when characterised by sigma dark. However, the high efficiency of the cell was not maintained through steady-state max power point tracking over 300 seconds and quickly dropped to a stabilised 13.3 %. ALD TiO_2 doped with aluminium in a 19:1 ratio produced a slightly lower PCE of 15.41 % but managed to maintain a higher stabilised efficiency of 14.0 % over 300 seconds of tracking when compared to the hafnium dopant. Finally, none of the mesoporous cells comprising of ALD TiO_2 doped with tin in a 19:1 ratio performed well. The highest PCE reached was 2.07 % which is far below all other cells. It is likely that there may be a fault with the ALD growth itself or with the deposition of one of the remaining layers in the cell as all TiO_2:Sn films in a 19:1 ratio were made up together. To verify if the low PCE obtained was due to the ALD thin film or contamination of one of the other layers this experiment should be repeated.

Table V. XIII: *Summary of IV parameters comparing different compositions of 20 nm ALD TiO_2 ETLs to 20 nm sputtered TiO_{2-x} ETLs in mesoporous perovskite solar cells*

ETL	*Scan direction*	*V_{oc} (mV)*	*J_{sc} (mA cm^{-2})*	*FF (%)*	*PCE (%)*	*Steady-state MPP over 300 s (%)*
Sputtered reference	Reverse	1086	20.031	74.421	16.192	15.0
	Forward	1092	19.707	68.157	14.667	
Plasma pre clean, thermal TiO_2	Reverse	1097	19.797	70.614	15.330	14.3
	Forward	1088	19.541	68.784	14.621	
Thermal TiO_2	Reverse	1091	20.056	64.135	14.422	13.7
	Forward	1100	19.583	59.360	13.405	
Thermal TiO_2, post growth plasma	Reverse	1069	18.851	58.744	11.841	8.5
	Forward	1062	18.300	60.090	11.680	
TiO_2:Hf 1:19	Reverse	1090	20.303	70.099	15.519	13.3
	Forward	1100	19.863	60.871	13.296	
TiO_2:Al 1:19	Reverse	1092	19.762	71.417	15.412	14.0
	Forward	1098	19.055	62.994	13.181	
TiO_2:Sn 1:19	Reverse	794	11.666	22.306	2.065	2.25
	Forward	807	9.738	22.654	1.781	

In this study ALD doping of the alternative ETL, SnO_2, was also investigated for mesoporous PSCs. J-V characteristics and EQE measurements of a mesoporous cell consisting of 20 nm thermal ALD SnO_2:Ti doped in 19:1 dopant:pulse ratio is presented in Appendix I, Figure 18. Max power point steady state tracking over 600 seconds for this device is also displayed in Figure 19 as it stabilises at 12.2 % PCE.

5.3.4.1 Reference sputtered TiO_2 as compact ETL

Mesoporous perovskite solar cell devices were assembled using ALD undoped and doped TiO_2, as well as RF sputtered TiO_{2-x} as the ETLs. RF sputtered TiO_{2-x} was chosen to act as a reference ETL because its use has been well established and optimised by those at CSEM. The solar cell devices were composed of a conductive FTO coated glass substrate, a compact 20 nm ALD TiO_2 thin film or a 20 nm sputtered TiO_{2-x} thin film, a mesoporous TiO_2 layer, a $MAPbI_3$ perovskite layer, a Spiro-OMeTAD hole transport layer and a gold counter electrode. The devices containing ALD ETLs were made up alongside RF sputtered ETLs to avoid variations in the other layers mentioned above allowing ETLs to be directly compared.

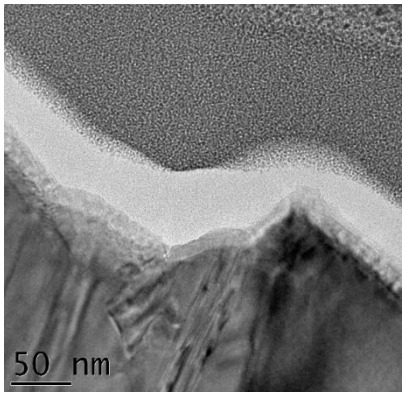

Figure 5. 16: *TEM image of a 20 nm RF sputtered TiO_{2-x} thin film deposited on TEC 7 FTO coated glass*

The TEM image of 20 nm sputtered TiO_{2-x} at 60°C on FTO coated glass in Figure 5.16 is observed to be conformal following the curves of the rough FTO underneath. The film is shown to be crystalline due to the high energy process involved in RF magnetron sputtering unlike that of ALD TiO_2 deposited at 185°C.

Perovskite cells with undoped and doped TiO_2 ETLs were measured under a two-lamp class AAA WACOM sun simulator with an AM 1.5 G irradiance spectrum at 100 Watts cm^{-2}. The cell area was 1.04 cm^2 and defined using a metal mask. The J–V characteristics of the cells were obtained under both reverse (from V_{oc} to J_{sc}) and forward (from J_{sc} to V_{oc}) bias. Maximum power point (MPP) tracking was performed to extract the stabilised power output. External quantum efficiency (EQE) spectra were acquired on a custom-made spectral response setup equipped with a xenon lamp, a grating monochromator and lock-in amplifiers.[1]

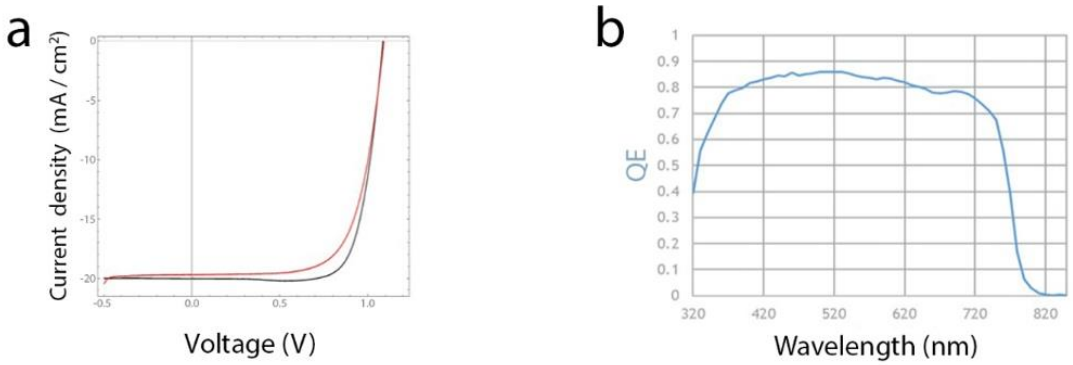

Figure 5. 17: (a) *J–V characteristics of mesoporous perovskite solar cell containing sputtered 20 nm TiO_{2-x}* ***(b)*** *External quantum efficiency of same perovskite solar cell containing sputtered 20 nm TiO_{2-x} ETL*

Table V. XIV: *Device performance parameters for a cell containing 20 nm sputtered TiO_{2-x} ETL*

Scan Direction	*V_{oc} (mV)*	*J_{sc} (mA cm^{-2})*	*FF (%)*	*PCE (%)*
Reverse	1086	20.031	74.421	16.192
Forward	1092	19.707	68.157	14.667

The J-V characteristics of the best PSC based on the reference, sputtered TiO_{2-x} ETL, is shown in Figure 5.17 (a) and the corresponding external quantum efficiency is displayed in Figure 5.17 (b). This device achieved a Voc, Jsc, and FF of 1086 mV, 20.03 mA cm^{-2}, and 74.42 %, respectively, leading to a PCE of 16.19 %. EQE displayed a current density of 20.25 mA cm^{-2} which is in agreement with J-V results.

5.4 Summary

Deposition of TiO_2 thin film ETLs was carried out on two commercial ALD reactors at Tyndall National Institute, a Cambridge Nanotech Fiji F200 and a Picosun R200 system. All metal oxides were deposited at 185°C to meet the thermal restrictions of perovskite/silicon heterojunction tandem cells[3]. The Cambridge NanoTech Fiji F200 was employed for the growth of TiO_2 using titanium (IV) isopropoxide (TTIP) or tetrakis (diemthylamido) titanium (TDMAT) and H_2O or Ar/O_2 plasma in an argon

carrier flow as the metal precursors and oxygen sources respectively, leading to a deposition rate of 0.2 Å per cycle with TTIP and 0.5 Å per cycle with TDMAT. The Picosun R200 grew TiO_2 using a N_2 carrier flow. TDMAT and H_2O or Ar/O_2 plasma were used as the Ti precursor and co-reactants. The growth rate per cycle at 185°C for TDMAT was 0.5 Å using the Picosun R200 system.

Doping the ALD TiO_2 thin films with nanolaminate layers was investigated using different metal oxides which could influence the electrical properties of the thin film. TMA, TEMAH, Ag(fod)(PEt_3), TDMASn, TDMAV were all employed as secondary metal dopant precursors and used with either O_2 plasma or H_2O as the reactant. These secondary oxides incorporated as laminate dopants span a range of band gaps from the wide band gap Al_2O_3 (7-8 eV), to semiconducting oxides such as SnO_2, and the mid-range band gap of HfO_2 (~5.9 eV). The laminate doping was applied by introducing the secondary metal precursors in a 19:1 and 99:1 ratio of TiO_2 to dopant. This was performed to establish whether there was a difference in electrical properties between the thin films depending on titanium precursor, reactant, dopant and ratio of applied dopant, any of which could enhance performance when incorporated into a mesoporous PSC.

Dark conductivity measurements of the nominally undoped and doped ALD TiO_2 thin films on glass were performed under a 1 mbar N_2 atmosphere. During the measurement, the temperature was ramped from room temperature to 180°C at a rate of 10°C min^{-1}. The samples were then cooled at a rate of 1°C min^{-1}. Their conductivity was measured during the cooling phase. Arrhenius plots of the surface conductivity demonstrated semi-conducting behaviour for all undoped and doped ALD thin films with conductivity increasing as temperature increases. The bulk conductivity of the thin films was observed to be precursor dependent. The titanium precursor, TDMAT, was found to be more reactive than TTIP as it only required H_2O as a reactant and provided the higher growth rate of 0.5 Å per cycle at 185°C. TDMAT allows for better coverage approaching ideal monolayer growth, resulting in a more uniform microstructure. It is expected that this is the reason for better resultant electrical properties. TiO_2 deposited using TDMAT and H_2O as titanium precursor and reactant, which was doped in a 99:1 ratio with Ag_2O, demonstrated marginally more conductive electrical behaviour than undoped thermal TiO_2. Despite the improved sigma dark

characterisation for TiO_2:Ag in a 99:1 ratio, the silver ALD growth did not behave as expected. Further characterisation by XPS gave no evidence of silver incorporation but did show an increased carbon concentration for TiO_2:Ag in a 19:1 ratio , suggesting that the carbon ligands from the silver precursor, Ag(fod)(PEt_3), were incorporated into the film. Due to the absence of evidence of Ag, the propensity of this element to diffuse in thin films, and the marginal electrical property gains achieved it was decided not to further investigate the 99:1 ratio of TiO_2:Ag in mesoporous PSCs.

Mesoporous perovskite solar devices were fabricated and composed of a conductive FTO coated glass substrate, a compact 20 nm ALD TiO_2 thin film or a 20 nm sputtered TiO_{2-x} thin film, a mesoporous TiO_2 layer, a $MAPbI_3$ perovskite layer, a Spiro-OMeTAD hole transport layer and a gold counter electrode with an active cell area of 1.04 cm^2. RF sputtered TiO_{2-x} was chosen to act as a reference ETL because its use had been well established and optimised. This reference cell achieved a stabilised PCE of 15.0 % after 300 seconds of MPP steady state tracking. This was a comparable result to the stabilised efficiency of the mesoporous cell comprising of the thermal TiO_2 ALD ETL on O_2 plasma treated substrates. This particular cell reached a stabilised efficiency of 14.3% PCE after 300 seconds of steady state MPP tracking. With regard the doped laminate ALD ETLs, TiO_2 doped with aluminium in a 19:1 ratio reached the highest stabilised efficiency when incorporated into a mesoporous PSC reaching 14.0 % stabilised PCE after 300 seconds of steady state MPP tracking. This was slightly lower than the undoped TiO_2 ALD ETL. TiO_2 doped with tin in a 19:1 ratio did not perform well when incorporated into a mesoporous PSC. The stabilised efficiency was found to be substantially lower than that obtained by all other cells.

While the thermal ALD TiO_2 is comparable to that of the sputtered TiO_{2-x} ETL when incorporated into a mesoporous cell, further study into optimisation of the ALD ETL would be beneficial. The sputtered film has been optimised with regard to composition and thickness, whereas the ALD TiO_2 film was maintained at 20 nm as a baseline test so that it could be directly compared to the sputtered ETL of the same thickness. In addition, it was thought that reducing the thickness of the compact ALD TiO_2 layer below 20 nm could lead to cracking during the 500°C sintering of the mesoporous

TiO_2 layer above. It would be interesting to implement a thickness series for the ALD undoped TiO_2 film in an effort to optimise efficiency. Removal of the mesoporous layer could also allow for higher efficiency in the overall cell containing ALD TiO_2 by reducing resistivity caused by the high temperature mesoporous scaffold. This is investigated in the next chapter.

5.5 Bibliography

[1] A. Walter, S-J. Moon, B. A. Kamino, L. Lofgren, D. Sacchetto, F. Matteocci, B. Taheri, J. Bailat, A. Di Carlo, C. Ballif, S, Nicolay, Closing the Cell-to-Module Efficiency Gap: A Fully Laser Scribed Perovskite Minimodule With 16% Steady-State Aperture Area Efficiency, IEEE J. of Photovoltaics, 8, 1, 2018

[2] H. Booth, Laser processing in industrial solar module manufacturing, J. Laser Micro/Nanoeng., 5, 3, 83–191, 2010

[3] J. P. Mailoa, C. D. Bailie, E. C. Johlin, E. T. Hoke, A. J. Akey, W. H. Nguyen, M. D. McGehee, T. Buonassisi, A 2-terminal perovskite/silicon multijunction solar cell enabled by a silicon tunnel junction, Appl. Phys. Lett., 106, 121105, 2015

[4] Q. Xie, Y.-L. Jiang, Atomic layer deposition of TiO_2 from tetrakis-dimethyl-amido titanium or Ti isopropoxide precursors and H_2O, J. Appl. Phys., 102, 083521, 2007

[5] B. Abendroth, T. Moebus, S. Rentrop, R. Strohmeyer, M. Vinnichenko, T. Weling, H. Stöcker, D. C. Meyer, Atomic layer deposition of TiO_2 from tetrakis(dimethylamino)titanium and H_2O, Thin Solid Films, 545, 176–182, 2013

[6] M. Reiners, K. Xu, N. Aslam, A. Devi, R. Waser, S. Hoffmann-Eifert, Growth and Crystallization of TiO_2 Thin Films by Atomic Layer Deposition Using a Novel Amido Guanidinate Titanium Source and Tetrakis-dimethylamido-titanium, Chem. Mater., 25, 15, 2934-2943, 2013

[7] Q. Xie, J. Musschoot, D. Deduytsche, R. L. Van Meirhaeghe, C. Detavernier, S. Van den Berghe, Y.-L. Jiang, G.-P. Ru, B.-Z. Lia, X.-P. Qu, Growth Kinetics and Crystallization Behavior of TiO_2 Films Prepared by Plasma Enhanced Atomic Layer Deposition, J. Electrochem. Soc., 155, 9, 2008

[8] J. Pointet, P. Gonon, L. Latu-Romain, A. Bsiesy, C. Vallée, Rutile-structured TiO_2 deposited by plasma enhanced atomic layer deposition using tetrakis(dimethylamino)titanium precursor on in-situ oxidized Ru electrode, J. Vac. Science & Technology A, 32, 01A120, 2014

[9] Li Lezhong, Yang Weiqing, Ding Yingchun, Zhu Xinghua, First principle study of the electronic structure of hafnium-doped anatase TiO_2, J. Semicond., 33, 012002, 2012

[10] J. W. Pan, C. Li, Y. F. Zhao, R. X. Liu, Y. Y. Gong, L. Y. Niu, X. J. Liu, B. Q. Chi, Electronic properties of TiO_2 doped with Sc, Y, La, Zr, Hf, V, Nb and Ta, Chemical Physics Letters, 628, 43–48, 2015

[11] Y. Liu, C.-Y. Liu, Q.-H. Rong, Z. Zhang, Characteristics of the silver-doped TiO_2 nanoparticles, Applied Surface Science, 220, 7–11, 2003

[12] N. A. M. Barakat, M. A. Kanjwal, I. S. Chronakis, H. Yong Kim, Influence of temperature on the photodegradation process using Ag-doped TiO_2 nanostructures: Negative impact with the nanofibers, Journal of Molecular Catalysis A: Chemical, 366, 333–340, 2013

[13] Y.-C. Liang, C.-C. Wang, C.-C. Kei, Y.-C. Hsueh, W.-H. Cho, T.-P. Perng, Photocatalysis of Ag-Loaded TiO_2 Nanotube Arrays Formed by Atomic Layer Deposition, J. Phys. Chem. C, 115, 9498–9502, 2011

[14] R. D. Shannon, C. T. Prewitt, Effective ionic radii in oxides and fluorides, Acta Cryst., B 25, 925-946, 1969

[15] Y. Duan, N. Fu, Q. Liu, Y. Fang, X. Zhou, J. Zhang, Y. Lin, Sn-Doped TiO_2 Photoanode for Dye-Sensitized Solar Cells, J. Phys. Chem. C, 116, 8888−8893, 2012

[16] J. Liqiang, F. Honggang, W. Baiqi, W. Dejun, X. Baifu, L. Shudan, S. Jiazhong, Effects of Sn dopant on the photoinduced charge property and photocatalytic activity of TiO_2 nanoparticles, Applied Catalysis B: Environmental, 62, 282–291, 2006

[17] F. Fresno, C. Guillard, J. M. Coronado, J.-M. Chovelon, D. Tudela, J. Soria, J.-M. Herrmann, Photocatalytic degradation of a sulfonylurea herbicide over pure and tin-doped TiO_2 photocatalysts, Journal of Photochemistry and Photobiology A: Chemistry, 173, 13–20, 2005

[18] M. M. Islam, T. Bredow, A. Gerson, Electronic Properties of Vanadium- Doped TiO_2, Chem. Phys. Chem., 12, 3467 – 3473, 2011

[19] Y. Shen, T. R. B. Foong, X. Hu, Towards atomic level vanadium doping of TiO_2 via liquid-phase atomic layer deposition, Applied Catalysis A: General, 409–410, 87-90, 2011

[20] S.-M. Chang, W.-S. Liu, Surface doping is more beneficial than bulk doping to the photocatalytic activity of vanadium-doped TiO_2, Applied Catalysis B: Environmental, 101, 333–342, 2011

[21] S. K. Kim, G.- J. Choi, S. Y. Lee, M. Seo, S. W. Lee, J. H. Han, H.- S. Ahn, S. Han, C. S. Hwang, Al- Doped TiO_2 Films with Ultralow Leakage Currents for Next Generation DRAM Capacitors, Adv. Mater., 20, 1429–1435, 2008

[22] G.-J. Choi, S. K. Kim, S.-J. Won, H. J. Kim, C. S. Hwang, Plasma-Enhanced Atomic Layer Deposition of TiO_2 and Al-Doped TiO_2 Films Using N_2O and O_2 Reactants, J. Elecrtochem. Soc., 156, 9, 2009

[23] S. K. Kim, G.-J. Choi, J. H. Kim, C. S. Hwang, Growth Behaviour of Al-Doped TiO_2 Thin Films by Atomic Layer Deposition, Chem. Mater., 20, 3723–3727, 2008

[24] G. E. Testoni, W. Chiappim, R. S. Pessoa, M. A. Fraga, W. Miyakawa, K. K. Sakane, N. K. A. M. Galvão, L. Vieira, H, S, Maciel, Influence of the Al_2O_3 partial-monolayer number on the crystallization mechanism of TiO_2 in ALD TiO_2/Al_2O_3 nanolaminates and its impact on the material properties, J. Phys. D: Appl. Phys., 49, 375301, 2016

[25] W. Weinreicha, L. Wilde, J. Müller, J. Sundqvist, Structural properties of as deposited and annealed ZrO_2 influenced by atomic layer deposition, substrate, and doping, J. Vac. Science & Technology A, 31, 01A119, 2013

[26] Y. Wu, P. M. Hermkens, B. W. H. Van De Loo, H. C. M. Knoops, S. E. Potts, M. A. Verheijen, F. Roozeboom, W. M. M. Kessels, Electrical Transport and Al Doping Efficiency in Nanoscale ZnO Films Prepared by Atomic Layer Deposition. J. Appl. Phys., 114, 2, 24308, 2013

[27] D. J. Lee, H. M. Kim, J. Y. Kwon, H. Choi, S. H. Kim, K. B. Kim, Structural and electrical properties of atomic layer deposited Al-doped ZnO films, Adv. Funct. Mater., 21, 448, 2011

[28] Y. Wu, A. D. Giddings, M. A. Verheijen, B. Macco, T. J. Prosa, D. J. Larson, F. Roozeboom, W. M. M. Kessels, Dopant Distribution in Atomic Layer Deposited ZnO:Al Films Visualized by Transmission Electron Microscopy and Atom Probe Tomography, Chem. Mater., 30, 1209−1217, 2018

[29] J. H. Lee, J. W. Lee, S. Hwang, S. Y. Kim, H. K. Cho, J. Y. Lee, J. S. Park, Effects of Al concentration on microstructural characteristics and electrical properties of Al-doped ZnO thin films on Si substrates by atomic layer deposition, J. Nanosci. Nanotechnol., 12, 5598, 2012

[30] T. Dhakal, D. Vanhart, R. Christian, A. Nandur, A. Sharma, C. R. Westgate, Growth morphology and electrical/optical properties of Al-doped ZnO thin films grown by atomic layer deposition, J. Vac. Sci. Technol. A Vacuum, Surfaces, Film. 30, 021202, 2012

[31] X. Qian, Y. Cao, B. Guo, H. Zhai, A. Li, Atomic Layer Deposition of Al-doped ZnO Films Using Aluminum Isopropoxide as the Al Precursor, Chem. Vap. Deposition, 19, 180–185, 2013

[32] G. Luka, L. Wachnicki, B. S. Witkowski, R. Jakiela, I. S. Virt, Structure-property relationships in ZnO:Al-hydroquinone films grown on flexible substrates by atomic and molecular layer deposition, Materials and Design, 119, 297–302, 2017

[33] A. Rahtu, M. Ritala, Reaction Mechanism Studies on Titanium Isopropoxide–Water Atomic Layer Deposition Process, Chem. Vap. Deposition 8, 21, 2002

[34] A. Sinha, D. W. Hess, C. L. Henderson, Area selective atomic layer deposition of titanium dioxide: Effect of precursor chemistry, J. Vac. Sci. Technol. B 24, 6, 2006

[35] H. Döring, K. Hashimoto, A. Fujishima, TiO_2 Thin Films Prepared by Pulsed Beam Chemical Vapor Deposition from Titanium Tetraisopropoxide and Water, Phys. Chem., 96, 620, 1992

[36] M. Ritala, M. Leskela, L. Niinisto, P. Haussalo, Titanium Isopropoxide as a Precursor in Atomic Layer Epitaxy of Titanium Dioxide Thin Films, *Chem. Mater.*, *5*, 8, 1174–1181, 1993

[37] J. Aarik, A. Aidla, T. Uustare, M. Ritala, M. Leskela, Titanium isopropoxide as a precursor for atomic layer deposition: characterization of titanium dioxide growth process, Applied Surface Science, 161, 3–4, 2000

[38] H. Y. Jeong, J. Y. Lee, M.-K. Ryu, S.-Y. Choi, Bipolar resistive switching in amorphous titanium oxide thin film, Phys. Status Solidi RRL 4, 1–2, 28–30, 2010

[39] K. Choi, S. Ghosh, J. Lim, C.M. Lee, Removal efficiency of organic contaminants on Si wafer by dry cleaning using UV/O_3 and ECR plasma, Appl. Surface Science, 206, 355-364, 2003

[40] X. He, Y. Cai, H. Zhang and C. Liang, Photocatalytic degradation of organic pollutants with Ag decorated free-standing TiO_2 nanotube arrays and interface electrochemical response, J. Mater. Chem., 21, 475-480, 2011

[41] B. Xin, L. Jing, Z. Ren, B. Wang, H. Fu, Effects of Simultaneously Doped and Deposited Ag on the Photocatalytic Activity and Surface States of TiO_2, J. Phys. Chem. B, 109, 2805-2809, 2005

[42] A.N. Afaah, N.A.M. Asib, A. Aadila, R. Mohamed, M. Rusop, Z. Khusaimi, Electrically conductive nanostructured silver doped zinc oxide (Ag:ZnO) prepared by solution-immersion technique, AIP Conference Proceedings, 1733, 020055, 2016

[43] R. C. Adochite, D. Munteanu, M. Torrell, L. Cunha, E. Alves, N. P. Barradas, A. Cavaleiro, J. P. Riviere, E. Le Bourhis, D. Eyidi, F. Vaza, The influence of annealing treatments on the properties of Ag:TiO_2 nanocomposite films prepared by magnetron sputtering, Applied Surface Science, 0169-4332, 258, 8, 4028-4034, 2012

[44] A. A. Mosquera, J. M. Albella, V. Navarro, D. Bhattacharyya, J. L. Endrino, Effect of silver on the phase transition and wettability of titanium oxide films, Scientific Reports, 6, 32171, 2016

[45] M.R. Sanchis, V. Blanes, M. Blanes, D. Garcia, R. Balart, Surface modification of low density polyethylene (LDPE) film by low pressure O_2 plasma treatment, European Polymer Journal, 42, 1558–1568, 2006

CHAPTER 6:

A study of planar PSCs incorporating ALD TiO_2 ETLs with passivation through ALD and RTA

6.1 Introduction

In addition to the mesoporous perovskite devices discussed previously, it is essential to understand how ALD TiO_2 ETLs perform in planar perovskite solar devices. In this chapter the optimisation of the undoped ALD TiO_2 layer in terms of thickness and passivation is detailed. The deposition temperature of all thin films deposited was maintained at 185°C as in Chapter 5 to meet the thermal restrictions of perovskite/silicon heterojunction tandem cells. The fabrication of the resulting thin films into planar architecture perovskite devices is then discussed.

The progression to a planar architecture, as depicted in Figure 6.1 (a), would require removal of the high temperature sintered mesoporous TiO_2 layer. The entire cell structure, excluding FTO coated glass, could then be feasibly processed through low temperature means permitting it to monolithically integrate as the top component of a tandem configuration without damaging the bottom cell.

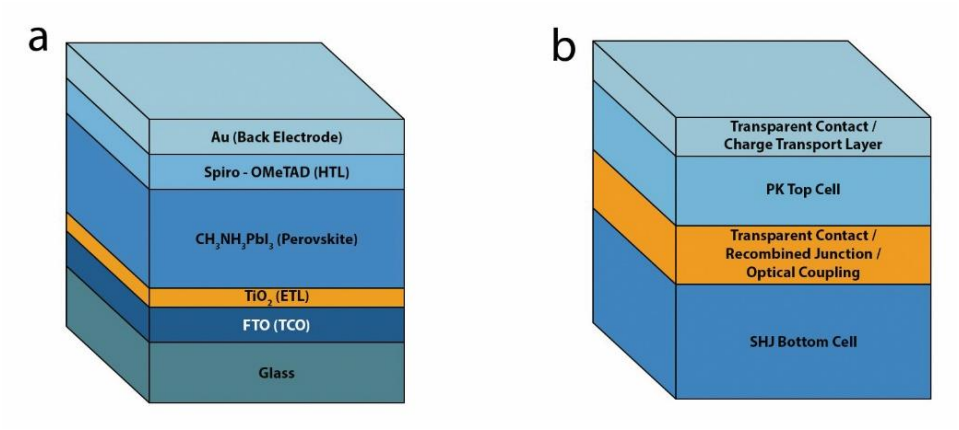

Figure 6. 1: *Schematic illustration of* ***(a)*** *planar perovskite structure and* ***(b)*** *tandem cell comprising of a silicon heterojunction bottom cell and a planar perovskite top cell*

Tandem devices (Figure 6.1 (b)) are composed of two or more cells whose composition allow absorption of a much larger range of the solar spectrum. Through design, the top sub-cell would have a large band gap absorbing higher energy photons, while lower energy photons are permitted to pass through and be absorbed by the narrow band gap bottom sub-cell. This allows the total obtainable PCE of the tandem cell to increase beyond the theoretical limits of single junction cells.[1, 2] The tandem concept is a promising route to commercialisation for perovskite solar devices, not only due to its higher attainable efficiencies but also due to its low temperature fabrication process. Maintaining low temperatures (< 200°C) for the processing of all layers would allow compatibility with large scale industry commercialisation using ALD and printing techniques on glass or even flexible substrates.[3, 4]

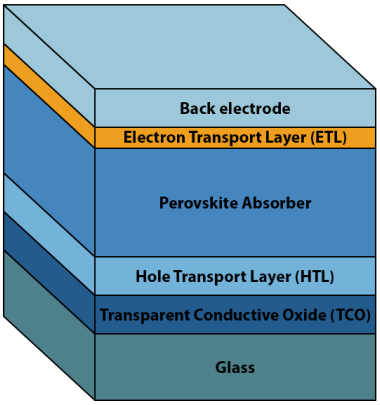

Figure 6. 2: *Schematic illustration of a p-i-n perovskite solar cell architecture*

In this chapter the concept of *p-i-n* or reverse architecture perovskite devices (Figure 6.2) is also introduced. The *p-i-n* structure is based on ITO or FTO transparent conductive oxide/ HTL/ perovskite absorber/ ETL/ and a back electrode such as gold or silver, as depicted in Figure 6.2. For this architecture the current flow is reversed as the polarity of the electrodes are changed. Depositing TiO_2 by use of ALD on top of the temperature sensitive perovskite layer itself is investigated in this chapter.

6.2 Experimental

All perovskite cells were prepared on high temperature resistant alumino-boroscilicate glass coated with fluorine-doped tin oxide (FTO) which served as a transparent electrode (TEC-15, 15 Ω cm^{-1} or TEC-7, 7 Ω cm^{-1} from Solaronix).

FTO coated glass, glass and quartz samples were all cleaned by sequentially ultra-sonicating in 5 % Decon 90, acetone, and then IPA. The FTO coated glass substrates were diced and then scribed with a P1 line using a UV ArF excimer laser (193 nm Lasertechnik ATLEX 300i) 5 mm from the edge of each 25 mm^2 substrate as outlined previously in Chapter 5 section 5.2.1.

6.2.1 ALD of undoped thermal TiO_2 for *n-i-p* PSCs

Nominally undoped TiO_2 thin films were deposited on glass, quartz, n-Si(100) wafers, and FTO coated glass by ALD using the Picosun R200 system. Despite sigma dark characterisation in Chapter 5 demonstrating an improved conductivity with the

Cambridge Nanotech ALD system, the Picosun system was selected as it allowed for less underlapping growth and therefore more transparent thin films. To avoid run-by-run variation in growth experiments all substrate types were loaded together for each TiO_2 thickness. The titanium precursor and reactant used for the depositions were TDMAT and H_2O. The TDMAT precursor vessel was maintained at 65°C, while the vessel neck was held at 80°C. The H_2O reactant was maintained at a room temperature of approximately 27°C. All samples were given a 40 minute stabilisation time within the reaction chamber prior to a 5 minute in situ O_2 plasma treatment followed by ALD growth. A pulse/purge sequence was adopted as outlined in Chapter 5 section 5.2.2.2 (i). A thickness series of 2 nm, 5 nm, 10 nm, 20 nm, 25 nm, and 100 nm TiO_2 at 185°C was investigated assuming a 0.05 nm per cycle growth rate.

6.2.2 ALD of undoped thermal TiO_2 on top of perovskite absorber

Nominally undoped TiO_2 thin films were deposited by the Picosun R200 system on to the perovskite layer of a thermal ALD TiO_2 coated, O_2 plasma cleaned FTO/glass substrate. This test structure was fabricated to determine how the temperature sensitive perovskite material reacted to the process of depositing an ALD thin film directly on top. This is an important consideration if the process is to be developed for the fabrication of *p-i-n* architecture devices. As with section 6.2.1, the titanium precursor and reactant used for the deposition were TDMAT and H_2O. The stack was provided with a short 5 minute thermal stabilisation time within the reaction chamber prior to growth at 100°C. This brief time was selected in an attempt to help provide some thermal stabilisation without causing degradation to the thermally sensitive perovskite absorber layer. The chamber was purposely set at 100°C as this was the same temperature used for annealing the perovskite layer after spin coating. Despite this precaution, prolonged time at this temperature could cause deterioration of the perovskite stack as total thermal budget and maximum temperature exposure are both significant. O_2 plasma was not utilised as a reactant or to clean the stack prior to ALD growth as it was thought likely to negatively impact the perovskite absorber layer underneath.

Table VI. I: *Experimental parameters for deposition of thermal TiO_2 at 100°C on top of the perovskite material using a Picosun R200*

Precursor	*Pulse*	*Purge*	*Repeat*
TDMAT	1.6 s		400
Purge		6s	
H_2O	0.1 s		
Purge		6s	

Table VI. I summarises the recipe used for the growth of thermal TiO_2 at 100°C directly on to a perovskite absorber. After 5 minutes of a stabilisation, the first precursor, TDMAT, was introduced for 1.6 seconds using a boost function. Following a 6 second purge a 0.1 second pulse of H_2O was introduced with another 6 second purge directly after to complete the cycle. The cycle of TDMAT and H_2O was repeated for a total of 400 cycles. The nominal thickness of the thin film grown was 20 nm assuming a growth rate of 0.05 nm per cycle. The shorter purge time of 6 seconds was used to minimise the thermal budget exposure of the sensitive perovskite absorber material whilst maintaining ALD behaviour through a purge time sufficient to allow extraction of unreacted precursor and by-products.

6.2.3 Fabrication of planar *n-i-p* PSCs

For the synthesis of the perovskite solution, 225.05 mg of MAI (Dyesol) was added to 652.52 mg PbI_2 (TCI) in a 4 ml vial in the glovebox. A magnetic stirrer was added to the vial, followed by 1,000 µl of a 1:9 volume ratio of DMSO:DMF (Sigma Aldrich). The 1.4 M perovskite solution was allowed to stir overnight in the glove box before being filtered into a clean vial using a 0.45 µm PTFE filter. The filtered perovskite solution was then removed from the glove box and spin coated on to the ALD TiO_2 or RF sputtered TiO_{2-x}/ FTO coated glass substrates. Immediately prior to spin coating the samples were subjected to a 15 minute UV O_3 treatment and blown with a N_2 gun to remove any contaminants from the environment. 65 µl $MAPbI_3$ solution was micro-pipetted on to the centre of the substrates before they were spun at 1,000 rpm for 10 seconds, then 5,000 rpm for 45 seconds. 0.75 ml of diethyl ether (Sigma Aldrich) was carefully used as an anti-solvent treatment 35 seconds before the end of the spin coating process. Samples were then dried for 2 minutes at 50°C and annealed for 10 minutes at 100°C.

The HTL was prepared by dissolving 43.4 mg 2,2',7,7'-tetrakis- (N,N-di-4-

methoxyphenylamino) -9,9'spirobi-fluorenes (Spiro-OMeTAD) (Merck) in 17.3 µl/ml 4-tert-butylpyridine (tBP) (TCI), 10.5 µl/ml stock solution of 520 mg/ml lithium bis (trifluoromethylsulfonyl) imide (LiTFSI) (Sigma-Aldrich) in acetonitrile, in 600 µl chlorobenzene. This was spin coated on top of the perovskite layer at 4,000 rpm for 30 seconds. The devices were completed with the evaporation of a 100 nm gold electrode.

Table VI. II: Spin coating programmes for planar PSC

	$MAPbI_3$ Step 1	*$MAPbI_3$ Step 2*	*Spiro-OMeTAD HTL*
Rate (rpm)	1,000	5,000	4,000
Time (s)	10	45	30
Acceleration	20	1,000	1,650

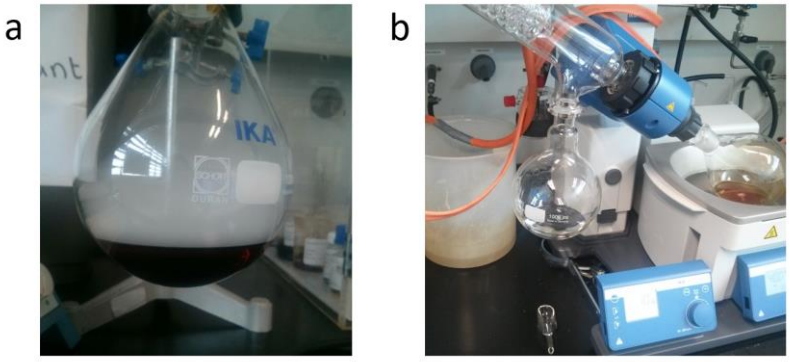

Figure 6. 3: (a) *Reaction of methylamine and ethanol with hydroiodic acid slowly added, and* ***(b)*** *rotary evaporator set up for $MAPbI_{3-x}Cl_x$ crystallisation*

For initial exploration of the topic of *p-i-n* PSCs and how ALD would affect the perovskite layer, two methods of perovskite absorber layer fabrication were investigated. The first method employed was the synthesis of a mixed halide perovskite solution, $MAPbI_{3-x}Cl_x$, as previously reported by Lee et al.[5] 33 wt % CH_3NH_3 in absolute ethanol was first reacted with 57 wt % hydroiodic acid in water and crystallised using a rotary evaporator (Figure 6.3). The resultant crystals were washed three times with diethyl ether to reveal white CH_3NH_3I crystals which were then dried overnight in an oven at 50°C. CH_3NH_3I and $PbCl_2$ were then dissolved in anhydrous N,N-Dimethylformamide (DMF) at a 3:1 molar ratio. The perovskite material was deposited at different spin coating speeds to determine which produced the best homogenous perovskite layer, then dried at 100°C for 30 minutes. The second method for fabrication of planar PSCs was that acquired from time spent at CSEM and

outlined above. MAI crystals were purchased directly from Dyesol and not synthesised in the lab. This provided less batch to batch variation and higher purity MAI crystals. This second method of depositing the perovskite layer was observed to be the superior procedure due to the homogenous nature of the thin films deposited, and so was selected as the exclusive method of perovskite deposition moving forward in Tyndall National Institute.

ALD TiO_2 was first deposited on FTO coated glass. The $MAPbI_{3-x}Cl_x$ or $MAPbI_3$ perovskite solution was prepared as described above and spin coated on the samples. The $MAPbI_3$ employed solvent quenching using diethyl ether 35 seconds before the end of the spin coating process. Afterward, samples were dried and annealed before low temperature ALD of the TiO_2 ETL was deposited and the stack investigated.

Unless stated otherwise in this Chapter, all perovskite solutions were composed of $MAPbI_{3-x}Cl_x$ or $MAPbI_3$.

6.3 Results and Discussion

A thickness series of 2 nm, 5 nm, 10 nm, 20 nm, and 25 nm ALD TiO_2 which were pre-treated with 5 minutes of an O_2 plasma prior to deposition was successfully grown on a range of substrates by a Picosun R200 ALD system at 185°C. The thickness series was grown in an attempt to optimise the ETL and enhance performance once incorporated into planar PSCs. Planar PSCs were then fabricated and their J-V characteristics were analysed in relation to the ALD ETLs.

ALD of 20 nm thermal TiO_2 grown at 100°C on a stack of perovskite absorber/ 20 nm thermal TiO_2 on a O_2 plasma pre-treated FTO coated glass stack was fabricated and examined. This was carried out to establish if good contact was made between the top ALD layer and the perovskite material and to investigate if the perovskite material was damaged in the process.

6.3.1 Morphology

The morphologies of the deposited ALD films and FTO coated glass were examined using scanning electron microscopy (SEM, FEI Quanta FEG 650) and transmission electron microscopy (TEM, Jeol ARM 200F). For TEM characterisation, specimens for cross section analysis (XTEM) were prepared using the conventional method of

gluing face to face small sections cut from an area of interest using M-bond. This was followed by mechanical polishing and ion milling in a Gatan PIPS model 691 apparatus before imaging. Plan view SEM, depicted in Figure 6.4 (a) and (b), shows that the surface morphology of 20 nm ALD TiO_2 on plasma pre-treated FTO coated glass is indistinguishable from that of blank FTO coated glass.

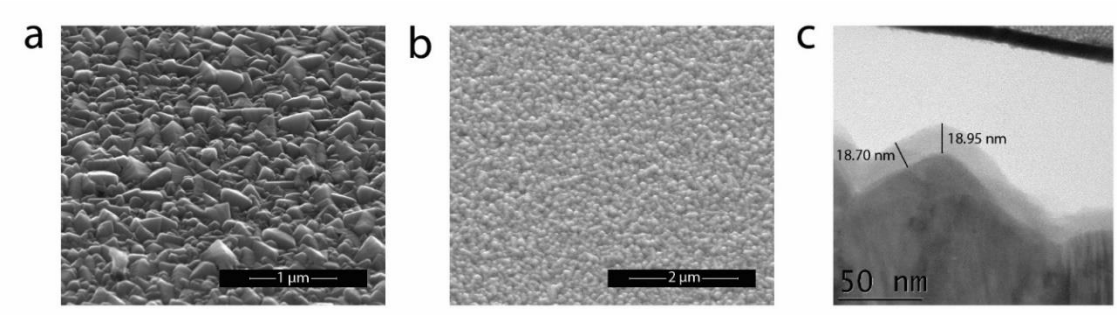

Figure 6. 4: *Plan view SEM showing surface morphology of* ***(a)*** *blank FTO coated glass and* ***(b)*** *20 nm thermal ALD TiO_2 pre-treated with O_2 plasma on FTO coated glass.* ***Figure 6. 4 (c):*** *Cross sectional TEM of 20 nm thermal ALD TiO_2 pre-treated with O_2 plasma on FTO coated glass.*

The TEM image exhibited in Figure 6.4 (c) supports the claim of ALD conformality as it shows the TiO_2 growth following the curves of the rough FTO coated glass underlayer. Ellipsometry was used to measure the thickness of the nominally 20 nm ALD TiO_2 film on a n-Si(100) wafer, while TEM was used to measure the thickness of the same film on FTO coated glass. A slight difference in thickness can be observed. SE using a Woollam M2000D system measured a thickness of 21.25 nm for a growth of thermal ALD TiO_2 on a n-Si(100) wafer which was subjected to a pre-growth 5 minute O_2 plasma treatment. This thickness did not include the native oxide of 1.45 nm on the wafer surface before ALD growth. A Cauchy TiO_2 model was used and the mean square error (MSE) obtained was 10.455. Through TEM of the same ALD growth run but on FTO coated glass a lower TiO_2 thickness was observed. The highest thickness obtained was 18.95 nm as observed in Figure 6.4 (c). After consideration of growth variability and errors in the different measurement techniques, this suggests that the TiO_2 has a slightly lower growth rate on FTO coated glass as compared to the silicon wafer. However, a TEM should also be obtained of the ALD growth on n-

Si(100) from the same growth to confirm, as using two different methods to measure ALD thickness on two separate substrates does not allow a direct comparison.

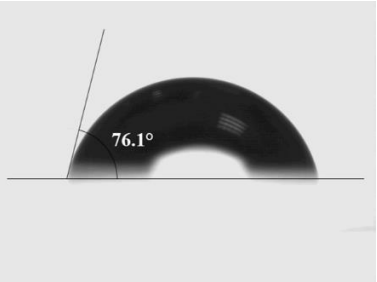

Figure 6. 5: *Contact angle measurement of 1 µl water on ALD thermal TiO_2 pre-treated with 5 minutes of O_2 plasma on FTO coated glass*

Contact angle measurements were performed at room temperature using a Dataphysics OCA 20 wetting angle system. These were carried out on the ETL to determine how well the perovskite layer would wet the surface when spin-coated. For mesoporous PSCs, the mesoporous TiO_2 layer was sandwiched between the compact ALD TiO_2 layer and the perovskite absorber material. However, for a planar cell, the ALD ETL would be in direct contact with the perovskite material and thus any changes in wetting behaviour, due to the ALD process, would be significant. The measured contact angle of 76.1 °, using 1 µl water, indicates that the ALD TiO_2 exhibits good wetting as displayed in Figure 6.5.

XRD was performed using a Philips X'pert PM3719 powder x-ray diffractometer with Cu Kα radiation (λ = 1.540598 Å). As would be expected at a deposition temperature of 185°C, all ALD films in this study were found to be amorphous as grown.

6.3.2 UV-visible spectrometry

UV-Vis was performed with a Perkin-Elmer Lambda 900 spectrophotometer (Chapter 5 section 5.3.2) to obtain optical transmittance from the thickness series of the ALD thermal TiO_2 on quartz pre-treated with 5 minutes of O_2 plasma.

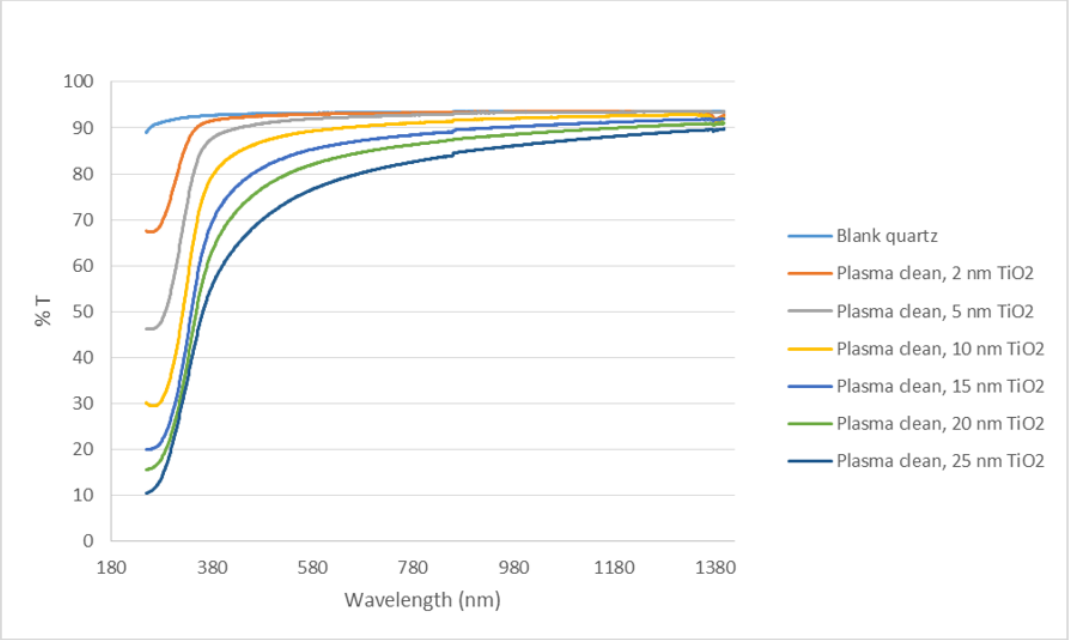

Figure 6. 6: *Graph illustrating % transmission spectrum for 20 nm nominally undoped and doped ALD TiO_2 films on quartz substrates*

As expected, optical transmittance of ALD on quartz, Figure 6.6, was found to scale with thickness. Values above 65 % were retained in the 400 nm – 1400 nm range of the spectrum even in the thickest film of 25 nm.

The bandgap of 20 nm ALD thermal TiO_2 pre-treated with a 5 minute O_2 plasma clean was calculated via UV-Vis spectrometry. The reflection percentage was determined and a tauc plot graphed plotting (αhν)^(1/n) versus photon energy (hν). Here "α" is the optical absorption coefficient, which can be calculated from absorbance "A", and thickness of the ALD layer "t" using the formula from equation 6.1:

$$\alpha = \frac{2.303\ A}{t} \qquad \textbf{6.1}$$

Energy (hν) is then calculated from the wavelength using the formula:

$$h\nu = \frac{1240}{wavelength\ (nm)} \qquad \textbf{6.2}$$

The power factor, "n", takes the values of 0.5, 2, 1.5, and 3 for allowed direct, allowed indirect, forbidden direct and forbidden indirect transitions respectively. Extrapolating the straight line portion of the curve to the zero absorption coefficient value gives the energy band gap value.

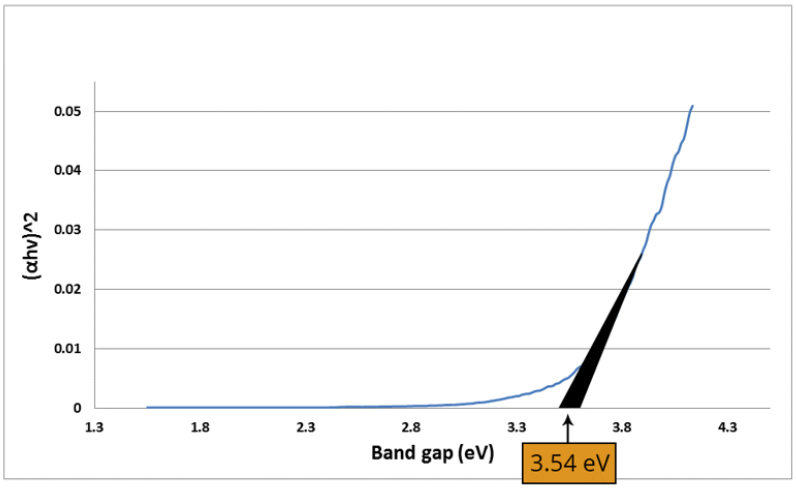

Figure 6. 7: *Tauc plot of ALD thermal TiO_2 pre-treated with a 5 minute O_2 plasma clean*

The calculated tauc plot (Figure 6.7) exhibits a bandgap of 3.54 ± 0.053 eV for ALD thermal TiO_2 pre-treated with a 5 minute O_2 plasma clean. This bandgap value obtained for the indirect transition is quite high compared to bandgap values obtained in the literature for crystalline versions of TiO_2. Rutile TiO_2 is expected to have a bandgap of ~ 3.0 eV [6,7], while that of anatase is calculated to be ~ 3.4 eV[8], and that of brookite is calculated to be ~3.3 eV[9]. While the shift to a higher value in this tauc plot for amorphous TiO_2 is inconclusive due to the large margin of error, there is evidence that suggests the morphology of TiO_2 materials can be determined by optical absorption techniques. Welte et al.[10] used a sol-gel method at various temperatures to synthesise amorphous, amorphous-crystalline, and crystalline TiO_2 films. The thin films heated to room temperature and 200°C were found to be amorphous by XRD and Raman characterisation. The extrapolated bandgap values of these films were found to lie in the 3.5 eV range, much higher than the crystallised films. This higher bandgap exhibited by amorphous TiO_2 films was likewise observed by Valencia and co-workers[11] in the case of TiO_2 synthesised through a sol-gel and hydrothermal treatment method which exhibited a bandgap of 3.4 eV for indirect transitions. A shift in band gap has also been observed in non-stoichiometric TiO_2 in the literature. Cation doping using transition metal ions of V, Cr, Mn, Fe, and Ni has been shown to cause TiO_2 to exhibit a large shift in the absorption band towards the visible region,

achieving a narrow band gap.[12] Undoped TiO_2 can also be modified by non-metals such as N, S, or C to form non-stoichiometric films.[13-15] TiO_xN_y deposited by PEALD, using TTIP or TDMAT and NH_3 or N_2 as the respective titanium precursors and co-reactants, achieved a narrow band gap compared to stoichiometric ALD TiO_2. This band gap narrowing was tuned by altering the ALD processing and parameters.[16]

6.3.3 Complete planar solar cell

Following the author's work depositing and characterising ALD ETLs at Tyndall National Institute, an internship was arranged at CSEM to study established deposition methods with which to deposit the remaining PSC layers. Here the author fabricated planar perovskite devices using 20nm ALD TiO_2 and reference 20 nm sputtered TiO_{2-x} as ETLs. The remainder of the ALD ETL thickness series was sent to CSEM along with ALD passivated ETLs for fabrication into planar devices. The study of structures containing low temperature ALD thin films on top of the perovskite absorber material was carried out at Tyndall National Institute. The performance of these devices are compared and discussed herein.

6.3.3.1 Reference sputtered TiO_2 as compact ETL

To evaluate planar *n-i-p* perovskite solar cell devices assembled using ALD thermal TiO_2, RF sputtered TiO_{2-x} was chosen to act as a reference ETL because its use in a mesoporous structure has been well established and optimised at CSEM.[17] These reference solar cell devices were composed of a conductive FTO coated glass substrate, a 20 nm sputtered TiO_{2-x} thin film, a $MAPbI_3$ perovskite layer, a Spiro-OMeTAD hole transport layer and a gold or a MoO_x/ITO/Ag counter electrode. The devices containing ALD ETLs were fabricated alongside the RF sputtered ETLs to minimise process variability and allow the ETLs to be directly compared.

These planar perovskite devices were measured under a two-lamp class AAA WACOM sun simulator with an AM 1.5 G irradiance spectrum at 100 W cm^{-2}. The cell area was 1.04 cm^2 and defined using a metal mask. The J–V characteristics of the cells were obtained under both reverse (from V_{oc} to J_{sc}) and forward (from J_{sc} to V_{oc}) bias. Maximum power point (MPP) tracking was performed to extract the stabilised power output. External quantum efficiency (EQE) spectra were acquired on a custom-made spectral response setup equipped with a xenon lamp, a grating monochromator

and lock-in amplifiers.

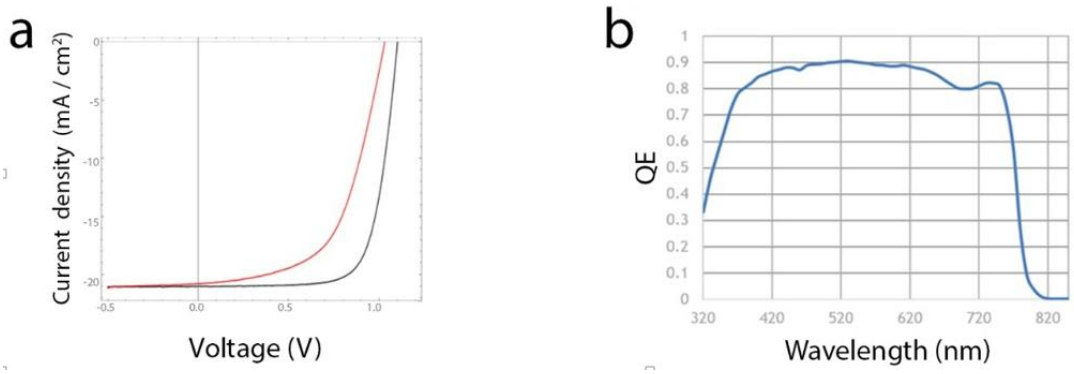

Figure 6. 8: (a) *J–V characteristics of planar perovskite solar cell containing sputtered 20 nm TiO_{2-x}.* ***(b)*** *External quantum efficiency of same perovskite solar cell containing sputtered 20 nm TiO_{2-x} ETL*

Table VI. III: *Device performance parameters for a planar cell containing 20 nm sputtered TiO_{2-x} ETL*

Scan Direction	*V_{oc} (mV)*	*J_{sc} (mA cm^{-2})*	*FF (%)*	*PCE (%)*
Reverse	1103	21.039	73.044	16.955
Forward	1032	20.804	57.503	12.364

The J-V characteristics of the best PSC based on the reference ETL, sputtered TiO_{2-x}, is shown in Figure 6.8a and the corresponding external quantum efficiency is displayed in Figure 6.8b. This device achieved a Voc, Jsc, and FF of 1103 mV, 21.39 mA cm^{-2}, and 73.044 %, respectively, leading to a remarkably high PCE of 16.96 %. However, pronounced hysteresis could be observed in the J-V curve of the PSC. EQE displayed a current density of 21.74 mA cm^{-2} which is slightly higher than that provided by the J-V results. These results were unexpectedly higher than the mesoporous PSC containing the same ETL which had reached a PCE of 16.19 %. Both V_{oc} and J_{sc} measurements were notably higher in the planar configuration leading to a higher overall efficiency. This result had not previously been observed at CSEM. The same fabrication process had been performed on ITO coated glass previously, yielding results expectedly lower than the mesoporous PSC. It is thought that the rough FTO coated glass substrate provided more surface area for the perovskite absorber allowing

a higher efficiency to be achieved compared to the same stack on ITO coated glass. This and the use of a MoO_x/ITO/Ag evaporated contact contributed to the overall higher PCE obtained.

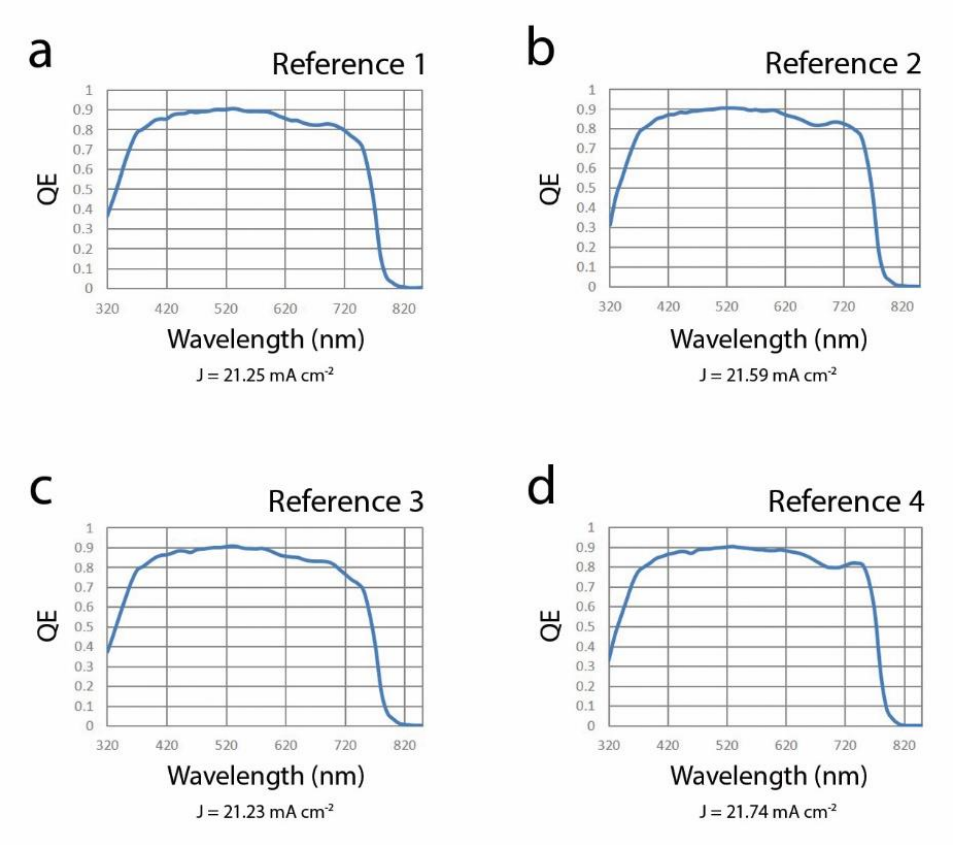

Figure 6. 9: *EQE of all reference planar cells fabricated. All cells exhibited an EQE >21 mA cm^{-2} with cell "reference 4" reaching 21.74 mA cm^{-2}*

All reference planar cells obtained similarly high PCEs with the best PSC based on the reference sputtered TiO_{2-x} displayed above in Figure 6.8. Similarly, all EQE measurements of each of the four reference cells exhibited currents > 21 mA cm^2, confirming the reproducibility of the cell fabrication method (Figure 6.9).

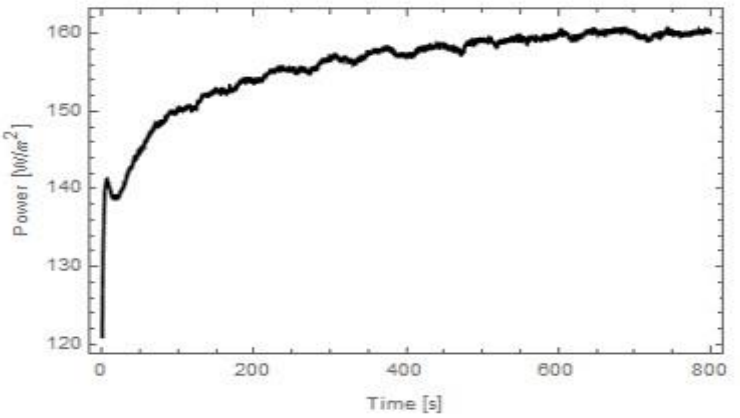

Figure 6. 10: *Max power point steady state tracking over 800 seconds of planar PSC containing sputtered TiO_{2-x} as ETL*

MPP steady state tracking for each of the reference cells was shown to approach 16 % PCE with one cell reaching 16.05 % PCE over 800 seconds of tracking as depicted in Figure 6.10. After the internship this experiment was repeated by collaborators at CSEM and a MPP steady state tracking as high as 17 % PCE was achieved, though pronounced hysteresis in the J-V characterisation was still observed.

6.3.3.2 ALD plasma pre clean, thermal TiO_2 as ETL

It was expected that the thermal ALD TiO_2 ETL which was treated with 5 minutes of O_2 plasma prior to ALD growth would perform similarly well in a planar configuration to the sputtered TiO_{2-x} reference cell. The results from the mesoporous PSCs showed a comparable result between both ETLs, with the cell incorporating sputtered TiO_{2-x} exhibiting a slightly higher PCE of 16.19 % compared to 15.33 % obtained from the cell fabricated using a plasma pre clean, 20 nm thermal ALD TiO_2 ETL.

In the fabrication of a mesoporous PSC, the mesoporous TiO_2 layer, and subsequently each layer underneath, undergoes a sintering process to 500°C. This high temperature anneal could influence the resistance characteristics of the underlying compact ALD TiO_2 film. To investigate this 20 nm TiO_2 was thermally grown on FTO coated glass substrates treated with a 5 minute O_2 plasma clean. Half of these samples were then subjected to the same sintering process to 500°C that the mesoporous TiO_2 scaffold requires. All samples were then evaporated with a 5 nm Ti adhesion layer followed by a 150 nm Katya mask. Electrical conductivity was then measured on 100 nm^2 pads in

different areas across the 25 mm^2 sample by applying a voltage sweep from 0 to ± 1 V, in 0.015 V steps. J-V characteristics of the as grown ALD film was compared to a film sintered at 500°C is shown in Figure 6.11.

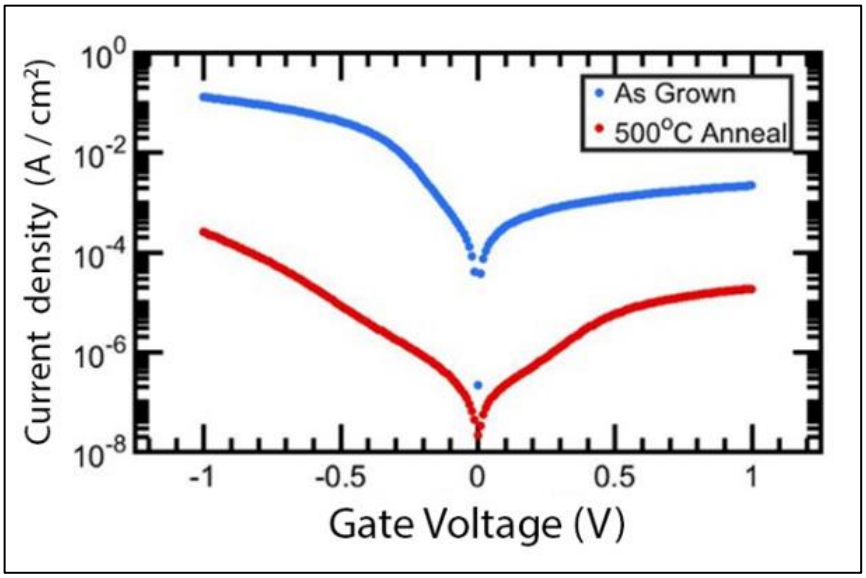

Figure 6. 11: *J-V sweep comparing 20 nm thermally grown TiO_2 on FTO coated glass treated with 5 minutes of O_2 plasma prior to ALD growth to the same film sintered at 500°C*

From electrical conductivity measurements, it is clear that the sintering applied to ALD films when fabricating the mesoporous PSCs increased their resistance characteristics by several orders of magnitude. This increase in resistivity with increased temperature is likely due to impurities migrating to the interfaces or grain boundaries of the thin film. Removal of the mesoporous layer would allow the ALD TiO_2 to maintain its conductivity which could contribute to a higher overall PCE, while also lowering the thermal budget of the entire cell enabling tandem cell fabrication.

In the previous chapter 20 nm ALD TiO_2 films were chosen as compact hole blocking layers in mesoporous PSCs. Despite the belief that ALD could enable a thinner blocking layer, a thickness of 20 nm TiO_2 was chosen to allow direct comparison with the equivalent thickness of CSEMs RF sputtered TiO_{2-x}. Furthermore, it was believed that thinner amorphous ALD films would not be able to stand the high temperature anneal (500°C) employed in the mesoporous PSC fabrication method without cracking

and hence forming shunt pathways. Removal of the mesoporous layer allowed exploration into thinner ALD TiO_2 films. A thickness series of 5 nm, 10 nm, 15 nm, 20 nm, and 25 nm thermal ALD TiO_2 pre-treated with a 5 minute O_2 plasma clean was deposited on TEC-15 FTO coated glass using the Picosun R200 system. The 20 nm film was examined by the author while at CSEM and the remaining thicknesses grown at Tyndall, were sent to CSEM for investigation and comparison to reference cells deposited on TEC-7 FTO coated glass.

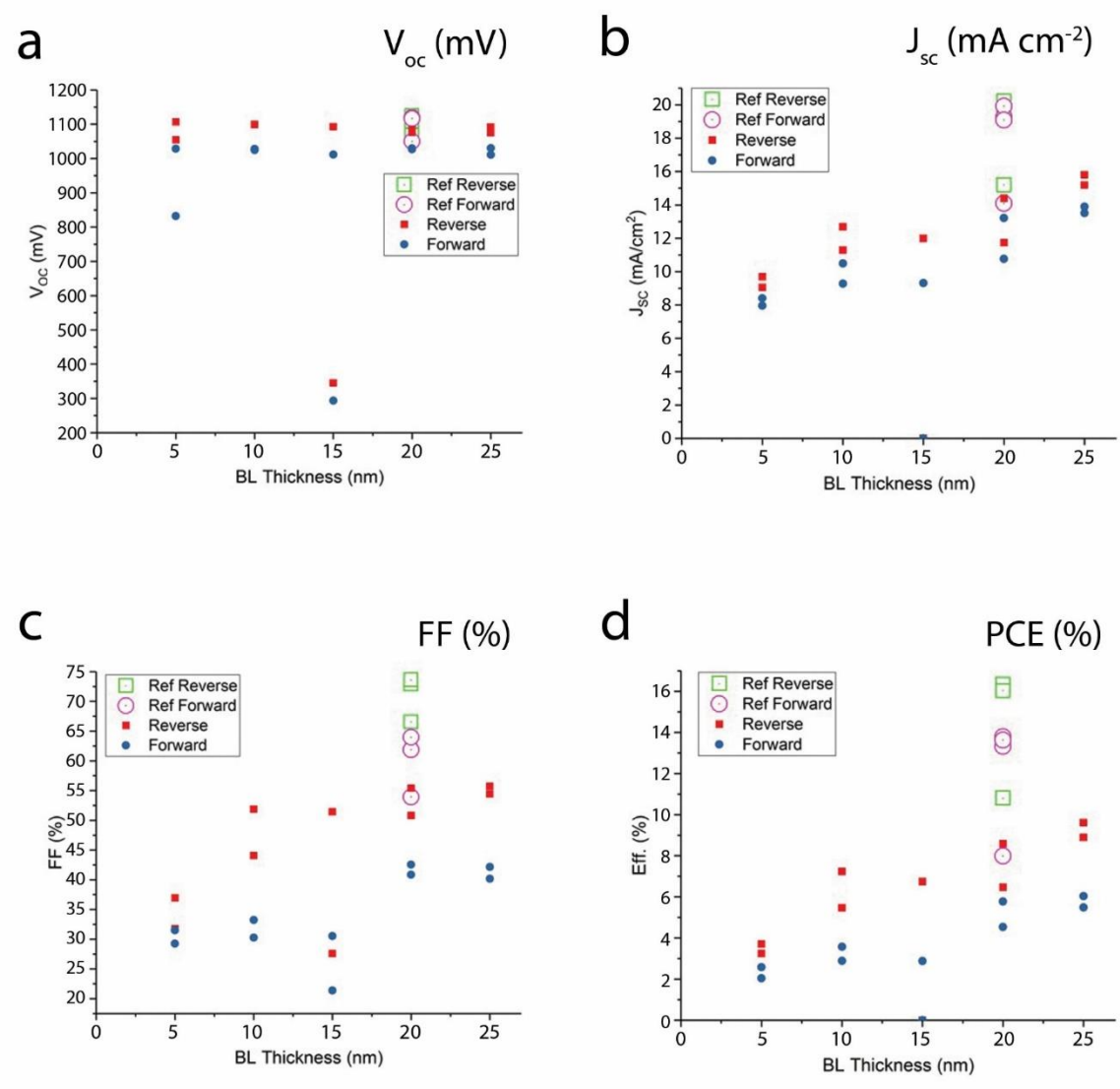

Figure 6. 12: *J–V characteristics of planar perovskite solar cell containing sputtered 20 nm TiO_{2-x} as the reference ETL and 5 nm, 10 nm, 15 nm, 20 nm, 25 nm thermal TiO_2 pre-treated with a 5 minute O_2 plasma as the ALD thickness series ETLs.*

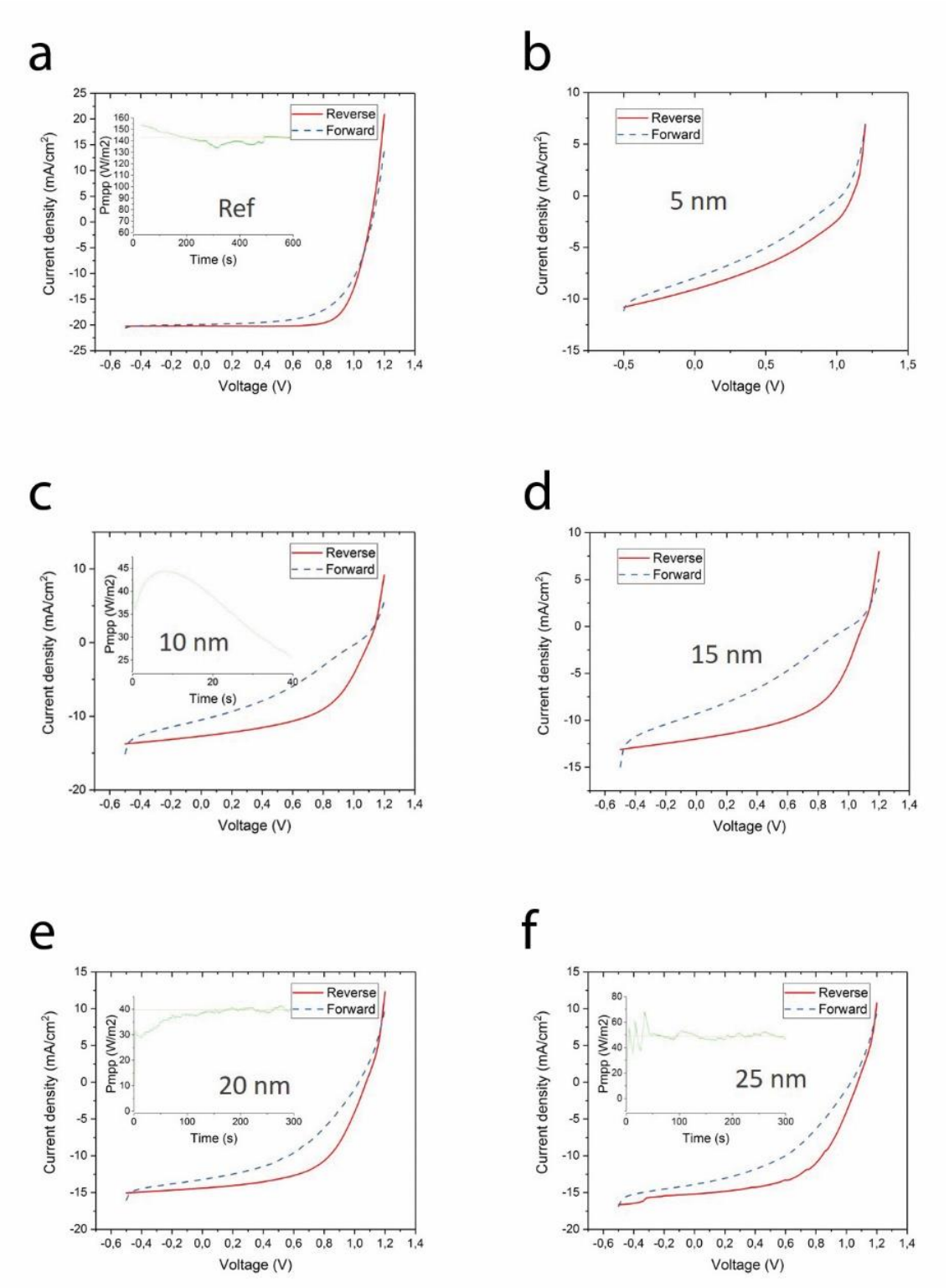

Figure 6. 13: *Best J-V curves obtained for planar PSCs containing* ***(a)*** *reference sputtered TiO_{2-x},* ***(b)*** *5 nm,* ***(c)*** *10 nm,* ***(d)*** *15 nm,* ***(e)*** *20 nm, and* ***(f)*** *25 nm thermal ALD TiO_2 pre-treated with a 5 minute O_2 plasma before growth*

From the J-V characteristics and curves shown in Figures 6.12 and 6.13 it can be observed that the ALD TiO_2 ETLs did not perform as well as expected when fabricated into planar PSCs. The V_{oc} obtained was shown to be high in all cells containing ALD TiO_2 regardless of ETL thickness and was comparable to that achieved by the reference planar cells containing 20 nm sputtered TiO_2. The J_{sc} was found to increase with increased ALD ETL thickness, however results were still lower than the J_{sc} obtained from the reference cells. The current for the planar cell containing the 20 nm ALD ETL film was also significantly lower than the mesoporous cells fabricated in Chapter 5 which incorporated the same 20 nm thermal ALD TiO_2 on FTO coated glass as an ETL. The FF obtained from the planar cells was also quite low when compared to the reference cells and found to increase slightly with ALD thickness. Again, the FF in the cell containing 20 nm ALD TiO_2 was much lower than the 70.61 % previously achieved in the mesoporous version in Chapter 5. A max PCE of 8 % was achieved for the planar cells containing 20 nm thermal ALD TiO_2 as an ETL. Overall, the PCE of the planar cells containing the thickness series of ALD TiO_2 was significantly reduced, being limited by the poor J_{sc} and FF.

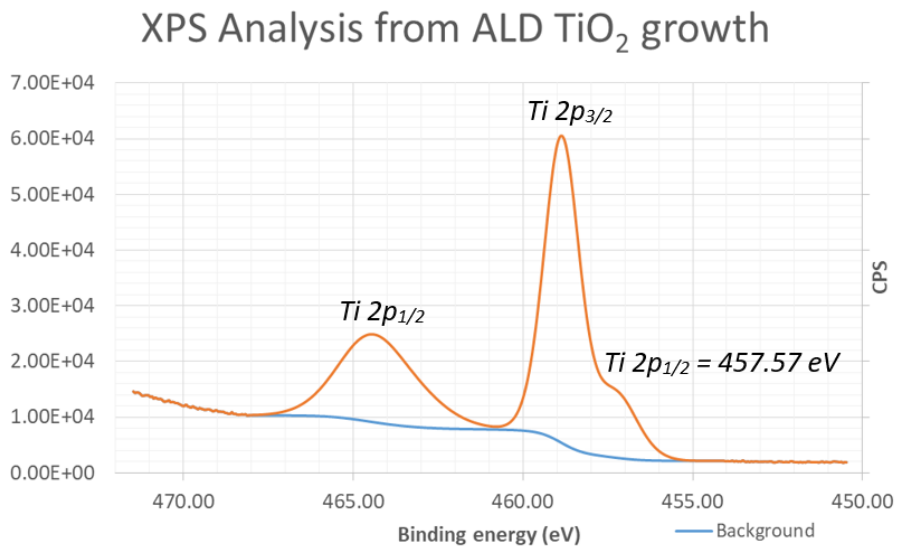

Figure 6. 14: *XPS spectra of as grown 20 nm ALD TiO_2 pre-treated with an O_2 plasma clean*

Removal of the mesoporous TiO_2 layer to form planar PSCs did not give the expected boost in performance anticipated by the use of an ALD TiO_2 ETL. While the sintering

process required for the TiO_2 mesoporous layer increased resistivity of the ALD compact TiO_2 this was clearly not the dominant property. Examination of the XPS Ti 2p signatures of the as grown and mesoporous process annealed ALD TiO_2 show that the significantly sub-stoichiometric nature of this low temperature ALD material (Figure 6.14) was improved by the anneal, with the ratio of Ti^{3+} to Ti^{4+} being reduced from 1:3.9 to 1:4.1. As deposited TiO_2 from the TDMAT ALD process at 185°C was found, in addition to being non-stoichiometric, to contain measurable quantities of N and C from unreacted precursors as previously described. When annealed to 500°C the nitrogen content was reduced from 0.6 % to 0.3 % concentration. Similarly the carbon content was reduced from 8.9 % to 5.2 % concentration. This suggests that the levels of unreacted precursor ligands were reduced by the high temperature anneal. The stoichiometry of the films along with N and C content were obtained after 10 seconds of sputtering with an Ar cluster beam to remove the top layers of the thin films. The highly defective nature of the as grown material could give rise to significant charge trapping in both the bulk and the interface.

6.3.3.3 Passivation and Rapid Thermal Annealing

In an attempt to improve the performance of planar cells using ALD TiO_2 as the ETL, interface passivation was explored using ALD Al_2O_3. Two 50 mm^2 cleaned TEC-7 FTO coated glass substrates were patterned with 0.6 mm kapton tape and placed in the Picosun R200 reactor (Appendix I, Figure 1). The substrates were allowed to thermally stabilise for 40 minutes before being subjected to a 5 minute O_2 plasma clean and a routine 20 nm thermal TiO_2 growth using TDMAT and H_2O as precursor and reactant respectively. Afterward, one of the 50 mm^2 substrates received an additional growth of 7 cycles Al_2O_3 using a pulse/purge sequence of 0.1 second TMA pulse, 6 second purge, and 0.1 second H_2O pulse. An identical deposition of 20 nm thermal TiO_2 pre-treated with 5 minutes of O_2 plasma and capped with Al_2O_3 using the Cambridge Nanotech reactor was carried out. Table VI. IV details the XPS data gathered on these samples and shows that the carbon content increased due to Al_2O_3 passivation. This suggests that the 185°C deposition temperature of the Al_2O_3 capping is not sufficient for complete decomposition of the TMA ligands, leading to increased carbon impurities. The presence of Al_2O_3 was observed in both samples.

Table VI. IV: *XPS results detailing the percentage concentration of the Ti^{3+}, the Ti^{4+}, the nitrogen, the carbon, the oxygen and the aluminium contents in standard and passivated 20 nm TiO_2 films on FTO coated glass*

Reactor	*Sample*	*C 1s %conc*	*N 1s %conc*	*Ti^{3+} %conc*	*Ti^{4+} %conc*	*Ti^{3+}/Ti^{4+}*	*O 1s %conc*	*Ti/Al*
Picosun	Standard	6.2	0.3	3.7	15.0	0.247	57.0	-
Picosun	Standard, passivated 7 cycles Al_2O_3	6.9	0.2	2.6	13.0	0.200	55.3	2.4
CNT	Standard	6.9	0.5	3.3	15.1	0.219	57.6	-
CNT	Standard, passivated 7 cycles Al_2O_3	7.9	0.2	2.6	12.6	0.206	53.0	2.3

TEM images of samples before and after Al_2O_3 treatment were captured to determine how well the ALD Al_2O_3 nucleated on ALD TiO_2. If the Al_2O_3 layer was above the expected growth rate of 0.1 nm per cycle then it may have blocked extraction of charge when fabricated into a planar PSC. If the TiO_2 under layer inhibited the growth of Al_2O_3 then the Al_2O_3 may have not nucleated with the 7 cycles and failed to passivate the TiO_2 surface when fabricated into a planar PSC. During TEM imaging there was a charging issue with the sample capped with Al_2O_3. The images were sharpened and due to this the scale bar size differs between samples (a) and (b) in Figure 6.15. An increase in thickness between 0.14 – 0.68 nm can be observed when 7 cycles of Al_2O_3 are deposited on the TiO_2 thin film. These thickness measurements along with the charging issue observed suggest that the Al_2O_3 was successfully deposited without inhibited nucleation on ALD TiO_2.

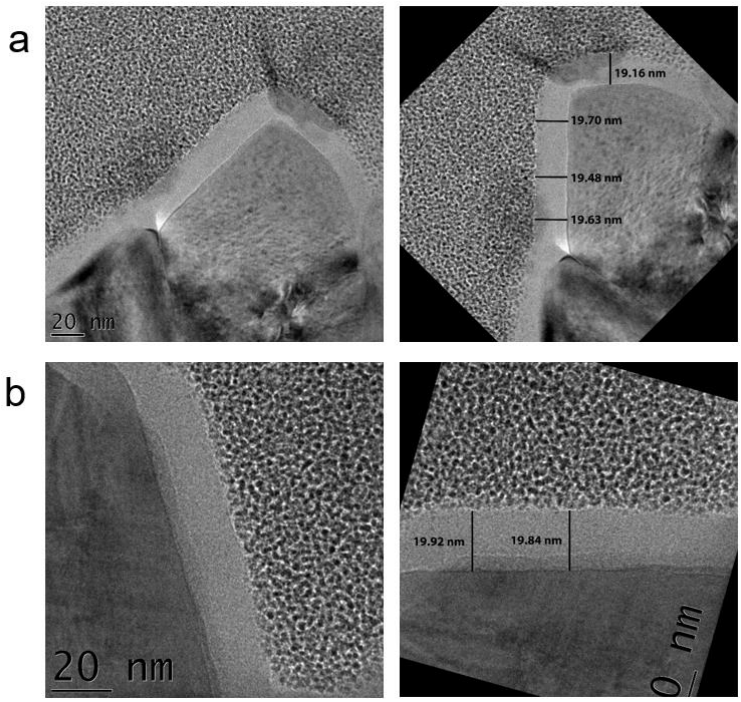

Figure 6. 15: *TEM images and thickness measurements of* ***(a)*** *20 nm thermal ALD TiO_2 on FTO coated glass treated with 5 minutes of O_2 plasma prior to ALD growth and* ***(b)*** *the same film capped with 7 cycles of Al_2O_3 by ALD*

Another avenue investigated was rapid thermal annealing (RTA) of the ALD film in an effort to improve the quality of the TiO_2. However the increased thermal budget of this method could make it unsuitable for use in tandem cells. Again, 20 nm thermal TiO_2 which was pre-treated with 5 minutes of O_2 plasma was grown by ALD using the Picosun R200 system on two cleaned and patterned 50 mm^2 TEC-7 FTO coated glass substrates. One of the 50 mm^2 substrates then underwent rapid thermal annealing (RTA) in O_2 to 500°C using a Jipelec JetFirst 200 system. After placing the substrate in the RTA chamber, the chamber was vacuumed for 30 seconds and then purged with O_2 gas for 30 seconds. This process was repeated for a total of three times. The chamber was vacuumed again before 1,000 sccm of O_2 gas was introduced for 30 seconds. The O_2 was then reduced to a constant flow of 100 sccm as the temperature began a ramp to 200°C at a rate of 10°C per second. A stabilisation period of 30 seconds followed before the temperature was again ramped to 500°C at a rate of 10°C per second. The substrate was maintained at a temperature of 500°C for 2 minutes before RTA ended and the chamber was purged with N_2 for 240 seconds. Once the chamber reached 80°C after approximately 15 minutes, the chamber was opened and

the substrate was removed.

All passivated and annealed samples, were diced and scribed with a P1 line before being sent to CSEM for fabrication into planar PSCs. The perovskite absorber material for these planar cells was a triple cation mixed halide perovskite, $Cs_{0.05}(FA_{0.83}MA_{0.17})_{99.5}Pb(Br_{0.17}I_{0.83})_3$. Immediately prior to addition of the absorbing layer at CSEM, the TiO_2/FTO coated glass samples were treated with a 15 minute UV-O_3 treatment. The perovskite solution was spin coated in the glovebox using chlorobenzene in a solvent quenching technique. The final planar cell architecture comprised of FTO coated glass/ ALD TiO_2 or RF sputtered TiO_2/ $CsFAMAPb(BrI)_3$ perovskite/ Spiro-OMeTAD HTL/ Au contact. All cells had an active area of 1.04 cm^2.

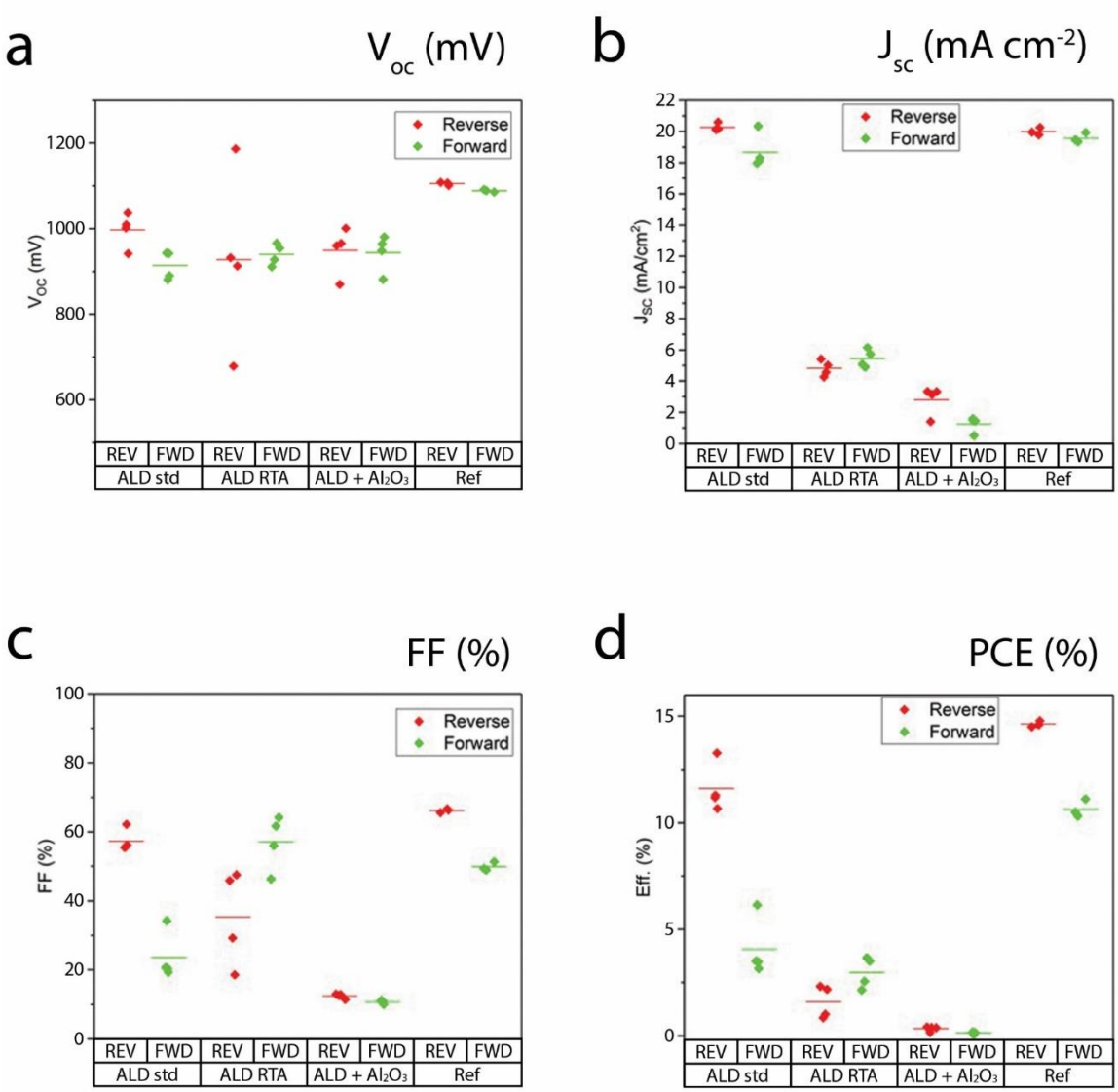

Figure 6. 16: *J–V characteristics of planar perovskite solar cells containing ETLs of sputtered 20 nm TiO_{2-x} as the reference, 20 nm thermal ALD TiO_2 pre-treated with 5 minutes of O_2 plasma as the standard ETL, the standard ETL rapid thermal annealed to 500°C, and the standard ETL with 7 cycles of Al_2O_3 as passivation.*

Figure 6.16 outlines the J-V characteristics of planar cells containing a "reference" RF sputtered 20 nm TiO_{2-x} ETL, a "standard" ALD growth of 20 nm thermal TiO_2 pre-treated with 5 minutes of O_2 plasma, a standard ALD growth which was rapid thermal annealed to 500°C in O_2, and a standard ALD growth which had been capped with 7 cycles of ALD Al_2O_3. The V_{oc} obtained was shown to be high in all cells containing ALD TiO_2 and comparable to the sputtered reference ETL. The J_{sc} was high in the planar cell containing the standard ALD TiO_2 corresponding to the reference cell. Current was observed to be strongly suppressed in both cells containing ALD ETLs which had undergone rapid thermal annealing and Al_2O_3 capping. V_{oc} and FF

exhibited in all cells containing ALD TiO_2 was far below that of the reference leading to a lower PCE.

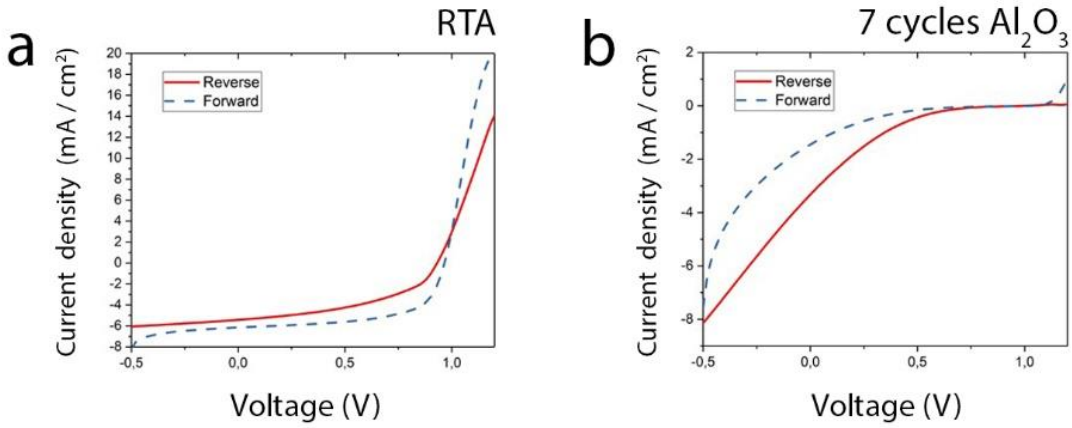

Figure 6.17: *J-V curves obtained for planar PSCs containing a 20 nm thermal ALD TiO_2 ETL pre-treated with 5 minutes O_2 plasma which had (a) undergone RTA to 500°C, and (b) been passivated with 7 cycles of Al_2O_3*

From the J-V curves obtained from the planar cell measurements in Figure 6.17, a disappearance in the s-shape can be observed for the ALD TiO_2 sample which underwent RTA to 500°C in O_2. This s-shape had been present for standard ALD J-V curves obtained previously as described in Figure 6.13. Despite this, the current was strongly reduced by the RTA process. The J-V curve of 20 nm thermal ALD TiO_2 pre-treated with 5 minutes of O_2 plasma and capped with 7 cycles of Al_2O_3 suggests that the thin Al_2O_3 film was too thick and completely blocks the extraction of charges.

In an effort to resolve this passivation issue, 1 cycle of Al_2O_3 was deposited on 20 nm thermal ALD TiO_2 pre-treated with 5 minutes of O_2 plasma/ FTO coated glass by both the Picosun and Cambridge Nanotech reactors. Deposition was carried out using both ALD systems to establish if a difference in Al_2O_3 resistivity could be observed once thin films had been fabricated into planar devices. The two reactors have different chamber sizes and utilise different flow rates, both of which can affect growth. Previous work in Chapter 5 demonstrated that doped TiO_2 thin films were reactor dependant, producing more resistive films when grown using the Picosun R200 system despite the same precursor and reactants being utilised. To help clean the

interface, a 5 minute O_2 plasma treatment was also employed after TiO_2 growth and directly prior to deposition of the Al_2O_3. It is difficult to determine if a single pulse of Al_2O_3 is sufficient to produce a saturated monolayer of growth. To combat this, the TMA pulse was increased from 0.1 seconds to 0.2 seconds to ensure saturation of the TiO_2 surface. Five 0.2 second pulses of TMA were introduced into the reaction chamber separated by a 0.5 second purge between each pulse. A long 15 second purge was allowed following the 5 consecutive TMA pulses before a single 0.1 second pulse of the reactant, H_2O, was introduced (Figure 6.18).

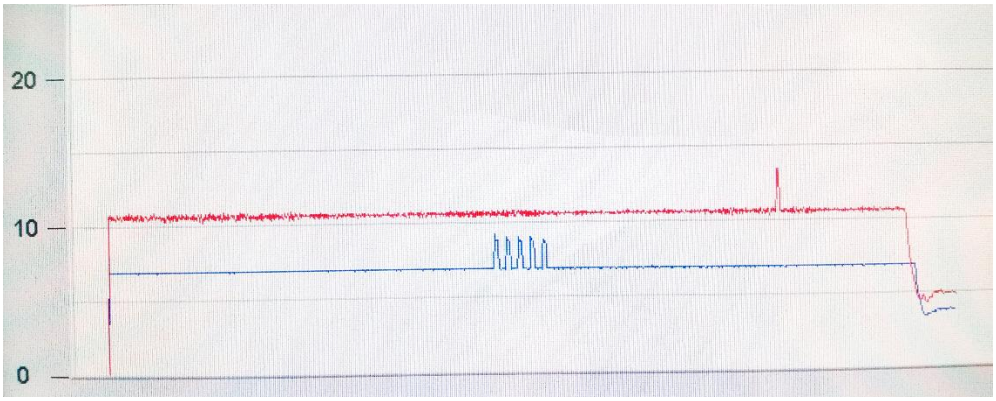

Figure 6.18: *Pressure pulses on Picosun R200 reactor showing five rapid 0.2 second pulses of TMA followed by a long 15 second purge and one 0.1 second pulse of H_2O used for the 1 cycle Al_2O_3 passivation layer.*

These 20 nm thermal TiO_2 thin films pre-treated and post-treated with 5 minutes of O_2 plasma prior to capping with 1 cycle of Al_2O_3 were fabricated into planar cells and compared to a reference cell containing 20 nm sputtered TiO_2. Unlike the comparison between a 7 cycle capping of Al_2O_3 and RTA TiO_2 ETLs, these planar cells were composed of a regular architecture of FTO coated glass/ ALD TiO_2 capped with 1 cycle Al_2O_3/ $MAPbI_3$/ Spiro-OMeTAD/ Au contact.

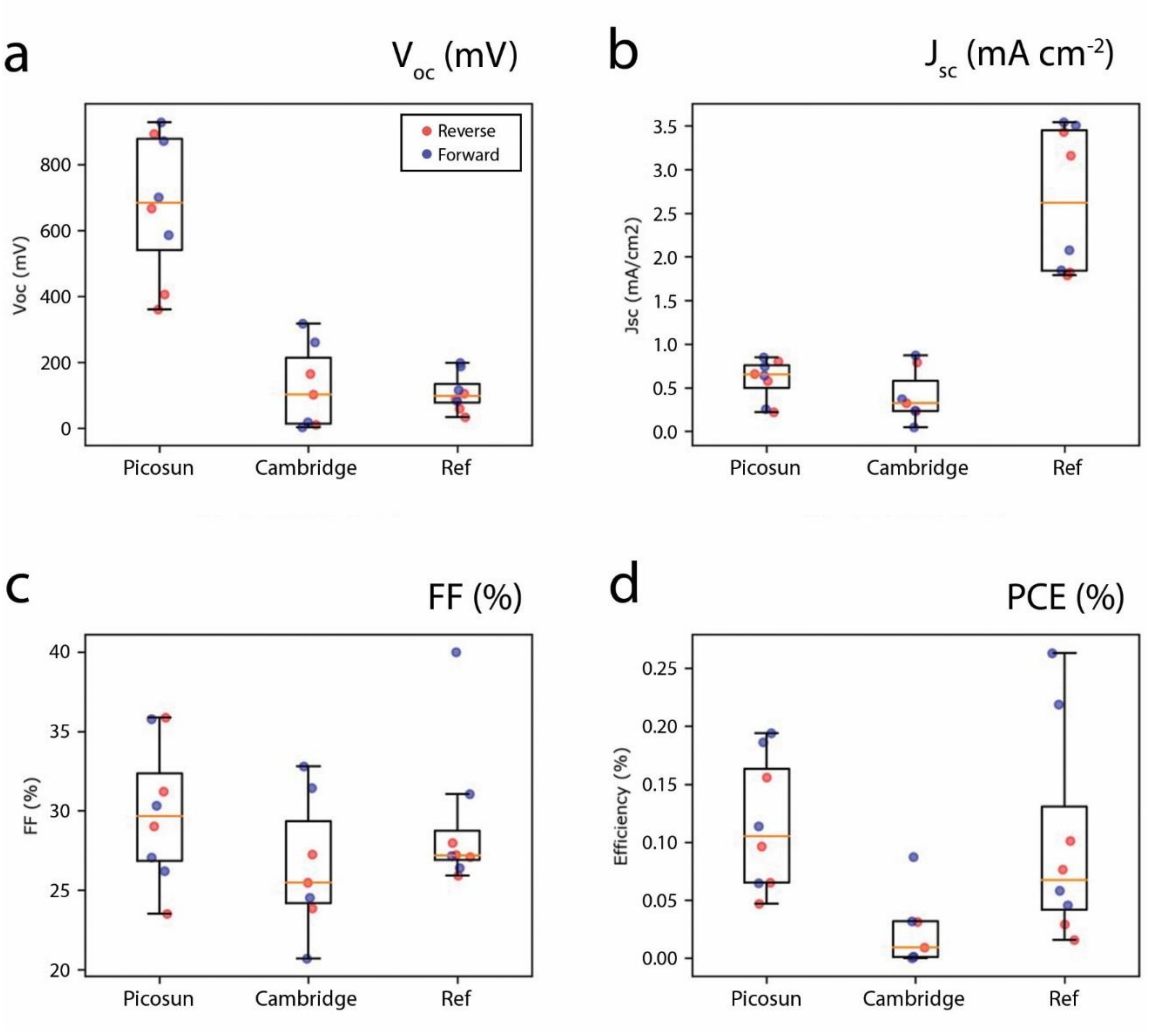

Figure 6. 19: *J–V characteristics of planar perovskite solar cells containing ETLs of sputtered 20 nm TiO_{2-x} as the reference, and 20 nm thermal ALD TiO_2 pre-treated with 5 minutes of O_2 plasma passivated with 1 cycle of Al_2O_3 on both the Cambridge Nanotech and Picosun R200 reactors*

From the J-V characteristics above in Figure 6.19 it can be observed that there was an issue with the perovskite absorber or Spiro-OMeTAD layer as the PCE of the reference cell containing a sputtered TiO_{2-x} is far lower than the expected values. Nevertheless, the 1 cycle Al_2O_3 passivation layer gives significantly lower current (~ 0 mA cm^{-2}) which is in line with what was previously shown with 7 cycles of Al_2O_3. Thus it appears that the single cycle of Al_2O_3 is still capable of blocking the extraction of charge. This result could be due to the single cycle forming a negative charge on the surface of the TiO_2 layer inhibiting current. It is possible that a higher deposition temperature of the Al_2O_3 could aid in cleaning up the surface of TiO_2,[18] however this was not investigated further as the higher deposition temperature ~ 300°C for Al_2O_3

could interfere with the ALD TiO_2 under layer which was deposited at 185°C.

Due to the resistive nature of Al_2O_3, ALD passivation using ZnO was also investigated in the fabrication of planar PSCs containing ALD TiO_2 pre-treated with 5 minutes of O_2 plasma. The zinc precursor, diethylezinc (DEZ), contains ethyl ligands which may also aid in cleaning the surface of the ALD TiO_2 thin film without completely blocking charge extraction. ZnO has previously been shown to act as a suitable ETL[19], however it has also been reported that ZnO nanoparticles may react with the perovskite absorber material upon annealing.[20,21] This reaction appears to be induced by heat rather than light as both ZnO and TiO_2 are photoactive in nature.[22-24] It was speculated that if the ZnO passivation by ALD was successful in passivating the surface of TiO_2 then ALD ZnO itself could be employed as the sole ETL.

As with the Al_2O_3 passivation described above, FTO coated glass and ITO coated glass substrates were deposited with 20 nm thermal TiO_2 pre-treated with a 5 minute O_2 plasma clean at 185°C in both the Picosun and Cambridge Nanotech reactors. Afterward a 5 minute O_2 plasma treatment was applied to the thin films to aid in cleaning the TiO_2 surface directly prior to the deposition of 3 cycles of ZnO on the Cambridge Nanotech reactor. The DEZ vessel was maintained at room temperature where an adequate vapour pressure was achieved. For deposition of ZnO, the reaction chamber was reduced to 130°C to maintain ZnO growth within the ALD window. 0.2 seconds of DEZ was pulsed followed by a 20 second purge, a 0.1 second H_2O pulse, and another 20 second purge. This was repeated for a total of three cycles. The assumed growth rate of ZnO was 0.2 nm per cycle.[25,26] Ellipsometry measurements were extracted from the thin films grown on n-Si(100) wafers before and after ZnO passivation using a layered TiO_2 Cauchy model and a ZnO GenOsc model. The end measurements proposed a thickness of 0.52 nm ZnO/ 20.24 nm TiO_2 /a fixed 1.45 nm SiO_2 interlayer/ n-Si(100) wafer. The MSE for this measurement was 11.194. These passivated samples were investigated by CSEM along with non-passivated 10 nm and 20 nm TiO_2 films which used the same recipe to act as a reference.

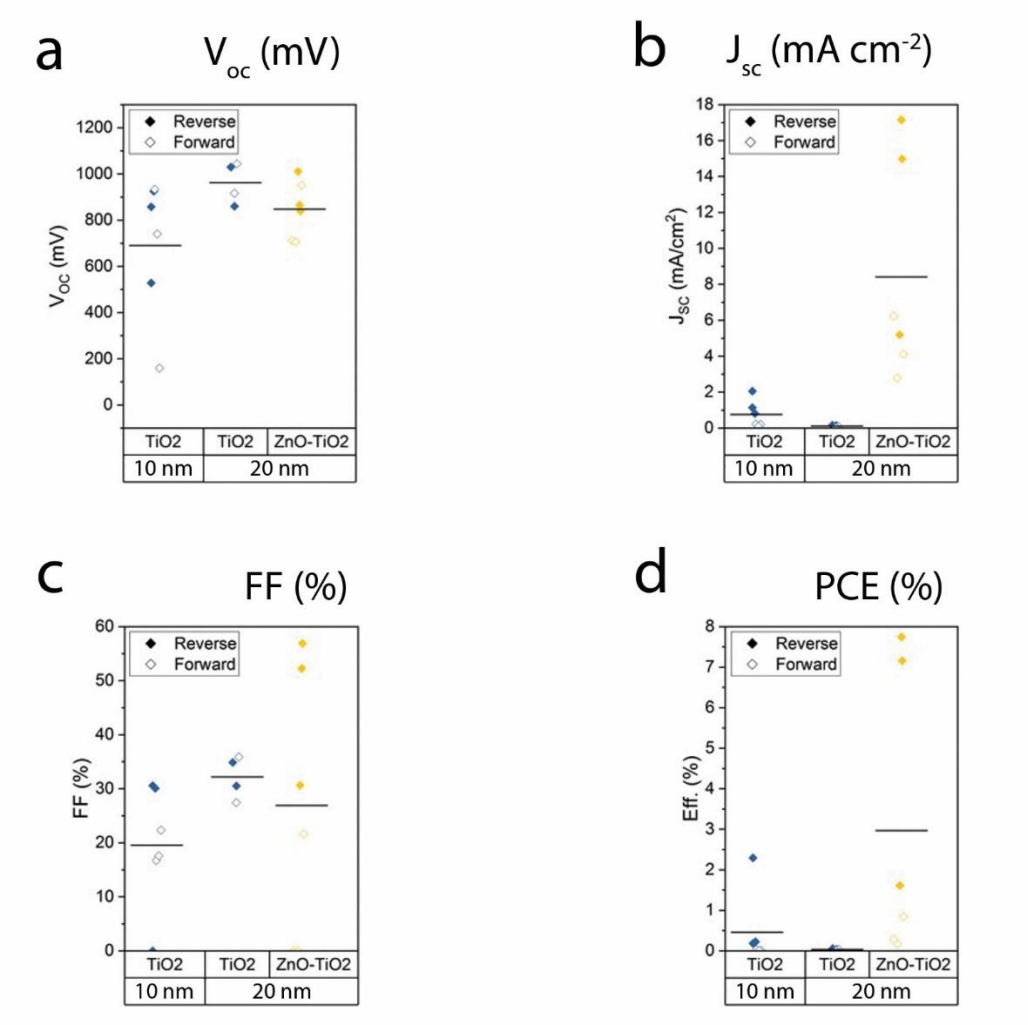

Figure 6. 20: *J–V characteristics of planar perovskite solar cells on ITO coated glass substrates containing ETLs of 10 nm and 20 nm thermal ALD TiO_2 pre-treated with 5 minutes of O_2 plasma, as well as a 20 nm thermal ALD TiO_2 pre-treated with 5 minutes of O_2 plasma passivated with 3 cycles of ZnO on the Cambridge Nanotech reactor*

The ALD layers on ITO coated glass were chosen to be fabricated into planar PSCs by CSEM. These samples were treated to 15 minutes UV-O_3 prior to deposition of the double cation perovskite, $CsFAPb(IBr)_3$, which has a bandgap of ~1.62 eV. The solar cell devices were composed of a conductive ITO coated glass substrate, a compact 20 nm or 10 nm ALD TiO_2 thin film pre-treated with 5 minutes of O_2 plasma or a 20 nm TiO_2 thin film pre and post-treated with 5 minutes of O_2 plasma and passivated with ZnO, a $CsFAPb(IBr)_3$ perovskite layer, a Spiro-OMeTAD hole transport layer and a gold counter electrode. From the J-V characteristics in Figure 6.20 it can be observed that the planar cells incorporating ALD TiO_2 without passivation exhibited extremely low current which indicates poor extraction through the TiO_2 ETL. When ZnO

passivation was employed the planar cells' currents improved. Unfortunately this boost coupled with low FF measurements was not enough to significantly improve PCEs to be comparable to those of planar cells containing sputtered TiO_{2-x} in previous studies.

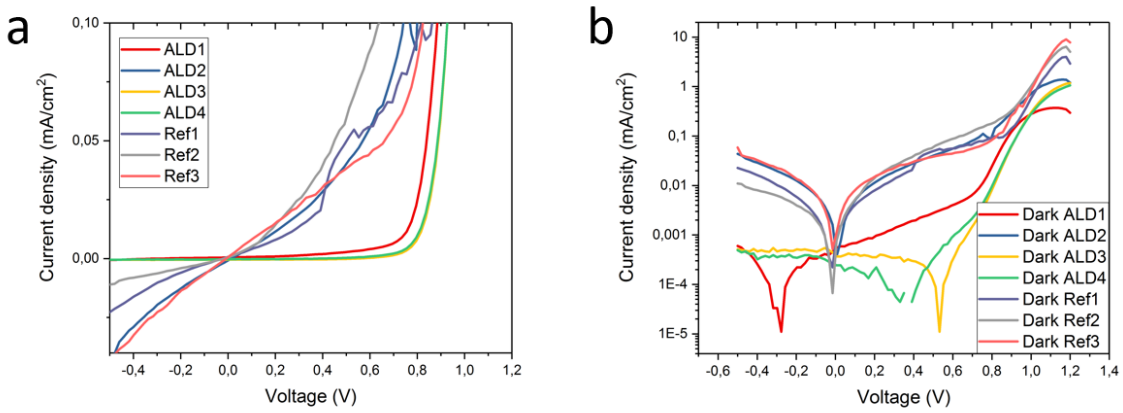

Figure 6.21: *Dark J-V comparing planar cells which incorporate a reference ETL of 20 nm sputtered TiO_{2-x} to planar cells incorporating 20 nm thermal ALD TiO_2 pre-treated with 5 minutes of O_2 plasma as an ETL in (a) the linear and (b) the vertical scale*

Despite the low performance of ALD TiO_2 thin films as ETLs in planar cells, the planar devices containing ALD TiO_2 perform better in the absence of light than the same cells containing reference sputtered TiO_{2-x}. This can be observed in Figure 6.21 where ALD 1, ALD 2, ALD 3, and ALD 4 correspond to four planar PSCs fabricated together using 20 nm ALD TiO_2 pre-treated with a 5 minute O_2 plasma clean as the ETL and $CsFAMAPb(IBr)_3$ as the perovskite material. Ref 1, Ref 2, and Ref 3 are planar devices containing sputtered TiO_{2-x} as the ETL which were made up alongside the PSCs containing ALD TiO_2 and which contain the same perovskite material. The dark current was orders of magnitude lower for cells containing ALD TiO_2 confirming its good hole blocking properties. This suggests that charge extraction is being inhibited by the ALD TiO_2 perovskite interface, and it is this that limits performance and not the bulk properties of the ALD material.

6.3.3.4 Investigation of ALD TiO_2 on $MAPbI_{3-x}Cl_x$ and $MAPbI_3$

The study of how ALD TiO_2 behaves when deposited on a perovskite absorber material was carried out to determine if low temperature ALD could be utilised in the

deposition of ETLs for *p-i-n* architecture devices. Two separate perovskite absorber materials were utilised for this investigation.

The first was $MAPbI_{3-x}Cl_x$ which was synthesised through the crystallisation of CH_3NH_3I using a rotary evaporator. $PbCl_2$ was added in a 3:1 molar ratio of CH_3NH_3I:$PbCl_2$ and dissolved in anhydrous DMF forming the $MAPbI_{3-x}Cl_x$ perovskite solution. Upon spin coating and annealing at 100°C the XRD analysis of the perovskite material matched that of Lee et al.[5] The peaks at 14.1 ° and 28.42 ° correspond to the (110) and (220) tetragonal formation of the perovskite material. Excess PbI_2 or $PbCl_2$ was unreacted and crystallised as can be seen from the peak at 12.7 ° (Figure 6.22).

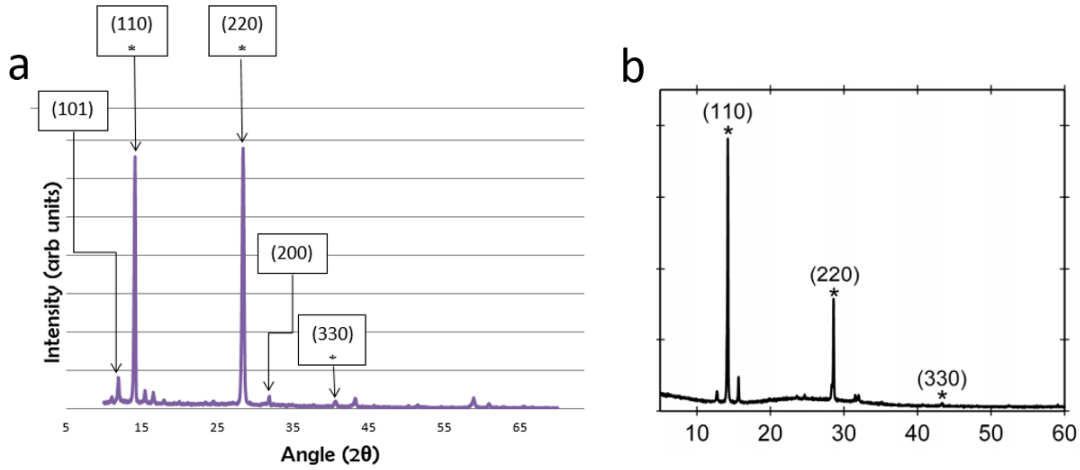

Figure 6.22: *XRD analysis of* ***(a)*** *$MAPbI_{3-x}Cl_x$ thin film on annealing at 100°C and* ***(b)*** *the same film formed by M. Lee as a literature reference*[5]

The second method of perovskite synthesis was that adopted during time spent at CSEM. MAI crystals were purchased directly from Dyesol and combined with PbI_2 in a 9:1 solution of DMF:DMSO to form the $MAPbI_3$ perovskite solution. XRD analysis comparing the two perovskite synthesis methods shows both procedures to exhibit highly crystalline perovskite peaks in Figure 6.23. The precursor materials of PbI_2, $PbCl_2$ which appear at 12.7 °, 38.7 °, and 52.4 °, as well as CH_3NH_3I peaks which can be particularly dominant at 19.7 ° are not observed indicating complete conversion to the perovskite material upon annealing at 100°C. $MAPbI_3$ is observed to have a higher

intensity of crystallinity compared to $MAPbI_{3-x}Cl_x$. This could be due to the higher purity of the MAI crystals purchased compared to those synthesised in the lab.

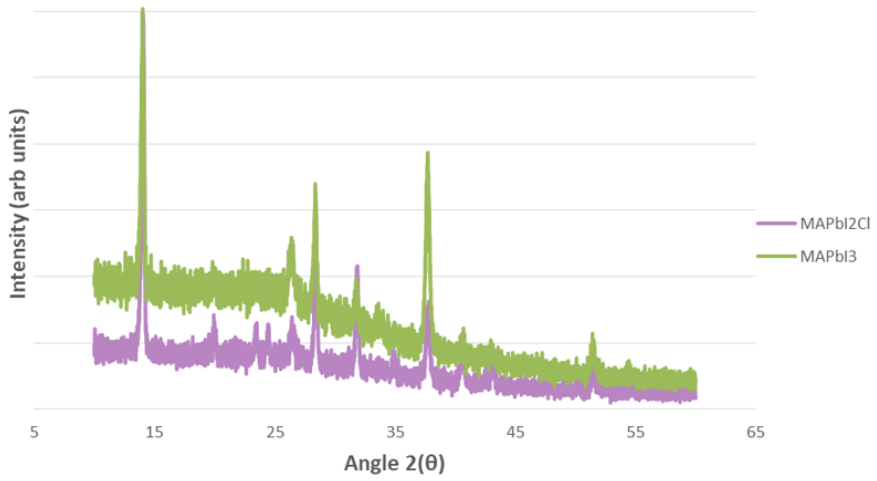

Figure 6.23: *XRD analysis comparing $MAPbI_{3-x}Cl_x$ to $MAPbI_3$*

Visually the $MAPbI_3$ films were much more homogenous on annealing forming a compact black perovskite phase. The $MAPbI_{3-x}Cl_x$ films converted from the yellow precursor solution to a grey film on annealing. This is thought to be due to the impurities remaining in the MAI precursor crystals. The morphologies of the deposited perovskite films on 20 nm TiO_2 pre-treated with 5 minutes of O_2 plasma on FTO coated glass were examined using scanning electron microscopy (SEM, FEI Quanta FEG 650). Plan view SEM images depicted in Figure 6.24 show the morphology of both $MAPbI_{3-x}Cl_x$ and $MAPbI_3$ to be crystalline in nature supporting the results of XRD analysis.

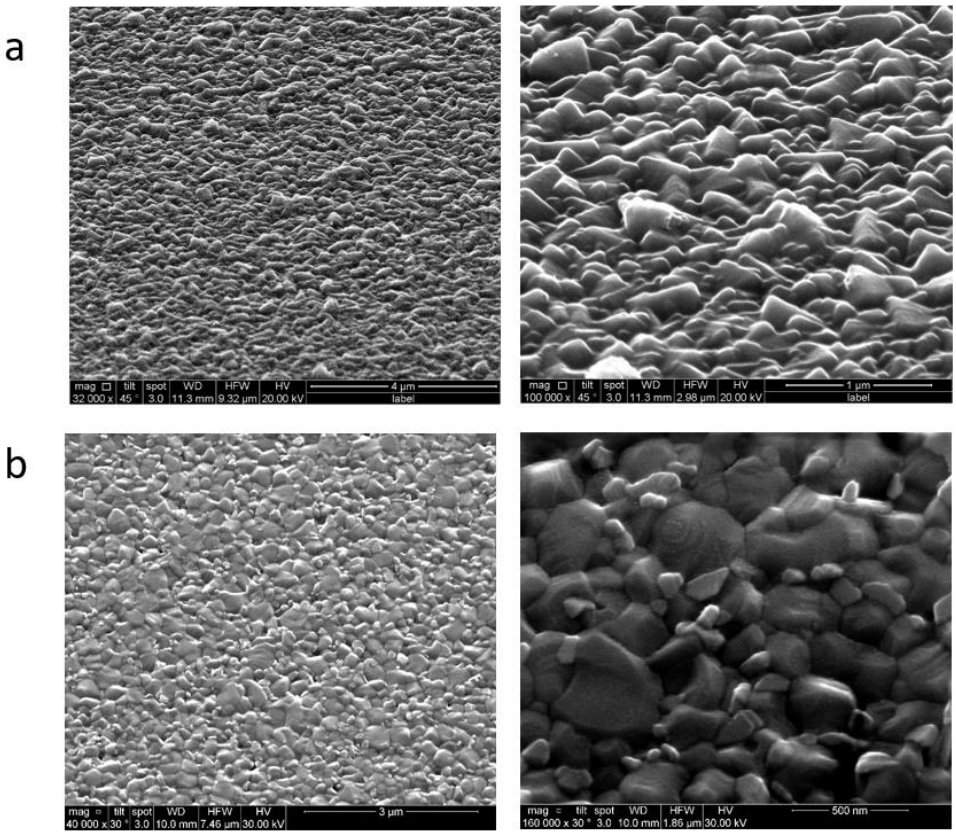

Figure 6.24: *SEM imaging of* ***(a)*** *$MAPbI_{3-x}Cl_x$ deposited on ALD TiO_2/ FTO coated glass, and* ***(b)*** *$MAPbI_3$ deposited on ALD TiO_2/FTO coated glass*

20 nm ALD thermal TiO_2 was deposited on a stack of $MAPbI_3$ or $MAPbI_{3-x}Cl_x$ thin films / ALD TiO_2 / FTO coated glass. While the target application for this study was *p-i-n* perovskite solar cells, ALD TiO_2 was deposited both below and on top of the perovskite material. This was carried out as the fabrication process for *p-i-n* devices was still under development at Tyndall National Institute. The top ALD TiO_2 layer was intentionally deposited at a low temperature of 100°C, as this corresponded to the perovskite annealing temperature. This low deposition temperature is essential to prevent degradation of the thermally sensitive perovskite absorber. Prolonged exposure to this temperature could also induce degradation of the perovskite material. To combat this, a 5 minute stabilisation time was employed in an effort to provide thermal stabilisation before growth, considerably shorter than the 40 minute stabilisation time allowed in previous studies. No O_2 plasma pre-treatment was employed either as it was believed this could affect the underlying perovskite layer. A pulse/purge sequence was adopted with a 1.6 second TDMAT pulse duration which

utilised the boost function and a 0.1 second pulse of H_2O reactant. 20 nm thermal TiO_2 was deposited assuming a growth rate of 0.05 nm per cycle.

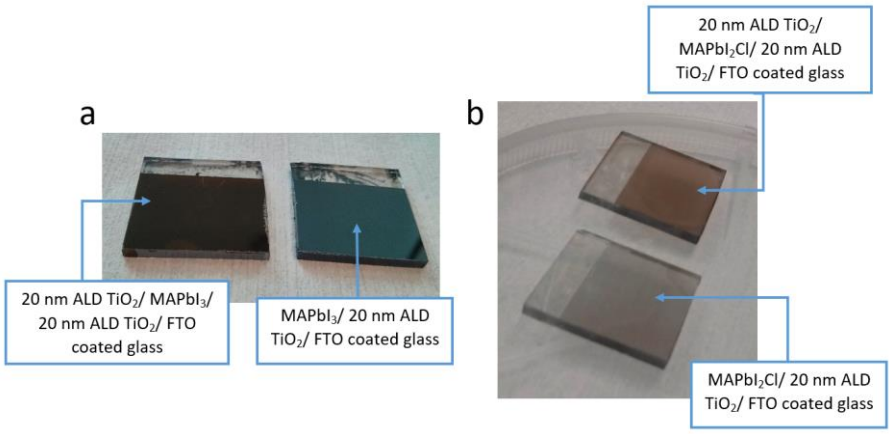

Figure 6.25: *Pictures comparing* ***(a)*** *$MAPbI_3$ films with and without 20 nm ALD TiO_2 deposited on top and* ***(b)*** *$MAPbI_{3-x}Cl_x$ films with and without 20 nm ALD TiO_2 deposited on top*

Following ALD growth, a change in colour was observed for samples adopting a red-orange hue from the growth as observed in Figure 6.25. XRD measurements taken directly after growth showed that the strong perovskite peaks were still present while intensity was slightly diminished mostly likely due to the 20 nm amorphous film deposited on top. No degradation peaks from PbI_2, $PbCl_2$ or MAI were observed suggesting that the perovskite material was not harmed by the subsequent ALD growth (Figure 6.26).

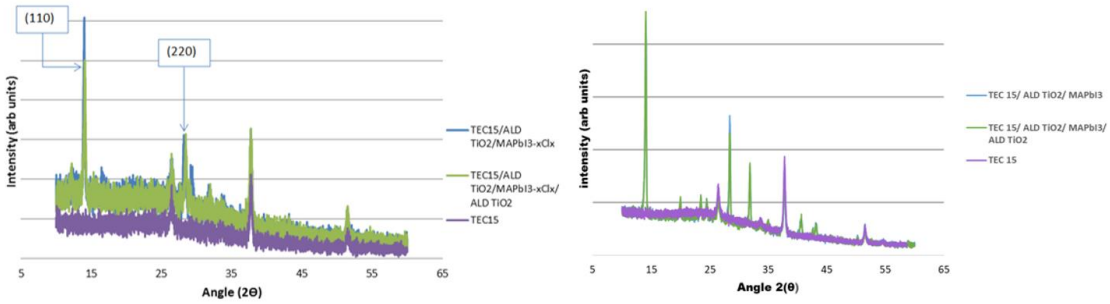

Figure 6. 26: *XRD analysis comparing blank TEC 15 FTO coated glass to $MAPbI_{3-x}Cl_x$ and $MAPbI_3$/20 nm thermal ALD TiO_2 pre-treated with 5 minutes of O_2 plasma/TEC 15 to 20 nm thermal TiO_2/ $MAPbI_{3-x}Cl_x$/20 nm thermal ALD TiO_2 pre-treated with 5 minutes of O_2 plasma/TEC 15*

The morphology of the deposited 20 nm thermal TiO_2/ $MAPbI_3$/ ALD TiO_2 / FTO coated glass was examined using TEM imaging. It was observed that the $MAPbI_3$ perovskite was sensitive to the lamella preparation method. Delamination can be observed in the image as large white voids in Figure 6.27. From the image, a clear layer structure can be observed with the perovskite material sandwiched between two 20 nm ALD TiO_2 thin films. This implies that thermal ALD can indeed be used to deposit ETL or HTL thin films on top of perovskite material provided that the deposition temperature is not high enough to degrade the perovskite material.

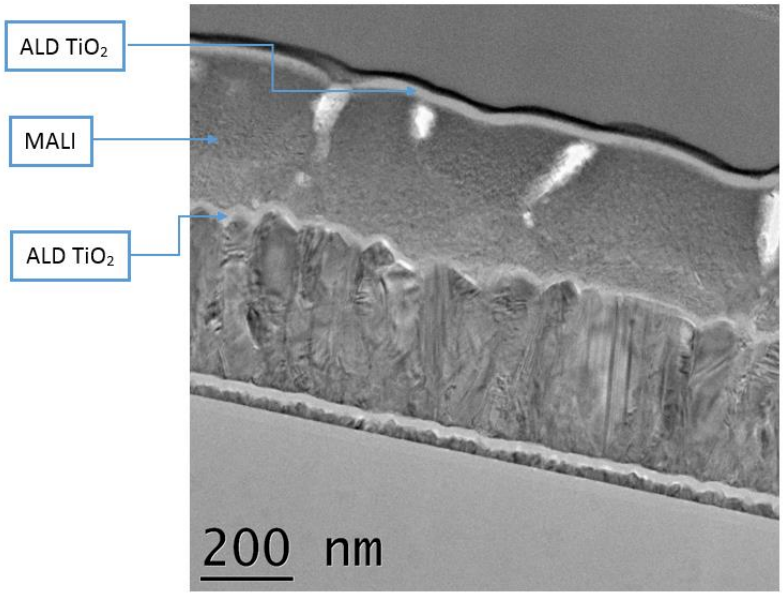

Figure 6. 27: *TEM image showing layered structure of 20 nm ALD TiO_2 deposited at 100°C on a $MaPbI_3$ perovskite on 20 nm ALD TiO_2 deposited at 185°C subjected to a 5 minute O_2 plasma pre-treatment on FTO coated glass*

6.4 Summary

In this chapter nominally undoped ALD TiO_2 was explored in terms of ideal ETL thickness and passivation for use in planar PSCs. Deposition of ALD TiO_2 on top of the perovskite absorber material was also investigated.

Deposition of TiO_2 thin film ETLs was carried out on a Picosun R200 ALD system. All metal oxides for the *n-i-p* architecture were deposited at 185°C to meet the thermal

restrictions of perovskite/silicon heterojunction tandem cells. TDMAT and H_2O were employed as the Ti precursor and co-reactant respectively, while 5 minutes of O_2 plasma was used immediately prior to deposition.

Reference planar PSCs utilising 20 nm RF sputtered TiO_{2-x} as the ETL were found to perform remarkably well reaching a maximum PCE of 16.96 %. The MPP steady state efficiency stabilised at 16.05 % after 800 seconds of tracking. These results had not previously been observed at CSEM using the same architecture on ITO coated glass. All reference cells deposited on FTO coated glass were found to be reproducible with high PCEs. Despite these impressive results hysteresis was observed to remain in the J-V curves due to the planar configuration.

Thin films of ALD thermal TiO_2, in a thickness series of 5 nm, 10 nm, 15 nm, 20 nm, and 25 nm were incorporated as ETLs in planar cells of the same architecture. The final device structure consisted of FTO coated glass/ ALD TiO_2 / $MAPbI_3$/ Spiro-OMeTAD/ Au contact. IV measurements of the ALD thin films on FTO coated glass showed that high temperature annealing to 500°C in mesoporous PSCs increased the resistivity of the underlying ALD TiO_2 films. It was anticipated that removal of the mesoporous layer could therefore contribute to a higher overall PCE in planar PSCs. Elimination of the mesoporous layer would also allow exploration into thinner ALD TiO_2 films which until now had been maintained at 20 nm.

From the J-V characteristics and curves it was observed that the ALD TiO_2 ETLs did not perform as well as expected when fabricated into planar PSCs. The J_{sc} was found to increase with increased ALD ETL thickness from 5 nm to 25 nm. However, current was still significantly lower than that of the reference cells which incorporated RF sputtered TiO_{2-x}. This, combined with a low FF led to a max PCE of 8 % for the planar cells containing 20 nm thermal ALD TiO_2 as an ETL. The poor performance compared with mesoporous PSCs incorporating ALD TiO_2 ETLs was surprising due to the anticipated lower blocking layer series resistance due to the absence of the high temperature anneal. Examination of the XPS of the Ti 2p signatures indicated that the stoichiometry was improved by the anneal as the ratio of Ti^{3+} to Ti^{4+} was reduced from 1:3.9 to 1:4.1. The levels of unreacted precursor ligand fragments was also curtailed by the anneal reducing the concentration of nitrogen and carbon present. It is proposed that the highly defective nature of the as grown material, which could give rise to

significant charge trapping in both the bulk and the interface, is the dominant feature of the material's performance. It should be noted that despite the low performance observed in planar PSCs, the measured dark current was orders of magnitude lower for ALD TiO_2 compared to RF sputtered TiO_{2-x} confirming the good hole blocking properties of the ALD material.

In an attempt to improve the performance of planar cells using ALD TiO_2 as the ETL, RTA of the TiO_2 layer in O_2 and interface passivation, using ALD Al_2O_2 and ZnO, were explored. Although RTA processing (500°C) would be unsuitable for tandem cell fabrication its inclusion in this study was hoped to provide insight into the nature of the ALD TiO_2. For Al_2O_3, an initial 7 cycles was deposited by ALD as a capping layer on top of a 20 nm thermal ALD TiO_2 thin film on FTO coated glass. XPS analysis of the thin films showed an increase in carbon concentration when the TiO_2 layer was capped with 7 cycles Al_2O_3. This rise in carbon concentration suggests that the Al_2O_3 deposition was not sufficiently complete to remove all of the organic ligands, most likely due to temperature constraints. TEM imaging confirmed that the nucleation of Al_2O_3 on TiO_2 was not inhibited and the growth rate was within expected limits.

Both the RTA approach and that of 7 cycles of Al_2O_3 on the TiO_2 ALD ETL were prepared into planar PSCs with a 1.04 cm^2 active area and compared with sputtered equivalents. The final cell architecture comprised of FTO coated glass/ ALD TiO_2 or RF sputtered TiO_2/ $CsFAMAPb(BrI)_3$ perovskite/ Spiro-OMeTAD HTL/ Au contact. From the J-V characteristics it was noted that current was strongly suppressed in the planar cells containing ALD ETLs, both those that had undergone RTA in O_2 and Al_2O_3 capping. Final PCEs were not improved by either of these techniques. From the J-V curves, a disappearance in the s-shape was observed for the ALD TiO_2 sample which had undergone RTA to 500°C in O_2. This s-shape had been present for all standard ALD J-V curves obtained previously. Despite this, the current was strongly reduced by the RTA process. The J-V curve of 20 nm thermal ALD TiO_2 capped with 7 cycles of Al_2O_3 suggests that the thin Al_2O_3 film completely blocks the extraction of charges. As a consequence, the use of a single ALD cycle of Al_2O_3 as a capping layer on ALD TiO_2 was examined. For this experiment an additional plasma clean and extended precursor pulses were utilised to aid nucleation and improve the interface. These samples were fabricated into planar PSCs using the conventional $MAPbI_3$

precursor absorber. Using the same architecture a 20 nm RF sputtered TiO_{2-x} ETL reference cell was used in the study. From the J-V characteristics an issue was noted with the perovskite absorber material or the Spiro-OMeTAD HTL causing all cells to perform less efficiently than expected. Nonetheless, it was apparent that even the 1 cycle of Al_2O_3 deposition to passivate the TiO_2 perovskite interface inhibited electron extraction in the cell. It is possible that Al_2O_3 could improve the interface, if higher temperatures or different chemistries were employed, however the combination of the insulating nature of the Al_2O_3 and the non-ideal nature of TiO_2 make it an unlikely combination.

For this reason the use of ALD ZnO as a passivation layer was explored. Three cycles of DEZ and H_2O as the metal precursor and reactant respectively at 130°C were employed. The zinc precursor contains Ethyl ligands which were thought to be able to aid in cleaning the ALD TiO_2 surface. Ellipsometry measurements of the ZnO capping film on ALD TiO_2 demonstrated that no nucleation delay was observed, this is likely due to the addition of a plasma treatment prior to ZnO deposition providing more nucleation sites and possibly removing residual TDMAT ligands. These samples were then fabricated into planar PSCs using a $CsFAPb(IBr)_3$ perovskite absorber. An increase in current could be observed for cells incorporating ZnO passivation, but this boost was not enough to significantly improve PCE but it does highlight possibilities for future study.

Finally, in this chapter the concept of *p-i-n* architecture perovskite devices was introduced where ALD must be performed directly on to the sensitive perovskite absorber. Low temperature deposition of 100°C was successfully achieved on both $MAPbI_3$ and $MAPbI_{3-x}Cl_x$ absorbers. A low temperature plasma free growth process was chosen to prevent damage to the perovskite film enabling films of 20 nm thickness to be grown. XRD analysis along with TEM imaging after ALD growth indicate that the perovskite material was not noticeably degraded or modified. This is a promising outcome which implies that low temperature ALD can be used to successfully deposit ETL or HTL thin films on top of the perovskite material.

6.5 Bibliography

[1] Q. Wali, N. K. Elumalai, Y. Iqbal, A. Uddin, R. Jose, Tandem perovskite solar cells, Renewable and Sustainable Energy Reviews, Volume 84, Pages 89-110, ISSN 1364-0321 (2018)

[2] T. Leijtens, K. A. Bush, R. Prasanna, M. D. McGehee, Opportunities and challenges for tandem solar cells using metal halide perovskite semiconductors, *Nature* Energyvolume 3, pages828–838 (2018)

[3] L. K. Ono, N-G. Park, K. Zhu, W. Huang, Y. Qi, Perovskite Solar Cells - Towards Commercialization, ACS Energy Letters 2 (8), 1749-1751 (2017)

[4] L. Qiu, L. K. Ono, Y. Qi, Advances and challenges to the commercialization of organic–inorganic halide perovskite solar cell technology, Materials Today Energy, 7 169-89 (2017)

[5] M. M. Lee, J. Teuscher, T. Miyasaka, T. N. Murakami, H. J. Snaith, Efficient Hybrid Solar Cells Based on Meso-Superstructured Organometal Halide Perovskites, Science, 338, 6107, pp. 643-647 (2012)

[6] J. Pascual, J. Camassel, H. Mathieu, Fine structure in the intrinsic absorption edge of TiO_2, Phys. Rev. B 18, 5606 (1978)

[7] A. Amtout, R. Leonelli, Optical properties of rutile near its fundamental band gap, Phys. Rev. B 51, 6842 (1995)

[8] H. Tang, F. Lévy, H. Berger, P. E. Schmid, Urbach tail of anatase TiO_2, Phys. Rev. B 52, 7771 (1995)

[9] A. Mattsson, L. Österlund, Adsorption and Photoinduced Decomposition of Acetone and Acetic Acid on Anatase, Brookite, and Rutile TiO_2 Nanoparticles, The Journal of Physical Chemistry C, 114, 33, 14121-14132 (2010)

[10] A. Welte, C. Waldauf, C. Brabec, P. Wellmann, Application of optical for the investigation of electronic and structural properties of sol-gel processed TiO2 films, Thin Solid Films, 516, 7256- 9 (2008)

[11] S. Valencia, J. M. Marín, G, Restrepo, Study of the Bandgap of Synthesized Titanium Dioxide Nanoparticules Using the Sol-Gel Method and a Hydrothermal Treatment, The Open Materials Science Journal, 4, 9-14 (2010)

[12] K. Iino, M. Kitano, M. Takeuchi, M. Matsuoka, M. Anpo, Design and development of second-generation titanium oxide photocatalyst materials operating under visible light irradiation by applying advanced ion-engineering techniques, Current Applied Physics, 6, 982–986, 2006

[13] M. S. Wong, H. P. Chou, T. S. Yang, Reactively sputtered N-doped titanium oxide films as visible-light photocatalyst, Thin Solid Films, 494, 244-249, 2006

[14] F. Dong, S. Guo, H. Li, X. Wang, Z. Wu, Enhancement of the visible light photocatalytic activity of C-doped TiO_2 nanomaterials prepared by a green synthetic approach, J. Phys. Chem. C, 115, 13285-13292, 2011

[15] R. G. Chaudhuri, S. Paria, Visible light induced photocatalytic activity of sulfur doped hollow TiO_2 nanoparticles, synthesized via a novel route, Dalton T., 43, 5526-5534, 2014

[16] K. Henkel, C. Das, M. Kot, D. Schmeißer, In-gap states in titanium dioxide and oxynitride atomic layer deposited films, J. Vac. Sci. Technol. A, 35, 01B135, 2017

[17] A. Walter, S.-J. Moon, B. A. Kamino, L. Lofgren, D. Sacchetto, F. Matteocci, B. Taheri, J. Bailat, A. Di Carlo, C. Ballif, S. Nicolay, Closing the Cell-to-Module Efficiency Gap: A Fully Laser Scribed Perovskite Minimodule With 16% Steady-State Aperture Area Efficiency, IEEE J. Photovoltaics, 8, 1, 2018

[18] A. Richter, J. Benick, M. Hermle, S. W. Glunz, Excellent silicon surface passivation with 5 Å thin ALD Al_2O_3 layers: Influence of different thermal post-deposition treatments, Rapid Research Letters, vol. 5, 5-6, 202-20, 2011

[19] D. Liu and T. L. Kelly, Perovskite solar cells with a planar heterojunction structure prepared using room-temperature solution processing techniques, Nat. Photonics, 8, 133-138 (2014)

[20] Y. Cheng, Q-D. Yang, J. Xiao, Q. Xue, H-W. Li, Z. Guan, H-L. Yip, S-W. Tsang, Decomposition of Organometal Halide Perovskite Films on Zinc Oxide Nanoparticles, ACS Appl. Mater. Interfaces, 7, 36, 19986-19993 (2015)

[21] A. Bahtiar, E. S. Nurazizah, E. Latiffah, Risdiana, Y. Furukawa, Structural Properties of Perovskite Films on Zinc Oxide Nanoparticles-Reduced Graphene Oxide (ZnO-NPs/rGO) Prepared by Electrophoretic Deposition Technique, AIP Conference Proceedings, 1927, 030005 (2018)

[22] T. G. Smijs, S, Pavel, Titanium dioxide and zinc oxide nanoparticles in sunscreens: focus on their safety and effectiveness, Nanotechnol Sci Appl. 4, 95–112 (2011)

[23] M. Kobayashi, W. Kalriess, Photocatalytic Activity of Titanium Dioxide and Zinc Oxide, Cosmetics Toiletries, 112, 83–86 (1997)

[24] V. Houšková, V. Štengl, S. Bakardjieva, N. Murafa, Photoactive materials prepared by homogeneous hydrolysis with thioacetamide: Part 2—TiO_2/ZnO nanocomposites, Journal of Physics and Chemistry of Solids, 69, 7, 1623-1631 (2008)

[25] J. Lim, C. Lee, Effects of substrate temperature on the microstructure and photoluminescence properties of ZnO thin films prepared by atomic layer deposition, Thin Solid Films, 515, 3335–3338, 2007

[26] D. Kim, H. Kang, J.-M. Kim, H. Kim, The properties of plasma-enhanced atomic layer deposition (ALD) ZnO thin films and comparison with thermal ALD, Applied Surface Science, 257, 3776–3779, 2011

CHAPTER 7:

Investigation into ALD SnO_2 for use in planar PSCs

7.1 Introduction

As observed in the previous chapter, ALD TiO_2 does not behave well when incorporated into planar perovskite solar devices. Rapid thermal annealing of ALD TiO_2 to 500°C in a highly oxidising environment of O_2 was employed to aid in the removal of oxygen vacancy related defects. Despite this current was supressed when the thin film was fabricated into a planar device. Likewise, interface passivation of ALD TiO_2 using ALD metal oxides was not found to substantially boost the PCE of devices. Despite TiO_2 being the most commonly used ETL in perovskite devices to date, it does come with some substantial disadvantages. Planar PSCs which employ TiO_2 are restricted due to a conduction band misalignment with the perovskite layer. These types of solar cells exhibit unstable PCEs as electron injection is energetically hindered by the mismatched bands. As a result, accumulation of photogenerated charges can occur which can hamper the performance of the device. TiO_2 also provides poor charge extraction which causes pronounced hysteresis observed in current-voltage curves.[1-4]

One alternative option to TiO_2 for planar PSCs is SnO_2. Its deep conduction band enables a barrier-free band alignment between the perovskite light harvester and the ETL.[4] SnO_2 has also previously been seen to exhibit improved optical and electrical properties[5,6] and stability[7,8] compared to the TiO_2 traditionally used, making it a promising candidate for use in high efficiency PSCs. SnO_2 possesses a conduction band of approximately 4.5 eV which is lower than the conduction band for all other perovskite absorber materials, which lie between 3.4 eV – 4.0 eV. As illustrated in Figure 7.1, this favourable conduction band and deep valance band can allow efficient electron transfer from the perovskite layer to the SnO_2 compact layer. Simultaneously,

the low conduction band of SnO_2 may decrease the obtained voltage in PSCs due to a reduced Schottky barrier built-in potential between the perovskite layer and the ETL. Surface modification of the SnO_2 is a viable method to counteract this.[8]

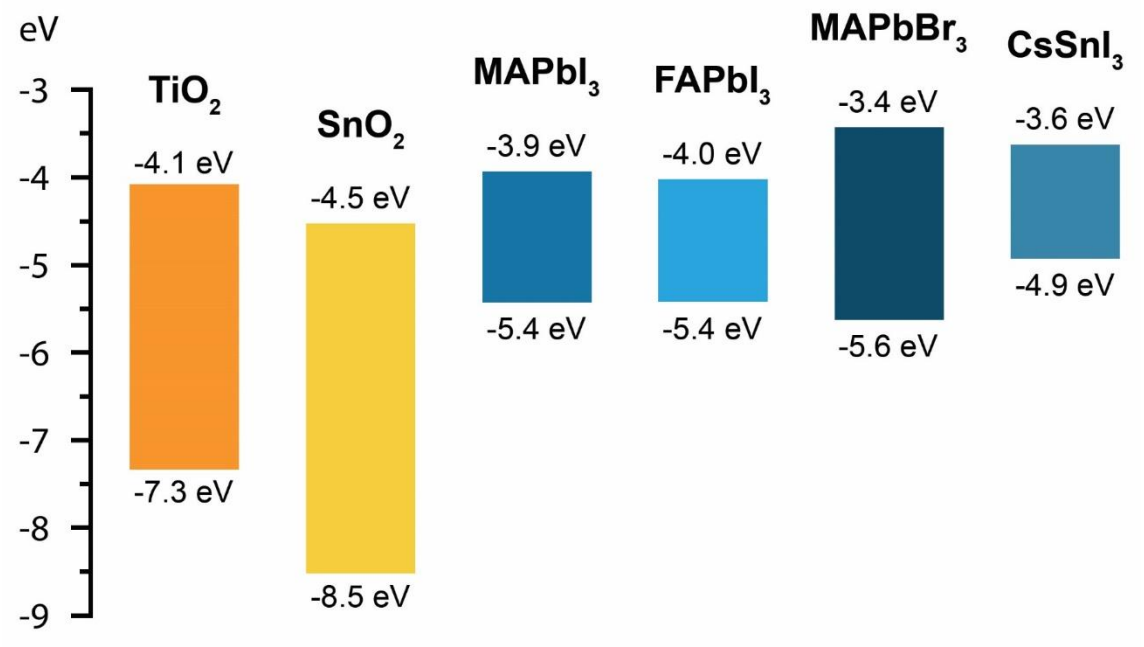

Figure 7. 1: *Diagram of heterojunction TiO_2 and SnO_2/perovskite energy levels*

In this chapter low temperature amorphous ALD SnO_2 is applied as the ETL for both *n-i-p* and *p-i-n* planar architectures. Surface modification and passivation methods are explored by means of spin-coating, evaporation and chemical bath deposition (CBD) in an effort to improve the performance of the PSCs.

7.2 Experimental

7.2.1 Substrate Cleaning and preparation

All perovskite cells were prepared on high temperature resistant alumino-boroscilicate glass coated with fluorine-doped tin oxide (FTO) which served as a transparent electrode (TEC-7, 7 Ω cm-1 from Solaronix and TEC-7, 7 Ω cm-1 from Hartford glass).

At Tyndall National Institute and CSEM, the TEC-7 FTO coated glass (Solaronix) was cleaned, P1 scribed and diced into 25 mm^2 substrates as described earlier in Chapter 5. At the University of Oxford, FTO coated glass was etched using zinc and HCl rather than laser scribed to form electrode patterns. 112 mm^2 TEC-7 FTO coated glass sheets (Hartford glass) were carefully patterned using 19 mm scotch tape, while avoiding the formation of air bubbles, as illustrated in Figure 7.2. Under the fume hood, zinc powder and 2 M HCl were used to etch the FTO areas not protected with tape. Deionised water was then used to clean the substrate sheets and remove zinc residue before the scotch tape was carefully removed to reveal the required electrode pattern. The FTO coated glass sheets were diced into 28 mm^2 substrates before being cleaned by successive ultra-sonication in Hellmanex (2% in deionised water), acetone and IPA for 15 min each. A compressed air gun was used to thoroughly dry samples between each step.

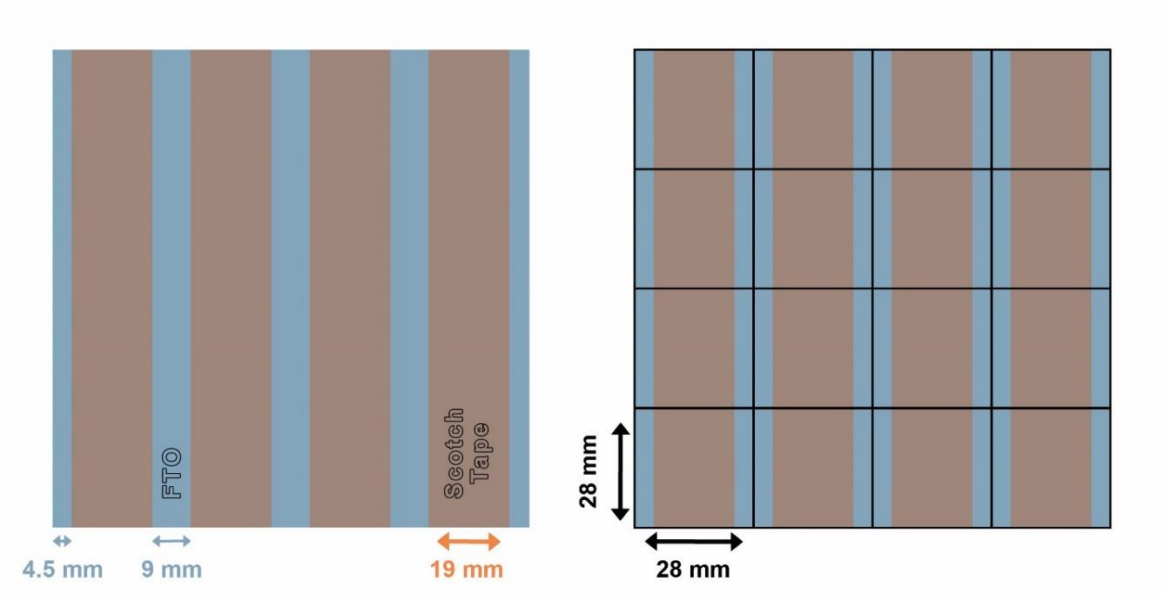

Figure 7. 2: *Schematic of FTO coated glass patterned using scotch tape for zinc etching to form electrode pattern*

7.2.2 Deposition of ALD SnO_2 for *n-i-p* PSCs

Nominally undoped SnO_2 thin films of a range of thicknesses (2 nm, 5 nm, 10 nm, 15 nm, 20 nm, 25 nm, 30 nm) were deposited on glass, quartz, n-Si(100) wafers, and FTO

coated glass by ALD. To avoid run-by-run variation in growth experiments all substrate types were loaded together for each SnO_2 variation. Films were deposited at 185°C in a Picosun R200 system using a thermal or plasma enhanced reaction. The tin precursor and reactant used for the depositions were TDMASn and either an O_2 plasma at 2.95 kW or H_2O. The precursor vessel for the TDMASn was maintained at 65°C, while the vessel neck was held at 80°C. The H_2O reactant was maintained at a room temperature of approximately 27°C where an adequate vapour pressure was achieved. The nominal growth rate per cycle at 185°C for TDMASn was 0.6 Å using the Picosun R200 system. All growth rates were in agreement with literature values.[9]

Similar to the ALD TiO_2 conditions discussed previously, samples were provided with a 40 minute stabilisation time within the reaction chamber prior to processing. The Picosun boost function was utilised for the solid precursor TDMASn, allowing better transportation of the precursor chemical to the reactor. The carrier gas maintained a constant pressure for each pulse allowing pulses of the same size to be dosed consistently. All samples also received a 5 minute O_2 plasma clean in situ in the ALD chamber prior to deposition.

Table VII. I: *Experimental parameters for deposition of thermal SnO_2 subjected to a 5 minute O_2 plasma treatment prior to deposition using TDMAT on Picosun R200*

Precursor	*Pulse*	*Purge*	*Repeat*
O_2 plasma	152 s		2
Purge		8 s	
TDMASn	1.6 s		336
Purge		8s	
H_2O	0.1 s		
Purge		8s	

Table VII. I outlines the recipe used for the growth of thermal SnO_2 at 185°C. Substrates were subjected to a 5 minute O_2 plasma treatment directly prior to ALD deposition as described in Chapter 5 section 5.2.2.2 (i). Following the plasma clean, an 8 second purge time was allowed before the first precursor, TDMASn, was introduced for 1.6 seconds using the boost function. After an 8 second purge a 0.1 second pulse of H_2O was introduced with another 8 second purge directly after to complete the cycle. The cycle of TDMASn and H_2O was repeated for a total of 336 cycles. The nominal thickness of the thin film grown was 20 nm assuming a growth rate of 0.06 nm per cycle.

In addition, nominally undoped SnO_2 and TiO_2 thin films were grown by ALD at an elevated temperature of 300°C to determine if a higher deposition temperature would increase stoichiometry and hence performance when incorporated into planar PSCs. The recipe for these growths remained the same, employing TDMASn or TDMAT as the metal precursor, H_2O as the reactant and the same plasma substrate clean to allow direct comparison between low temperature (185°C) and high temperature (300°C) depositions. The growth rate per cycle differed at the elevated temperature with SnO_2 requiring 1500 cycles to obtain a 20 nm thick film, equating to a growth rate of 0.013 nm per cycle. This deposition temperature is outside the ALD window of 100°C to 200°C for SnO_2 using TDMASn and H_2O. This resulted in a poorly controlled growth due to thermal decomposition of the precursor causing non-ALD type deposition.[10] The TiO_2 thin film had a growth rate of 0.04 nm per cycle at the elevated temperature, requiring 500 cycles to obtain 20 nm. TDMAT and H_2O have been reported to deposit ALD films with a decrease in growth rate with increased temperature.[11,12] A growth rate of 0.05 nm per cycle at 300°C was reported by M. Reiners et al, while at higher temperatures of 320°C CVD-like reactions were observed.[13]

Similarly, nominally undoped SnO_2 thin films were deposited using PEALD at 185°C. Here, the H_2O was replaced with O_2 plasma. A 5 minute O_2 plasma substrate treatment prior to ALD growth was again employed. The plasma reactant was utilised to allow for faster chemical reactions to take place at lower deposition temperatures.

7.2.3 Deposition of ALD SnO_2 for *p-i-n* PSCs

Nominally undoped SnO_2 thin films were deposited by the Picosun R200 system on the perovskite/ HTL/ FTO coated glass stack. As with section 7.2.2, the tin precursor and reactant used for deposition were TDMASn and H_2O, respectively. The stack was provided with a short 5 minute thermal stabilisation time within the reaction chamber prior to growth in an attempt to provide thermal stabilisation without causing degradation to the sensitive perovskite absorber layer. The chamber was purposely set to low deposition temperatures ranging from 100°C to 150°C to maintain a balance between the stoichiometric growth of SnO_2 and the preservation of the perovskite underlayer.

After the stabilisation period, a pulse/purge sequence was adopted. O_2 plasma was not utilised as a reactant or to clean the stack prior to ALD growth as it was thought likely

to negatively impact the perovskite absorber layer underneath. 10 nm and 20 nm depositions were grown on n-Si(100) wafers, and ellipsometry was employed to estimate thickness, recognising that nucleation may be significantly different.

Table VII. II: *Experimental parameters for deposition of thermal SnO_2 on top of perovskite material using a Picosun R200*

Precursor	*Pulse*	*Purge*	*Repeat*
TDMASn	1.6 s		x cycles
Purge		6s	
H_2O	0.1 s		
Purge		6s	

Table VII. II summarises the recipe used for the growth of thermal SnO_2 directly on top of a perovskite absorber. The tin precursor, TDMASn, was introduced for 1.6 seconds using a boost function. After a 6 second purge a 0.1 second pulse of H_2O was introduced, followed by another 6 second purge to complete the cycle. This process was repeated for a certain number of cycles depending on the desired thickness and deposition temperature. The shorter purge time of 6 seconds was applied to minimise the thermal exposure of the sensitive perovskite absorber material whilst maintaining ALD behaviour. Later a longer purge time was utilised to provide a limited and uniform growth as described in section 7.3.5.5. At low deposition temperatures of between 100°C and 150°C the growth rate of SnO_2 increased, varying from 0.088 nm per cycle to 0.132 nm per cycle depending on temperature used and purge length. This is described in more detail later in section 7.3.5.5.

7.2.4 Fabrication of *n-i-p* PSCs employing $CsFAMAPbI_3$ or $CsFAPb(IBr)_3$

Substrates containing ALD ETLs deposited on top of FTO and ITO coated glass were processed at CSEM where they were fabricated into PSCs. These substrates were subjected to a 15 minute UV O_3 treatment and blown with a N_2 gun to remove environmental contaminants. The samples were then placed in a Lesker mini-spectros system inside the glove box and a wait period of 45 minutes was applied for the sources to heat and stabilise. The sample holder was set at 30°C with the Lesker evaporator operating at a base pressure of 1.5×10^{-6} Torr. The perovskite absorber was realised through a two-step process by first co-evaporating PbI_2 and CsI. The CsI

source was heated to 400°C and evaporated at a rate of 0.15 Å per second until a thickness of 30 nm was achieved. This was followed by the evaporation of PbI_2 whose source was heated to 180°C and deposited at a rate of 1 Å per second until a thickness of 180 nm was obtained. An organohalide solution containing either MAI and FAI in EtOH or FAI and FABr in EtOH was spin coated onto the PbI_2:CsI precursor layer at 3,000 rpm for 33 seconds inside the glove box. This was followed by thermal annealing outside the glove box at 150°C for 30 minutes to promote interdiffusion and to obtain the final perovskite material.

The HTL, Spiro-OMeTAD, and evaporated contact, Au, were then added by the method described in Chapter 6, section 6.2.3

7.2.5 Fabrication of *n-i-p* PSCs through ACN/MA deposition route

Following ALD deposition of 2 nm, 5 nm and 10 nm SnO_2 thin films at Tyndall National Institute, samples were sent to the University of Oxford where they were fabricated into planar perovskite devices. A buffer layer of C_{60} (10 mg/ml in 1,2-dichlorobenzene) was deposited on the ALD SnO_2 thin films via spin coating at 3,500 rpm for 30 seconds. Following this, the substrates were dried at 80°C for 2 mins.

An acetonitrile/methylamine (ACN/MA) solvent mixture was prepared by placing a 33 % wt solution of MA in EtOH in an aerator which was placed in an ice bath. The MA solution was degassed by bubbling a carrier gas, N_2, into the solution. The MA vapour created then passed through a drying tube supplied with desiccant prior to bubbling into a solution of ACN containing 0.5 M of the perovskite precursors. These perovskite precursors consisted of 1:1.06 MAI:PbI_2. The gas was then bubbled into the black dispersion until the perovskite particles were entirely dissolved forming a yellow solution (Figure 7.3).[14]

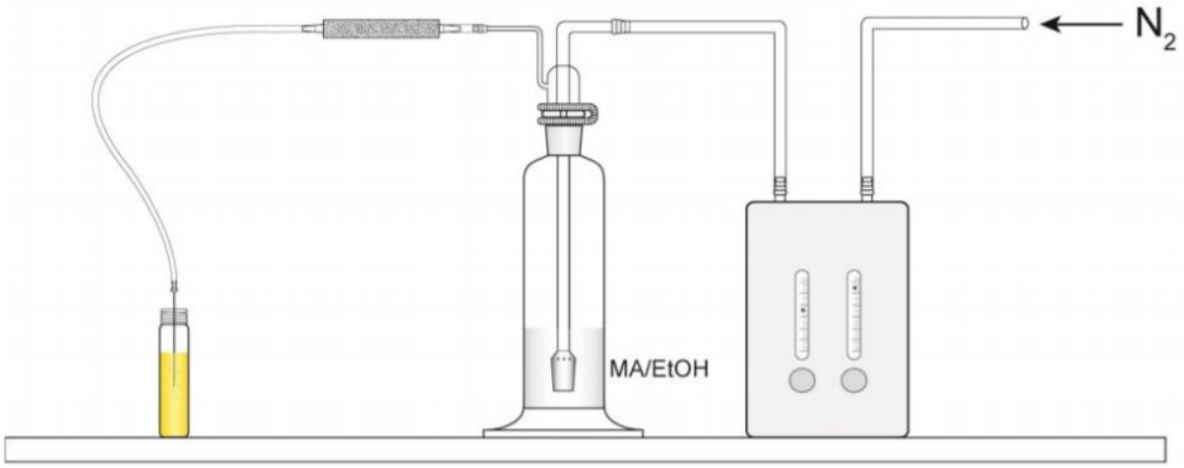

Figure 7. 3: *Schematic of the apparatus used in the University of Oxford for $MAPbI_3$ perovskite prepared by ACN/MA.*[14]

Once the C_{60}/ALD SnO_2/ FTO coated glass substrates had cooled from 80°C, the $MAPbI_3$ perovskite solution formed via ACN/MA was spin-coated in dry air at 2000 rpm for 45 seconds. 100 µl of 5 mg/ml MAI (Alfa Aesar) in IPA was spin coated on top as a post treatment before annealing at 100°C for 1 hour.

Upon cooling, the HTL was prepared by dissolving 85.0 mg spiro-OMeTAD (Merck) in 1 ml chlorobenzene (Sigma Aldrich) with additives of 23 µl tBP and 20 µl LiTFSI before it was spin coated at 2,500 rpm for 40 seconds. The devices were completed with the evaporation of a 110 nm silver electrode using a Kurt J. Lesker Nano-36 thermal evaporator with a base pressure of approximately 10^{-6} Torr.

7.2.6 Fabrication of *n-i-p* PSCs through surface modification and a $FACsPb(IBr)_3$ perovskite

Surface modification of the ALD SnO_2 thin film was explored through deposition of spin coated PCBM and CBD SnO_2 by the author. Passivation of ETLs such as SnO_2 can significantly enhance the performance of PSCs in many ways by altering the band energy to allow electron injection and prevent the admission of holes at the interface, whilst it may also be used to passivate the surface states for suppression of recombination.

In this study, the author fabricated devices while at the University of Oxford. Cells containing ALD SnO_2 were made up alongside ETLs comprised of spin coated SnO_2/CBD SnO_2 and spin coated SnO_2/PCBM to avoid any variations in the remaining layers, allowing ETLs to be directly compared. Spin coated SnO_2 which is followed by a CBD of SnO_2 is a commonly used low-temperature all-solution ETL process in the PV field which has obtained impressive PCEs. This method has previously been reported to outperform ALD SnO_2 in planar perovskite devices due to an increase in FF.[15] The method used here has been well established and optimised by those at the University of Oxford.

The perovskite solution was prepared in the glove box. 207.0 mg of FAI (Dyesol) and 64.0 mg CsI (Alfa Aesar) were added to 538.2 mg PbI_2 (TCI) and 103.8 mg $PbBr_2$ in a 4 ml vial. A magnetic stirrer was added to the vial, followed by 1,000 µl of a 1:4 volume ratio of DMSO:DMF (Sigma Aldrich). This perovskite solution was allowed to stir overnight in the glove box.

7.2.6.1 Spin coated SnO_2

17.5 mg $SnCl_4.5H_2O$ (Sigma Aldrich) was dissolved in 1ml 0.05M IPA. The solution was made fresh for each device batch and allowed to stir for 30 minutes before use. Clean, patterned FTO coated glass substrates were subjected to 10 min O_2 plasma immediately prior to spin coating 200 µl $SnCl_4.5H_2O$ in IPA solution at 3,000 rpm for 30 seconds producing 15-20 nm thick films. The samples were dried for 10 min at 100°C before annealing at 180°C for 1 hour and then allowed to cool.

7.2.6.2 SnO_2 Chemical Bath Deposition

2.5 g urea (98 %, Sigma Aldrich) was added to 200 ml deionised water in a large bottle containing a magnetic stir bar in the fume hood. 50 µl 3-mercaptopropionic acid (Sigma Aldrich) was then added, followed by 2.5 ml HCl (37 %, Alfa Aesar), and finally 540 g 0.012 M $SnCl_2.2H_2O$ (Sigma Aldrich). The bath solution was allowed to stir for 2 min.

The cooled c-SnO_2 (ALD or spin coated)/ FTO coated glass samples were placed face up in a clean shallow glass container. The contents of the large bottle were gently

poured into the glass container covering the samples. For ALD SnO_2, an O_2 plasma treatment was employed before the chemical bath solution was poured on due to the observed hydrophobicity of the as grown ALD film compared to spin coated SnO_2. The container was covered with aluminium foil and placed in an oven at 70°C. After 3 hours the glass container was removed from the oven and the solution was carefully poured out. A copious amount of deionised water was poured onto the samples before each sample was cleaned for 2 min via ultra-sonication in deionised water. The samples were then dried using a condensed air gun and annealed at 180°C for 1 hour. The recipe used to produce spin coated SnO_2 followed by CBD SnO_2 has been reported in the literature to be no thicker than 40 nm.[15]

7.2.6.3 PCBM Deposition

7.5 mg /ml of phenyl-C_{61}-butyric acid methyl ester (PCBM, 98%, nano-c) in chlorobenzene was made up and allowed to stir overnight. The solution was then filtered into a clean vial using a 0.45 µm PTFE filter before spin coating 40 µl on c-SnO_2 (ALD or spin coated)/ FTO coated glass samples at 2,000 rpm for 30 seconds. The samples were then dried on a hot plate at 70°C for 10 min producing 5-10 nm thick films.

7.2.6.4 Remaining stack layers

Directly prior to deposition of the perovskite absorber layer (and spin coating of the PCBM passivation layer), all ETL/FTO coated glass substrates were subjected to a 15 minute UV O_3 treatment and blown with a N_2 gun to remove any contaminants.

After stirring overnight, the perovskite solution was removed from the glovebox and heated to 70°C for 10 min before spin coating. Samples were transferred to a controlled atmosphere box at 23 % humidity where 40 µl $FACsPb(IBr)_3$ solution was micropipetted onto and carefully spread across the substrates before they were spun at 1,000 rpm for 10 seconds, followed by 6,000 rpm for 35 seconds. 100 µl of anisole (Sigma Aldrich) was carefully used as an anti-solvent treatment 10 seconds before the end of the spin coating process. Samples were then annealed for 25 minutes at 100°C.

The HTL was prepared by dissolving 85.0 mg Spiro-OMeTAD (Merck) in 1 ml chlorobenzene (Sigma Aldrich) with additives of 23 µl tBP and 20 µl LiTFSI before 40 µl of this HTL solution was spin coated on the substrates at 2,500 rpm for 40 seconds. The devices were completed with the evaporation of a 100 nm gold electrode using a Kurt J. Lesker Nano-36 thermal evaporator with a base pressure of approximately 10^{-6} Torr. Figure 7.4 below illustrates the entire stack for these perovskite devices using PCBM and CBD passivation methods.

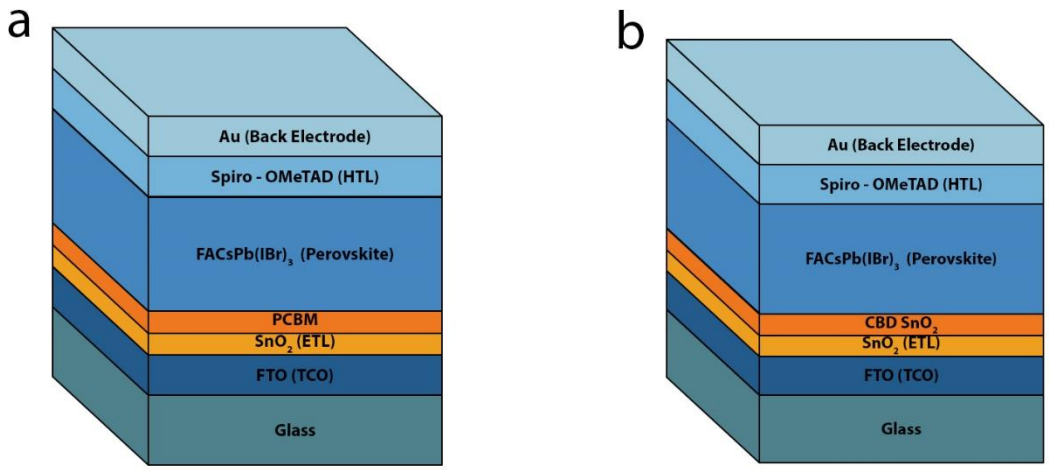

Figure 7. 4: *Schematic of PSCs incorporating* ***(a)*** *PCBM and* ***(b)*** *CBD SnO_2 passivation*

7.2.7 Fabrication of *p-i-n* PSCs employing $KCsFAMAPb(IBr)_3$ and $CsFAPb(IBr)_3$

10 nm of the HTL NiO_x was deposited on ITO coated glass by RF sputtering. The quadrupole cation perovskite, $KCsFAMAPb(IBr)_3$, was then prepared by combining 548.6 mg PbI_2 (TCI) and 77.07 mg $PbBr_2$ (TCI) with 190.12 mg FAI (Dyesol) and 21.84 mg (Dyesol) in a solvent mixture of 4:1 DMF:DMSO. Using stock 2 M iodide solution in DMSO 34 µL of CsI was also added, subsequently KI was added to form the perovskite solution as described by Bu et al.[16] This mixture was allowed to spin overnight using a magnetic stir bar before being filtered into a clean vial using a 0.45 µm PTFE filter.

The NiO_x/ITO coated glass substrates were subjected to a 15 minute UV O_3 treatment prior to spin coating 25 µL of the mixed perovskite solution at 6,000 rpm for 30 seconds. 100 µL of ethyl acetate was used as a solvent quenching method 5 seconds

prior to the end of the spin coating. The samples were then annealed at 120°C for 45 minutes. Once cooled half of the samples were deposited with an evaporated 20 nm C_{60} buffer layer before being sent from CSEM to Tyndall National Institute for ALD of the ETL. When returned, the devices were completed with the evaporation of a 100 nm gold electrode using a Lesker mini-spectros system, with substrate temperature of 80°C and a base pressure of 1.5 × 10−6 Torr.

For *p-i-n* devices incorporating the $CsFAPb(IBr)_3$ perovskite, NiO_x or Spiro-OMeTAD was first deposited by RF sputtering and spin coating using the methods previously described. The samples containing the NiO_x HTL were treated with 15 minutes of UV O_3 prior to spin coating of the perovskite layer. The perovskite absorber layer was realised by first co-evaporating PbI_2 and CsI with a molar ratio controlled via the respective deposition rates. Then, an organohalide solution containing a 1:2 M mixture of FAI and FABr was spin-coated onto the PbI_2:CsI precursor layer, followed by thermal annealing as outlined in section 7.2.4. Following evaporation of the thin C_{60} buffer layer, samples were sent to Tyndall National Institute for ALD deposition. On return, a semi-transparent indium zinc oxide (IZO)/Ag back contact was evaporated using a Lesker mini-spectros system.

7.3 Results and Discussion

A thickness series of 2 nm, 5 nm, 10 nm, 15 nm, 20 nm, 25 nm and 30 nm ALD SnO_2 on O_2 plasma treated substrates was successfully grown by a Picosun R200 ALD system at 185°C. The thickness series was grown in an attempt to optimise the ETL and enhance performance once incorporated into planar PSCs. Planar PSCs were then fabricated and their J-V characteristics were analysed in relation to the ALD ETLs.

ALD of 10 nm and 20 nm thermal SnO_2 grown at 100°C and 140°C on a stack of perovskite absorber/ HTL/ FTO coated glass were fabricated and examined. This was carried out to establish the quality of the interface between the top ALD layer and the perovskite material both in terms of contact properties and process damage of the perovskite.

7.3.1 Morphology

The morphologies of the deposited ALD SnO_2 films and FTO coated glass were examined using SEM (FEI Quanta FEG 650) and TEM (Jeol ARM 200F). Plan view SEM as depicted in Figure 7.5 shows the surface morphology of 20 nm ALD SnO_2 deposited thermally, deposited thermally with a pre-treatment of 5 minutes O_2 plasma, and deposited using PEALD on FTO coated glass. The surface morphologies were found to match that of blank FTO coated glass as seen earlier in Chapter 6.

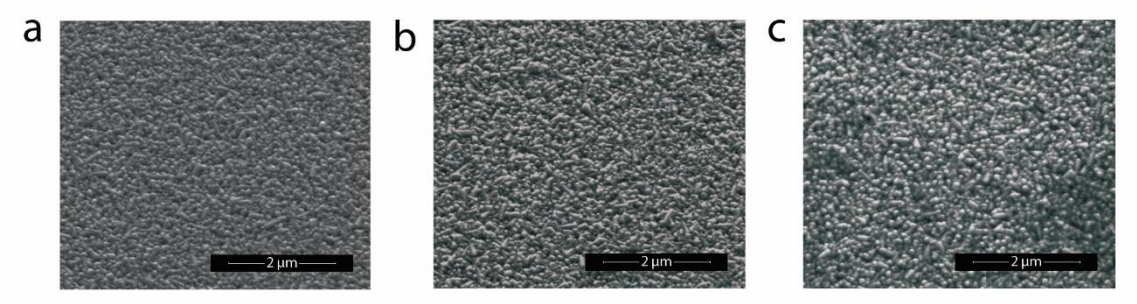

Figure 7. 5: *Plan view SEM showing surface morphology of* ***(a)*** *20 nm thermal ALD SnO_2* ***(b)*** *20 nm thermal ALD SnO_2 pre-treated with O_2 plasma and* ***(c)*** *PEALD of SnO_2, all deposited on FTO coated glass*

For TEM characterisation, specimens for cross section analysis (XTEM) were prepared using the conventional method of gluing face to face small sections cut from an area of interest using M-bond. This was followed by mechanical polishing and ion milling in a Gatan PIPS model 691 apparatus before imaging.

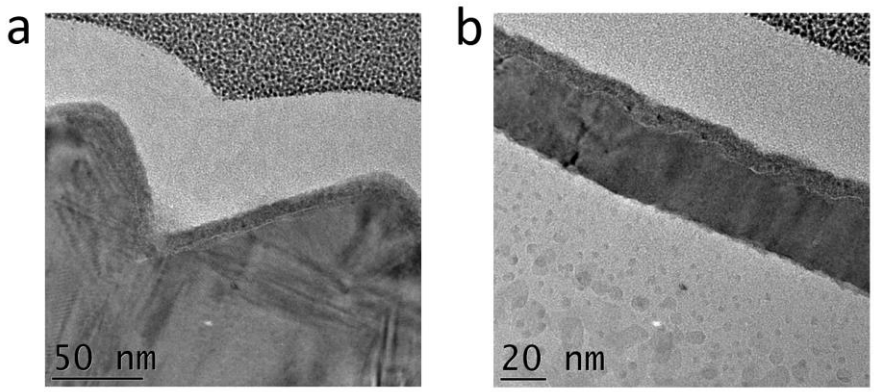

Figure 7. 6: *Cross sectional TEM showing 10 nm thermal ALD SnO_2 pre-treated with O_2 plasma deposited on* ***(a)*** *FTO coated glass and* ***(b)*** *ITO coated glass*

The TEM images exhibited in Figure 7.6 demonstrate the notable contrast between FTO and ITO coated glass substrates with a much increased surface roughness for FTO. While rough FTO is beneficial in PSCs as it provides more surface area for the subsequent layers, the smooth ITO has the benefit of allowing larger perovskite crystals to form.[17] This is advantageous as the large perovskite crystals enhance charge transport due to reduced grain boundaries from smaller crystallites and improve crystal orders. The TEM images also support the claim of ALD conformality as it shows the SnO_2 growth following the curves of the rough FTO coated glass and smooth ITO coated glass underlayers.

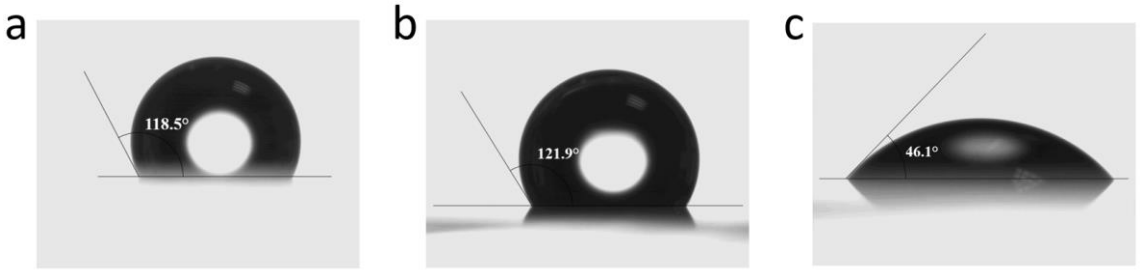

Figure 7. 7: *Contact angle measurement showing 1 µl water on* ***(a)*** *20 nm thermal ALD SnO_2,* ***(b)*** *20 nm thermal ALD SnO_2 pre-treated with O_2 plasma and* ***(c)*** *PEALD of SnO_2 all deposited on FTO coated glass*

Contact angle measurements were performed on various ALD SnO_2 ETLs at room temperature using a Dataphysics OCA 20 wetting angle system. These measurements

were carried out to determine how well the perovskite layer would wet the surface when spin-coated. Figure 7.7 displays the contact angles for various ALD SnO_2 films deposited on FTO coated glass. Using 1 µl water PEALD of 20nm SnO_2 exhibited good wetting, with a measured contact angle of 46.1°. In contrast, 20 nm thermal SnO_2 which was subjected to 5 minutes of O_2 plasma prior to ALD indicated poor wetting, with a contact angle of 121.9 ° using 1 µl water. Contact angle measurements performed using 1 µl water after a 15 minute O_2 plasma treatment post ALD demonstrated a reduction in contact angle from 121.9 ° to 3.8 °, to give a super hydrophilic surface as illustrated in Figure 7.8. This indicates that an O_3 or O_2 plasma treatment before deposition of the perovskite would be required for this metal oxide to be fabricated successfully into a planar PSC.

Figure 7. 8: *Contact angle measurement showing 1 µl water on 20 nm thermal ALD SnO_2 pre-treated with O_2 plasma on FTO coated glass* ***(a)*** *as grown and* ***(b)*** *and* ***(c)*** *treated with 15 minutes O_2 plasma prior to measurement*

XRD was performed using a Philips X'pert PM3719 powder x-ray diffractometer with Cu Kα radiation (λ = 1.540598 Å). As expected at a deposition temperature of 185°C, all ALD films in this study were found to be amorphous as grown.

7.3.2 UV-vis spectrometry

UV-Vis was performed with the Perkin-Elmer Lambda 900 spectrophotometer described previously in Chapter 5, section 5.3.2 to obtain optical transmittance from the thickness series of the ALD thermal SnO_2 on O_2 plasma pre-treated quartz.

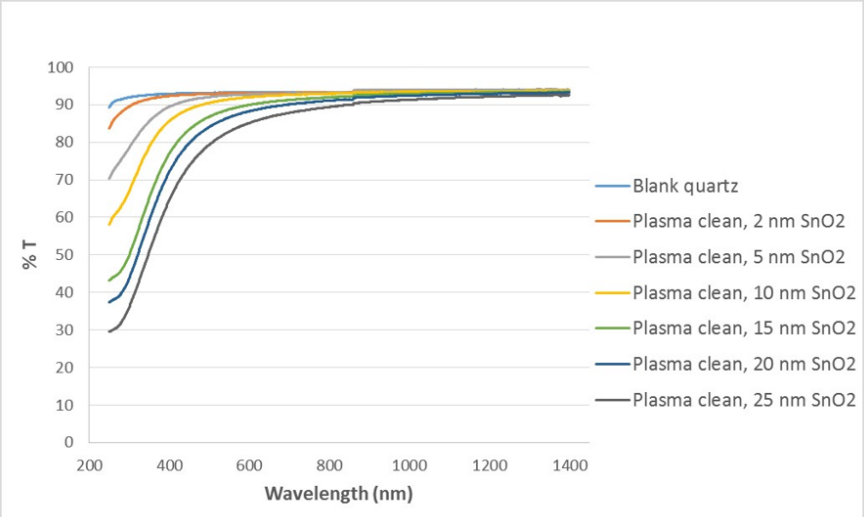

Figure 7. 9: *Graph showing percentage transmission for thickness series of SnO_2 pre-treated with O_2 plasma on quartz*

As with the ALD TiO_2 in Chapter 6, a general decrease in transmission can be observed as the films increase in thickness from 2 nm to 25 nm. ALD SnO_2 in terms of percentage transmission proved to be optically favourable relative to ALD TiO_2, with values above 75 % retained in the 400 nm – 1400 nm range of the spectrum even in the case of the thickest film (Figure 7.9).

7.3.3 Electrical properties

Electrical conductivity measurements were carried out on various ALD SnO_2 films to determine if a difference could be observed in J-V characteristics. 20 nm thermal ALD SnO_2, thermal ALD SnO_2 pre-treated with 5 minutes of O_2 plasma and SnO_2 grown through PEALD were all deposited on FTO coated glass. The samples were then evaporated with a 5 nm Ti adhesion layer followed by a 150 nm Katya mask. Electrical conductivity was measured on 100 nm^2 pads in different areas across the 25 mm^2 samples by applying a voltage sweep from 0 to +/- 0.8 V, in 0.015 V steps. J-V characteristics of the as grown ALD films are displayed in Figure 7.10.

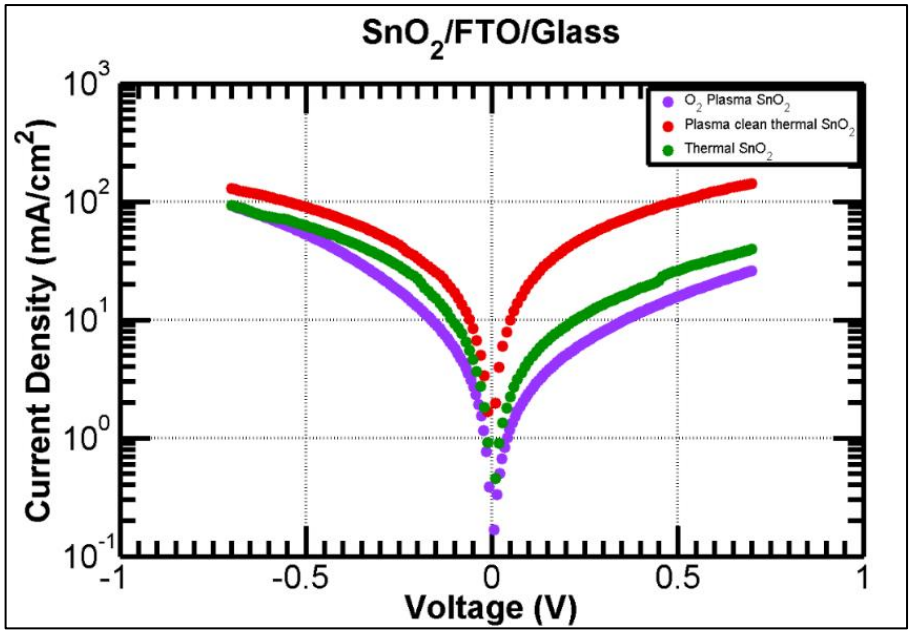

Figure 7. 10: *J-V sweep comparing 20 nm thermal ALD SnO_2, 20 nm thermal ALD SnO_2 pre-treated with 5 minutes of O_2 plasma, and 20 nm PEALD SnO_2 all deposited on FTO coated glass*

From Figure 7.10, it can be observed that thermal SnO_2 which was subjected to an O_2 plasma clean prior to growth performed the best electrically. This was followed by thermal SnO_2 and then PEALD SnO_2. These results are similar to the sigma dark measurements obtained for ALD TiO_2 variations deposited in the same way from Chapter 5, section 5.3.1. Similarly to ALD TiO_2, the plasma clean directly prior to ALD growth produced the best films in terms of conductivity. A plasma clean is likely to provide more nucleation sites for ALD and remove adventitious carbon, which would result in a non-uniform growth, from the substrate surface as described earlier.

Following this, 20 nm thin films of ALD SnO_2 and TiO_2 were grown at 185°C using the champion deposition methods and their J-V characteristics were directly compared as shown in Figure 7.11. ALD SnO_2 which was subjected to a pre-growth O_2 plasma treatment was observed to produce a higher conductivity than ALD TiO_2 which was also subjected to the same plasma treatment. Both the tin precursor, TDMASn, and the titanium precursor, TDMAT, contain the same ligands and the H_2O reactant was utilised for both depositions. Both SnO_2 and TiO_2 are composed of similar bond lengths (1.90 Å) and chemical bonds, while their electronic band gap energies are also comparable (E_g 3 eV – 4 eV). Despite this, their optical and electronic properties are quite different due to their differing band-edge structures.[18] SnO_2 is typically optically

transparent with large electron conductivity while TiO_2 is optically absorbing with weak electron mobility due to a high level of electron and hole traps. This information is not only valuable for the fabrication of efficient PSCs but also for applications such as oxide thin-film transistors and dye-sensitive solar cells.

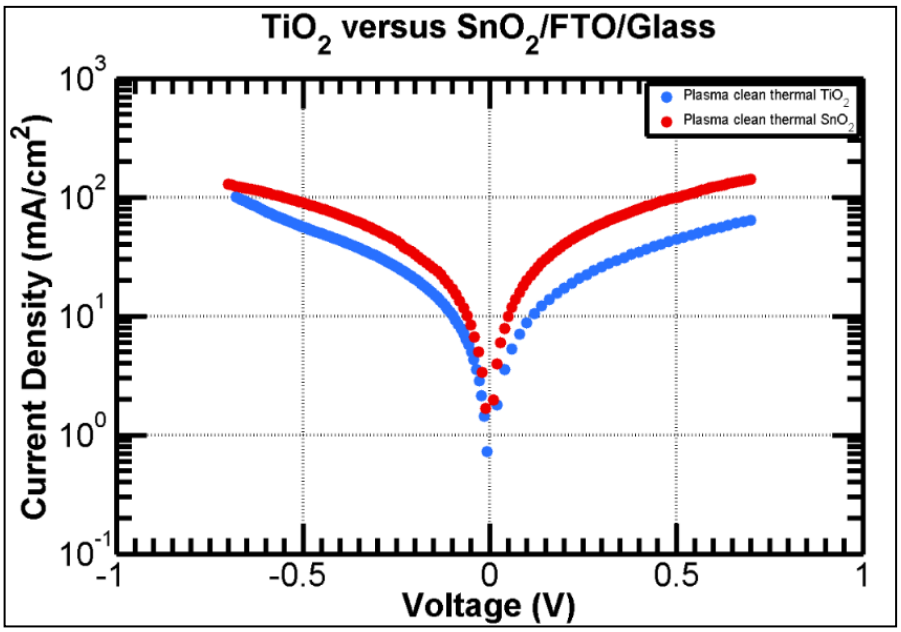

Figure 7. 11: *J-V sweep comparing 20 nm thermal ALD SnO_2 pre-treated with a 5 minute O_2 plasma clean to 20 nm thermal ALD TiO_2 pre-treated with a 5 minute O_2 plasma clean*

Hall Effect measurements were carried out to compare the electrical properties of ALD SnO_2 and TiO_2 deposited using the champion deposition methods on glass. The measurements were obtained using a LakeShore HMS 8404 Hall Measurement System with both DC and AC magnetic field capability.[19] Both DC and AC magnetic field methods were used with field reversal strength of ±1.7 T for the DC technique and +1.2 T RMS for the AC method using a lock-in amplifier.

100 nm of ALD SnO_2 and TiO_2 were deposited on glass and as previously described subjected to a 5 minute O_2 plasma treatment prior to ALD deposition. 100 nm films were chosen to allow conductivity to be measured by the Hall Effect instrument with a sufficiently high signal to noise ratio. The glass substrates were diced post ALD into 1 cm^2 samples from the back face of the glass and a centre sample was chosen from

each to be measured. This was carried out to ensure that no growth was deposited on the edge or back side of the samples.

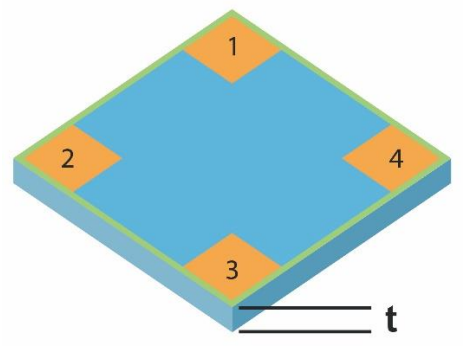

Figure 7. 12: *Schematic of 1 cm^2 sample for Hall Effect measurement with thickness, t, and ohmic contacts on the four corners of the sample by the boundary*

The objective of the Hall measurement in the Van der Pauw technique is to determine the sheet carrier density, n_s, by measuring the Hall voltage, V_H. In order to determine both the mobility, μ, and the n_s a combination of a resistivity measurement and a Hall measurement is needed.

The measurement requires a 1 cm^2 solid sample which is roughly 2D in nature (ie. much thinner than 1 cm^2) with small ohmic contacts placed on the four corners at the very bounds of the sample (Figure 7.12). A four point probe is then placed on these points allowing the van der Pauw method to provide an average resistivity of the sample. Ideally the ohmic contacts are required to be infinitesimally small as any errors produced by their non-zero size would be of the order D/L, where D is the diameter of the contact and L is the distance between contacts. As well as this, leads from the contacts are required to be from the same batch of wire to minimise any thermoelectric effects.

$$n_S = \frac{IB}{q|V_H|} \qquad \textbf{7.1}$$

The equation for calculating sheet carrier density is displayed above in equation 7.1 where I is the current, B is the magnetic field, and q is the elementary charge (1.602 x 10^{-19} C).

V_H is measured when electrons are travelling through a magnetic field and are subjected to Lorentz force, leading to a build up of negative charge on one side of the sample and a positive charge on the other. The potential difference between the two sides of the sample is measured as the V_H. Equation 7.2 below is used to calculate Lorentz force:

$$F_{Lorentz} = q(E + (v\ x\ B)) \quad \textbf{7.2}$$

To measure the sheet resistance, R_s, a DC current, *I*, is set up before an automatic measuring sequence is started, measuring the resistance between two opposing leads. For Hall Effect measurements, a voltage is applied between the contacts placed at diagonally opposite corners and the current, *I*, flowing between them is measured. In addition, a magnetic field, *B*, is applied in the direction perpendicular to the sample and the change in V_H between the contacts in opposite corners is measured The van der Pauw method consists of two measurements of resistivity, R_1 and R_2 as displayed in equation 7.3 and 7.4:

$$R_1 = R_{4,1,\ 3,2} + R_{1,4,\ 2,3} + R_{2,3,\ 1,4} + R_{3,2,\ 4,1} \quad \textbf{7.3}$$

$$R_2 = R_{3,2,\ 2,1} + R_{4,3,\ 1,2} + R_{1,2,\ 4,3} + R_{2,1,\ 3,4} \quad \textbf{7.4}$$

From these two measurements and the knowledge of the sample thickness under test, *t*, the conductivity of the sample may be measured. As all sides of the sample are the same length, resistivity, ρ, can be measured using sheet resistance, R_s, and the correction factor, *f* as displayed in equation 7.5:

$$\rho = R_s t = \frac{\pi t}{\ln 2} \frac{R_{1,2,\ 3,4} + R_{2,3,\ 4,1}}{2} f \quad \textbf{7.5}$$

where;

$$R_{1,2,\ 3,4} = \frac{V_{3,4}}{I_{1,2}} \quad \textbf{7.6}$$

and

$$R_{2,3,\ 4,2} = \frac{V_{4,1}}{I_{2,3}} \quad \textbf{7.7}$$

Mobility can then by calculated using the R_s or Hall coefficient, R_H, measured by the Hall Effect instrument.[20]

$$R_H = \frac{V_H t}{IB} \quad \textbf{7.8}$$

$$\mu = \frac{|V_H|}{R_S IB} = \frac{1}{q n_s R_S} = \frac{R_H}{\rho} \quad \textbf{7.9}$$

Table VII. III: *Hall Effect properties of 100 nm ALD SnO_2 in DC and AC*

100 nm SnO_2 on glass			*DC*	*AC*
μ_H	*Hall mobility*	$cm^2/V \cdot s$	1.19948	N/A
	Carrier type		n	n
n	*Carrier concentration*	$1/cm^3$	6.63733×10^{18}	6.73002×10^{18}
n_{sheet}	*Sheet carrier concentration*	$1/cm^2$	6.63733×10^{13}	6.73002×10^{13}
R_H	*Hall coefficient*	cm^3/C	9.40364×10^{-1}	9.27413×10^{-1}
$R_{H\,sheet}$	*Sheet hall coefficient*	cm^2/C	9.40364×10^{4}	9.27413×10^{4}
ρ	*Resistivity*	$\Omega \cdot cm$	7.83974×10^{-1}	N/A
ρ_{sheet}	*Sheet resistivity*	Ω/sq	7.83974×10^{4}	N/A
V_H	*Hall voltage*	V	-1.59886×10^{-4}	1.15407×10^{-4}

The SnO_2 thin film exhibited excellent ohmic behaviour during ohmic checks, however the thermal electric voltage was found to be quite high, i.e. within the mV range from the intercept of the linear relation. A results summary of the Hall Effect analysis on SnO_2 is outlined in Table VII. III. Four-point resistivity measurements provided information on the sheet resistivity and resistivity based on the nominal thickness of 100 nm. Both DC and AC Hall measurements indicated that the material was 100 % n-type. The signal to noise ratio for DC was quite high at 15:1, but for AC was very good at 50:1 confirming the carrier type and sheet concentration. Hall mobility was based on four-point sheet resistivity displaying 1.2 $cm^2/V.s$. These Hall results were based on the assumption that the entire SnO_2 thickness was contributing to the measurements without any interface layer contribution.

Table VII. IV: *Hall Effect properties of 100 nm ALD TiO_2 in DC*

100 nm TiO_2 on glass			*DC*
μ_H	*Hall mobility*	$cm^2/V \cdot s$	5.22254×10^{-1}
	Carrier type		n/p
n	*Carrier concentration*	$1/cm^3$	1.02105×10^{17}
n_{sheet}	*Sheet carrier concentration*	$1/cm^2$	1.02105×10^{12}
R_H	*Hall coefficient*	cm^3/C	6.11281×10^{1}
$R_{H\,sheet}$	*Sheet hall coefficient*	cm^2/C	6.11281×10^{6}
ρ	*Resistivity*	Ω . cm	1.17047×10^{2}
ρ_{sheet}	*Sheet resistivity*	Ω/sq	1.17047×10^{7}
V_H	*Hall voltage*	V	-3.11638×10^{-3}

The TiO_2 thin film was found to be much more resistive than SnO_2 when measured using the Hall Effect instrument. Similarly to the SnO_2, the TiO_2 sample exhibited excellent ohmic behaviour during ohmic checks with very high thermal electric voltage. Four-point resistivity measurements provided information on the sheet resistivity and resistivity based on the nominal thickness of 100 nm as detailed in Table VII. IV. When initially tested the DC Hall measurement provided a very poor signal to noise ratio of 1:2 meaning that the Hall results could not be trusted. The measurements were repeated using a long wait time of 300 seconds which improved the signal to noise ratio to 50:1. Despite this precaution, both n-type carrier and p-type carriers were exhibited from the DC Hall measurement. Fresh 1 cm^2 TiO_2 samples were also measured and it was determined that the carrier type was random. While bulk TiO_2 is commonly considered a n-type semiconductor, undoped TiO_2 can also exhibit a p-type response due to dominant counterpart surface charge carriers, the holes.[21,22] From these measurements only resistance and sheet resistance are reliable from the data obtained.

7.3.4 XPS

XPS was carried out on 20 nm ALD SnO_2 films deposited on FTO coated glass to determine the tin content. The details of XPS have been described previously in Chapter 5, section 5.3.3. It is difficult to differentiate between SnO and SnO_2 from the

XPS Sn 3d peaks alone. However, it is possible to distinguish from the Sn valence spectra displayed in Figure 7.13 (a).

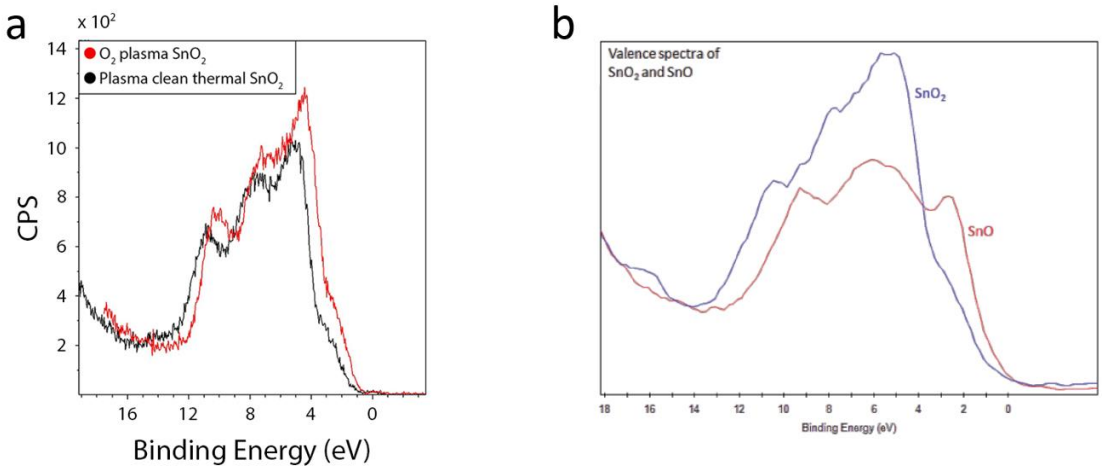

Figure 7. 13: (a) *XPS of Sn valence spectra for 20 nm thermally deposited SnO_2 pre-treated with a 5 minute O_2 plasma clean on FTO coated glass and 20 nm of plasma enhanced SnO_2 on FTO coated glass* ***(b)*** *XPS from the literature demonstrating difference between Sn^{4+} and Sn^{2+}* [23]

The Sn valence spectra is characteristic of Sn^{4+} in both plasma enhanced SnO_2 and thermally deposited SnO_2 pre-treated with an O_2 plasma clean. If Sn^{2+} was present, a shoulder would be observed on the right hand side of the peak at a binding energy of ~2.8 eV (Figure 7.13 (b)).

No signal was detected from the underlying FTO during XPS which indicates conformal and pinhole-free SnO_2 coverage.

7.3.5 Complete planar perovskite solar cells

Following the author's work depositing and characterising ALD SnO_2 ETLs at Tyndall National Institute, samples were sent to CSEM and the University of Oxford to be fabricated into planar PSCs. An internship was then arranged at the University of Oxford to study established methods of depositing mixed cation perovskite materials. Here, the author carried out a study comparing passivation layers on ALD SnO_2 to the same layers on spin-coated SnO_2. The performances of the cells are compared and discussed.

7.3.5.1 n-i-p architecture PSCs, no passivation

10 nm and 20 nm thermal ALD SnO_2 thin films which were treated with 5 minutes of O_2 plasma prior to deposition at 185°C were grown on TEC-7 FTO coated glass (Solaronix) as well as ITO coated glass (Sigma Aldrich 8-12 Ω/sq). The ALD layers on ITO coated glass were chosen to be fabricated into planar PSCs by CSEM using a triple cation $CsFAMAPbI_3$ perovskite material. These were compared to 10 nm and 20 nm thermal ALD TiO_2 thin films which were treated with the same pre-growth O_2 plasma clean on ITO coated glass. The TiO_2 thin films were fabricated into planar perovskite devices using the $MAPbI_3$ perovskite material. The J-V characteristics of these cells on a 1.04 cm^2 active area are displayed in Figure 7.14.

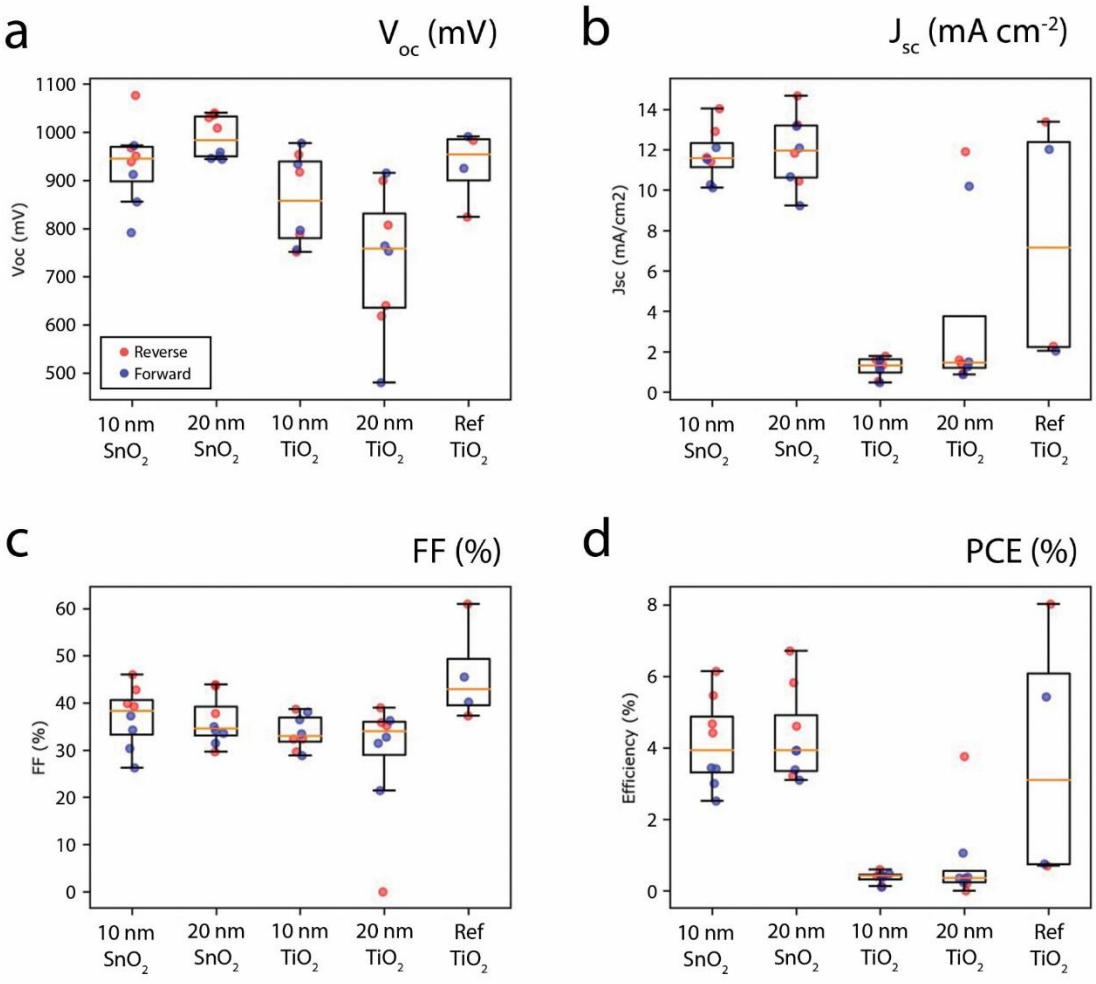

Figure 7. 14: *J–V characteristics of planar perovskite solar cells on ITO coated glass substrates containing ETLs of 10 nm and 20 nm thermal ALD SnO_2 and TiO_2 pre-treated with 5 minutes of O_2 plasma*

From these J-V characteristics it can be observed that there was an issue with one or more of the process steps, namely the $MAPbI_3$ perovskite, the Spiro-OMeTAD HTL synthesis or deposition, as the PCE of the reference cell containing a sputtered TiO_{2-x} ETL is far lower than the expected value observed previously in Chapter 6. Planar devices containing ALD SnO_2 had an improved performance in terms of V_{oc}, J_{sc}, and PCE over their ALD TiO_2 counterparts. However, this improved performance may be due to the $CsFAMAPbI_3$ perovskite absorber employed. All PSCs were made up together using the same HTL solution. The source of the poor PCEs of devices containing ALD SnO_2 could not be determined conclusively. Hence, it remains unclear whether ALD SnO_2 outperforms ALD TiO_2 when incorporated into devices, or if, similarly to ALD TiO_2, it requires passivation.

10 nm and 20 nm thermal ALD SnO_2 and ALD TiO_2 thin films which were treated with O_2 plasma prior to deposition at 300°C were grown on TEC-7 FTO coated glass (Solaronix) as well as ITO coated glass (Sigma Aldrich 8-12 Ω/sq). The high temperature ETL sample set was decided upon in an attempt to improve PCE in planar cells. It was discussed in Chapter 6 that ALD TiO_2 deposited at 185°C is not stoichiometric. XPS of the Ti 2p signatures indicated that the stoichiometry was improved by the 500°C mesoporous sintering as the ratio of Ti^{3+} to Ti^{4+} was reduced from 1:3.9 to 1:4.3. While it has been observed that ALD SnO_2 deposited at 185°C is stoichiometric, containing only Sn^{4+}, both metal oxides were found to contain measurable quantities of N and C from unreacted precursors. The higher deposition temperature of 300°C could aid in the removal of these impurities.

The ALD layers on ITO coated glass were chosen to be fabricated into planar PSCs at CSEM using a spin coated double cation mixed halide perovskite material, $CsFAPb(IBr)_3$. These planar cells were composed of ITO coated glass/ ALD TiO_2 or ALD SnO_2/ $CsFAPb(IBr)_3$/ Spiro-OMeTAD/ Au contact. The J-V characteristics of these cells on a 1.04 cm^2 active area are displayed in Figure 7.15.

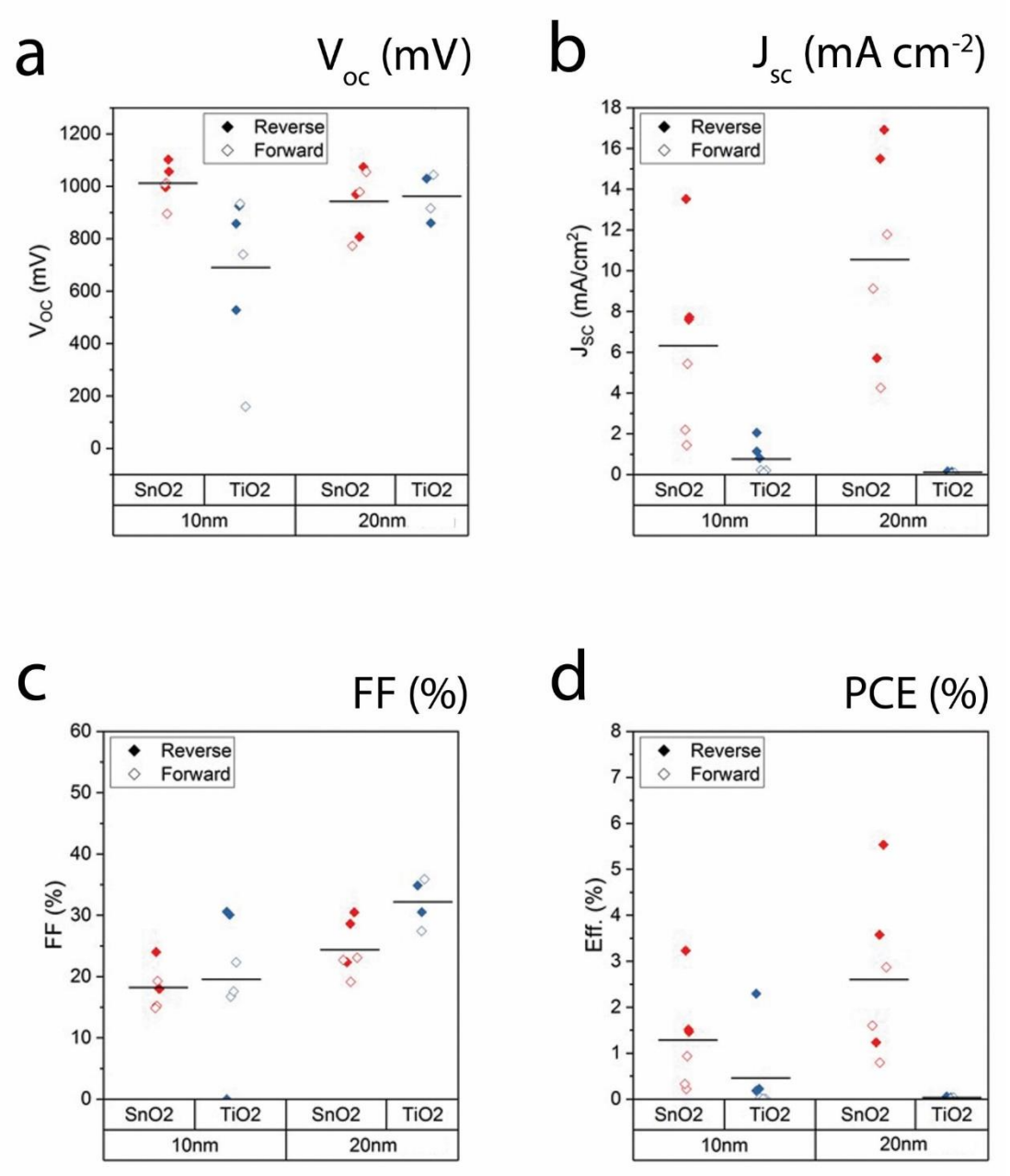

Figure 7. 15: *J–V characteristics of planar perovskite solar cells on ITO coated glass substrates containing ETLs of 10 nm and 20 nm thermal ALD SnO_2 and TiO_2 pre-treated with 5 minutes of O_2 plasma and grown at 300°C*

The J-V characteristics show the V_{oc} of all devices to be suitably high, with the cells containing 10 nm ALD TiO_2 being slightly lower. The current was found to be strongly supressed in all devices most notably those containing the TiO_2 films, indicating poor electron extraction through the ALD TiO_2. This corresponds well to the results obtained for 20 nm ALD TiO_2 which had undergone a RTA treatment to 500°C discussed in Chapter 6. The FF obtained was markedly low for all cells, though

low illumination R_{sc} values indicate that the films are likely not shunted (not shown). This combined with poor J_{sc} lead to inferior PCEs.

7.3.5.2 n-i-p architecture PSCs, C_{60} passivation

2 nm, 5 nm, and 10 nm thermal ALD SnO_2 thin films on O_2 plasma cleaned TEC-7 coated glass (Hartford Glass) were deposition at 185°C. These ALD layers were sent to the University of Oxford to be fabricated into planar PSCs using a $MAPbI_3$ perovskite material prepared through the acetonitrile/methylamine method.[14] The final device architecture was composed of FTO coated glass/ ALD SnO_2 / C_{60}/ $MAPbI_3$/ Spiro-OMeTAD/ Ag. Devices were measured using a class AAB ABET solar simulator with an AM 1.5 G irradiance spectrum at 100 mW cm^{-2}. The irradiance was calibrated using an NREL-calibrated KG5 filtered silicon reference cell. The J-V characteristics of the cell were recorded using a source meter (Keithley 2400, USA). The cell areas were defined using a metal mask.

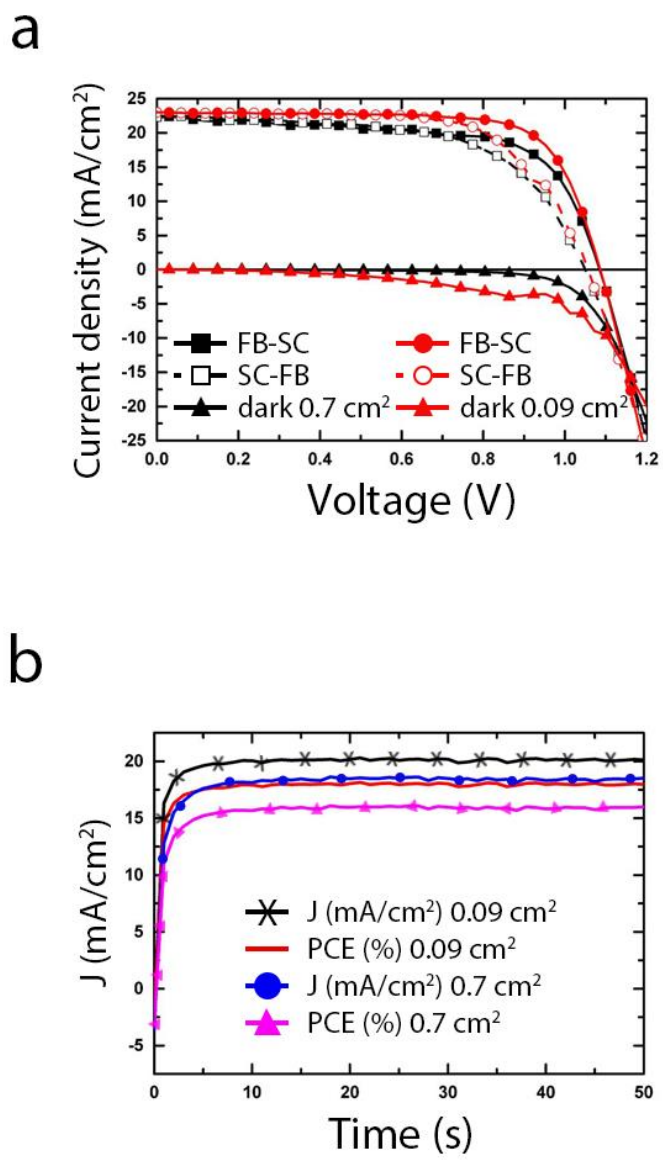

Figure 7. 16: (a) *J–V characteristics of planar perovskite solar cells containing 10 nm ALD SnO_2 pre-treated with 5 minutes of O_2 plasma on 0.7 cm^2 and 0.09 cm^2 active areas* ***(b)*** *Steady state max power point tracking of same cells over 50 seconds*

10 nm ALD SnO_2 was found to perform best from the ALD thickness series reaching 18.3 % PCE on a 0.09 cm^2 active area and 15.9 % PCE on a 0.7 cm^2 active area. The J-V characteristics of the devices containing 10 nm ALD SnO_2 are displayed in Figure 7.16 (a). Steady state tracking was employed for 50 seconds (Figure 7.16 (b)) with the 0.09 cm^2 active area cell maintaining 17.9 % PCE_{MPP} and the larger 0.7 cm^2 active area cell maintaining a 15.8 % $PCE_{MPP.}$

Table VII. V: *Device performance parameters for an ETL of 10 nm ALD SnO_2 pre-treated with a 5 min O_2 plasma clean*

Aperture area (cm^2)	*V_{oc} (mV)*	*J_{sc} (mA/cm^2)*	*FF (%)*	*PCE (%)*	*Steady-state MPP (%)*
0.7	1070	22.5	67	15.9	15.8
0.09	1070	23.0	75	18.3	17.9

These results show a marked improvement in performance due to the incorporation of a C_{60} buffer layer between the SnO_2 ETL and the perovskite absorber. A substantial difference can be observed between the two device active areas with a larger series resistance exhibited with the larger active area. Possible reasons for this could be that only two wire probes were used for contacting the larger active area device and that the metal pad design employed was not optimal.

7.3.5.3 n-i-p architecture PSCs, spin coated PCBM and CBD passivation

Whilst on an internship at Oxford University the author also fabricated planar perovskite devices comparing the ALD ETLs and reference spin coated SnO_2 ETLs. Thermal ALD SnO_2 thin films (15 nm, 20 nm, 25 nm, 30 nm) where grown at 185°C on O_2 plasma pre-treated TEC-7 coated glass (Hartford Glass). Each ALD thickness consisted of sixteen substrates each of which produced 8 pixels with active areas of 0.0919 cm^2 once fabricated into perovskite solar devices. For buffer layers between the SnO_2 ETLs and the active perovskite medium a comparison between spin coated PCBM and CBD SnO_2 was made. Devices were measured using a class AAB ABET solar simulator with an AM 1.5 G irradiance spectrum at 100 mW cm^{-2}. The irradiance was calibrated using an NREL-calibrated KG5 filtered silicon reference cell. The J-V characteristics of the cell were recorded using a source meter (Keithley 2400, USA). The cell areas were defined using a metal mask.

7.3.5.3 (i) Spin coated PCBM study

PCBM was chosen to be studied in conjunction with SnO_2 due to its high mobility (~10^{-3} cm^2 V.s).[24] Low reported PCEs from pure PCBM have led to further modifications in the PV field such as n-type doping, solution engineering and interface control. The use of PCBM as an interlayer between ALD TiO_2 and a perovskite absorber material in an inverted *p-i-n* architecture has been reported, reaching 8.8 %

PCE.[25] The purpose of this study was to determine how well it worked as an interlayer between ALD SnO_2 and the perovskite absorber.

Planar perovskite devices employing two SnO_2 deposition methods, ALD and spin coating, were fabricated into cells in parallel. In this way performance changes could be attributed to the influence of the inclusion of an ALD ETL or a spin coated ETL. The final device stack was comprised of TEC7 FTO coated glass/ SnO_2 deposited by ALD or spin coating/ PCBM/ $FACsPb(IBr)_3$/ Spiro-OMeTAD/ Ag. The J-V characteristics of the reference cells incorporating a spin coated SnO_2 ETL on a 0.09 cm^2 active area are displayed in Figure 7.17

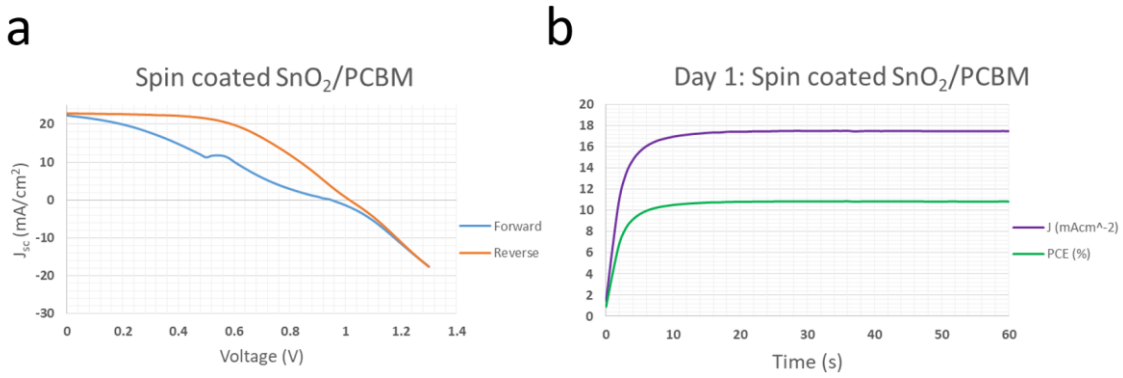

Figure 7. 17: (a) *J–V characteristics of best planar perovskite solar cell containing spin coated SnO_2/PCBM as an ETL and buffer layer respectively* ***(b)*** *Steady state max power point tracking of same cell over 60 seconds*

The reference cell containing a spin coated SnO_2 ETL followed by spin coated PCBM exhibits severe hysteresis between the reverse and forward scans. While V_{oc} is reasonably high in the reverse scan, the low FF produces a PCE of 11.97 %. The V_{oc} is observed to drop in the forward scan further decreasing the FF and producing a PCE of 6.54 % as shown in Table VII. VI. Steady state MPP tracking over 60 seconds produced a stabilised efficiency of 10.85 %. The poor FF and drop in V_{oc} here may be attributed to poor charge extraction at the ETL interface, or a high recombination rate in the perovskite material and at the ETL/perovskite interface.

Table VII. VI: *Device performance parameters of best planar perovskite solar cell containing spin coated SnO_2/PCBM as an ETL and buffer layer respectively*

Scan direction	*V_{oc} (mV)*	*J_{sc} (mA/cm²)*	*FF (%)*	*PCE (%)*
Reverse	1020	22.87	51	11.97
Forward	940	22.36	31	6.54

The J-V characteristics of the same cell were re-measured three days later and while some hysteresis still persisted, the steady state MPP tracking produced an enhanced stabilised efficiency of 13.65 % as displayed in Figure 7.18. This enhanced performance is due to an increased FF of 71.37 % for the reverse scan. Since FF is largely dependent on R_s, it is likely that this improvement was caused by oxidation of the Spiro-OMeTAD HTL which enhances charge transfer at the HTL/Ag interface.[26,27]

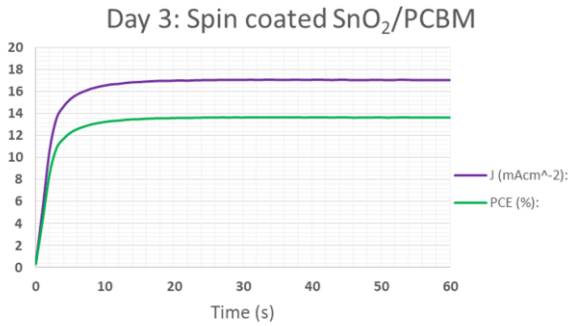

Figure 7.18: *Steady state max power point tracking of best planar perovskite solar cell containing spin coated SnO_2/PCBM as an ETL and buffer layer respectively over 60 seconds after three days*

The J-V characteristics of the cell using 20 nm ALD SnO_2 ETL are displayed in Figure 7.19.

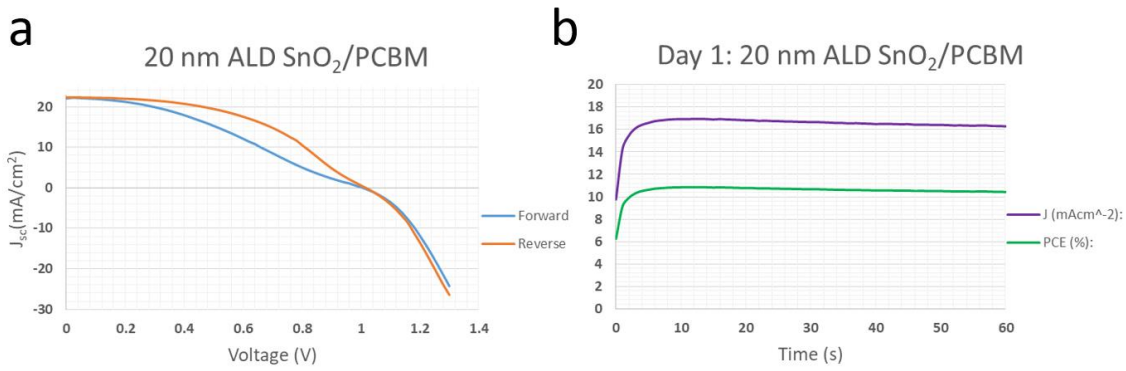

Figure 7. 19: (a) *J–V characteristics of best planar perovskite solar cell containing 20 nm ALD SnO_2/PCBM as an ETL and buffer layer respectively* ***(b)*** *Steady state max power point tracking of same cell over 60 seconds*

The cell containing 20 nm ALD SnO_2 as an ETL followed by spin coated PCBM also exhibits notable hysteresis. The s-shape of the hysteresis as graphed is not as pronounced as that produced by the reference cell beforehand. While V_{oc} and J_{sc} are sufficiently high for both scan directions, the low FF leads to PCEs of 10.60 % for the reverse scan and 7.64 % for the forward scan (Table VII. VII). Steady state MPP tracking over 60 seconds measured a stabilised efficiency of 10.42 % which is comparable to that produced by the reference cell incorporating the spin coated ETL.

Table VII. VII: *Device performance parameters of best planar perovskite solar cell containing 20 nm ALD SnO_2/PCBM as an ETL and buffer layer respectively*

Scan direction	*V_{oc} (mV)*	*J_{sc} (mA/cm²)*	*FF (%)*	*PCE (%)*
Reverse	1020	22.34	47	10.60
Forward	1000	22.04	35	7.64

The J-V characteristics of the same cell were re-measured three days later. However, unlike the efficiency boost observed in the reference cell previously, a steady state MPP tracking over 60 seconds measured a stabilised efficiency of 9.925 % (Figure 7.20). This is slightly lower than that produced by the same cell when measured fresh. FF was marginally increased by the oxidised Spiro-OMeTAD when measured on day three, but a slight dip in J_{sc} to 21.99 mA cm^{-2} lead to the reduced stabilised efficiency. While cells can be observed to improve over time due to oxidation of the Spiro-OMeTAD, the inevitable degradation of the cell reduces J_{sc}.

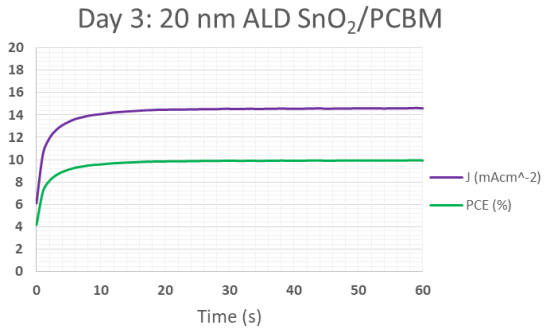

Figure 7. 20: *Steady state max power point tracking of the best planar perovskite solar cell containing 20 nm ALD SnO_2/PCBM as an ETL and buffer layer respectively over 60 seconds after three days*

From the above results it can be observed that spin coated SnO_2 is comparable to ALD SnO_2 as an ETL in planar *n-i-p* perovskite devices. With the inclusion of PCBM as an interlayer between the ETL and perovskite material, devices reached stabilised efficiencies of 10.85 % when spin coated SnO_2 was incorporated and 10.42 % when 20 nm ALD SnO_2 was incorporated when both were measured fresh after contact evaporation.

7.3.5.3 (ii) Chemical Bath Deposition of SnO_2 study

CBD was chosen for this study due to its inexpensive low temperature processing and capacity to be adapted for deposition over scalable areas. The use of CBD has previously been reported for the deposition of CdS and Zn(SOOH) films.[28,29] A thin CBD SnO_2 layer has also been reported as the sole ETL in a planar perovskite device reaching a PCE of 14.8 %. Higher FF and V_{oc} values compared to those of devices using spin coated TiO_2 were observed due to the lower surface roughness of SnO_2 on ITO coated glass, as well as a favourable interface between the SnO_2 and $MaPbI_3$ perovskite.[30] A technique involving spin coated SnO_2 followed by a CBD of SnO_2 has also been well reported in the literature as discussed previously, with Anaraki et al. comparing spin coated SnO_2 followed by CBD to ALD SnO_2.[15] This CBD procedure has been well established and optimised by those at the University of Oxford. The purpose of this study was to compare spin coated SnO_2 followed by CBD to ALD SnO_2 followed by CBD when incorporated into planar devices. This dual layer

electron transport medium would, it was hoped, improve the interface characteristics of the ALD layer whilst maintaining an entirely inorganic structure.

Planar perovskite devices consisting of the alternative SnO_2 deposition methods of ALD and spin coating were fabricated into cells in parallel. In this way performance changes could be attributed to the influence of the ALD or spin coating ETL step. The final device stack was comprised of TEC7 FTO coated glass/ SnO_2 deposited by ALD or spin coating/ CBD SnO_2/ $FACsPb(IBr)_3$/ Spiro-OMeTAD/ Au. A thickness series of 15 nm, 20 nm, 25 nm and 30 nm ALD SnO_2 was employed in an effort to optimise the ETL while the spin coated SnO_2 remained constant at a thickness of 15-20 nm. A change in SnO_2 thickness has the potential to alter series resistance in the final device. Reducing ETL thickness can also reduce series resistance due to the short distance of transfer for photogenerated charges. Shunt resistance is expected to remain relatively unchanged with alteration in ALD thickness due to the good hole blocking ability of ALD.

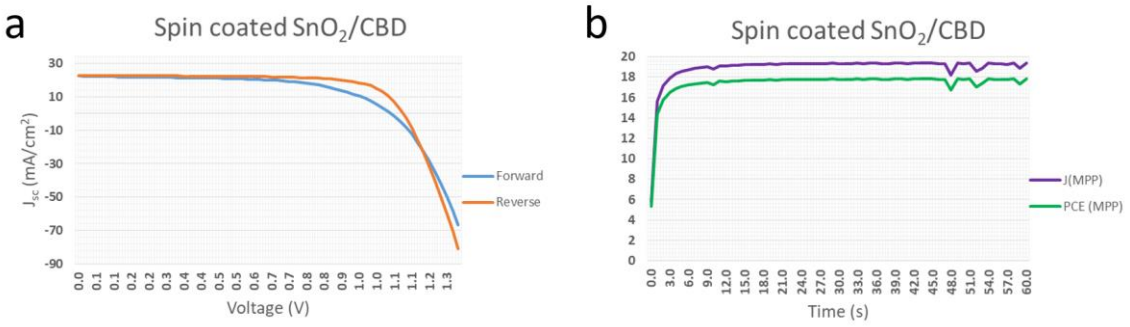

Figure 7. 21: (a) *J–V characteristics of best planar perovskite solar cell containing spin coated SnO_2/CBD SnO_2 as an ETL and buffer layer respectively* ***(b)*** *Steady state max power point tracking of same cell over 60 seconds*

The J-V characteristics of the champion reference cell incorporating a CBD SnO_2 layer on a 0.09 cm^2 active area are displayed in Figure 7.21. This pixel produced an impressive 18.36 % PCE in the reverse scan and 14.52 % PCE in the forward scan (Table VII. VIII). Despite the notable hysteresis in the J-V curve, MPP tracking stabilised at 17.82 % over 60 seconds. This device exhibited an improved V_{oc} and FF compared to its PCBM counterpart, thus enhancing the overall performance. While hysteresis remained in the planar cell, it was notably reduced compared to the same architecture incorporating PCBM.

Table VII. VIII: *Device performance parameters of best planar perovskite solar cell containing spin coated SnO_2/CBD SnO_2 as an ETL and buffer layer respectively*

Scan direction	*V_{oc} (mV)*	*J_{sc} (mA/cm²)*	*FF (%)*	*PCE (%)*
Reverse	1120	22.57	71	18.36
Forward	1060	22.41	60	14.52

From the ALD thickness series, 20 nm SnO_2 using CBD SnO_2 as a passivation layer was found to perform best. The champion pixel produced 15.24 % PCE in the reverse scan and 11.15 % PCE in the forward scan, with MPP tracking stabilising at 14.79 % PCE over 60 seconds as displayed in Figure 7.22. Hysteresis throughout the ALD SnO_2 thickness series was similar to that observed in devices containing ETLs produced using the spin coating method.

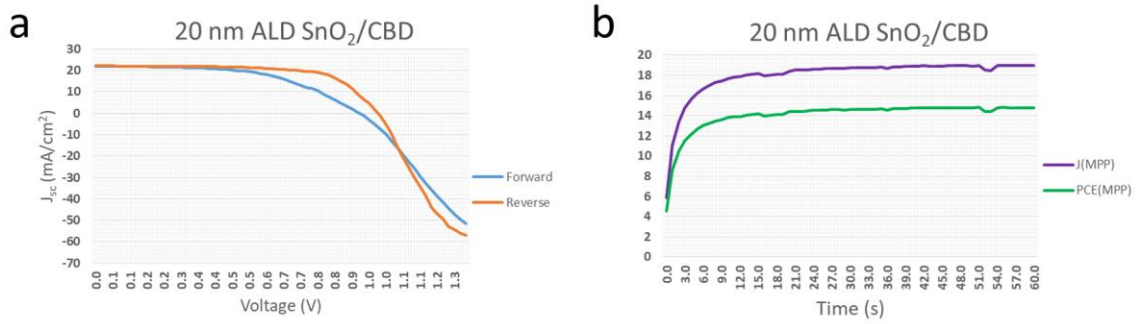

Figure 7. 22: (a) *J–V characteristics of best planar perovskite solar cell containing 20 nm ALD SnO_2/CBD SnO_2 as an ETL and buffer layer respectively* ***(b)*** *Steady state max power point tracking of same cell over 60 seconds*

While J_{sc} was similarly high for all SnO_2/CBD cells containing spin coated and ALD ETLs, a lower V_{oc} and FF could be observed for the ALD/CBD devices resulting in reduced efficiencies. While CBD in combination with spin coated SnO_2 is a process which has been well optimised over time, this initial study of ALD/CBD exhibits promise pending further optimisation.

Table VII. IX: *Device performance parameters of best planar perovskite solar cell containing 20 nm ALD SnO_2/CBD SnO_2 as an ETL and buffer layer respectively*

Scan direction	*V_{oc} (mV)*	*J_{sc} (mA/cm^2)*	*FF (%)*	*PCE (%)*
Reverse	1000	22.12	67	15.24
Forward	920	22.08	54	11.15

Despite not achieving the same efficiencies observed with the spin coating technique in this preliminary study, thermally grown amorphous ALD SnO_2 has proven to be a viable alternative. ALD allows for a more scalable process than spin coating and remains an interesting candidate for future development.

7.3.5.4 p-i-n architecture PSCs, initial test with and without C_{60} passivation

A set of perovskite samples was sent from CSEM to Tyndall National Institute to determine how well ALD SnO_2 would perform in a *p-i-n* architecture. Half of the sample set included evaporated C_{60} as a buffer layer on top of the perovskite absorber material, while the other half had a top layer of bare perovskite. The absorber material was composed of a quadruple cation mixed halide perovskite, $KCsFAMAPb(IBr)_3$, which was deposited through spin coating, while the HTL employed was sputtered NiO_x. The final device architecture was composed of ITO (6-7 Ω/sq) coated glass/ sputtered NiO_x/ $KCsFAMAPb(IBr)_3$/ C_{60} buffer layer or bare/ ALD SnO_2/ Ag

10 nm SnO_2 was deposited by ALD at 100°C on all but four of the perovskite samples, with an assumed growth rate of 0.06 nm per cycle. Of these four samples, two had been deposited with C_{60} and two were left bare. These samples were left untouched and returned to CSEM for fabrication into PSCs to determine if any damage had been caused by transportation. The PCE obtained from the final devices is displayed in Figure 7.23.

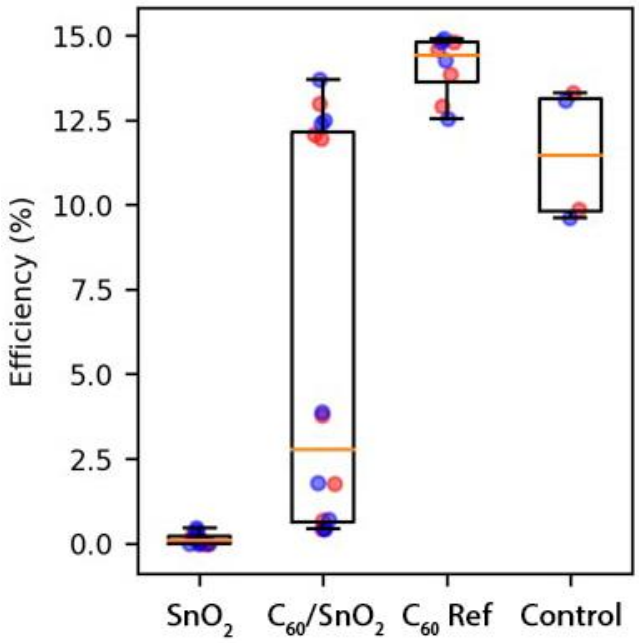

Figure 7. 23: *PCE of 1.04 cm^2 aperture area p-i-n devices incorporating 163 cycles of ALD SnO_2 deposited at 100°C compared to C_{60}*

The data points marked *C_{60} Ref* represent *p-i-n* cells from the same batch which were fabricated at CSEM but were not subjected to transport. The data points marked *control* represent those cells which were transported to Tyndall and returned untouched for electrode evaporation to assess any damage due to transport.

It is clear from this figure that ALD SnO_2 deposited directly on the perovskite absorber material does not perform well in a *p-i-n* device. Current for these cells was strongly supressed leading to the poor PCEs observed. A large R_{oc} was observed for the devices under illumination of one sun suggesting a poor interface between the SnO_2 and perovskite material. The ALD SnO_2 deposited on C_{60} produced more complicated results. While current reached over 20 mA/cm^2 for all of these devices and the V_{oc} obtained was suitably high, half of the cells exhibited poor FF and PCE while the other half achieved FF > 60 % and reached PCEs >13 %. The control devices exhibited a notable decrease in PCE compared to their reference counterparts which did not undergo transportation. The J-V curve for the best of each type of device in the sample set is displayed in Figure 7.24.

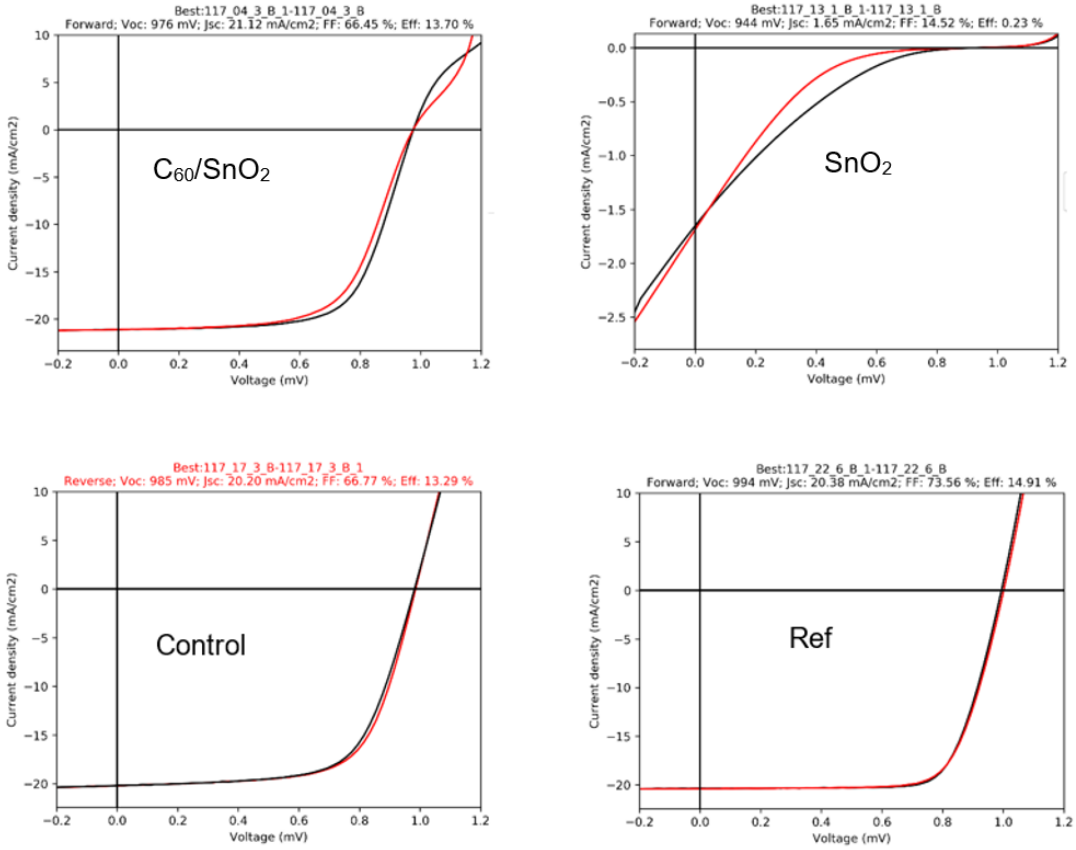

Figure 7. 24: *J-V curves for best performing p-i-n devices of each type fabricated*

To understand why the *p-i-n* devices incorporating the bilayer of C_{60}/ALD SnO_2 produced split results in terms of efficiency TEM was carried out at Tyndall National Institute on one of the cells which had performed well. From the image in Figure 7.25 all cell layers are clearly defined. Their thicknesses are listed in Table VII. X.

Table VII. X: *Thicknesses observed in each layer of a p-i-n device incorporating C_{60}/ALD SnO_2 through TEM imaging*

Material	ITO	NiO_x	$KCsFAMAPb(IBr)_3$	C_{60}	SnO_2	Ag
Thickness (nm)	210	12	327-290	20	20	128

The ALD SnO_2 layer was observed to be 20 nm in thickness, twice that anticipated in respect of the assumed growth rate. This measurement was confirmed through ellipsometry of ALD SnO_2 at 100°C on a n-Si(100) wafer which was grown along with the perovskite samples. This strongly suggests that the ALD growth was not limited at 100°C which calls into question the uniformity achieved across the substrate holder. The ALD window for SnO_2 using TDMASn and H_2O or H_2O_2 as respective

precursor and reactants is reported to be between 100°C and 200°C.[31-33] The growth rate has been reported to be higher at lower temperatures, increasing up to 2 Å per cycle by lowering the deposition temperature to 30°C. It was determined that as the conditions chosen were at the minimum of the self-limiting window, further studies should be carried out with increased deposition temperatures whilst ensuring that the perovskite underlayer is not thermally damaged.

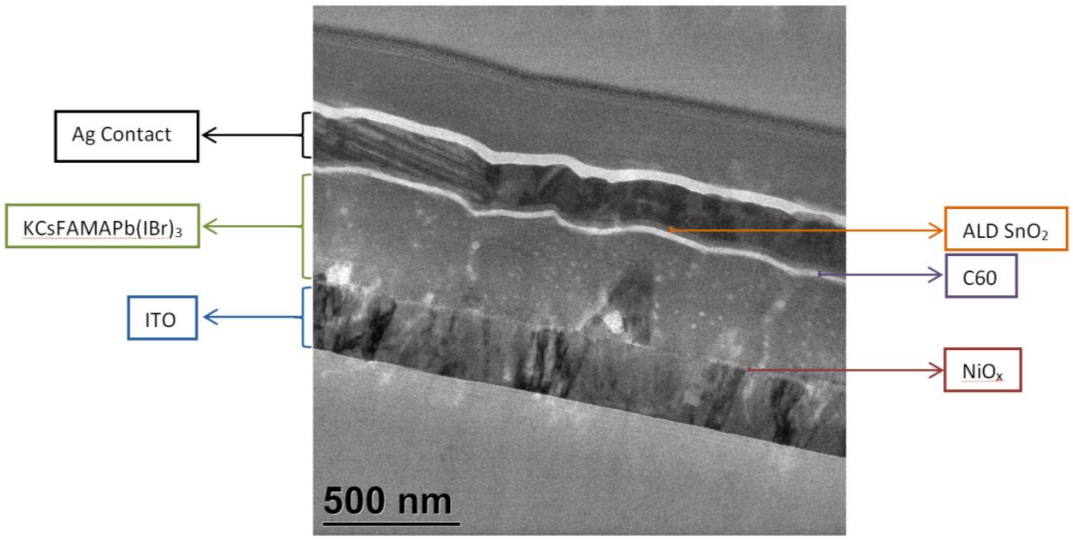

Figure 7. 25: *TEM image of complete p-i-n perovskite device incorporating C_{60}/ALD SnO_2*

Smaller scale TEM images of each of the device layers were captured to determine their respective thicknesses. In addition to the larger than expected SnO_2 layer, an interfacial layer could be observed between the thin sputtered NiO_x HTL and the perovskite material interface as shown in Figure 7.26. This suggests that the NiO_x diffused into the perovskite material. The inferior contact properties and high density defects at the NiO_x interface can reduce FF and J_{sc} in PSCs hampering the device performance.[34]

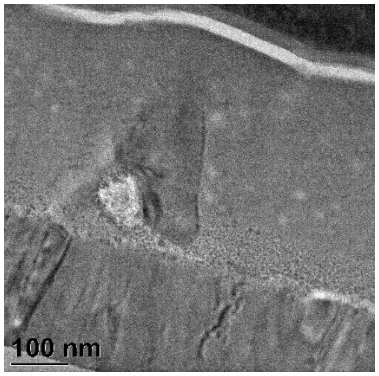

Figure 7. 26: *TEM image showing NiO_x / perovskite interface*

To examine the stability of the post ALD perovskites, a sample comprised of ITO (6-7 Ω/sq) coated glass/ sputtered NiO_x/ $KCsFAMAPb(IBr)_3$/ C_{60} buffer layer/ ALD SnO_2 without a Ag contact was measured using XRD. The sample was cleaved with one half left in air and ambient light for nine weeks while the other half remained in a N_2 environment within the glovebox. A 2θ scan was applied from 10° - 70°.

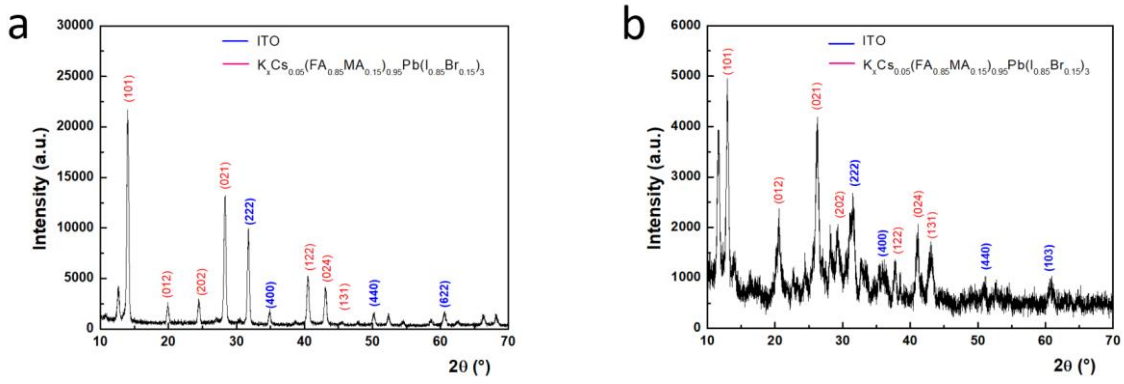

Figure 7. 27: *XRD measurements for ITO (6-7 Ω/sq) coated glass/ sputtered NiO_x/ $KCsFAMAPb(IBr)_3$/ C_{60} buffer layer/ ALD SnO_2 which was **(a)** kept in a N_2 environment and **(b)** kept unencapsulated in air*

XRD measurements show a clear difference in intensity in the $KCsFAMAPb(IBr)_3$ perovskite peaks for the sample kept in a N_2 environment compared to that left in air in Figure 7.27. The sample left in air had degraded substantially with an increase in the precursors PbI_2 and $PbBr_2$. Visually the sample that remained in air was bleached after nine weeks indicating that it had returned to its yellow non-perovskite form. A

third sample was also measured by XRD. This was the full cell capped with a Ag contact and had been kept in a N_2 environment in the glovebox (Table VII. XI).

Table VII. XI: *Sample ID for 2θ XRD and GIXRD measurements*

Sample Composition	*Sample ID*	*Environment*
ITO/ NiO_x/ KCsFAMAPb$(IBr)_3$/ C_{60}/ALD SnO_2	A1	Air
ITO/ NiO_x/ KCsFAMAPb$(IBr)_3$/ C_{60}/ALD SnO_2	A2	N_2
ITO/ NiO_x/ KCsFAMAPb$(IBr)_3$/ C_{60}/ALD SnO_2/Ag	B1	N_2

Figure 7.28 shows the perovskite peak at 14.3°, which corresponds to the (101) lattice plane, to have almost completely disappeared in sample A1. Meanwhile the peak at 12.6°, corresponding to the (001) diffraction of PbI_2, has increased in intensity. The overwhelmingly intense peak located at 38.1° for sample B1 corresponds to the diffraction of the (111) Ag lattice plane of face-centered (fcc) structure. This indicates that (111) planes of Ag were highly oriented parallel to the supporting substrate.

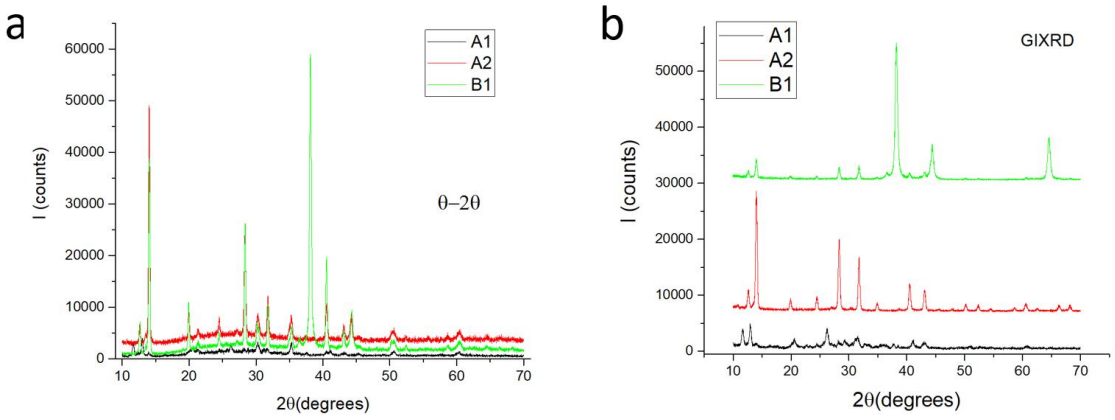

Figure 7. 28: *Graphs showing* ***(a)*** *2θ XRD and* ***(b)*** *GIXRD measurements of samples A1, A2, B1 from 10° - 70°*

GIXRD measurements were carried out for the determination of phase structure from lattice planes that are perpendicular to the sample surface. The presence of PbI_2 is observed in all samples at 12.6° with an increased intensity in samples A1 and A2 indicating degradation. The perovskite peak at 14.3° is shown to have very low intensity in sample B1. This result is not unexpected as the sample is capped with approximately 130 nm Ag.

7.3.5.5 p-i-n architecture PSCs, with and without C_{60} passivation

Subsequent to further depositions of ALD SnO_2 at 100°C on the perovskite absorber, multiple SnO_2 growths were carried out varying the deposition temperature as well as the TDMASn and H_2O purge lengths. While deposition at 100°C was found to be non-limiting, increasing the deposition temperature above that of the perovskite annealing temperature, 150°C for $CsFAPb(IBr)_3$, would likely cause degradation to the perovskite material. Increasing the purge length could aid in a more uniform growth by removing excess physisorbed precursor but would also increase the time the perovskite is exposed to ALD conditions.

Table VII. XII outlines the reaction conditions used in these SnO_2 deposition tests. A large n-Si(100) wafer was placed on the chuck for each growth. After the growths, the centre and 5 points along the perimeter of each sample were measured using ex-situ ellipsometry. These measurements were carried out to establish the thickness spread across each wafer. Employing a larger purge of 16 seconds not only reduced the thickness of the thin films but demonstrated a good spread across the wafers. At a deposition temperature of 140°C, the increased purge length produced a film thickness of 14.62 nm after 163 cycles, while the range across the wafer was between 14.54 nm and 15.05 nm. The long 16 second purge for the growth at 150°C similarly exhibited ~0.5 nm spread of thickness across the wafer, however prolonged purges at this temperature could further anneal and degrade the perovskite.

Table VII. XII: *Picosun ALD reaction conditions for growth of SnO_2 using TDMAT and H_2O*

Deposition temperature	*Purge length*	*No. of cycles*	*Thickness at centre of wafer*
100°C	6 seconds	163	21.53 nm
120°C	8 seconds	163	20.27 nm
130°C	8 seconds	163	19.02 nm
140°C	8 seconds	163	17.70 nm
140°C	16 seconds	163	14.62 nm
150°C	8 seconds	163	15.61 nm
150°C	16 seconds	163	14.41 nm
186°C	8 seconds	163	12.01 nm

A deposition at a temperature of 140°C which employed a 16 second purge time for both TDMASn and H_2O would require a total growth time of 1 hour and 37 minutes to complete 163 cycles. To reduce this time it was decided that a sufficiently long purge length of 12 seconds would be employed over 111 cycles to achieve 10 nm ALD SnO_2 at 140°C on top of subsequent perovskite materials. The total growth time for this recipe would be 52 minutes including the 5 minute temperature stabilisation time required in a hot wall reactor.

A set of perovskite samples was sent from EPFL to Tyndall National Institute to determine how well ALD SnO_2 would perform in a *p-i-n* architecture. Half of the sample set included evaporated C_{60} as a buffer layer on top of the perovskite absorber material, while the other half had a top layer of bare perovskite. The final device architecture was composed of ITO (6-7 Ω/sq) coated glass/ Spiro-OMeTAD/ $CsFAPb(IBr)_3$/ C_{60} buffer layer or bare/ 10 nm or 20 nm ALD SnO_2/IZO/Ag. 10 nm and 20 nm ALD SnO_2 was deposited on the films using the optimised ALD method with a fraction of the samples left untouched to assess any transport damage incurred by the samples. The J-V characteristics of these cells are displayed in Figure 7.29.

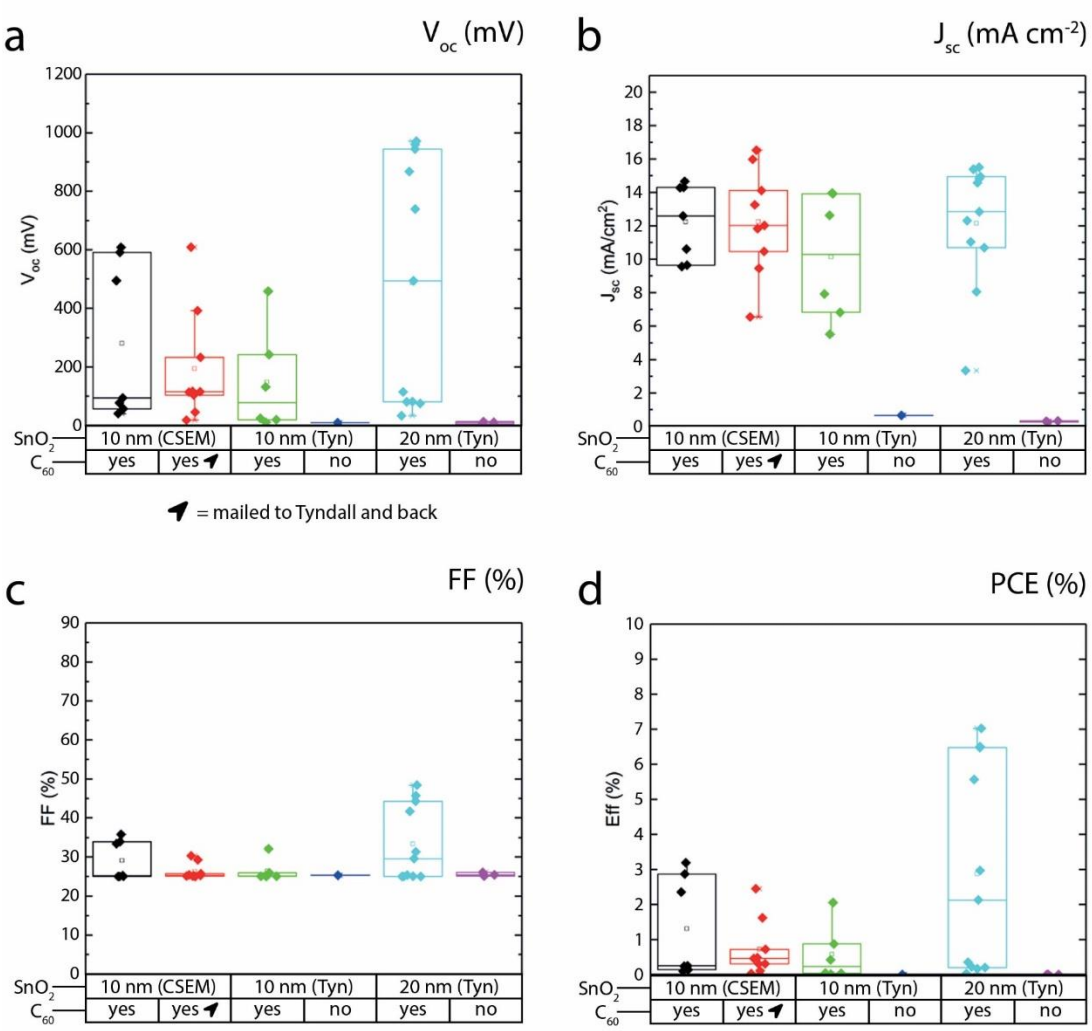

Figure 7. 29: *J–V characteristics of p-i-n PSCs on ITO coated glass containing ETLs of 10 nm and 20 nm thermal ALD SnO_2 with a Spiro-OMeTAD HTL*

An issue with the IZO/Ag deposition caused all cells to perform poorly in the J-V characteristics due to shorting. While cells containing SnO_2 deposited on C_{60} exhibited reasonable J_{sc}, low V_{oc} and FF lead to the poor PCEs obtained. 20 nm ALD SnO_2 deposited at 140°C on C_{60} was found to outperform the 10 nm ALD SnO_2 deposited at 140°C on C_{60} as well as the 10 nm ALD SnO_2 deposited at 100°C on C_{60} by CSEM, obtaining 7.5 % PCE in the best cell. It can again be observed that ALD SnO_2 does not perform well when deposited directly onto the perovskite material due to a probable interface issue.

This experiment was repeated on another two perovskite sample sets using the more stable NiO_x as a HTL. This time all *p-i-n* architectures contained C_{60} as a passivation

layer. The final cell structure was composed of ITO (6-7 Ω/sq) coated glass/ NiO_x/ $CsFAPb(IBr)_3$/ C_{60}/ 10 nm or 20 nm ALD SnO_2/IZO/Ag.

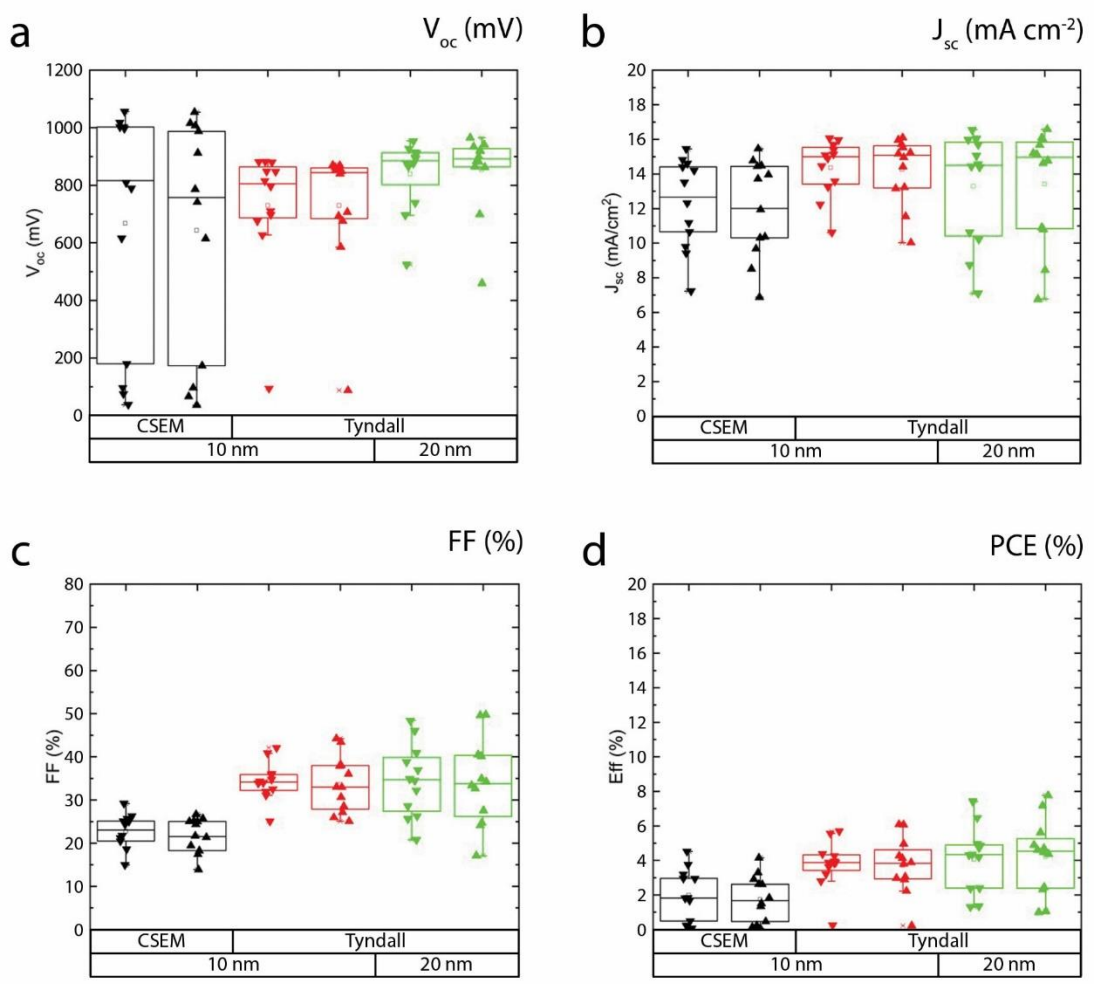

Figure 7. 29: *J–V characteristics of p-i-n PSCs on ITO coated glass containing ETLs of 10 nm and 20 nm thermal ALD SnO_2 with a NiO_x HTL*

The J-V characteristics of the cells displayed in Figure 7.30 again show low efficiencies achieved for all cells. For this study V_{oc} and J_{sc} were found to be reasonably high for all devices, but the low FF and shunt resistance caused a reduction in the PCEs obtained. Both 10 nm and 20 nm ALD SnO_2 deposited by Tyndall outperformed the ALD SnO_2 deposited by CSEM. It is not clear what caused the low shunt resistance in these devices but the deposition of the semi-transparent IZO/Ag contact may again be the origin of the issues.

7.4 Summary

In this chapter nominally undoped ALD SnO_2 was investigated to determine ideal ETL thickness and the efficacy of passivation in planar *n-i-p* PSCs. Also investigated was the deposition of low temperature ALD SnO_2 on top of the perovskite absorber material with and without passivation and its contribution to the performance of *p-i-n* devices. A summary of both *n-i-p* and *p-i-n* PSCs fabricated in this chapter are outlined below in Table VII.XIII and Table VII.XIV respectively.

Table VII. XIIII: *Outline of n-i-p architecture devices fabricated in this chapter*

Study No.	*TCO*	*ETL*	*Passivation*	*Perovskite*	*HTL*	*Electrode*
1	ITO	10 nm ALD SnO_2 185°C		$CsFAMAPbI_3$	Spiro-OMeTAD	Au
	ITO	10 nm ALD TiO_2 185°C		$CsFAMAPbI_3$	Spiro-OMeTAD	Au
	ITO	20 nm ALD SnO_2 185°C		$CsFAMAPbI_3$	Spiro-OMeTAD	Au
	ITO	20 nm ALD TiO_2 185°C		$CsFAMAPbI_3$	Spiro-OMeTAD	Au
	ITO	20 nm RF sputtered TiO_2 (CSEM)		$CsFAMAPbI_3$	Spiro-OMeTAD	Au
2	ITO	10 nm ALD SnO_2 300°C		$CsFAMAPb(IBr)_3$	Spiro-OMeTAD	Au
	ITO	10 nm ALD TiO_2 300°C		$CsFAMAPb(IBr)_3$	Spiro-OMeTAD	Au
	ITO	20 nm ALD SnO_2 300°C		$CsFAMAPb(IBr)_3$	Spiro-OMeTAD	Au
	ITO	20 nm ALD TiO_2 300°C		$CsFAMAPb(IBr)_3$	Spiro-OMeTAD	Au
3	FTO	2 nm ALD SnO_2 185°C	C_{60}	$MAPbI_3$	Spiro-OMeTAD	Ag
	FTO	5 nm ALD SnO_2 185°C	C_{60}	$MAPbI_3$	Spiro-OMeTAD	Ag
	FTO	10 nm ALD SnO_2 185°C	C_{60}	$MAPbI_3$	Spiro-OMeTAD	Ag
4	FTO	15 nm ALD SnO_2 185°C	PCBM	$CsFAPb(IBr)_3$	Spiro-OMeTAD	Ag
	FTO	20 nm ALD SnO_2 185°C	PCBM	$CsFAPb(IBr)_3$	Spiro-OMeTAD	Ag
	FTO	25 nm ALD SnO_2 185°C	PCBM	$CsFAPb(IBr)_3$	Spiro-OMeTAD	Ag
	FTO	30 nm ALD SnO_2 185°C	PCBM	$CsFAPb(IBr)_3$	Spiro-OMeTAD	Ag
	FTO	15-20 nm spin coated SnO_2	PCBM	$CsFAPb(IBr)_3$	Spiro-OMeTAD	Ag
5	FTO	15 nm ALD SnO_2 185°C	CBD SnO_2	$CsFAPb(IBr)_3$	Spiro-OMeTAD	Ag
	FTO	20 nm ALD SnO_2 185°C	CBD SnO_2	$CsFAPb(IBr)_3$	Spiro-OMeTAD	Ag
	FTO	25 nm ALD SnO_2 185°C	CBD SnO_2	$CsFAPb(IBr)_3$	Spiro-OMeTAD	Ag
	FTO	30 nm ALD SnO_2 185°C	CBD SnO_2	$CsFAPb(IBr)_3$	Spiro-OMeTAD	Ag
	FTO	15-20 nm spin coated SnO_2	CBD SnO_2	$CsFAPb(IBr)_3$	Spiro-OMeTAD	Ag

Table VII. XIV: *Outline of p-i-n architecture devices fabricated in this chapter*

Study No.	*TCO*	*HTL*	*Perovskite*	*Passivation*	*ETL*	*Electrode*
1	ITO	NiO_x	$KCsFAMAPb(IBr)_3$	C_{60}	20 nm ALD SnO_2 100°C	Ag
	ITO	NiO_x	$KCsFAMAPb(IBr)_3$		20 nm ALD SnO_2 100°C	Ag
2	ITO	Spiro-OMeTAD	$CsFAPb(IBr)_3$	C_{60}	10 nm ALD SnO_2 140°C	IZO/Ag
	ITO	Spiro-OMeTAD	$CsFAPb(IBr)_3$		10 nm ALD SnO_2 140°C	IZO/Ag
	ITO	Spiro-OMeTAD	$CsFAPb(IBr)_3$	C_{60}	20 nm ALD SnO_2 140°C	IZO/Ag
	ITO	Spiro-OMeTAD	$CsFAPb(IBr)_3$		20 nm ALD SnO_2 140°C	IZO/Ag
	ITO	Spiro-OMeTAD	$CsFAPb(IBr)_3$	C_{60}	10 nm ALD SnO_2 100°C (CSEM)	IZO/Ag
3	ITO	NiO_x	$CsFAPb(IBr)_3$	C_{60}	10 nm ALD SnO_2 140°C	IZO/Ag
	ITO	NiO_x	$CsFAPb(IBr)_3$	C_{60}	20 nm ALD SnO_2 140°C	IZO/Ag
	ITO	NiO_x	$CsFAPb(IBr)_3$	C_{60}	10 nm ALD SnO_2 100°C (CSEM)	IZO/Ag

Deposition of SnO_2 thin film ETLs was carried out on a Picosun R200 ALD system. TDMASn was employed as the Sn precursor, while H_2O or O_2 plasma was used as the co-reactant. The effects of implementing a 5 minute O_2 plasma clean immediately prior to deposition were also examined. Initially, films were deposited at 185°C to meet the thermal restrictions of perovskite/silicon heterojunction tandem cells. 20 nm ALD SnO_2 deposited thermally, 20 nm ALD SnO_2 deposited thermally with a pre-treatment of 5 minutes O_2 plasma, and 20 nm ALD SnO_2 deposited using PEALD on FTO coated glass were examined in terms of morphology, hydrophilicity and electrical properties. 20 nm ALD SnO_2 deposited thermally with a pre-treatment of 5 minutes O_2 plasma was chosen to be incorporated into *n-i-p* planar PSCs.

Once fabricated, these devices were compared to *n-i-p* cells incorporating ALD TiO_2 as an ETL. Due to an issue with the synthesis or deposition of the perovskite material or HTL it was unclear whether ALD SnO_2 outperformed ALD TiO_2 when incorporated into devices, or if, similarly to ALD TiO_2, it required passivation. Deposition of 10 nm and 20 nm ALD SnO_2 was carried out at 300°C in an effort to improve interfacial contact between the metal oxide and the perovskite absorber material. These films were fabricated into planar PSCs and their J-V characteristics were compared to devices containing 10 nm and 20 nm ALD TiO_2 deposited at 300°C. While SnO_2 exhibited a marginally improved performance compared to TiO_2, current was significantly reduced in all cells. Low illumination R_{sc} values indicated that the ETLs

were not causing shunting but that electron injection was hindered, suggesting a need for passivation.

2 nm, 5 nm, and 10 nm thermal ALD SnO_2 thin films which were treated with O_2 plasma prior to deposition at 185°C were grown on TEC-7 FTO coated glass and fabricated into planar devices utilising the acetonitrile/methylamine perovskite method. These cells included evaporated C_{60} as a passivation layer between the ALD SnO_2 and the perovskite material. While all ALD ETL thicknesses produced efficient cells, 10 nm SnO_2 provided the highest PCEs of 18.3 % on a 0.09 cm^2 active area and 15.9 % on a 0.7 cm^2 active area. This demonstrated the importance of interfacial modification between the ETL and perovskite.

A thickness series of 15 nm, 20 nm, 25 nm and 30 nm thermal (185°C) ALD SnO_2 on O_2 plasma cleaned substrates was used in planar PSCs in conjunction with PCBM or CBD SnO_2 passivation layers. These devices were then compared to cells fabricated in parallel incorporating spin coated SnO_2 with the same passivation layers. The reference cell containing a spin coated SnO_2 ETL and a spin coated PCBM passivation layer exhibited severe hysteresis between the reverse and forward scans when measured immediately after fabrication. Steady state max power tracking over 60 seconds lead to a stabilised PCE of 10.85 % in the best pixel. The same champion pixel re-measured three days later exhibited an improved stabilised PCE of 13.65 %. This enhancement was likely caused by oxidation of the Spiro-OMeTAD HTL. 20 nm ALD SnO_2 was used as an ETL and fabricated into planar devices which incorporated PCBM as a passivation layer. The best cell achieved a stabilised PCE of 10.42 % over 60 seconds when measured on day one. This stabilised efficiency was comparable to that produced by the reference cell incorporating the spin coated SnO_2 on day one of measuring.

CBD SnO_2 was then employed as a passivation layer on reference spin coated SnO_2 and ALD SnO_2. From the ALD thickness series, 20 nm ALD SnO_2 was found to be the optimal thickness, producing enhanced efficiencies in planar devices. Reduced hysteresis and an enhanced V_{oc} and FF were observed for both sets of devices using CBD compared to their PCBM counterparts. The reference cell reached an impressive 18.36 % PCE in the reverse scan and 14.52 % PCE in the forward scan, stabilising at 17.82 % over 60 seconds of steady state MPP tracking. The cell containing 20 nm

ALD SnO_2 as an ETL produced 15.24 % PCE in the reverse scan and 11.15 % PCE in the forward scan, with MPP tracking stabilising at 14.79 % PCE over 60 seconds. The device incorporating the optimal thickness of ALD SnO_2 as an ETL did not measure efficiencies as high as the reference cells due to a lower FF. While the recipe for the spin coated SnO_2 with CBD SnO_2 reference cells has been well optimised at the University of Oxford, the ALD SnO_2 with CBD SnO_2 counterparts may prove to be a viable alternative after further optimisation.

Finally, in this chapter the concept of *p-i-n* architecture PSCs, in which ALD SnO_2 was deposited directly onto the sensitive perovskite absorber, was investigated. 163 cycles of low temperature (100°C) thermal SnO_2 was first deposited on a batch of samples which incorporated the quadruple cation $KCsFAMAPb(IBr)_3$ as the perovskite absorber material with sputtered NiO_x as the HTL underneath, deposited on ITO coated glass. Half of the sample set included evaporated C_{60} as a buffer layer on top of the perovskite absorber material, while the other half had a top layer of bare perovskite. After ALD SnO_2 deposition, the devices were completed with an evaporated gold contact before their J-V characteristics were measured and analysed. From this study it was observed that devices containing low temperature ALD SnO_2 deposited directly on top of the perovskite material without passivation did not perform well due to suppressed current.

The results obtained from devices containing ALD SnO_2/C_{60} on top of the perovskite layer were more difficult to interpret. While high V_{oc} was observed in all of these cells, half of the cells exhibited poor FF and PCE while the other half achieved FF > 60 % and reached PCEs >13 %. In an effort to understand the split efficiencies, TEM characterisation was carried out on one of the devices which performed well. From this it was established that the 163 cycles of SnO_2 deposited by ALD at 100°C measured a thickness of 20 nm instead of the expected 10 nm. This measurement was confirmed through ellipsometry of a thin film on a n-Si(100) substrate indicating that this thickness variation was not due to complex chemistry at the perovskite interface. This suggested that the ALD growth was not limited at 100°C and that further studies needed to be carried out with increased deposition temperatures to control thickness uniformity whilst ensuring that the perovskite underlayer was not damaged. From this study a uniform thickness of 10 nm SnO_2 was obtained using 111 ALD cycles at a 140°C deposition temperature and an optimised purge duration.

10nm and 20 nm thermal ALD SnO_2 were deposited on a batch of samples which incorporated $CsFAPb(IBr)_3$ as the perovskite absorber material with spin coated Spiro-OMeTAD as the HTL underneath, deposited on ITO coated glass. Again, half of the sample set included evaporated C_{60} as a buffer layer on top of the perovskite absorber material, while the other half had a top layer of bare perovskite. The final device architecture was composed of ITO (6-7 Ω/sq) coated glass/ Spiro-OMeTAD/ $CsFAPb(IBr)_3$/ C_{60} buffer layer or bare/ 10 nm or 20 nm ALD SnO_2/IZO/Ag. These devices were compared to cells made in parallel using ALD SnO_2 deposited at CSEM on C_{60}. An issue with the IZO/Ag deposition caused all cells to perform poorly in the J-V characteristics due to shorting. Of these, 20 nm ALD SnO_2 deposited by the author at Tyndall National Institute on top of C_{60} produced the highest efficiency with the best PCE at 7.5 %. It was again observed that ALD SnO_2 deposited directly on top of the perovskite material without a passivation layer did not perform well when fabricated into a PSC.

This experiment was repeated replacing the spin coated Spiro-OMeTAD HTL with sputtered NiO_x. All samples from this set were passivated with a C_{60} interlayer. Again 10nm and 20 nm thermal ALD SnO_2 were deposited at 140°C on top of the C_{60} layer, on top of the $CsFAPb(IBr)_3$ perovskite absorber. These were then fabricated into devices which were compared to cells containing 10 nm SnO_2 deposited at CSEM on top of C_{60}. For this study V_{oc} and J_{sc} were found to be reasonably high for all devices, but low FF and shunt resistance caused a reduction in the PCE obtained in all cells. Devices containing 10 nm and 20 nm ALD SnO_2 deposited at Tyndall National Institute were found to outperform ALD grown devices made in parallel at CSEM. The deposition of the IZO/Ag contact may again have caused the low shunt resistance and poor performance of these devices. From these preliminary studies it is clear that ALD SnO_2 can be deposited at low temperatures on top of the perovskite material without damage. These *p-i-n* devices exhibit promising performance which should be improved when a suitable passivation layer is incorporated.

7.5 Bibliography

[1] J. H. Heo, S. H. Im, J. H. Noh, T. N. Mandal, C.-S. Lim, J. A. Chang, Y. H. Lee, H.-J. Kim, A. Sarkar, M. K. Nazeeruddin, M. Grätzel, S. I. Seok, Efficient inorganic–organic hybrid heterojunction solar cells containing perovskite compound and polymeric hole conductors, Nature Photonics, 7, 6, 486–491, 2013

[2] E. Edri, S. Kirmayer, A. Henning, S. Mukhopadhyay, K. Gartsman, Y. Rosenwaks, G. Hodes, D. Cahen, Why Lead Methylammonium Tri-Iodide Perovskite-Based Solar Cells Require a Mesoporous Electron Transporting Scaffold (but Not Necessarily a Hole Conductor), Nano Lett., 14, 1000, 2014

[3] Y. Lee, J. Luo, M.-K. Son, P. Gao, K. T. Cho, J. Seo, S. M. Zakeeruddin, M. Grätzel, M. K. Nazeeruddin, Enhanced Charge Collection with Passivation Layers in Perovskite Solar Cells, Adv. Mater., 28, 3966, 2016

[4] J.-P. Correa Baena, L. Steier, W. Tress, M. Saliba, S. Neutzner,T. Matsui, F. Giordano, T. J. Jacobsson, A. R. S. Kandada, S. M. Zakeeruddin, A. Petrozza, A. Abate, M. K. Nazeeruddin, M. Grätzel, A. Hagfeldt, Highly efficient planar perovskite solar cells through band alignment engineering, Energy Environ. Sci., 8, 2928, 2015

[5] A. F. Khan, M. Mehmood, M. Aslam, M. Ashraf, Characteristics of electron beam evaporated nanocrystalline SnO_2 thin films annealed in air, Applied Surface Science, 256, 2252–2258, 2010

[6] B. Roose, J.-P. Correa Baena, K. C. Gödel, M. Grätzel, A. Hagfeldt, U Steiner, A. Abate, Mesoporous SnO_2 electron selective contact enables UV-stable perovskite solar cells, Nano Energy, 30, 517-522, 2016

[7] J. Song, E. Zheng, J. Bian, X.-F. Wang, W. Tian, Y. Sanehira, T. Miyasaka, Low-temperature SnO_2-based electron selective contact for efficient and stable perovskite solar cells, J. Mater. Chem. A, 3, 10837, 2015

[8] X. Qin, Z. Zhao, Y. Wang, J. Wu, Q. Jiang, J. You, Recent progress in stability of perovskite solar cells, J. Semicond., 38, 011002, 2017

[9] J.W. Elam, D.A. Baker, A.J. Hryn, A.B.F. Martinson, M.J. Pellin, J.T. Hupp, Atomic layer deposition of tin oxide films using tetrakis(dimethylamino) tin, J. Vac. Sci. Technol. A, 26, 244–252, 2008

[10] R. W. Johnson, A. Hultqvist, S. F. Bent, A brief review of atomic layer deposition: from fundamentals to applications, Materials Today, 17, 5, 236-246, 2014

[11] G. T. Lim, D.-H. Kim, Characteristics of TiO_x films prepared by chemical vapor deposition using tetrakis-dimethyl-amido-titanium and water, Thin Solid Films, 498, 254−258, 2006

[12] Q. Xie, J. Musschoot, D. Deduytsche, R. L. V. Meirhaeghe, C Detavernier, S. V. den Berghe, Y. Jiang, G. Ru, B. Li, X. J. Qu, Growth Kinetics and Crystallization Behavior of TiO_2 Films Prepared by Plasma Enhanced Atomic Layer Deposition Electrochem. Soc., 155, H688−H692, 2008

[13] M. Reiners, K. Xu, N. Aslam, A. Devi, R. Waser, S. Hoffmann-Eifert, Growth and Crystallization of TiO_2 Thin Films by Atomic Layer Deposition Using a Novel Amido Guanidinate Titanium Source and Tetrakis-dimethylamido-titanium, Chem. Mater., 25, 15, 2934-2943, 2013

[14] N. K. Noel, S. N. Habisreutinger, B. Wenger, M. T. Klug, M. T. Hörantner, M. B. Johnston, R. J. Nicholas, D. T. Moore, H. J. Snaith, A low viscosity, low boiling point, clean solvent system for the rapid crystallisation of highly specular perovskite films, Energy Environ. Sci., 10, 145-152, 2017

[15] E. H. Anaraki, A. Kermanpur, L. Steier, K. Domanski, T. Matsui, W. Tress, M. Saliba, A. Abate, M. Grätzel, A. Hagfeldt, J.-P. Correa-Baena, Highly efficient and stable planar perovskite solar cells by solution-processed tin oxide, Energy Environ. Sci., 9, 3128-3134, 2016

[16] T. Bu, X. Liu, Y. Zhou, J. Yi, X. Huang, L. Luo, J. Xiao, Z. Ku, Y. Peng, F. Huang, Y.-B. Cheng, J Zhong, Novel quadruple-cation absorber for universal hysteresis elimination for high efficiency and stable perovskite solar cells, Energy Environ. Sci., 10, 2509-2515, 2017

[17] N. Giesbrecht, J. Schlipf, L. Oesinghaus, A. Binek, T. Bein, P. Müller-Buschbaum, P Docampo, Synthesis of Perfectly Oriented and Micrometer-Sized $MAPbBr_3$ Perovskite Crystals for Thin-Film Photovoltaic Applications, ACS Energy Lett., 1, 1, 150–154, 2016

[18] M. Dou, C. Persson, Comparative study of rutile and anatase SnO_2 and TiO_2: Band-edge structures, dielectric functions, and polaron effects, J. Appl. Phys., 113, 083703, 2013

[19] G. Mirabelli, M. Schmidt, B. Sheehan, K. Cherkaoui, S. Monaghan, I. Povey, M. McCarthy, A. P Bell, R. Nagle, F. Crupi, P. K. Hurley, R. Duffy, Back-gated Nb-doped MoS_2 junctionless field-effect-transistors, AIP Advances, 6, 2 , 025323, 2016

[20] Standard Test Methods for Measuring Resistivity and Hall Coefficient and Determining Hall Mobility in Single-Crystal Semiconductors, ASTM Designation F76, Annual Book of ASTM Standards, Vol. 10.05 (2000)

[21] J. M. Coronado, F. Fresno, M. D. Hernández-Alonso, R. Portela, Design of Advanced Photocatalytic Materials for Energy and Environmental Applications, Springer, ISBN: 978-1-4471-5060-2, 2013

[22] A. A. Haidry, L. Sun, B. Saruhan, A. Plecenik, T. Plecenik, H. Shen, Z. Yao, Cost-effective fabrication of polycrystalline TiO_2 with tunable n/p response for selective hydrogen monitoring, Sensors and Actuators B: Chemical, 274, 10-21, 2018

[23] https://xpssimplified.com/elements/tin.php (accessed 20th November 2018)

[24] E. von Hauff, V, Dyakonov, J. Parisi, Study of field effect mobility in PCBM films and P3HT:PCBM blends, Sol. Energy Mater. Sol. Cells, 87, 149–156, 2005

[25] I. S. Kim, D. H. Cao, D. B. Buchholz, J. D. Emery, O. K. Farha, J. T. Hupp, M. G. Kanatzidis, A. B. F. Martinson, Liquid Water and Heat-Resistant Hybrid Perovskite Photovoltaics via an Inverted ALD Oxide Electron Extraction Layer Design, Nano Lett., 16, 12, 7786–7790, 2016

[26] S. Wang, W. Yuan, Y. S. Meng, Spectrum-Dependent Spiro-OMeTAD Oxidization Mechanism in Perovskite Solar Cells, ACS Appl. Mater. Interfaces, 7, 44, 24791-24798, 2015

[27] X. Wanga, H. Sarvari, H. Dang, Z. Chena, V. Singh, Evolution characteristics of perovskite solar cells in air and vacuum environments, Optik, 150, 111-116, 2017

[28] P. Jackson, D. Hariskos, R. Wuerz, O. Kiowski, A. Bauer, T. M. Friedlmeier, M. Powalla, Properties of $Cu(In,Ga)Se_2$ Solar Cells with New Record Efficiencies up to 21.7%, Phys. status solidi - Rapid Res. Lett., 9, 1, 28–31, 2015

[29] D. Shin, S. Kim, J. Kim, Study of Band Structure at the Zn(S,O,OH)/Cu(In,Ga)Se_2 Interface via Rapid Thermal Annealing and Their Effect on the Photovoltaic Properties, ACS Appl. Mater. Interfaces, 5, 12921–12927, 2013

[30] J. Barbe, M. L. Tietze, M. Neophytou, B. Murali, E. Alarousu, A. El Labban, M. Abulikemu, W. Yue, O. F. Mohammed, I. McCulloch, A. Amassian, S. del Gobbo, Amorphous Tin Oxide as a Low-Temperature-Processed Electron-Transport Layer for Organic and Hybrid Perovskite Solar Cells, ACS Appl. Mater. Interfaces, 9, 13, 11828-11836, 2017

[31] D.-W. Choi, W.J. Maeng, J.-S. Park, The conducting tin oxide thin films deposited via atomic layer deposition using Tetrakis-dimethylamino tin and peroxide for transparent flexible electronics Appl. Surf. Sci., 313, 585, 2014

[32] M.N. Mullings, C. Hagglund, S.F. Bent, Tin oxide atomic layer deposition from tetrakis(dimethylamino)tin and water, J. Vac. Sci. Technol. A, 31, 061503, 2013

[33] J. T. Tanskanen, S. F. Bent, Insights into the Surface Chemistry of Tin Oxide Atomic Layer Deposition from Quantum Chemical Calculations, J. Phys. Chem. C, 117, 19056−19062, 2013

[34] J. Zhang, H. Luo, W. Xie, X. Lin, X. Hou, J. Zhou, S. Huang, W. Ou-Yang, Z. Sun, X. Chen, Efficient and Ultraviolet Durable Planar Perovskite Solar Cells via Ferrocenecarboxylic Acid Modified Nickel Oxide Hole Transport Layer, Nanoscale,10, 5617-5625, 2018

CHAPTER 8:

Conclusions and Suggestions for Future Work

8.1 Conclusions

The initial work presented in this thesis compared the thermal ALD growth of TiO_2 to alternative methods of TiO_2 deposition for fabrication into mesoporous PSCs. Thicknesses of 10 nm, 20 nm and 30 nm nominally undoped TiO_2 were deposited at 200°C by ALD on APCVD FTO coated glass substrates. Of these thicknesses, mesoporous devices containing both 10 nm and 20 nm ALD TiO_2 were found to outperform devices containing 10-15 nm spin coated TiO_2. The 30 nm ALD thin film proved to be too thick, reducing R_{sc} and obtaining just 6.16 % PCE in the final device. The optimal ALD thickness was found to be 20 nm, which reached 10.37 % PCE. Thin films of this thickness were then deposited on a smoother and thinner APCVD FTO coated glass substrate as well as a reference commercial FTO coated glass substrate (TCO2215 Solaronix). These samples were fabricated into mesoporous PSCs using an improved perovskite deposition method in order to compare blocking layers deposited by ALD and spin coating. Again, ALD was found to outperform spin coating with final devices obtaining 15.18 % PCE on the reference FTO and 15.40 % PCE on the APCVD FTO when cells were measured three days post fabrication. The increased film density and conformal coverage achieved by the ALD technique enabled enhanced performance in mesoporous devices compared to spin coated ETLs.

Following this work, 20 nm ALD TiO_2 was compared to 20 nm RF sputtered TiO_{2-x} as blocking layers in mesoporous devices. The sputtered process was optimised by introducing 7.5 x 10^{-6} mbar of O_2 to the deposition. Reference FTO coated glass and an improved APCVD FTO coated glass were employed as substrates. The device containing a sputtered TiO_2 blocking layer on APCVD FTO coated glass obtained an impressive 16.66 % PCE. This efficiency was slightly higher than the 16.45 % PCE reached by ALD TiO_2 on the same APCVD FTO coated glass. From these results it

was clear that both RF sputtering and ALD were suitable deposition techniques to achieve conformal ETLs in mesoporous perovskite cells. Therefore, it was concluded that films deposited via ALD were comparable to those deposited by sputtering.

The second aim of this research was the optimisation of ALD TiO_2 to improve the overall cell efficiency of mesoporous PSCs. This involved the deposition of nominally undoped and nanolaminate doped TiO_2 thin films. The deposition temperature of all films was further reduced from 200°C to 185°C. This reduction was made in consideration of the later integration of ALD layers into perovskite/silicon heterojunction tandem cells. The growth of ALD TiO_2 was carried out on two commercial reactors, a Cambridge Nanotech Fiji F200 and a Picosun R200 system, to determine if a difference in film quality could be observed or if growths would be reproducible across both systems. Two titanium precursors, TTIP and TDMAT, were investigated along with reactants of either H_2O or Ar/O_2 plasma. Moreover, a 5 minute O_2 plasma treatment in situ within the ALD chamber was examined prior to growth. The influence of doping was explored using various dopants in a 19:1 and 99:1 TiO_2:dopant pulse ratio. These growth studies were carried out to ultimately determine if a difference in electrical properties could be observed depending on titanium precursor, reactant, dopant and ratio of applied dopant. From this work, a selection of ALD thin films were chosen to be fabricated into mesoporous cells and their resulting J-V performances analysed.

Arrhenius plots of surface conductivity using Sigma Dark characterisation demonstrated semi-conducting behaviour for all undoped and doped ALD thin films, and increased conductivity corresponding to increased temperature. The bulk conductivity of thin films was observed to be both precursor and reactant dependent. TDMAT was observed to be the superior titanium precursor over TTIP, whilst H_2O was deemed to be the reactant of choice. TDMAT's higher growth rate of 0.5 Å per cycle provided improved coverage resulting in increased conductivity. Employing a 5 minute O_2 plasma treatment directly prior to ALD growth also improved the overall conductivity of thin films by providing an increased number of nucleation sites for the titanium precursor through a higher density of surface OH species. Nanolaminate doped thin films treated with 5 minutes of O_2 plasma prior to deposition using TDMAT and H_2O and doped with Ag in a 99:1 ratio demonstrated marginally better conductivity than undoped thermal TiO_2 treated with 5 minutes of O_2 plasma prior to growth. Despite this improvement, no Ag was detected through XPS of a 19:1 doped

thin film. As the silver incorporation could not be conclusively verified it was decided not to investigate this film further.

It was noted that a clear difference in conductivity could be observed between films deposited under the same nominal reactor conditions in the two differing commercial ALD reactors. This observation is not totally surprising as ALD is a complex chemical process where ideal behaviour is rarely observed, underlying the need for caution when comparing data from differing laboratories.

Three nominally undoped and three nanolaminate doped 20 nm TiO_2 thin films were selected to be fabricated into mesoporous PSCs. 20 nm RF sputtered TiO_{2-x} was selected as a reference ETL. All ETLs were incorporated into perovskite devices in parallel to avoid any variation in the remaining layers. In this way performance differences from ETLs could be directly compared. Of the undoped ALD TiO_2 sample set, the amorphous deposition of TiO_2 using TDMAT and H_2O preceded by an O_2 plasma treatment exhibited a high PCE of 15.3 % on a 1.04 cm^2 active area, which stabilised at 14.3 % PCE after 300 seconds of steady state MPP tracking. This result corresponded to the improved conductivity observed on the same ETL via Sigma Dark characterisation. Of the cells incorporating nanolaminate doped ETLs, both TiO_2 doped with Hf and TiO_2 doped with Al in 19:1 ratios performed well reaching 15.5 % PCE and 15.4 % PCE respectively. Despite these performances being higher than those obtained by undoped TiO_2, the PCEs dropped after 300 seconds of MPP tracking to 13.3 % and 14.0 % PCE_{MPP}. Initially the high PCE obtained using TiO_2:Hf as an ETL was unexpected as this thin film had proven to be the most resistive according to Sigma Dark characterisation. The swift decline to 13.3 % after just 300 seconds of tracking corroborated the high resistivity of this film. The reference device incorporating sputtered TiO_{2-x} reached 16.19 % PCE and stabilised at 15.0 % PCE_{MPP} after 300 seconds. While ALD TiO_2 was comparable to RF sputtered TiO_2, device performance was not significantly improved by altering the ALD deposition process.

Despite the possibility of creating thinner blocking layers by ALD, a thickness of 20 nm ALD TiO_2 was maintained to allow direct comparison to 20 nm RF sputtered TiO_{2-x}. Furthermore, it was believed that thinner amorphous ALD films would not withstand the high temperature anneal (500°C) employed in the mesoporous perovskite device fabrication process without cracking and hence forming shunt pathways. In response

to this shortcoming, planar PSCs were fabricated incorporating ALD TiO_2 as the ETL in a series of thicknesses of between 5 and 25 nm. This undoped ETL was chosen due to its superior performance in mesoporous cells. Advancement to a planar architecture would allow the entire cell, excluding the commercial FTO coated glass, to be processed through low temperature means. This cell could then be monolithically integrated as the top component of a tandem configuration without damage to the bottom cell.

Electrical conductivity measurements on ALD TiO_2 thin films displayed that the sintering temperature of 500°C for mesoporous device fabrication increased the resistivity of the ALD layer by several orders of magnitude. It was believed that through its synthesis into planar devices ALD TiO_2 would be able to maintain its conductivity and contribute to a higher overall PCE. In practice however, the planar device behaved much less effectively than the mesoporous cell employing the same ETL of 20 nm TiO_2. A max PCE of 8 % was achieved with significantly lower J_{sc} and FF values than those observed in the mesoporous device. This reduced PCE was observed for all ALD thicknesses from 5 to 25 nm. Although annealing the mesoporous cells at 500 °C increased the resistivity of the ALD TiO_2 films, it was determined by examination of the XPS of the Ti 2p signatures that the stoichiometry was improved by the anneal. As deposited TiO_2 grown at 185 °C was found, in addition to being non-stoichiometric, to contain measurable quantities of N and C from unreacted precursors. The highly defective nature of the as grown material may have given rise to significant charge trapping in both the bulk and the interface which may have been improved by annealing. Separately, the reference planar cells incorporating 20 nm sputtered TiO_{2-x} as the ETL exhibited impressive PCEs, with the highest obtaining 16.96 % and stabilising at 16.05 % after 800 seconds of steady state MPP tracking. These cells exceeded the performances obtained using the same ETL in mesoporous devices. The improved performance had not been observed in cells using the same stack structure on ITO coated glass. It was likely that the rough FTO surface allowed more surface area for the subsequent layers, resulting in the high PCEs obtained.

In an attempt to improve the performance of planar cells using ALD TiO_2 as the ETL, interface passivation between the ETL and the perovskite was explored via ALD. As well as this, RTA of the ALD TiO_2 layer was investigated in an attempt to improve

the quality of the ETL. The 20 nm ALD TiO_2 ETL which underwent RTA treatment to 500°C in O_2 was fabricated into a planar device. Its J-V characteristics were analysed and compared to those of cells incorporating 20 nm ALD TiO_2 which had not undergone any treatment. In the J-V curves, the absence of an s-shape was observed for the ALD TiO_2 sample which had undergone RTA. This s-shape had been present in all standard ALD J-V curves obtained previously. Despite this, current was suppressed with a low J_{sc} exhibited in the RTA treated cell. The PCE obtained was lower than that of cells incorporating untreated ALD TiO_2. For interface passivation, seven cycles of Al_2O_3 was first deposited on a 20 nm ALD TiO_2 ETL. Its successful nucleation was confirmed through TEM imaging and XPS characterisation. Once fabricated into a planar device, J-V characteristics suggested that the thin Al_2O_3 had completely blocked charge extraction due to the significantly reduced J_{sc} and FF. This experiment was repeated with 1 cycle of Al_2O_3 employed as a capping layer. Examination of J-V characteristics of the resulting perovskite device revealed an issue with the perovskite absorber material or the Spiro-OMeTAD HTL which caused all cells to perform less efficiently than expected. Nonetheless, it was apparent that even 1 cycle of ALD Al_2O_3 deposition inhibited electron extraction producing poor PCEs. Due to the resistive nature of Al_2O_3, ALD passivation using ZnO was investigated. Three cycles were deposited on 20 nm ALD TiO_2 at 130°C which was then incorporated into a planar device. An increase in current due to this method of passivation was observed in the J-V characteristics of the resulting cell. Although the enhancement in J_{sc} was not enough to significantly improve PCE, it does warrant further study to aid in cleaning the ETL/perovskite interface.

A study of how ALD TiO_2 behaved when deposited on top of a perovskite absorber material was conducted to establish if ALD could be utilised in the deposition of ETLs for *p-i-n* architecture devices. ALD deposition at 100°C was successfully achieved on both $MAPbI_3$ and $MAPbI_{3-x}Cl_x$ absorbers. XRD analysis along with TEM imaging after ALD growth indicated that the perovskite material was not noticeably degraded or modified. This work showed promise for incorporation into a reverse *p-i-n* architecture without damage to the perovskite underneath.

Another aim of this work was to investigate ALD SnO_2 as an alternative to ALD TiO_2 for use in planar *n-i-p* and *p-i-n* perovskite architectures. The morphology of ALD SnO_2 was found to be comparable to that of ALD TiO_2 with both metal oxides being

amorphous as grown. Using 1 µl of water, a contact angle of 121.9 ° demonstrated the poor wetting of SnO_2 in comparison to TiO_2, which was measured at an angle of 76.1 °. This super hydrophilic surface indicated that an O_3 or O_2 plasma treatment prior to deposition of the perovskite was required for ALD SnO_2 to be fabricated into *n-i-p* planar solar cells. Contact angle measurements performed after 15 minutes of O_2 plasma treatment demonstrated a reduction from 121.9 ° to 3.8 °, indicating a super hydrophilic surface. ALD SnO_2 displayed improved optical transmittance and electrical properties when compared to its ALD TiO_2 counterpart. Informed by the results of a selection of deposition processes, TDMASn and H_2O were selected as the respective precursor and reactant. As with ALD TiO_2, a 5 minute O_2 plasma clean prior to ALD deposition was found to increase conductivity in the ALD SnO_2 thin film.

10 nm and 20 nm ALD SnO_2 was deposited on ITO coated glass substrates and fabricated into planar devices. These were directly compared to cells containing 10 nm and 20 nm ALD TiO_2 deposited on ITO coated glass and 20 nm sputtered TiO_{2-x} deposited on ITO coated glass. All of these ETLs had been synthesised into devices in parallel to allow direct comparison between them. Due to an issue with the deposition of the perovskite layer or the HTL, results from this study were inconclusive. The experiment was repeated with all ALD thin films deposited at an elevated temperature of 300°C. The increased deposition temperature was applied to observe whether the film quality or interfacial contact would be enhanced leading to improved PCE. While cells containing SnO_2 exhibited a marginally improved performance compared to TiO_2 cells, current was significantly reduced in all devices. This indicated that both SnO_2 and TiO_2 could not achieve high efficiencies when in direct contact with the perovskite material.

Surface passivation via evaporated C_{60} was applied to 2 nm, 5 nm, and 10 nm ALD SnO_2 deposited at 185°C. When fabricated into planar devices all SnO_2 thicknesses produced efficient cells. The champion device incorporated 10 nm ALD SnO_2 and obtained 18.3 % on a 0.09 cm^2 active area and 15.9 % on a 0.7 cm^2 active area. Following on from this result, passivation using PCBM and CBD SnO_2 was explored on various thicknesses of ALD SnO_2 and compared to the same passivation processes on spin coated SnO_2. For passivation using PCBM, devices from both ALD ETLs and spin coated ETLs exhibited significant hysteresis. The performance of both device

types was found to be comparable, with the planar device incorporating spin coated SnO_2 reaching 10.85 % PCE_{MPP} and the planar device incorporating ALD SnO_2 obtaining 10.60 % PCE_{MPP} on 0.09 cm^2 aperture areas. For surface passivation using CBD, 20 nm was found to be the optimum thickness of ALD SnO_2 as it produced enhanced efficiencies in planar devices. Reduced hysteresis and enhanced V_{oc} and FF were observed in all cells using CBD, both those containing spin coated ETLs and those containing ALD ETLs, when compared to their PCBM counterparts. The reference spin coated SnO_2 cell stabilised at an impressive 17.82 % over 60 seconds of steady state MPP tracking. The cell containing 20 nm ALD SnO_2 as an ETL produced a stabilised 14.79 % PCE_{MPP} over 60 seconds. The performance of devices incorporating ALD was lower due to a reduced FF. While the recipe for spin coated SnO_2 followed by CBD SnO_2 has been well optimised in the literature, this preliminary study of ALD SnO_2 followed by CBD SnO_2 exhibits promise for further development.

The final objective of this thesis was to explore *p-i-n* architecture PSCs utilising low temperature ALD SnO_2 as the ETL. 163 cycles of SnO_2 deposited at 100°C without the use of an O_2 plasma pre clean was grown on a sample set of perovskite/HTL/ITO coated glass substrates. Half of this set employed evaporated C_{60} as a buffer layer on top of the perovskite absorber material, while the other half had a top layer of bare perovskite. These samples were synthesised into reverse architecture devices and their J-V characteristics were subsequently analysed. It was evident that SnO_2 did not perform well when in direct contact with the perovskite material and that a passivation layer was required to enhance J_{sc}. A high V_{oc} was observed in all cells incorporating the C_{60} passivation layer along with ALD SnO_2. However final performances achieved by this passivated set were split, with half of the devices reaching high PCEs of over 13 % while the other half had limited PCEs due to low FF. It was determined from TEM imaging and ellipsometry that 163 cycles of SnO_2 at 100°C had produced a film which, at 20 nm, was twice as thick as had been anticipated. The deposition was not uniform across the substrate holder at this temperature, suggesting that the growth was not limited. By altering the deposition temperature, purge lengths and number of cycles the ALD process was optimised and obtained a uniform thickness across the substrate holder at a suitably low deposition temperature. Using the improved deposition process 10 nm and 20 nm of ALD SnO_2 was deposited on another sample set of perovskite/HTL/ITO coated glass substrates. Again, evaporated C_{60} was

employed as a passivation layer on half of the sample set. Once deposited, the samples were finished with an IZO/Ag semi-transparent contact. These devices were compared to cells made in parallel using 10 nm ALD SnO_2 deposited on C_{60} at CSEM. An issue with the IZO/Ag deposition reduced the performance of all cells, however 20 nm ALD SnO_2 still achieved the highest PCE of 7.5 % when used in conjunction with a C_{60} passivation layer. This experiment was repeated and devices containing 10 nm and 20 nm ALD SnO_2 as ETLs on C_{60} were found to outperform devices made in parallel containing 10 nm ALD SnO_2 deposited at CSEM on a C_{60} passivation layer. These initial studies exhibited promising performances for planar *p-i-n* devices incorporating low temperature ALD SnO_2 with a C_{60} passivation layer.

In conclusion, it can be determined that conformal ALD films of TiO_2 and SnO_2 ETLs perform well in *n-i-p* and *p-i-n* perovskite architectures with the inclusion of a suitable passivation layer at the perovskite interface. The excellent uniformity and controlled thickness obtained by the ALD process can be scaled up for large area applications in the future. Moreover, the mild deposition technique of ALD does not cause damage to sensitive underlying materials.

The conformal and dense film growth provided by ALD on a precise sub-nanometre scale provides many advantages for perovskite devices. Reduced thickness of charge transport layers can aid in reducing the series resistance of the device by providing a shorter transfer distance for photogenerated charges. Processing thin charge transport layers using conventional methods such as spin coating or spray pyrolysis usually results in pinholes or cracks in the thin film. This reduces the charge blocking property of the layer leading to electrical leakages. Using ALD, these films are conformal and of uniform thickness, even in the case of large area substrates.

The conformal nature of ultra-thin ALD TiO_2 in mesoporous perovskite devices has been demonstrated by Roelofs et al[1] where 4 nm of ALD TiO_2 was found to exhibit comparable PCEs to 50 nm TiO_2 deposited by spray pyrolysis. ALD TiO_2 was deposited on FTO coated glass using $TiCl_4$ and H_2O as respective precursor and reactant at a deposition temperature of 300°C. The substrates were subsequently annealed at 450°C for 1 hour to form the TiO_2 rutile phase. Mesoporous perovskite devices were fabricated with the remainder of the stack composed of m-TiO_2/$MAPbI_3$/Spiro-OMeTAD/Au. These devices were compared to mesoporous

cells containing 50 nm spray pyrolysis TiO_2 deposited at a substrate temperature of 500°C. On an aperture area of 0.1cm^2, devices fabricated from both TiO_2 methods exhibited similar PCEs of 11.4 % for ALD and 11.8 % for spray pyrolysis. A thicker ALD TiO_2 layer of 50 nm had previously been compared to compact layers of TiO_2 deposited by both spin coating and spray pyrolysis for use in mesoporous devices by Wu et al.[2] ALD TiO_2 was deposited at a temperature of 200°C using TDMAT and H_2O as titanium precursor and reactant. The ALD method was found to surpass spin coating and spray pyrolysis in terms of efficiency for mesoporous cells, reaching 12.56 % PCE.

For the work presented in this thesis a similar device stack was fabricated on up-scaled aperture areas of 0.43 cm^2 and 1.04 cm^2. Amorphous ALD TiO_2 was deposited at the low deposition temperatures of 200°C and 185°C using TDMAT and H_2O as the respective titanium precursor and reactant. Both 10 nm and 20 nm of ALD TiO_2 were found to outperform spin coated TiO_2 in mesoporous devices. 20 nm ALD TiO_2 was found to be comparable to 20 nm TiO_2 deposited by the conformal vacuum technique of RF sputtering in mesoporous devices. The ALD TiO_2 reached 16.45 % PCE on a large 1.04cm^2 active area, while the RF sputtered TiO_2 reached 16.66 % PCE on an active area of the same size. The use of ALD TiO_2 compact layers in mesoporous perovskite devices has been shown to produce enhanced PCEs both in the literature and within this thesis when compared to conventional deposition techniques. Comparing ALD to alternative conformal and vacuum techniques such as sputtering and evaporation will be an important consideration when establishing a suitable technique for manufacturing upscaled devices that may be used for commercialisation.

While the ALD of TiO_2 performs well in mesoporous PSCs, its use in planar devices has proved to be more problematic as evinced by conflicting results in the literature. Kim et al[3] demonstrated that low-temperature PEALD TiO_2 deposited on PEN/ITO substrates behave well in planar devices using a $MAPbI_{3-x}Cl_x$ perovskite. These 20 nm thick ALD films, deposited using TTIP and O_2 plasma, reached a PCE of 12.2% in planar cells compared to 4.3 % PCE achieved using a spin coated c-TiO_2 ETL in the same cell architecture. Conversely, it has also been shown that as deposited ALD TiO_2 does not perform well in planar devices.[4] 12 nm of amorphous TiO_2 was deposited by ALD using TDMAT and H_2O as respective titanium precursor and reactant at 120°C. When incorporated into planar devices using $MAPbI_{3-x}Cl_x$ as the perovskite a low

efficiency of 1.8 % PCE was achieved. Post-processing of the ALD TiO_2 using an UV-O_3 treatment or annealing to 500°C was found to increase J_{sc}, FF and ultimately PCE in the device J-V curves. An improved efficiency of 10.0 % PCE was achieved using an UV-O_3 treatment and 11.5 % PCE was achieved using a 500°C anneal on an active area of 0.16 cm^2. This improvement in performance was proposed to be due to the removal of oxygen vacancies and the reduction of defect states caused by the oxidising treatments on the ALD TiO_2.

In the work completed in this thesis low PCEs of 8 % were exhibited using as deposited amorphous TiO_2 in planar devices on a 1.04 cm^2 aperture area. Rapid thermal annealing of these ALD films to 500°C in O_2 was not found to improve efficiency and J_{sc} was found to be greatly reduced despite the oxidising post-treatment. This suggests that the bulk material of ALD TiO_2 may not be the overriding issue for use in planar devices and instead interface passivation and alteration should be considered.

Electron-hole recombination in perovskite devices is promoted by defects and impurities which are present at the interface between charge selective contacts and the perovskite material as well as charge selective contacts and the electrodes. Interfacial properties are therefore a key consideration in the development of highly efficient perovskite devices. The use of ALD TiO_2 as surface passivation on top of the mesoporous TiO_2 layer has been reported by Chandiran et al.[5] A thickness of 2 nm ALD TiO_2 was found to successfully block parasitic back reaction from the FTO and m-TiO_2 surface while simultaneously allowing suitable pore filling of the perovskite material. This boosted PCE from 7.2 % to 11.5 % for the mesoporous device on an aperture area of 0.159 cm^2. The use of ALD Al_2O_3 has also been explored as a suitable method for surface passivation in c-Si solar cells.[6-8] In this thesis both ALD Al_2O_3 and ZnO were investigated as sub-nanometre passivation layers on top of the ALD TiO_2 ETL. The thin insulating Al_2O_3 was expected to saturate dangling bonds and allow charge transport through tunnelling while the ethyl ligands present in the ZnO precursor DEZ could aid in cleaning the surface of the ALD TiO_2. Al_2O_3 was found to block charge extraction even at one cycle while ZnO improved J_{sc} providing promise for future studies. A recent report by Zardetto et al[9] has indicated that the interfacial properties between PEALD TiO_2 and the perovskite material can be improved using CF_4 plasma for 2 minutes as a surface treatment. In this study TiO_2

treated with CF_4 has a deeper energy level compared to untreated TiO_2 allowing for an improved band alignment between the perovskite material and the ETL resulting in improved electron extraction. Interfacial adhesion between the ALD TiO_2 and perovskite was also enhanced with strong F bonds. The efficiency of this planar PSC was boosted from 4 % PCE using pristine PEALD TiO_2 to 14.8 % PCE with the CF_4 surface treatment.

When used in planar PSCs, there is a conduction band misalignment between a c-TiO_2 ETL and the perovskite absorber material regardless of TiO_2 deposition method. ALD SnO_2 as an ETL is energetically favourable with the perovskite as demonstrated by Correa Baen et al.[10] 15 nm of ALD SnO_2 was deposited at 120°C using TDMASn and O_3 and fabricated into a planar perovskite device achieving 18.4 % PCE on an active area of 0.16 cm^2. Wang et al reported the improved efficiency of PEALD SnO_2 when used in conjunction with a spin coated C_{60}-SAM layer as passivation in planar perovskite devices.[11] 15 nm of SnO_2 deposited at 100°C using TDMASn and O_2 plasma produced an average PCE of 18.21 % on an active area of 0.08 cm^2 with the incorporation of the passivating self-assembled monolayer.

From the work in this thesis ALD SnO_2 was also found to work best in planar devices with the incorporation of passivation layers, reaching 18.3 % PCE on a 0.09 cm^2 active area and 15.8 % PCE on a 0.7 cm^2 active area when C_{60} was utilised as a passivation layer. Thin fullerenes such as C_{60} and C_{60}-SAM have the ability to passivate metal oxide surfaces promoting electron transfer. Alternative passivation layers of the fullerene PCBM and the inorganic CBD SnO_2 were also explored in this thesis. PCBM has previously been reported as an interlayer in *p-i-n* devices between the perovskite layer and an ALD TiO_2.[12] This passivation layer successfully reduced charge recombination at the interface producing cells with an efficiency of 8.8 % PCE on a 0.16 cm^2 area. From the work in this thesis, the stabilised max power point efficiency from devices incorporating PCBM on top of ALD SnO_2 (10.60 % PCE) was found to be comparable to devices with PCBM on top of spin coated SnO_2 (10.85 % PCE) with both types of planar *n-i-p* devices exhibiting notable hysteresis. In the literature planar devices incorporating spin coated SnO_2 passivated with CBD SnO_2 have only been compared to devices containing pristine ALD SnO_2 which has not been passivated.[13] In this thesis the use of CBD on top of ALD SnO_2 was found to boost efficiency compared to non-passivated ALD SnO_2. Despite final PCEs being lower than that of

spin coated SnO_2 followed by CBD, this initial study shows promise for future all inorganic ETLs on upscaled devices.

For reverse architecture *p-i-n* devices, depositing thin films using ALD on top of the temperature sensitive perovskite material is challenging. The ALD thin film needs to be capable of growing at a suitably low temperature to avoid damaging the perovskite layer underneath. The use of plasma, which is usually selected for low-temperature depositions, in ALD may also affect the perovskite layer which is prone to degradation. As an interface modification technique ALD Al_2O_3 has been reported on top of the $MAPbI_3$ perovskite/TiO_2/FTO stack as well as the Spiro-OMeTAD/$MAPbI_3$ perovskite material/TiO_2/FTO stack in *n-i-p* devices.[14] TMA and O_3 were used as the respective aluminium precursor and reactant and deposition took place at a low temperature of 70°C. XRD characterisation revealed the perovskite material to be degraded even after 1 cycle of ALD Al_2O_3, reducing the performance of the device. A similar study was later conducted by Koushik et al[15] employing TMA and H_2O at a deposition temperature of 100°C. A thickness series of 2 to 20 cycles was successfully deposited on top of the perovskite material without degradation. It was believed that the use of H_2O instead of the oxidising O_3 as an ALD reactant allowed the layers to be deposited on top of the sensitive perovskite material without degradation. Passivation using ALD Al_2O_3 improved the device efficiency from 15.1 % PCE to 18.0 % PCE using an optimised 10 cycles of Al_2O_3.

In this thesis, low temperature ALD SnO_2 was successfully deposited as an ETL on top of sensitive perovskite materials. The perovskite stack underwent up to 222 cycles of SnO_2 (20nm) with prolonged purge lengths at 140°C in the ALD chamber without any degradation or negative effects observed. 10 nm and 20 nm ALD SnO_2 deposited on perovskite stacks containing evaporated C_{60} as a passivation layer on upscaled devices of 1.04 cm^2 were found to produce enhanced PCEs outperforming devices fabricated in parallel containing 10 nm ALD SnO_2 deposited at CSEM on a C_{60} passivation layer.

The work completed in this thesis demonstrates impressive results for thermal ALD TiO_2 on upscaled mesoporous devices which is comparable to the alternative vacuum technique of RF sputtering. For planar perovskite solar cells ALD TiO_2 does not behave well when in direct contact with the perovskite material and a suitable

passivation method is required. The use of ALD ZnO passivation to alleviate this issue has shown potential for future development. To combat the conduction band misalignment between TiO_2 and the perovskite material, thermal ALD SnO_2 shows considerable promise in planar *n-i-p* devices when used in conjunction with a passivation layer reaching a notable 18.3 % PCE. The significant development of utilising low-temperature thermal ALD SnO_2 to deposit on top of the perovskite stack in *p-i-n* devices without damage to the perovskite under layer is an encouraging step for the field of perovskite solar cells. The mild ALD deposition technique and the conformal nature of its resultant films can aid in the upscaling and commercialisation of perovskite devices in the future.

8.2 Suggestions for Future Work

Several facets of the research described in this thesis offer scope for further investigation.

Additional investigation into TiO_2 doped with silver in a 99:1 ratio would be valuable to definitively determine if this dopant enhances the overall PCE when incorporated into a mesoporous PSC.

Repeating the fabrication of mesoporous PSCs comprised of ALD TiO_2 ETLs doped with tin in a 19:1 ratio would be advantageous to determine if the low PCEs from the doped materials obtained in Chapter 5 are due to the ALD thin film itself or an issue with one of the remaining layers in the cell.

It would be interesting to explore other dopant precursors for nanolaminate TiO_2 ETLs. TiO_2 doped with conductive niobium as an ETL, for instance, may improve the overall PCE of a mesoporous cell compared to undoped thermal ALD TiO_2 due to the influence of the niobium on the electrical properties of the thin film.

While doping ratios of 19:1 and 99:1 have been shown to work well for ZnO:Al, effective ratios for TiO_2 doping have not been extensively reported in the literature. Investigation into a wider series of doping ratios via ALD would be beneficial to determine the optimised doping ratio for different dopants in TiO_2 matrix thin films. Each dopant should be investigated in a range of ratios as the doping efficiency depends on the dopant's solubility level within the TiO_2 thin film. If the local dopant

density is below the solubility limit then the local dopant atoms can be incorporated in the Ti positions in the TiO_2 matrix and effectively act as electron donors.

A study should be conducted to determine if an etching effect takes place when TiO_2 is doped with each of the various doping precursors used in this thesis. This can occur via surface reactions during the ALD growth. The dopant may remove surface titanium atoms and occupy their surface sites. Alternatively, the TDMAT or TTIP precursor may remove dopant atoms from the surface and occupy their sites. The study could be executed by growing bilayers of the TiO_2 thin film and the dopant material and examining their interfaces using TEM imaging.

It would be beneficial to compare the conductivity of doped TiO_2 thin films which incorporate the same dopant using alternative dopant precursors. If an alternative dopant precursor provided steric hindrance then the number of dopant atoms deposited in one cycle would be significantly reduced. A larger spacing between the dopant atoms in one ALD cycle could enhance film conductivity.

Repeating the interface passivation using a single cycle of ALD Al_2O_3 deposited or annealed at elevated temperatures of 300°C or above could aid in cleaning up the surface of TiO_2 and removal of the negative charge on the surface.

ZnO passivation exhibited promise by increasing current in planar devices. Further investigation could lead to successful passivation with improved PCE.

Exploration of surface passivation via fluorination or chlorination would be constructive. This would determine if the interface between the ALD TiO_2 film or the ALD SnO_2 film and the perovskite absorber material can be improved by either surface modification technique. The SnO_2 CBD treatment described in Chapter 7 utilised $SnCl_2.2H_2O$, which mitigates interfacial recombination when fabricated into planar devices. This treatment could significantly enhance PCEs in planar perovskite architectures.

Further exploration and optimisation of ALD SnO_2 using CBD SnO_2 as a passivation layer could lead to improved efficiencies in resulting *n-i-p* perovskite devices.

8.3 Bibliography

[1] K. E. Roelofs, V. L. Pool, D. A. Bobb-Semple, A. F. Palmstrom, P. K. Santra, D. G. Van Campen, M. F. Toney, S. F. Bent, Impact of Conformality and Crystallinity for Ultrathin 4 nm Compact TiO_2 Layers in Perovskite Solar Cells, Adv. Mater. Interfaces, 3, 1600580, 2016

[2] Y. Wu, X. Yang, H. Chen, K. Zhang, C. Qin, J. Liu, W. Peng, A. Islam, E. Bi, F. Ye, M. Yin, P. Zhang, L. Han, Highly compact TiO_2 layer for efficient hole-blocking in perovskite solar cells, Appl. Phys. Express, 7, 052301, 2014

[3] B. J. Kim, D. H. Kim, Y.-Y. Lee, H.-W. Shin, G. S. Han, J. S. Hong, K. Mahmood, T. Ahn, Y.-C. Joo, K. S. Hong, N.-G. Park, S. Lee and H. S. Jung, Highly Efficient and Bending Durable Perovskite Solar Cells: Toward Wearable Power Source Energy Environ. Sci., 8, 916–921, 2015

[4] I. Soo Kim, R. T. Haasch, D. H. Cao, O. K. Farha, J. T. Hupp, M. G. Kanatzidis, A. B. F. Martinson, Amorphous TiO_2 Compact Layers via ALD for Planar Halide Perovskite Photovoltaics, ACS Appl. Mater. Interfaces, 8, 24310−24314, 2016

[5] A. K. Chandiran, A. Yella, M. T. Mayer, P. Gao, M. K. Nazeeruddin, M. Grätzel, Sub-Nanometer Conformal TiO_2 Blocking Layer for High Efficiency Solid-State Perovskite Absorber Solar Cells, Adv. Mat., 26, 25, 2014

[6] F. Werner, W. Stals, R. Görtzen, B. Veith, R. Brendel, J. Schmidt, High-rate atomic layer deposition of Al_2O_3 for the surface passivation of Si solar cells, Energy Procedia, 8, 301–306, 2011

[7] T. Lüder, G. Hahn, B. Terheiden, Passivation of Si Wafers by ALD-Al_2O_3 Films with Different Surface Conditioning, Energy Procedia, 8, 660–665, 2011

[8] B. Hoex, J. Schmidt, P. Pohl, M. C. M. Sanden, van de, W. M. M. Kessels, Silicon surface passivation by atomic layer deposited Al_2O_3, J. App. Phys., 104, 4, 044903-1/12, 2008

[9] V. Zardetto, F. di Giacomo, H. Lifka, M. A. Verheijen, C. H. L. Weijtens, L. E. Black, S. Veenstra, W. M. M. Kessels, R. Andriessen, M, Creatore, Surface

Fluorination of ALD TiO2 Electron Transport Layer for Efficient Planar Perovskite Solar Cells, Adv. Mater. Interfaces, 5, 1701456, 2018

[10] J.-P. Correa Baena, L. Steier, W. Tress, M. Saliba, S. Neutzner,T. Matsui, F. Giordano, T. J. Jacobsson, A. R. S. Kandada, S. M. Zakeeruddin, A. Petrozza, A. Abate, M. K. Nazeeruddin, M. Grätzel, A. Hagfeldt, Highly efficient planar perovskite solar cells through band alignment engineering, Energy Environ. Sci., 8, 2928, 2015

[11] C. Wang, D. Zhao, C. Grice, W. Liao, Y. Yu, A. Cimaroli, N. Shrestha, P. J. Roland, J. Chen, Z. Yu, P. Liu, N. Cheng, R. Ellingson, X. Zhao and Y. Yan, Low-temperature plasma-enhanced atomic layer deposition of tin oxide electron selective layers for highly efficient planar perovskite solar cells, J. Mater. Chem. A, 4, 12080–12087, 2016

[12] I. S. Kim, D. H. Cao, D. B. Buchholz, J. D. Emery, O. K. Farha, J. T. Hupp, M. G. Kanatzidis, A. B. F. Martinson, Liquid Water and Heat-Resistant Hybrid Perovskite Photovoltaics via an Inverted ALD Oxide Electron Extraction Layer Design, Nano Lett., 16, 12, 7786–7790, 2016

[13] E. H. Anaraki, A. Kermanpur, L. Steier, K. Domanski, T. Matsui, W. Tress, M. Saliba, A. Abate, M. Grätzel, A. Hagfeldt, J.-P. Correa-Baena, Highly efficient and stable planar perovskite solar cells by solution-processed tin oxide, Energy Environ. Sci., 9, 3128-3134, 2016

[14] X. Dong, X. Fang, M. H. Lv, B. C. Lin, S. Zhang, J. N. Ding, N. Y. Yuan, Improvement of the humidity stability of organic/inorganic perovskite solar cells using ultrathin Al_2O_3 layers prepared by atomic layer deposition, J. Mat. Chem. A, 3, 5360, 2015

[15] D. Koushik, W. J. H. Verhees, Y. H. Kuang, S. Veenstra, D. Zhang, M. A. Verheijen, M. Creatore and R. E. I. Schropp, High-efficiency humidity-stable planar perovskite solar cells based on atomic layer architecture, Energy Environ. Sci., 10, 91, 2017

APPENDIX I:

Design of masks and sample holders as well as characterisation of layers

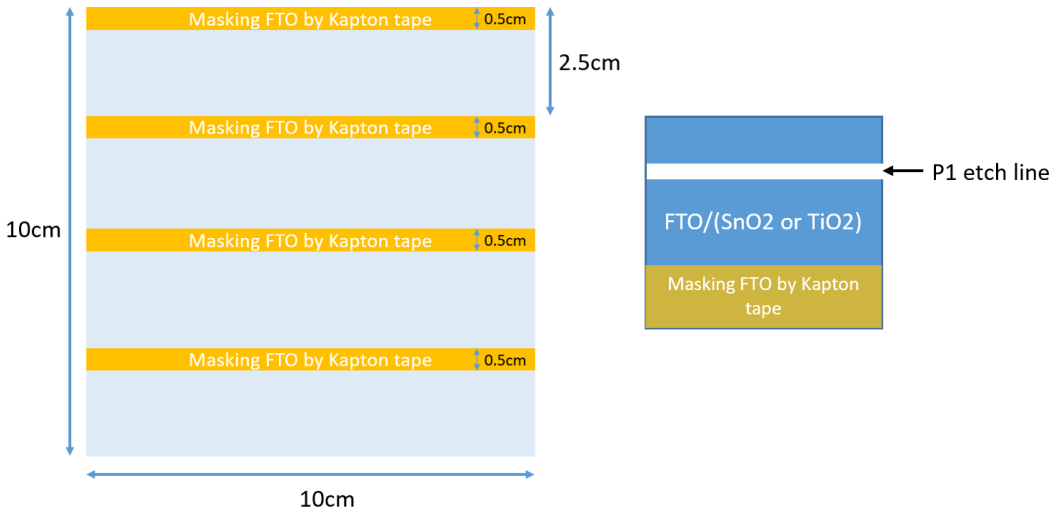

Figure 1: *Schematic for Kapton tape placement on 10 cm^2 FTO coated glass sheet and P1 etch line on 2.5 cm^2 substrate*

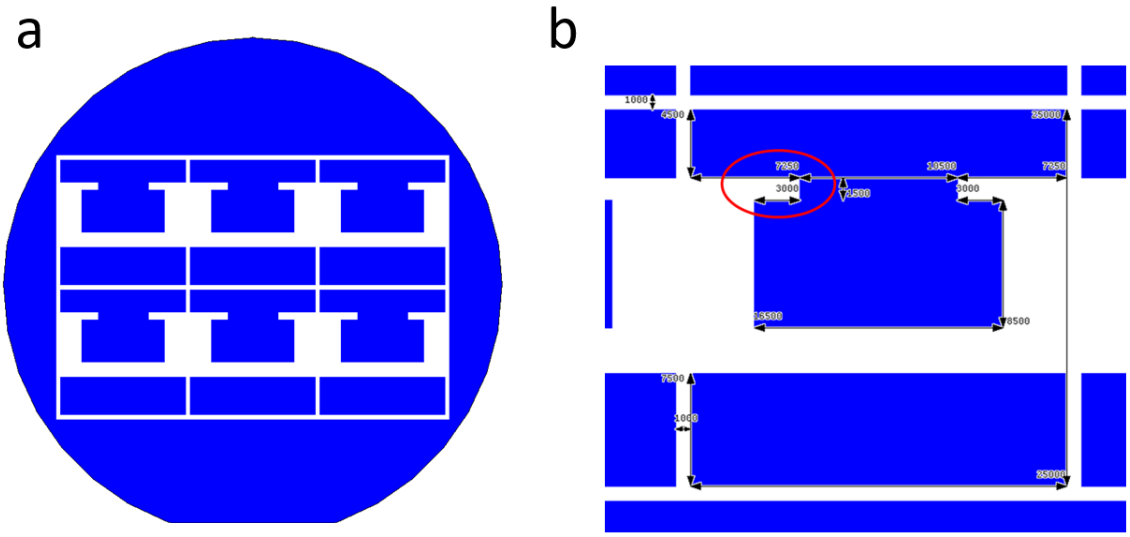

Figure 2: *Photomask design for Au e-beam evaporation.* ***(a)*** *Mask design for 6 cells,* ***(b)*** *measurements for each cell design in micrometres*

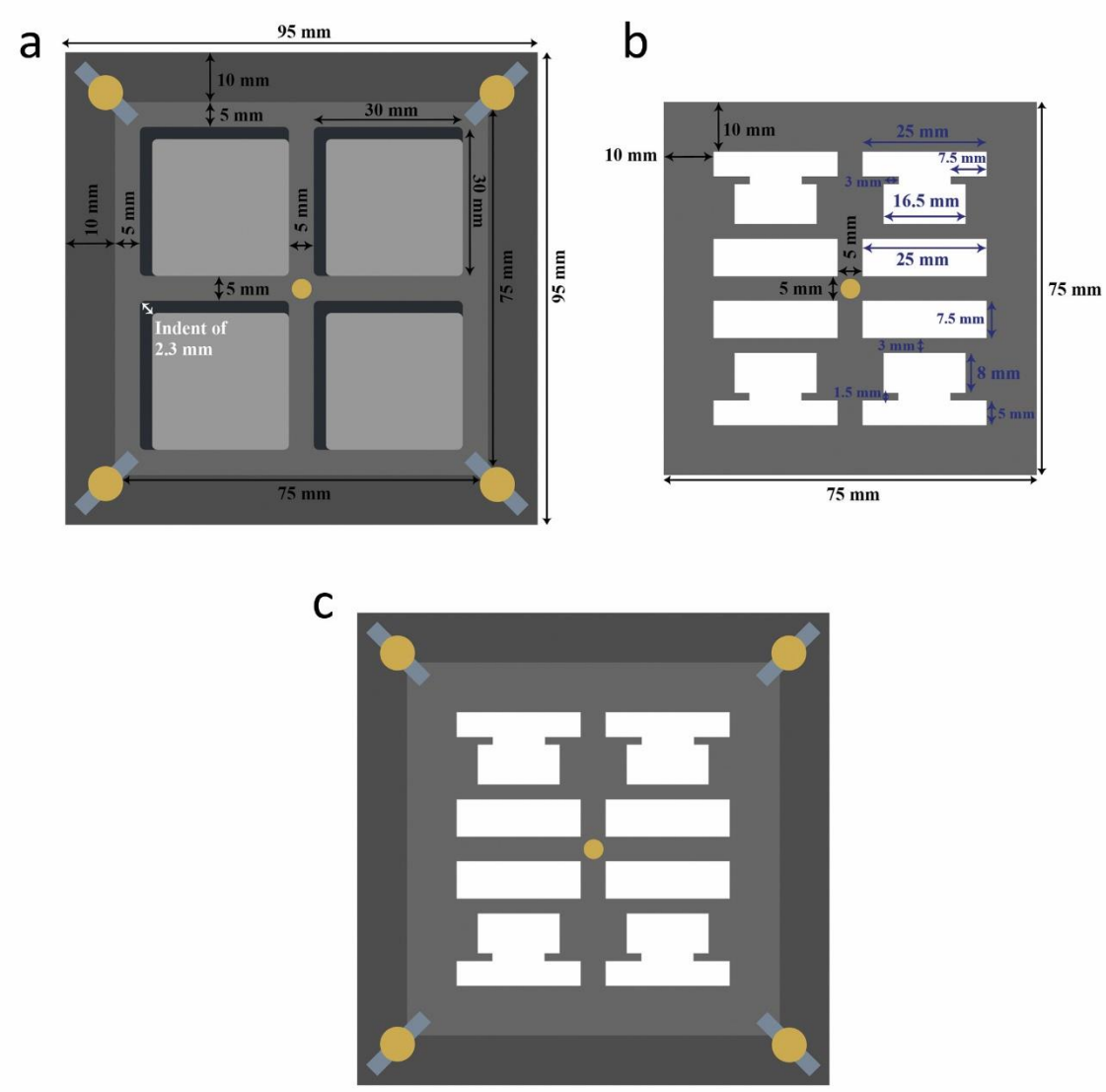

Figure 3: *Mask design for Au thermal evaporation.* ***(a)*** *Aluminium quad sample holder with centre screw and metal snaps on each corner to hold mask,* ***(b)*** *thin aluminium mask with hole for centre screw, and* ***(c)*** *sample holder with evaporation mask clipped in along with centre screw*

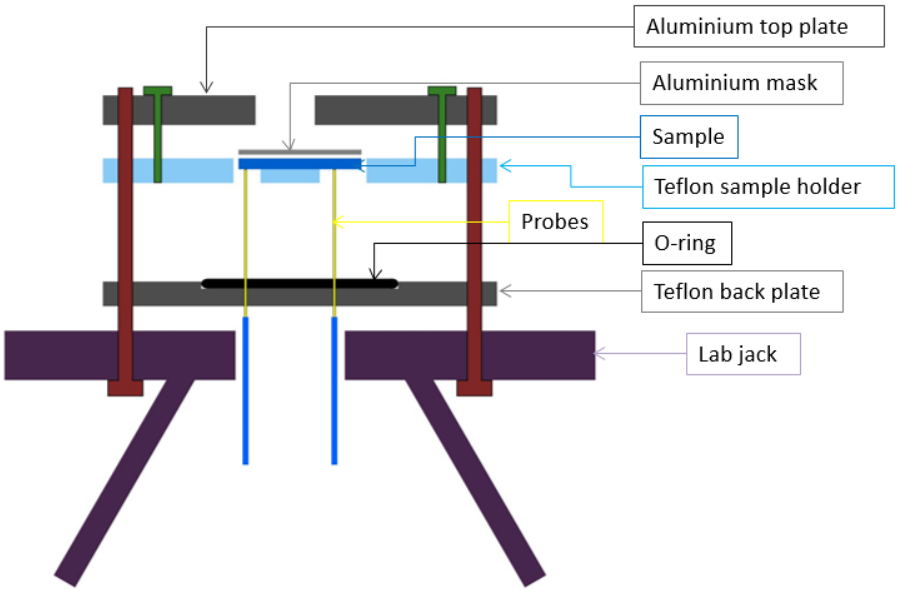

Figure 4(a): *Cross sectional overview of design for solar simulator sample holder with labels*

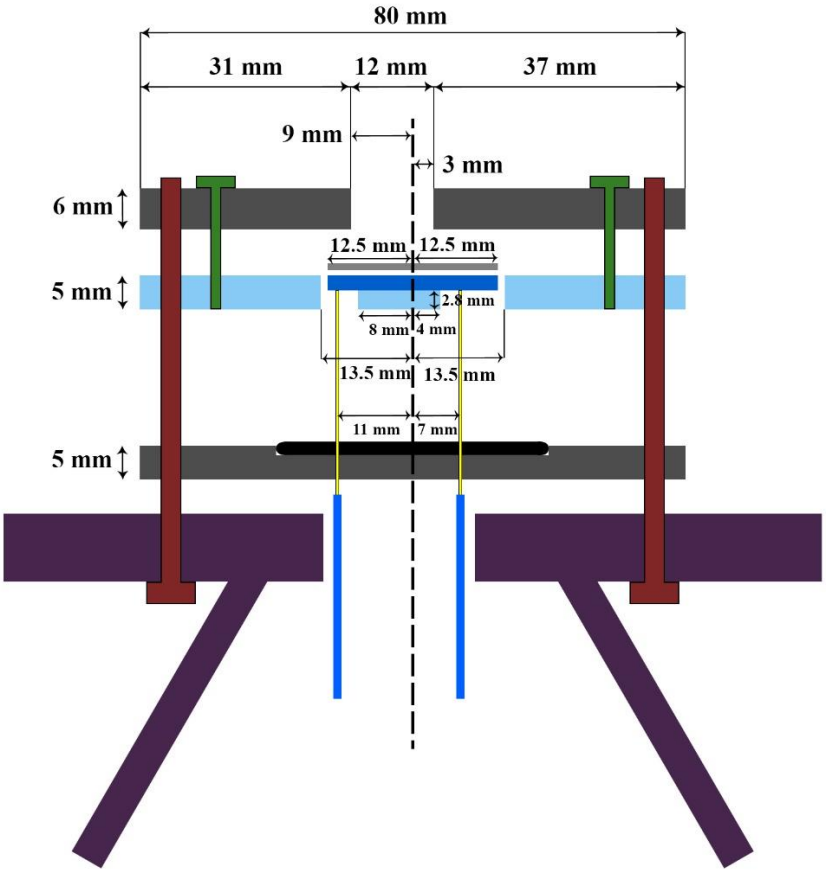

Figure 4(b): *Cross sectional overview of design for solar simulator sample holder with measurements*

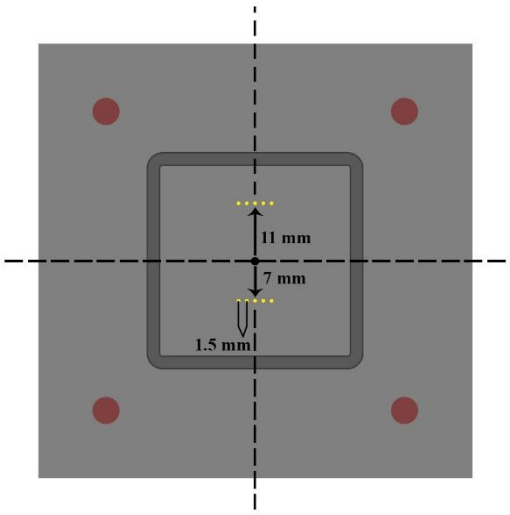

Figure 5: *Plan view design of back plate for solar simulator sample holder*

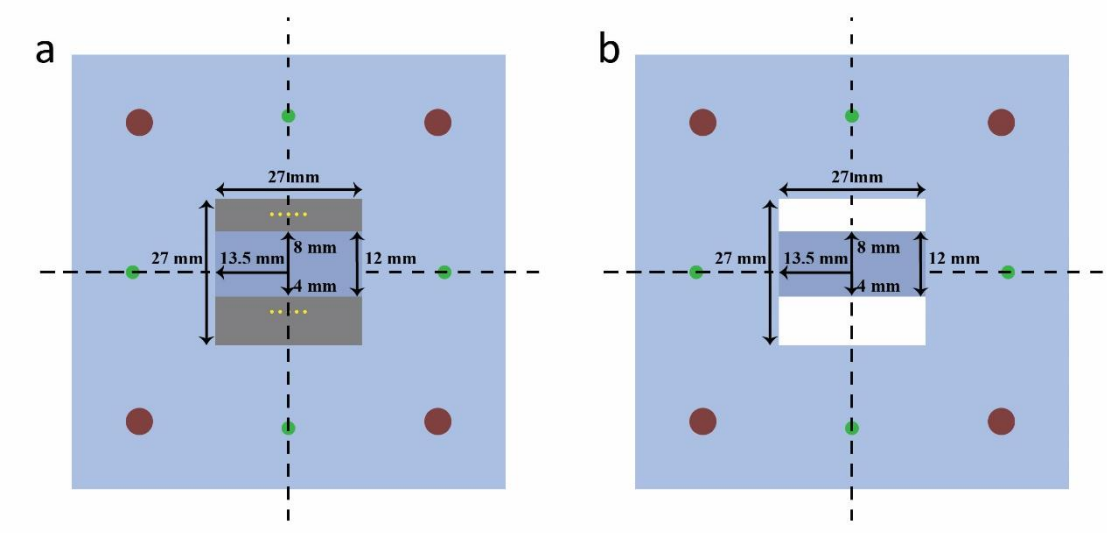

Figure 6: *Plan view design of sample holder for solar simulator sample holder* ***(a)*** *showing underneath back plate and* ***(b)*** *on its own*

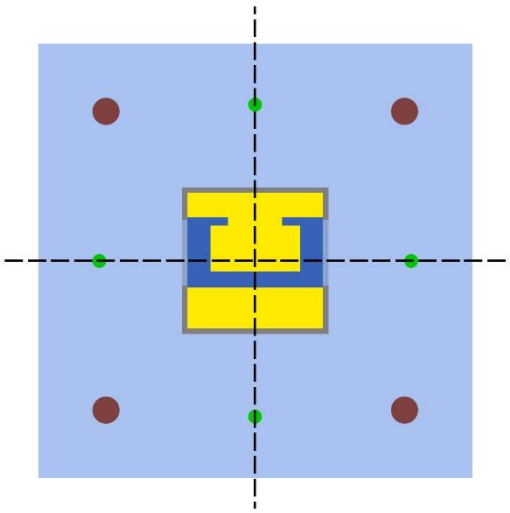

Figure 7: *Plan view design of sample in solar simulator sample holder*

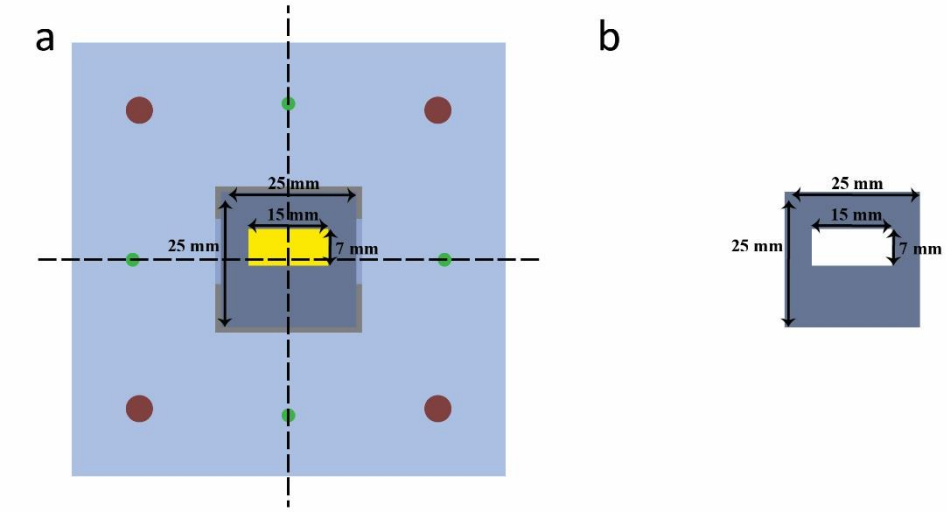

Figure 8: *Plan view design of mask for solar simulator sample holder* ***(a)*** *showing underneath layers and* ***(b)*** *on its own*

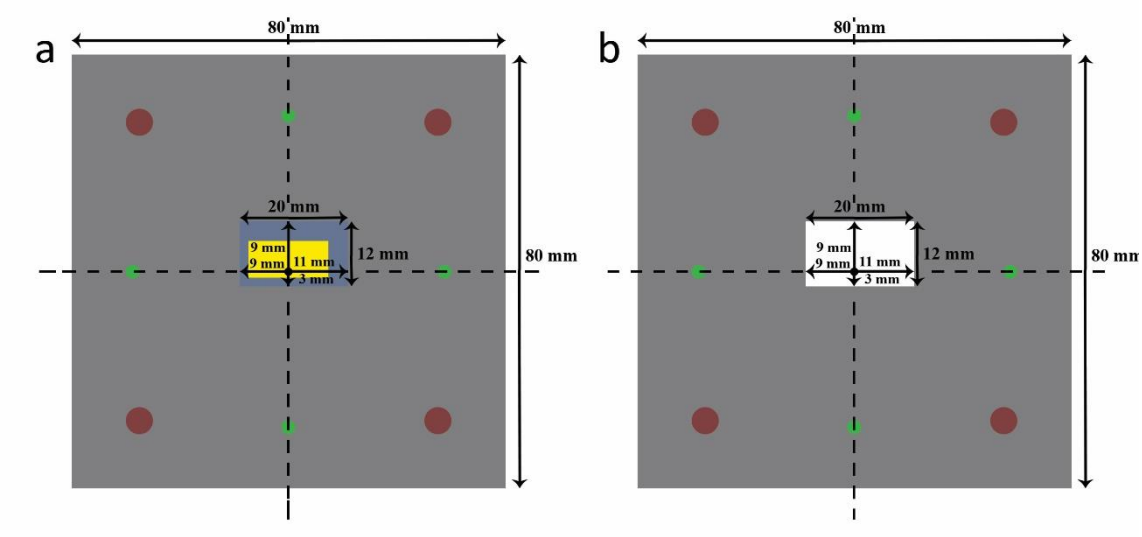

Figure 9: *Plan view design of top plate for solar simulator sample holder* ***(a)*** *showing underneath layers and* ***(b)*** *on its own*

Alterations to solar simulator sample holder design:

- Top plate made from black nylon instead of aluminium. An aluminium plate would need to be painted black which is likely to flake off over time.
- Sample holder made from aluminium instead of Teflon.
- Back plate made from PTFE as the softer material allows contact pins to better fit through the 0.6 mm drill hole.
- Inclusion of O-ring not necessary.

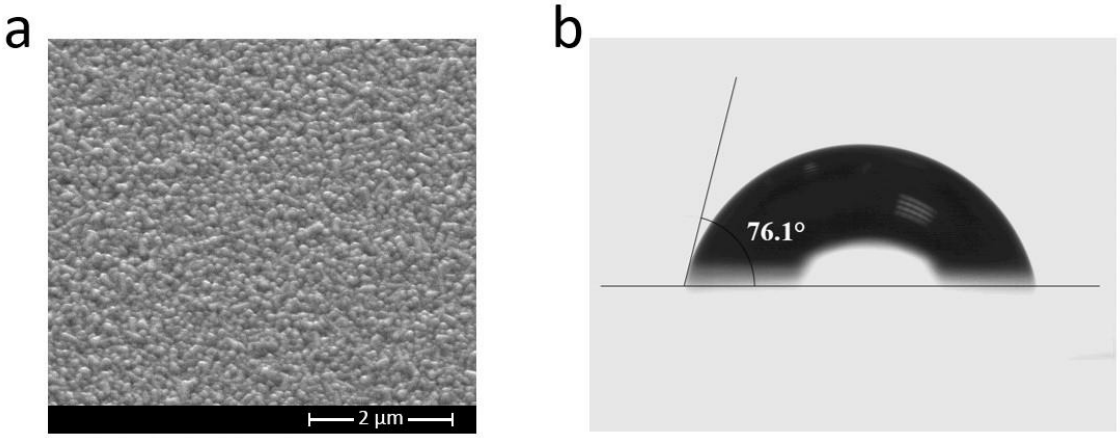

Figure 10: ***(a)*** *SEM of surface morphology and* ***(b)*** *contact angle measurement on ALD thermal TiO_2 pre-treated with 5 minutes of O_2 plasma on FTO coated glass*

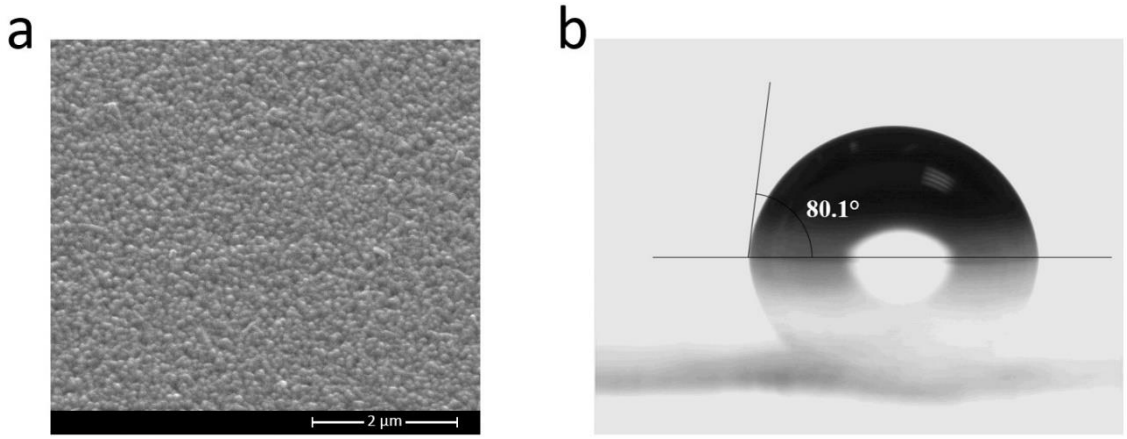

Figure 11: ***(a)*** *SEM of surface morphology and* ***(b)*** *contact angle measurement on ALD thermal TiO_2 doped with Al in 19:1 TiO_2:dopant pulse ratio*

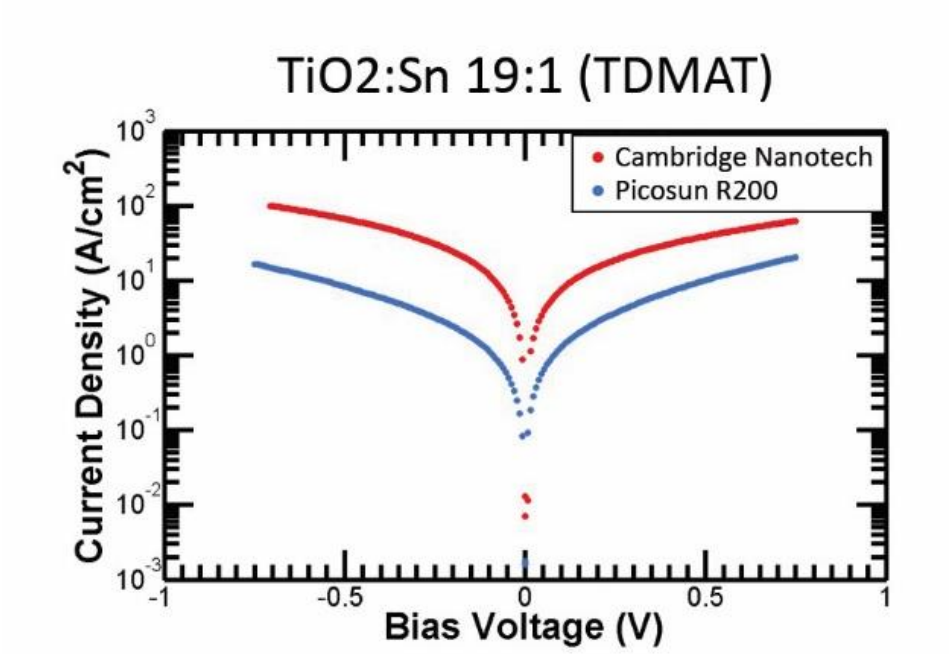

Figure 12: *J-V sweep comparing 20 nm thermal ALD TiO_2:Sn doped in a 19:1 dopant:pulse ratio and pre-treated with 5 minutes of O_2 plasma deposited by the Cambridge Nanotech system and the Picosun R200 system*

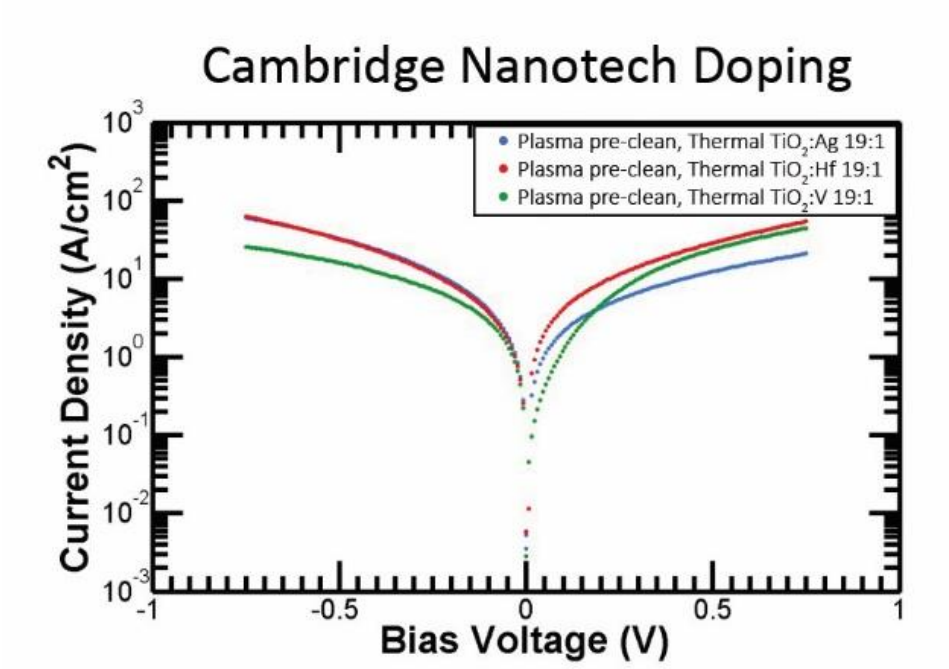

Figure 13: *J-V sweep comparing 20 nm thermal ALD TiO_2:Ag, TiO_2:Hf, and TiO_2:V doped in a 19:1 dopant:pulse ratio and pre-treated with 5 minutes of O_2 plasma deposited by the Cambridge Nanotech system*

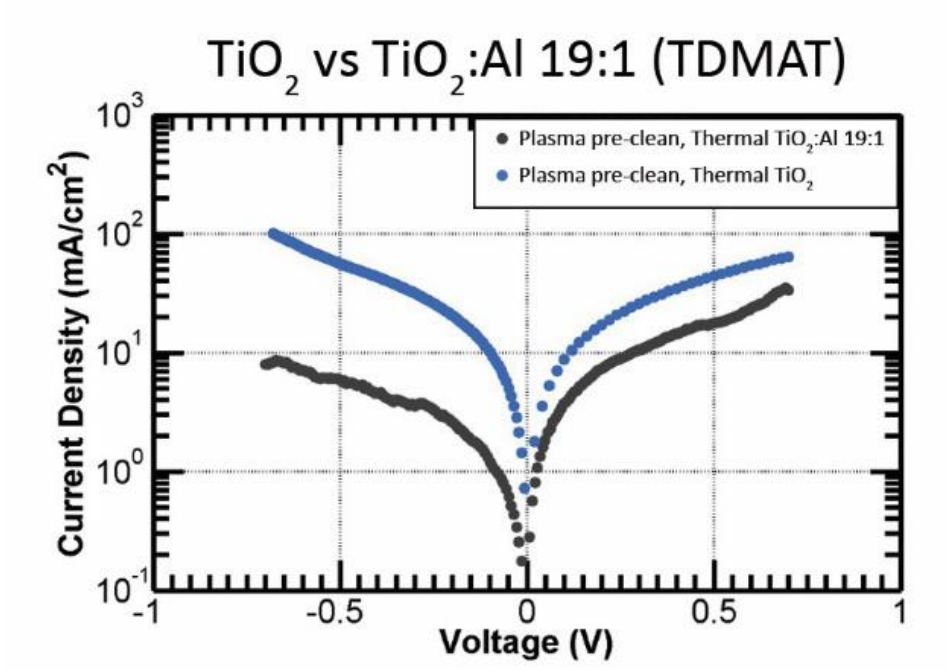

Figure 14: *J-V sweep comparing 20 nm thermal ALD TiO_2 pre-treated with 5 minutes of O_2 plasma to 20 nm thermal ALD TiO_2:Al doped in a 19:1 dopant:pulse ratio and pre-treated with 5 minutes of O_2 plasma deposited by the Picosun R200 system*

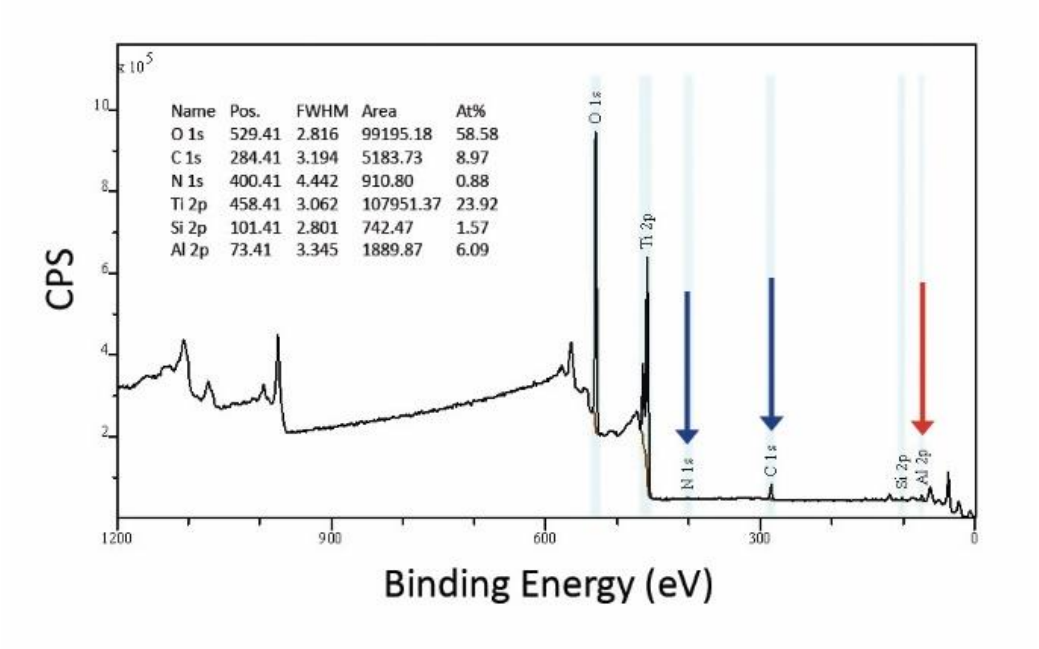

Figure 15: *XPS showing binding energy of as grown 20 nm thermal ALD TiO_2:Al doped in a 19:1 dopant:pulse ratio and pre-treated with 5 minutes of O_2 plasma deposited by the Picosun R200 system*

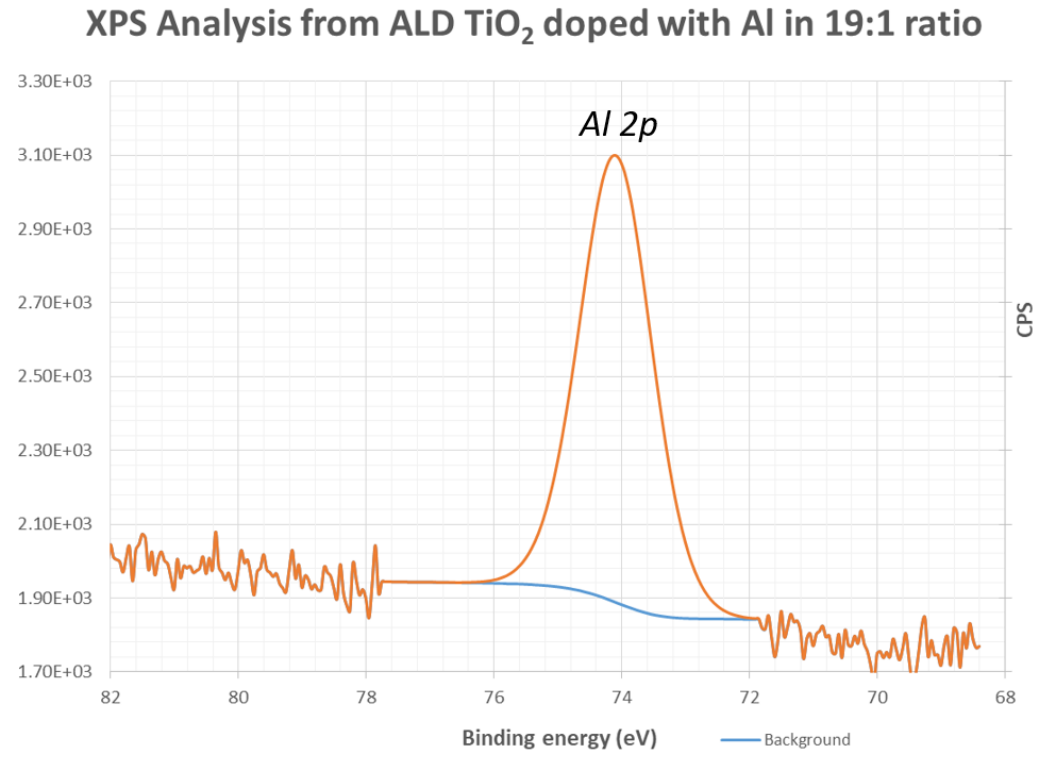

Figure 16: *XPS spectra of as grown 20 nm thermal ALD TiO_2:Al doped in a 19:1 dopant:pulse ratio and pre-treated with 5 minutes of O_2 plasma deposited by the Picosun R200 system*

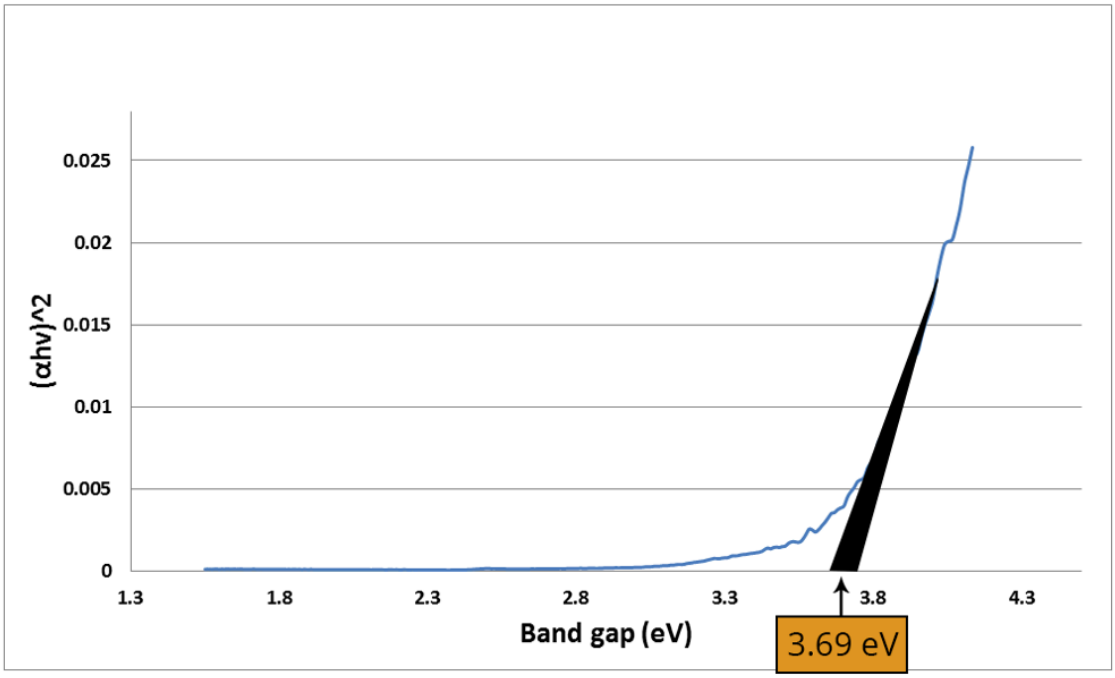

Figure 17: *Tauc plot of thermal ALD TiO_2:Al doped in a 19:1 dopant:pulse ratio and pre-treated with 5 minutes of O_2 plasma deposited by the Picosun R200 system*

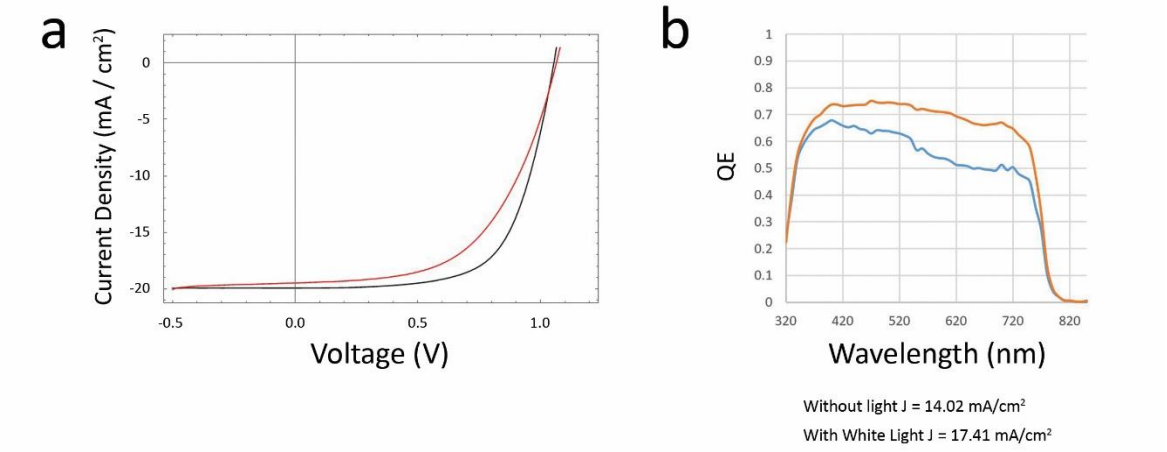

Figure 18: *J–V characteristics of mesoporous perovskite solar cell containing plasma pre clean, 20 nm thermal ALD SnO_2:Ti doped in 19:1 dopant:pulse ratio. (b) External quantum efficiency of same perovskite solar cell containing plasma pre clean, 20 nm thermal ALD SnO_2:Ti doped in 19:1 dopant:pulse ratio ETL.*

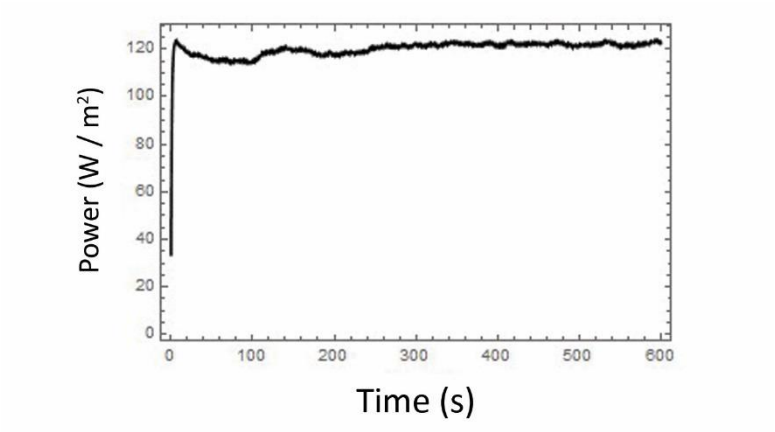

Figure 19: *Max power point steady state tracking over 600 seconds of mesoporous perovskite solar cell containing 20 nm thermal ALD SnO_2:Ti doped in 19:1 dopant:pulse ratio as ETL stabilising at 12.2 % PCE*

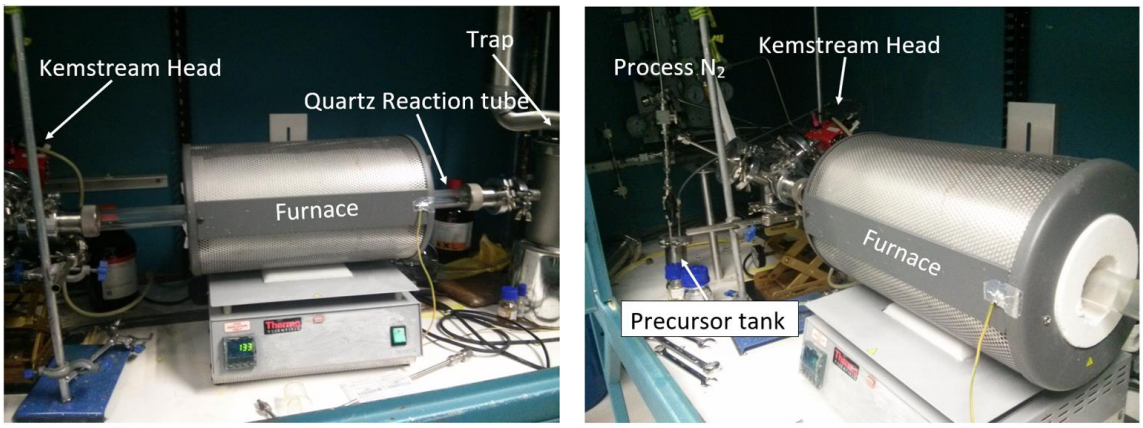

Figure 20: *Spray pyrolysis set up outlining main components for depositing perovskite material*

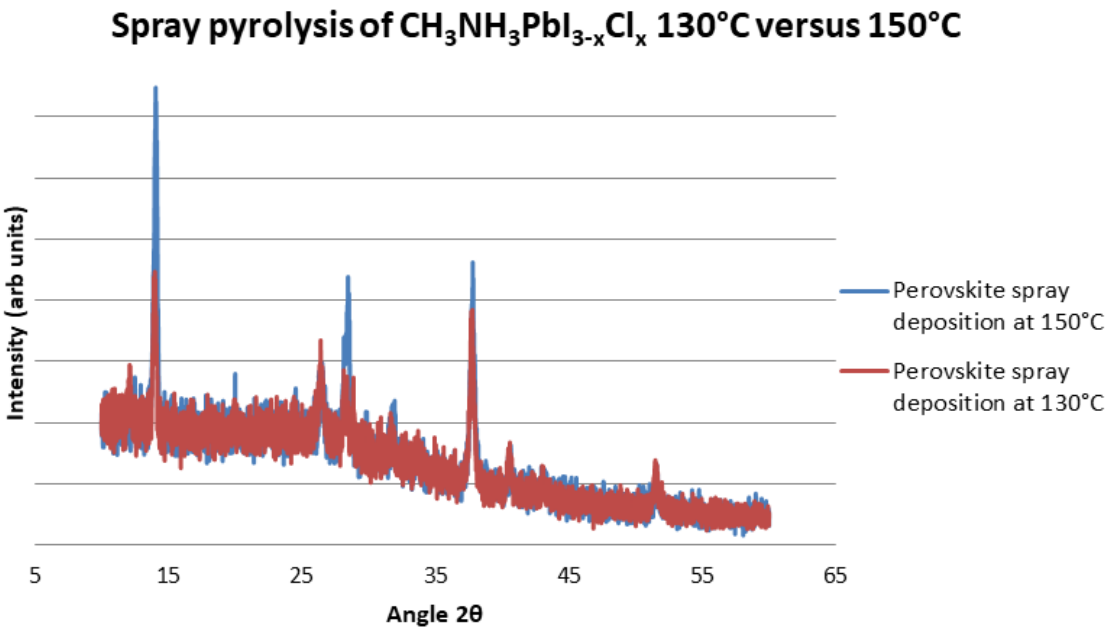

Figure 21: *XRD analysis comparing $CH_3NH_3PbI_{3-x}Cl_x$ thin films deposited by spray pyrolysis at 150°C and 130°C*

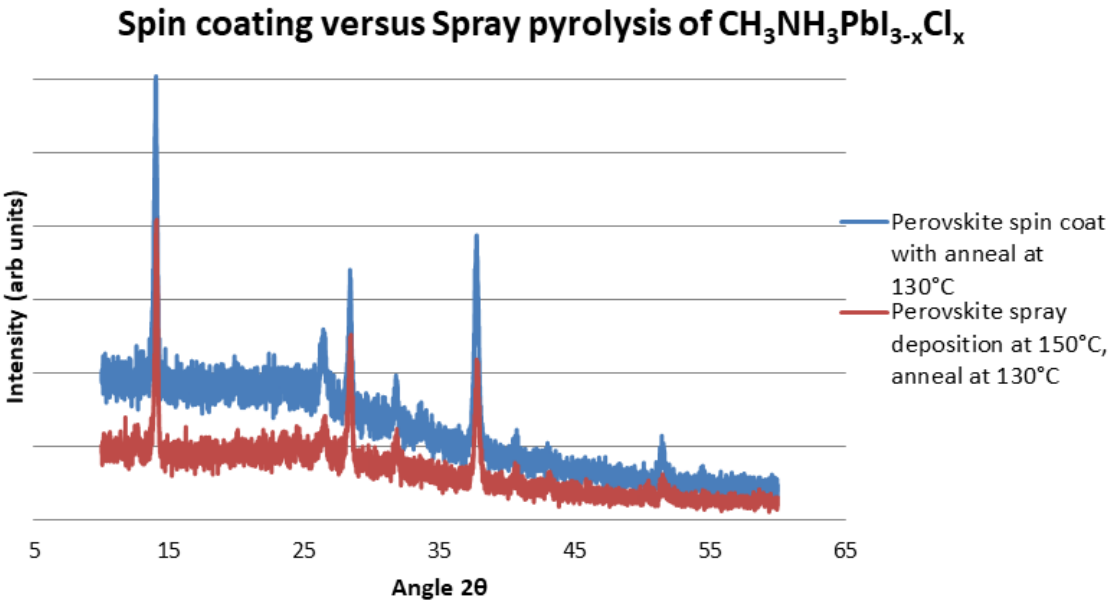

Figure 22: *XRD analysis comparing a $CH_3NH_3PbI_{3-x}Cl_x$ thin film deposited by spin coating with subsequent annealing at 130°C and a $CH_3NH_3PbI_{3-x}Cl_x$ thin film deposited by spray pyrolysis at 150°C with subsequent annealing at 130°C*

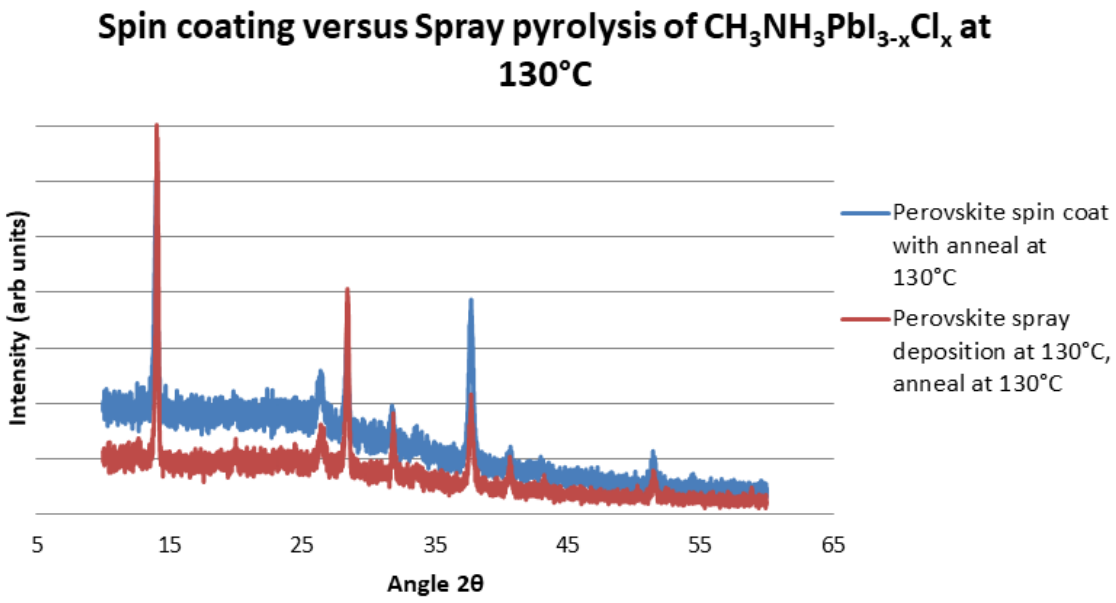

Figure 23: *XRD analysis comparing a $CH_3NH_3PbI_{3-x}Cl_x$ thin film deposited by spin coating with subsequent annealing at 130°C and a $CH_3NH_3PbI_{3-x}Cl_x$ thin film deposited by spray pyrolysis at 130°C with subsequent annealing at 130°C*

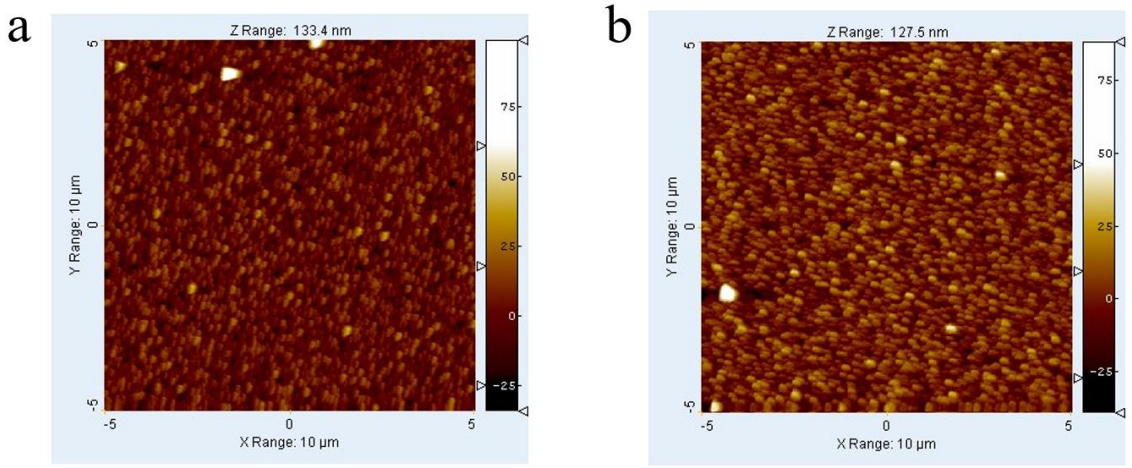

Figure 24: *10 µm topography image of blank TCO22-15, 15 Ω cm^{-1}Solaronix FTO coated glass at* ***(a)*** *0 ° rotation and* ***(b)*** *90 ° rotation. Roughness RMS value calculated at 9 nm*

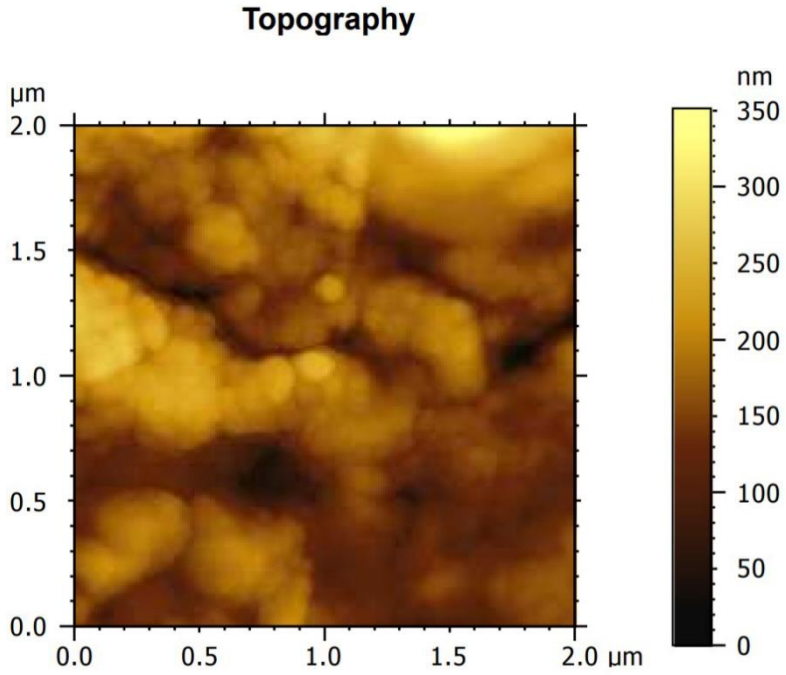

Figure 25: (a) *2 µm topography image of $CH_3NH_3PbI_3$/ 20 nm ALD TiO_2/ TCO22-15 Solaronix FTO coated glass showing grains and cracks in the surface. Roughness RMS value calculated at 44.4 nm.*

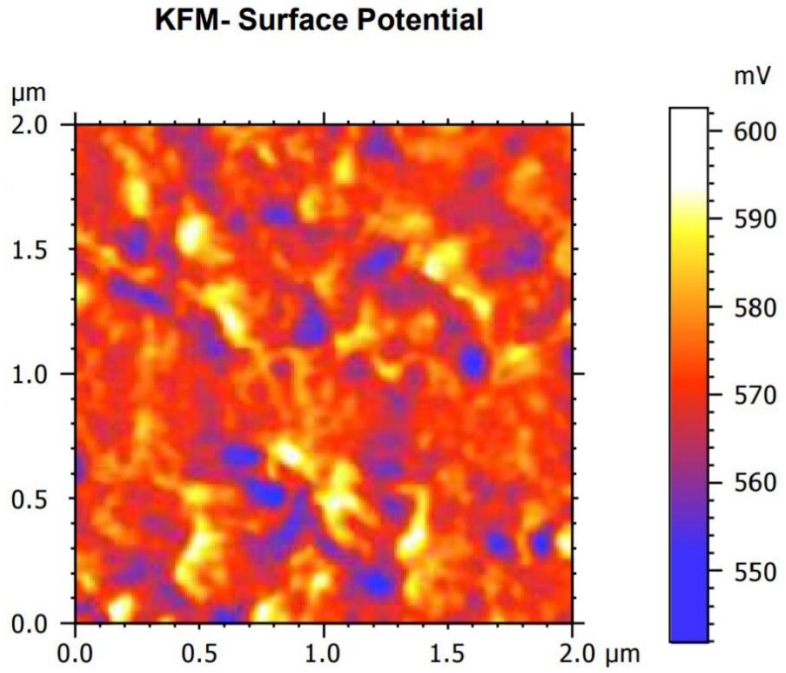

Figure 25: (b) *2 µm corresponding surface potential image (using frequency modulation KFM) revealing differences in work function on different parts of the sample*

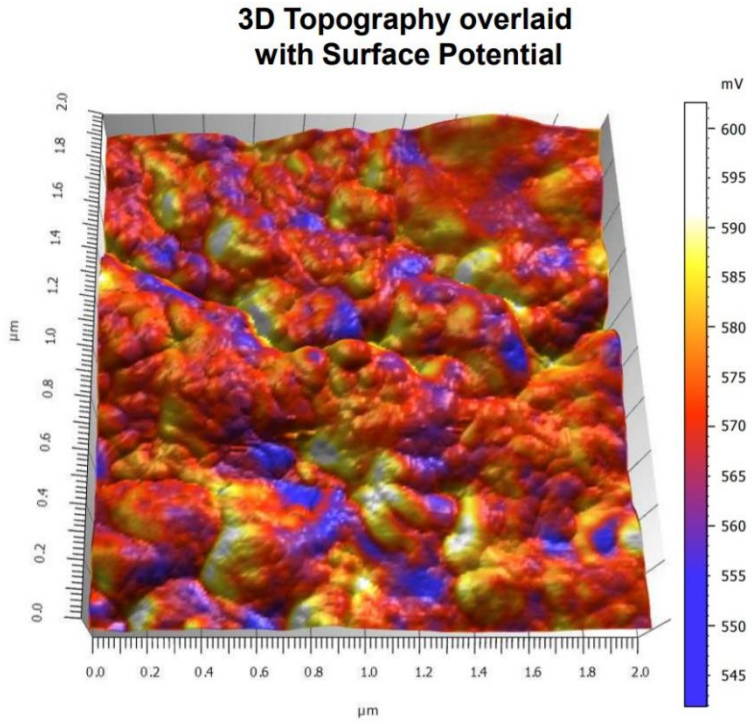

Figure 25: (c) *2µm topography image of same sample overlaid with the surface potential map showing correlations between grain features and furrows (blue is lower potential, yellow is highest)*

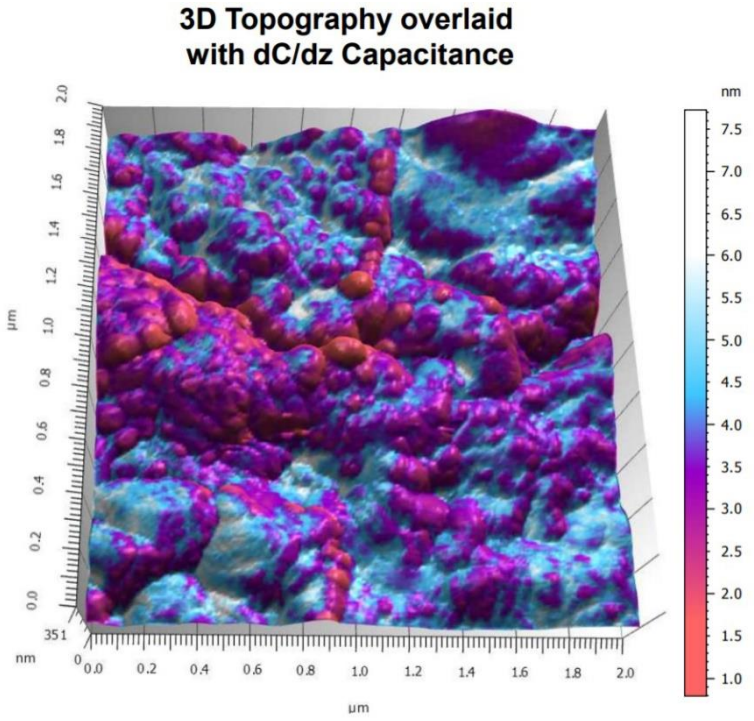

Figure 25: (d) *2µm topography image of same sample overlaid with dC/dz capacitance, revealing highly interesting differences in the dielectric properties on this sample area*

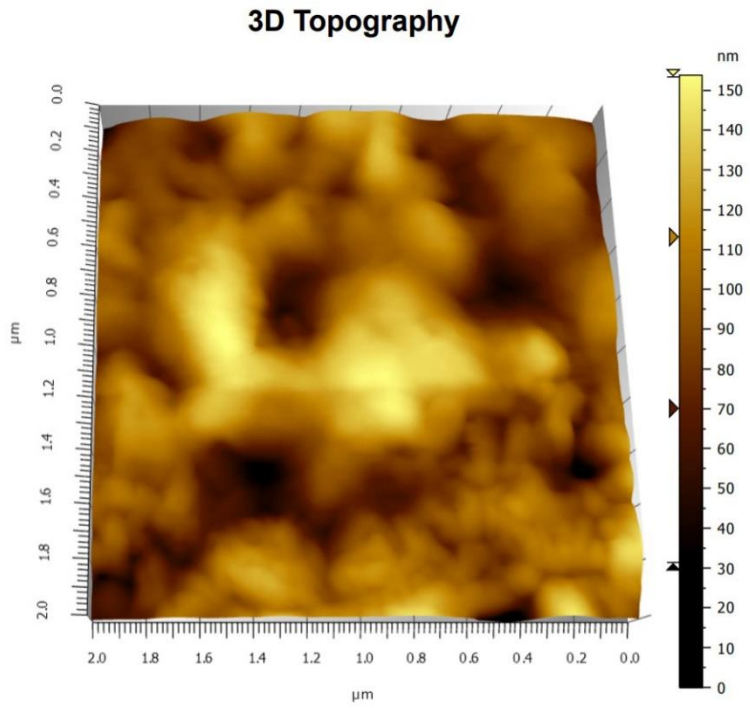

Figure 25: (e) *2µm 3D topography image of sample showing two different areas, the lower one being finer in grain size and with worm-like features, the other area towards the top is smoother and has bigger grains*

During the internship at the University of Oxford, preliminary studies on the development of alternative passivation layers were performed. These solution based studies, in the *p-i-n* architecture, were performed in order to screen for possible candidate materials for the HTL/perovskite interface prior to the development of ALD processes. These passivation layers were placed between p-type NiO_x which acted as the HTL and the perovskite material. In these studies p-type In_2O_3 and PbO were chosen as the interlayers for investigation to produce device stacks composed of TEC7 FTO coated glass/ NiO_x/ p-type PbO or In_2O_3/ $MAFACsPb(IBr)_3$/ PCBM/ BCP/ Ag. Both chosen interface layers produced functioning cells with PbO outperforming In_2O_3 significantly.

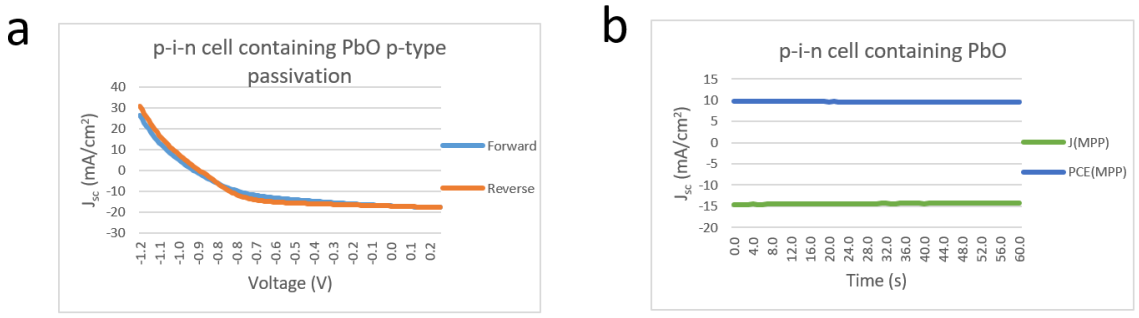

Figure 26: (a) *J-V characteristics of the champion PbO passivated p-i-n cell and* ***(b)*** *Stabilised photocurrent and efficiency of the champion PbO passivated p-i-n cell*

The best pixel incorporating PbO achieved 9.30 % PCE in the reverse scan and 7.89 % PCE in the forward scan, stabilising at 9.56 % PCE over 60 seconds of MPP tracking (Figure 29) . Due to low J_{sc} (17.93 mA/cm^2) and FF (0.67), this cell did not compare well with the reference which contained no p-type passivation layer (Table I). The reference cell achieved 15.68 % PCE in the reverse scan and 11.15 % PCE in the forward scan (Figure 30 a). This stabilised at 14.57 % PCE after 60 seconds of MPP tracking (Figure 30 b)

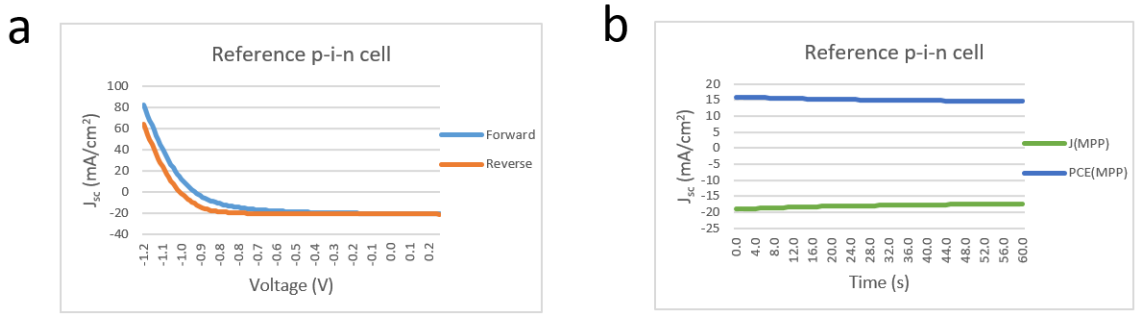

Figure 37: (a) *J-V characteristics of the champion non passivated p-i-n cell and* ***(b)*** *Stabilised photocurrent and efficiency of the champion non passivated p-i-n cell*

Table I: *Device performance parameters. Champion performance parameters for devices made with PbO passivation and reference cell without*

Cell Type	*Scan direction*	*J_{sc} (mA cm^{-2})*	*V_{oc} (V)*	*FF (%)*	*η (%)*
PbO passivated p-i-n	Reverse	17.228	0.93	0.587	9.298
	Forward	17.201	0.95	0.489	7.895
Reference p-i-n	Reverse	21.199	1.03	0.726	15.682
	Forward	20.805	0.96	0.564	11.147

The PCE of the p-type passivation cell may be lower due to the effect of the long UV-ozone which was employed to aid in switching the metal oxide from n-type to p-type. To investigate this, more reference cells were fabricated which were subjected to UV-ozone after deposition of the NiO_x layer and prior to perovskite deposition. The final MPP stabilised PCE was lower than the cell without UV-ozone obtaining 11.66 % after 60 seconds. It is clear that the UV-ozone treatment had a negative impact on the cell.

It should be noted that for *p-i-n* devices, synthesis techniques outside and inside the glovebox were tested. Although higher efficiencies could be obtained using techniques inside the glovebox, the passivation study was conducted outside the glovebox due to better reproducibility.

APPENDIX II:

Publications, Conference Presentations and Awards

Publications

M. M. McCarthy, M. Bräuninger, A. Walter, L. Ryan, S. O'Brien, M. E. Pemble, S. Nicolay, C. Ballif, B. Wenger, H. J. Snaith and I. M. Povey
"Effects of Interface Passivation Techniques on Low-Temperature Atomic Layer Deposited SnO_2 for Efficient Perovskite Solar Devices"
To be submitted (2019)

M. M. McCarthy, A. Walter, S-J. Moon, N. K. Noel, S. O'Brien, M. E. Pemble, S. Nicolay, B. Wenger, H. J. Snaith and I. M. Povey
"Atomic Layer Deposited Electron Transport Layers in Efficient Organometallic Halide Perovskite Devices"
MRS Advances, 3, 51, 3075-3084 (2018)

H. M. Yates, M. Afzaal, A. Walter, J. L. Hodgkinson, S-J. Moon, D. Sacchetto, M. Bräuninger, B. Niesen, S. Nicolay, **M. M. McCarthy**, M. E. Pemble, I. M. Povey and C. Ballif
"Progression towards high efficiency perovskite solar cells via optimisation of the front electrode and blocking layer"
J. Mater. Chem. C, 4, 11269-11277 (2016)

S. Monaghan, F. Gity, R. Duffy, G. Mirabelli, **M. McCarthy**, K. Cherkaoui, I. M. Povey, R. E. Nagle and P. K. Hurley
"Hall-effect Mobility for a Selection of Natural and Synthetic 2D Semiconductor Crystals"
2017 Joint International EUROSOI Workshop and International Conference on Ultimate Integration on Silicon (*EUROSOI-ULIS*), Athens, 27-30 (2017)

G. Mirabelli, C. McGeough, M. Schmidt, E.K. McCarthy, S. Monaghan, I.M. Povey, **M. McCarthy**, F. Gity, R. Nagle, G. Hughes, A. Cafolla, P.K. Hurley and R. Duffy
"Air sensitivity of MoS_2, $MoSe_2$, $MoTe_2$, HfS_2, and $HfSe_2$"
J. Appl. Phys., 120, 125102 (2016)

G. Mirabelli, M. Schmidt, B. Sheehan, K. Cherkaoui, S Monaghan, I. Povey, **M. McCarthy**, A. P. Bell, R Nagle, F. Crupi, P. K. Hurley and R. Duffy
"Back-gated Nb-doped MoS2 junctionless field-effect-transistors"
AIP Advances, 6, 025323 (2016)

Conference Presentations

M. M. McCarthy, A. Walter, S-J. Moon, N. K. Noel, S. O'Brien, M. E. Pemble, S. Nicolay, B. Wenger, H. J. Snaith and I. M. Povey
"Atomic Layer Deposited Electron Transport Layers in Efficient Organometallic Halide Perovskite Devices"
MRS Conference, Phoenix, USA, 2018 (Oral presentation)

M. M. McCarthy, A. Walsh, L. Ryan, J. Kegel, M. E. Pemble, S. O'Brien and I. M. Povey
"Comparison of TiO_2 and SnO_2 Electron Transport Layers in Planar Perovskite Solar

Cells”
ECS Conference, San Diego, USA, 2016 (Oral presentation)

M. M. McCarthy, A. Walsh, L. Ryan, A. Walter, B. Kamino, J. Werner, S-J. Moon, S. Nicolay, C. Ballif, F. Laffir, S. O’Brien, M. E. Pemble and I. M. Povey,
“Doped Electron Transport Layers for Perovskite Solar Cells”
ALD Conference, Denver, USA, 2017 (Poster presentation)

M. M. McCarthy, A. Walsh, S. O'Brien, M.E. Pemble and I.M. Povey
“ALD of various Transparent Electron Transport Layers (ETLs) for use in Planar Perovskite Solar Cells”
TCM Conference, Crete, Greece, 2016, (Poster presentation)

M. M. McCarthy, A. Walsh, M. E. Pemble, S. O'Brien and I. M. Povey
“ALD of Electron Transport Layers (ETL) for Planar Perovskite Solar Cells”
ALD Conference, Dublin, Ireland, 2016, (Poster presentation)

Achievements

Awarded HERALD (Hooking together European research in Atomic Layer Deposition) grant for short term scientific mission at the University of Oxford

Third prize at Tyndall Postgraduate Poster Competition 2017